Field and experimental characterisation of tephra sedimentation and resuspension processes

Fries, Allan Alexis

Université de Genève
Département des Sciences de la Terre

Faculté des sciences
Professeure Costanza Bonadonna

Field and experimental characterisation of tephra sedimentation and resuspension processes

THÈSE

présentée à la Faculté des sciences de l'Université de Genève
pour obtenir le grade de Docteur ès sciences, mention Sciences de la Terre

par

Allan Alexis Fries

de Lengnau, Argovie (né à Strasbourg, France)

Thèse N^o 5670

Genève
Atelier de reprographie ReproMail
2022

UNIVERSITÉ
DE GENÈVE
FACULTÉ DES SCIENCES

DOCTORAT ÈS SCIENCES, MENTION SCIENCES DE LA TERRE

Thèse de Monsieur Allan Alexis FRIES

intitulée :

«Field and Experimental Characterisation of Tephra Sedimentation and Resuspension Processes»

La Faculté des sciences, sur le préavis de Madame C. BONADONNA, professeure ordinaire et directrice de thèse (Département des sciences de la Terre), Monsieur J. RUCH, professeur assistant (Département des sciences de la Terre), Monsieur P. JARVIS, docteur (GNS Science, Wellington, New Zealand), Madame I. MANZELLA, professeure associée (Department of Applied Earth Sciences, University of Twente, the Netherlands), Monsieur J. PHILLIPS, professeur (School of Earth Sciences, University of Bristol, United Kingdom) et Monsieur M. MANGA, professeur (Earth and Planetary Science, University of Califronia, Berkley, United States of America), autorise l'impression de la présente thèse, sans exprimer d'opinion sur les propositions qui y sont énoncées.

Genève, le 2 août 2022

Thèse - 5670 -

Le Doyen

N.B. - La thèse doit porter la déclaration précédente et remplir les conditions énumérées dans les "Informations relatives aux thèses de doctorat à l'Université de Genève".

“Dans des terrains cendreux, calcinés, sans verdure,
Comme je me plaignais un jour à la nature, [...]
Je vis en plein midi descendre sur ma tête
Un nuage funèbre et gros d’une tempête”

“One day as I was making complaint to nature
In a burnt, ash-gray land without vegetation, [...]
I saw in broad daylight descending on my head
A leaden cloud, pregnant with a tempest ”

"La Béatrice", Charles Baudelaire
in *Les Fleurs du mal.* Paris: Poulet-Malassis et De Broise, 1857.
Translation by William Aggeler
in *The Flowers of Evils.* Fresno, CA: Academy Library guild, 1954

Acknowledgements

I would like to thank my supervisor Prof. Costanza Bonadonna for providing constant motivation, support, and help throughout this PhD. She has created an optimal work environment for me and the rest of her research group, being always available and taking time for each student despite her countless assignments, even in the midst of the COVID-19 pandemic. I utterly respect her for that, and have learned so much from her during these years, not only about sciences. I am grateful that I had the opportunity to work with such a rockstar in volcanology, who have trusted me to work on my lifelong passion for volcanoes.

I also want to express my most sincere gratitude to Dr. Paul Jarvis, for teaching me how to do science at an academic level, and for his support. I have learned from him how to better perform laboratory experiments, analyse data, write or present my work, and this is not an exhaustive list. Undoubtedly, the work presented in this thesis would have been poorer without his great help.

The members of the jury, namely Prof. Joël Ruch, Prof. Irene Manzella, Prof. Jeremy Phillips and Prof. Michael Manga, are also thanked for their important contribution to finalise this thesis, and for the interesting discussion following the defence. In particular, I want to thank Irene Manzella and Jeremy Phillips, who accompanied me during my PhD, strengthening this work.

Prof. Amanda Clarke is thanked for the invaluable help she has provided throughout these years. I am notably grateful she guided me with first exploratory experiments performed in her laboratory in Arizona at the beginning of my PhD. Also, I want to thank her and Ramon Arrowsmith for supporting me so naturally when I had to prematurely come back to Europe during the darkest times of my life.

I want to thank everyone who assisted me during field works. I am grateful to Simona Scollo for providing videos of eruptions at Mount Etna, as well as for helping me analysing them, together with Michele Prestifilippo. Rigoberto Aguilar, Nelida Manrique, David Valvidia, Ivonne Lazarte, Marco Rivera and the whole

INGEMMET team of Arequipa is thanked for their support during the campaign at Sabancaya volcano, and for providing additional data/samples after the field trip. For the field campaign at Sakurajima volcano, I want to thank Alexandros Poulidis and Masato Iguchi. I also want to thank Eveanjelene Snee who helped me so much calibrating videos acquired in the field.

All my amazing colleagues (and ex-colleagues) from the first floor are thanked for all the good memories, their great help for my work and in life, as well as the things they taught me: Eduardo Rossi (boh), Lucia Dominguez Barragan (y paquita), Valentin Freret-Lorgeril (la fissure), Maria-Paz Reyes Hardy (arroz blanco), Luigia Di Maio (true strength), Sebastian Biass (thank you so much for the extremely useful Matlab packages), Corine Frischknecht (professionalism), Bocar Sy (serenity), Stefano Pollastri (evening music), Valérie Baumann, Matthew Edwards, Luigi Passarelli and Laura Pioli.

Of course, I am particularly grateful to Jonathan Lemus, my brother in this adventure. Jo is a real motivation in my work, and a great help throughout this PhD. I am glad that we met and that we had the occasion to work so closely.

This whole work could not be conducted without the support of the members of the Department of Earth Sciences and of the Section of Earth and Environmental Sciences. Many thanks to Rossana Martini, Sébastien Castelltort, Christine Lovis, Rolanda Freitas Lopes, Maria Pilar Reymond-Gonzales, Elisabeth Lagut, Josephine Romagnoli, Agathe Martignier and Nino Isabella Valenzi. In particular, I would like to thank Frédéric Arlaud who did a fantastic job to build, maintain and repair field and laboratory equipments (and facilities). I also want to thank colleagues from the Department of Earth Sciences: Susanne Theodora Schmidt for allowing me to have first experiences in teaching, Oliver Higgins and Thomas Sheldrake with whom we organised the field trip to Martinique.

I would like to thank my Master's supervisors Olivier Roche and Guillaume Carazzo for allowing me to start working in physical volcanology. I hope to bump into them at conferences and meet them for other reasons in the future!

Now, I would like to thank my friends, in Geneva and elsewhere for all the good times. I especially want to thank Stefano Mannini for sharing this student adventure

with me in between Clermont-Ferrand and Geneva. Introducing me to padel and giving me the motivation to do sports was essential to stay in good physical and mental health when writing this thesis! Thanks to Alexian Ajas and Antonin Bouillet (les zouaves), I hope that we will see many more volcanoes together!

Special thanks to Juliette (Le Juju) who had to live with a PhD student for so long. Thanks for supporting me in good and bad times! Les aléas de la vie font que, malgré nous, nous sommes désormais en état de surmonter de nombreux défis ensemble : *la pierre retombe en bas du ravin, alors on la remonte* ! Merci aussi à la famille Luczak, je suis reconnaissant d'avoir pu partager avec vous autant de moments inoubliables.

Finally, I am most deeply thankful to my familly ('Ohana), and I have no right words to express my gratitude to them. Bref, merci papa, David, Mémé et Sylvain (évidemment) ! Nous avons vécu des évènements traumatisants ces dernières années, mais nous restons groupés et c'était un immense plaisir d'être tous réunis lors de la soutenance de thèse. Merci aux cousins, oncles et tantes aussi (notamment à Éric, le Dr. Fries originel, qui a fait le déplacement pour la soutenance). Bien sûr, j'espère que maman serait fière de moi, tout comme papi. Je leur dédie cette thèse, merci maman d'avoir toujours cru en moi, ainsi que pour tout l'amour dont tu as innondé la famille !

This work was supported by the Swiss National Science Foundation (project N. 200021_169463)

Contents

List of Figures

List of Tables

Summary

Explosive volcanic eruptions directly pose multiple hazards to societies. Among these, the widespread dispersal and deposition of volcanic fragments ejected in the atmosphere (i.e., tephra) can threaten human health and the environment, but also cause heavy economic losses in many sectors, including transportation, tourism, agriculture and farming. In particular, tephra particles with diameters below 2 mm (i.e., volcanic ash) can travel in the atmosphere during long periods before settling very far from their source, possibly generating disruptions at regional and global scales.

Once sedimented on the ground, tephra form deposits whose characteristics can be interpreted to determine various eruptive physical parameters, including intensity and magnitude. However, under the action of environmental factors such as water, snow or wind, tephra can be remobilised after deposition. This potentially alters the preservation of deposits, and generates long-lasting secondary hazard (e.g., lahars and ash storms) that extend the impact of primary tephra fallout in space and time. Volcanic ash can notably undergo aeolian remobilisation and be resuspended by winds in the atmosphere, even thousands years after initial deposition.

In order to mitigate the impacts related to the dispersal and sedimentation of both primary and resuspended volcanic ash, efficient Volcanic Ash Transport and Dispersal Models (VATDMs) are needed to predict affected areas and forecast the intensity of hazards. VATDMs are being continuously improved, notably by incorporating more accurate parametrisations of aeolian remobilisation processes and of particle sedimentation. In particular, rapidly descending ash fingers are observed at the base of volcanic ash clouds. Whilst they have the potential to significantly enhance the deposition of fine ash, ash fingers are not sufficiently understood to accurately quantify their effect on volcanic ash sedimentation.

In this thesis new insights are provided to characterise the sedimentation of volcanic ash within ash fingers and aeolian remobilisation. First, new field measure-

ments based on visual observations of ash fingers formed below wind-bent plumes are presented. Higher vertical finger velocities than in previous studies are found for the ash fingers studied in this thesis at Etna (Italy), Sabancaya (Peru) and Sakurajima (Japan) volcanoes. This implies that fine volcanic ash, with sizes ranging from the smallest grains up to maximum diameters of 613 ± 130 µm, potentially settled within ash fingers. Observations are also interpreted to study the mechanisms at the origin of ash fingers that possibly resulted from settling-driven gravitational instabilities (SDGIs) strongly influenced by the wind. Conditions favouring the onset of SDGIs are separately identified in laboratory experiments, depending on the thickness of volcanic clouds, ash concentration and grainsize. It is found that ash fingers develop preferentially below thick volcanic ash clouds associated with high ash concentrations and fine grainsizes. Experimental measurements additionally confirm previous findings regarding the size and dynamics of ash fingers over a wider set of initial conditions. The velocity of fingers increases with increasing particle concentrations, whereas their characteristic length scales (i.e., the width and spacing of fingers, as well as the thickness of the destabilising layer) decrease with increasing particle concentrations. All finger characteristic length scales are found to be proportional to each other, scaling with a Grashof number of 10^4.

Moreover, the post-2016 explosive activity of Sabancaya volcano has been considered as a case study for the description of aeolian remobilisation using a combination of various sampling and imaging strategies. Recurrent syn-eruptive aeolian remobilisation phenomena are observed and different transport mechanisms are identified. In this volcanic context where new tephra are frequently deposited and readily remobilised by the wind, remobilised particles show negligible morphological differences with respect to primary deposits.

Results presented in this thesis provide new measurements of ash fingers properties and aeolian remobilisation. This constitutes a basis for quantifying the role of ash fingers on the deposition of volcanic ash and provides new insights into syn-eruptive processes of aeolian remobilisation of volcanic ash. The analysis of both ash fingers and aeolian remobilisation will benefit from the use of complementary field techniques in the future to validate interpretations presented in this thesis.

Résumé en Français

Les éruptions volcaniques explosives occasionnent de multiples aléas. Parmi ceux-ci, la dispersion et la sédimentation de fragments de roches volcaniques (téphras) peut menacer la santé des personnes ainsi que l'environnement. Cela peut aussi causer de lourdes pertes économiques dans de nombreux secteurs, y compris dans les domaines du transport, du tourisme, de l'agriculture et de l'élevage. En particulier, les téphras avec un diamètre inférieur à 2 mm (cendres volcaniques) peuvent se déplacer dans l'atmosphère sur de longues périodes avant de se déposer au sol très loin de leur source, en engendrant des perturbations à des échelles régionales et globales.

Une fois sédimentées au sol, les téphras forment des dépôts dont les propriétés peuvent être étudiées pour déterminer divers paramètres éruptifs, dont intensité et la magnitude des éruptions. Cependant, les téphras peuvent être remis en mouvement après déposition sous l'influence de plusieurs facteurs environnementaux tels que l'eau, la neige, ou le vent. Cela peut potentiellement altérer la préservation des dépôts, mais aussi générer des aléas secondaires durables (ex. lahars, tempêtes de cendres) qui étendent dans le temps et l'espace l'impact initial de la chute des téphras. Les cendres volcaniques peuvent notamment subir une remobilisation éolienne et être remises en suspension dans l'atmosphère par le vent, même plusieurs milliers d'années après avoir été déposées.

Afin de minimiser les impacts associés à la dispersion et la sédimentation des cendres volcaniques primaires et remises en suspension, il est nécessaire de développer des modèles (VATDMs) capables de prédire les zones affectées et l'intensité des évènements. Les VATDMs sont en perpétuelle amélioration, notamment grâce à l'incorporation de meilleures descriptions des processus de remobilisation éolienne et des mécanismes affectant la chute des cendres. Ils ne prennent cependant pas encore en compte les effets associés aux traines de cendres, qui sont des courants descendant rapidement vers le sol depuis la base des nuages de cendre volcanique, et ayant la capacité de considérablement accélérer la chute des cendres volcaniques fines. En ef-

fet, malgré leur potentiel rôle dans la dépositions des cendres volcaniques, les traines de cendres ne sont pas suffisamment bien décrites pour permettre de correctement quantifier leurs effets sur la sédimentation des cendres volcaniques.

Dans cette thèse, de nouvelles connaissances sont apportées pour caractériser la sédimentation des cendres volcaniques dans les traines de cendres ainsi que la remobilisation éolienne des dépôts de téphras. De nouvelles mesures de terrain basées sur des observations de traines de cendres formées sous des panaches volcaniques courbés par le vent sont présentées. La vitesse de chute moyenne des traines étudiées dans cette thèse aux volcans Etna (Italie), Sabancaya (Pérou) et Sakurajima (Japon) est plus grande que celle rapportée dans de précédentes études. Cela implique que des cendres volcaniques fines, dont le diamètre va des grains les plus fins à des tailles maximales de 613 $\pm$ 130 µm, ont pu sédimenter dans les traines. Les observations permettent aussi d'examiner les mécanismes à l'origine des traines de cendres. Ces dernières ont potentiellement résulté d'Instabilités Gravitationnelles Produites par Sédimentation (IGPS) fortement influencées par le vent. Les conditions favorisant le développement d'IGPS sont identifiées à l'aide d'expériences de laboratoire, et dépendent notamment de l'épaisseur des nuages volcaniques, de la concentration en cendres et de leur taille. Il en est déduit que les traines de cendres se développent préférentiellement sous des nuages de cendre volcanique épais contenant de grandes concentrations de cendres, ainsi que pour des particules volcaniques avec de petits diamètres. De plus, les mesures expérimentales confirment les conclusions d'études précédentes concernant la dynamique et la taille des traines de cendres pour des conditions initiales plus vastes. La vitesse des traines augmente en fonction de la concentration en particules, alors que leurs dimensions caractéristiques (c.-à-d. la largeur et l'espacement entre les traines, ainsi que l'épaisseur de la couche instable) diminuent avec la concentration en particules. Toutes les dimensions caractéristiques des traines sont proportionnelles entre elles, ainsi qu'à un nombre de Grashof égal à 10^4.

De plus, l'activité explosive post-2016 du volcan Sabancaya a été considérée pour étudier la remobilisation éolienne sur le terrain. Des phénomènes de remobilisation éoliennes syn-éruptifs sont fréquemment observés et différents mécanismes de trans-

port sont identifiés. Dans ce contexte volcanique actif où de nouveaux téphras sont fréquemment déposés puis immédiatement remis en mouvement par le vent, les différences morphologiques entre les particules ayant été remises en mouvement et les particules primaires des dépôts sont très faibles.

Les résultats présentés dans cette thèse fournissent de nouvelles mesures des propriétés des traines de cendres et de la remobilisation éolienne. Cela constitue une base afin de quantifier le rôle des traines de cendre dans le dépôt des cendres volcaniques tout en donnant une nouvelle vision des processus de remobilisation éolienne syn-éruptifs. L'analyse sur le terrain des traines de cendres et de la remobilisation éolienne bénéficiera à l'avenir de l'utilisation de techniques de terrain complémentaires permettant de valider les interprétations exposées ici.

Chapter 1

Introduction

Volcanoes are fascinating and complex natural systems related to multiple primary hazards including lava flows (Harris, 2015), pyroclastic density currents (Sulpizio et al., 2014), or gas emissions (Edmonds et al., 2015), that occur as a direct product of eruptions. Among primary volcanic hazards, the most frequent and widespread phenomena are certainly the dispersal (i.e., the atmospheric transport of particles) and fallout (i.e., the deposition of particles to the ground) of volcanic fragments produced during explosive eruptions. These fragments are called tephra when emitted in the atmosphere, irrespective of their size, shape and composition, in the sense of Thorarinsson (1944). Tephra particles with diameter $d < 2$ mm (i.e., volcanic ash) can travel for hundreds to thousands of kilometres before sedimentation. Although not often causing direct casualties (Auker et al., 2013; Brown et al., 2017), potential impacts on society resulting from the dispersal and fallout of volcanic ash cover wide areas, and vary as a function of the distance from the volcano (Figure 1.1). Close to the vent, in the proximal zone, accumulation of tephra can cause major structural damage to buildings such as roof collapse (Spence et al., 2005), destroy power and water supplies or severely pollute ecosystems (Arnalds, 2013). Further from the vent, in the medial zone, tephra can cause non-structural damage to buildings, disruption of critical services (Wilson et al., 2012), and requires frequent cleaning operation in order to reduce impacts. Far from the vent, in the distal zone, the presence of airborne respirable ash represents a significant threat to human health (Forbes et al., 2003; Horwell and Baxter, 2006; Gudmundsson, 2011). At all distances from the volcano, volcanic ash can disturb air traffic, with potentially heavy economic losses even for moderate-intensity eruptions (Guffanti et al., 2009;

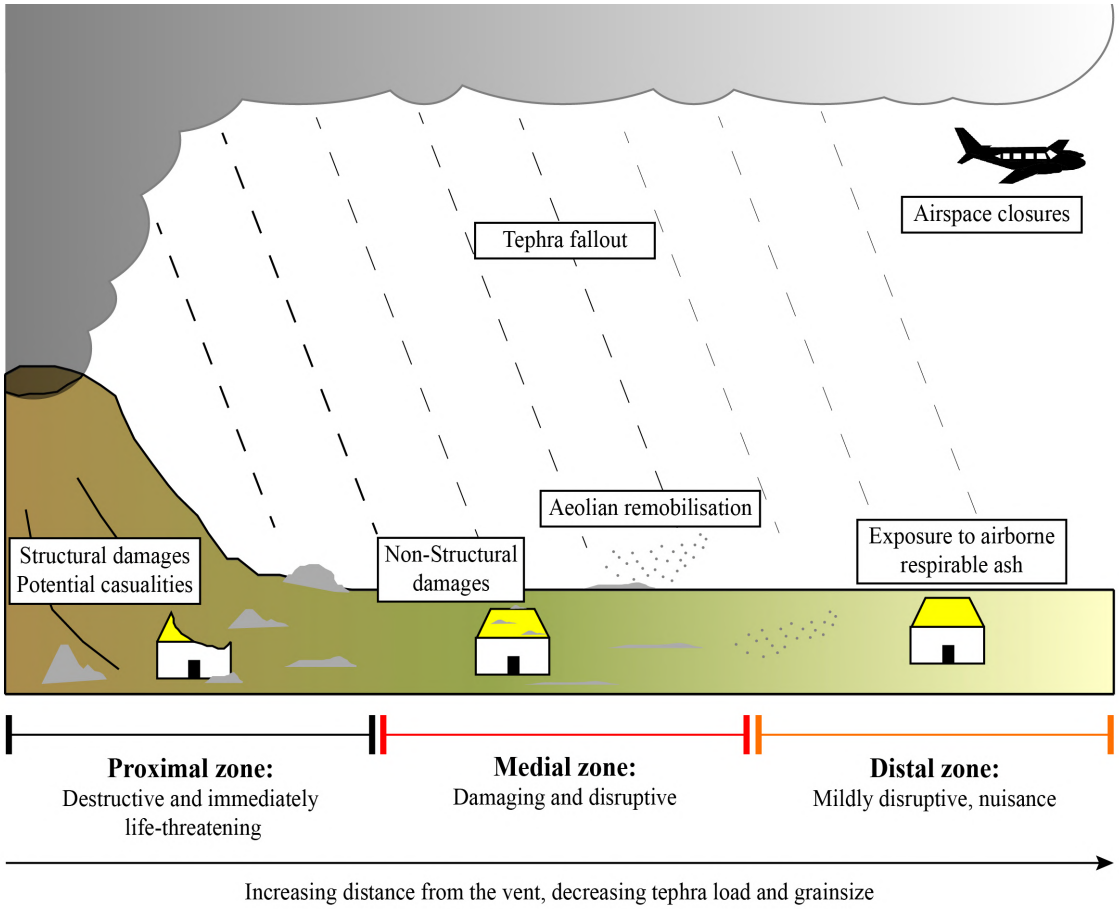

Figure 1.1: Sketch illustrating the variations in tephra dispersal and fallout impacts with distance from the vent. Simplified from Jenkins et al. (2015).

Mazzocchi et al., 2010). Moreover, primary hazards can be extended in space and time by secondary hazards that are the consequence of factors external to volcanic eruptions. These notably include lahars and the remobilisation of volcanic ash by wind that can both occur during eruptions, but also long-after the cessation of the volcanic activity (Dominguez et al., 2020b; Thouret et al., 2020).

During an eruption, volcanologists can use a wide variety of tools (e.g., remote sensing techniques, real-time sampling) to monitor the evolution of the eruption intensity. The information obtained provides the basis for assessing potential impacts. Eruptive source parameters are combined with atmospheric models in Volcanic Ash Transport and Dispersal Models (VATDMs) to operationally forecast the spatial and temporal variations in the concentration of volcanic ash in the atmosphere and predict areas affected by fallout (Bonadonna et al., 2012; Folch, 2012). To do so, VATDMs require a parameterisation of the volcanic ash transport and dispersal

that includes a description of the source (i.e., eruptive parameters) and sink (i.e., sedimentation) terms. Better evaluating these terms is therefore essential in order to improve the accuracy of VATDMs. In particular, collective settling mechanisms can significantly modulate the residence time of volcanic ash in the atmosphere and possibly lead to misestimations in the results of VATDMs if not accounted for.

Similarly, the secondary transport of volcanic ash in the atmosphere during and after an eruption can be modelled in order to assess and mitigate impacts resulting from aeolian remobilisation (Leadbetter et al., 2012; Folch et al., 2014; Reckziegel et al., 2016; Mingari et al., 2020). In this case, the source term is complex, constrained as a function of the location and properties of volcanic ash deposits, but is also dependent on meteorological conditions and surface characteristics such as the terrain roughness (e.g., vegetation cover) and soil moisture, which are particularly challenging to quantify (Jarvis et al., 2020). The effects of these factors on ash emission schemes need to be better evaluated, notably through field analysis of remobilised ash that can be used to validate emission schemes.

Tephra fallout deposits retain critical information on eruptive dynamics. They are essential for understanding the history of volcanoes. The magnitude, intensity and frequency of explosive volcanic eruptions can be derived from deposits, constituting a base for assessing hazards in an area (Lindsay and Robertson, 2018; Bonadonna et al., 2021), notably using a probabilistic approach (Biass et al., 2016b). For the purpose of reconstructing eruptions from deposits, a good understanding of primary tephra fallout is fundamental. Inaccurate description of the processes governing tephra fallout would lead to erroneous interpretations. Moreover, remobilisation of tephra has the potential to significantly alter the preservation of the deposits, whose original characteristics can be significantly modified (Cutler et al., 2018; Dugmore et al., 2020). It is therefore essential to improve our comprehension of both primary tephra deposition and secondary processes, as well as their impact on deposits.

1.1 Phenomena studied in this thesis

As any other sediment, tephra are subjected to complex transport and deposition mechanisms after being produced by fragmentation. These phases of alternate transport and deposition constitute a continuous history (or *life cycle*; Dominguez et al., 2020a) including primary and secondary processes. Whilst primary processes are direct results of an eruption, secondary processes are triggered by the action of erosive agents such as the wind, water or snow. Within these different processes, I focus on primary tephra fallout (Chapters 2, 3, 4) and the subsequent remobilisation by wind (Chapter 5) in this thesis.

1.1.1 Tephra sedimentation and the role of ash fingers

During explosive eruptions, volcanic ash and lapilli ($d < 64$ mm) are entrained upward by convective motions in volcanic plumes that rise until reaching the level of neutral buoyancy at which their density equals that of the surrounding atmosphere (Sparks, 1986). At this level, volcanic plumes spread horizontally, carrying tephra particles until sedimentation. Plume rise and transport of tephra are both affected by surrounding winds, with rising plumes potentially bending into the wind direction, depending on the ratio between the plume buoyancy and wind advection (i.e., strong versus weak plumes; Bonadonna and Phillips, 2003; Degruyter and Bonadonna, 2012). Tephra are predominantly transported downwind, but also upwind for strong, subvertical, plumes.

Tephra settle from plumes at distances that depend on their terminal fall velocity. This is generally controlled by the size, density and shape of volcanic ash (Bonadonna et al., 1998; Saxby et al., 2018), with coarse, dense and spherical particles sedimenting closer to the vent than fine, light and non-spherical particles. However, the terminal fall velocity of tephra particles can be affected by orographic effects that potentially create vertical atmospheric circulations that force particles downward (Watt et al., 2015; Eychenne et al., 2017; Takemi et al., 2021). Moreover, volcanic ash (especially in the fine ash fraction; $d < 63$ µm) commonly settles collectively as aggregates or within ash fingers instead of individually.

Volcanic ash aggregation describes the collision and sticking of volcanic ash particles that notably occurs because of electrostatic attraction (Pollastri et al., 2021), hydrometeor formation (Durant et al., 2009), or the creation of liquid bridges binding particles by capillary forces (Schumacher and Schmincke, 1995). From this variety of formation mechanisms results several types of aggregates classified as accretionary pellets, associated with wet aggregation, and particle clusters, generally associated with dry aggregation, according to Brown et al. (2012) and Bagheri et al. (2016). The preservation of aggregates is rare in ash fallout deposits, as they usually break upon impact (especially fragile particle clusters), potentially producing bimodal deposits (Carey and Sigurdsson, 1982; Bonadonna et al., 2011). Volcanic ash settling as aggregates generally sediment faster than individually, thus causing premature sedimentation (i.e., reduction of the residence time of volcanic ash in the atmosphere). Hence, some VATDMs and plume models now include a parameterisation of the effect of particle aggregation on the dispersal and sedimentation of volcanic ash (Folch et al., 2016; Beckett et al., 2022).

Ash fingers are descending ash-laden currents produced by instabilities forming underneath volcanic ash plumes. These currents take the distinctive form of sedimenting columns that have been observed to form below several volcanic ash clouds produced various type of eruptions and volcanoes, including Mount Redoubt (USA) in 1990 (Hobbs et al., 1991), Ruapehu (New Zealand) in 1996 (Bonadonna, 2005a), Soufrière Hills (Montserrat) in 1997 (Bonadonna et al., 2002a), Grimsvötn (Iceland) in 2004 (Eliasson et al., 2014), Eyjafjallajökull (Iceland) in 2010 (Figure 1.2A; Bonadonna et al., 2011; Manzella et al., 2015; Eliasson, 2020), Etna (Italy) in 2013 (Andronico et al., 2015; Scollo et al., 2017), Sakurajima (Japan) in 2013 (Eliasson et al., 2014), and Stromboli (Italy) in 2015 (Freret-Lorgeril et al., 2020). They propagate downward, entraining fine volcanic ash at speeds greater than the particle terminal fall velocity. Among the observations listed above, very few are accompanied by quantitative descriptions of ash fingers dynamics that remain poorly constrained. In particular, Manzella et al. (2015) found finger downward velocities corresponding to the terminal fall velocity of ash particles with diameters $d \approx$ 200 µm during the May 2010 Eyjafjallajökull eruption. They also reported the oc-

currence of bimodal ash fallout deposits and of aggregates at the distance fingers reached the ground. If entrained within fingers, the sedimentation of the particles finer than 200 μm collected at the distance fingers reached the ground could have been significantly enhanced, explaining the presence of a fine grainsize mode in deposits, concomitantly with the fallout of aggregates. Figures 1.2B-C schematically illustrate the observations of Manzella et al. (2015), regarding both the dynamics of the volcanic plume and tephra deposits. Based on these measurements, it is clear that the fallout within ash fingers is another size-selective collective settling process that also has the potential to enhance the deposition of volcanic ash. However, unlike aggregation, it is far from being sufficiently understood for integration in plume models and VATDMs. The occurrence of particle aggregation simultaneously with the observation of ash fingers brings into question the existence of a possible relationship between the origin of the two processes.

Several mechanisms can be responsible for the production of ash fingers below volcanic clouds, and below particle suspensions in general. These include settling-driven gravitational instabilities (SDGIs) (Hoyal et al., 1999b; Carazzo and Jellinek, 2012; Manzella et al., 2015; Scollo et al., 2017), diffusive convection (Green, 1987; Hoyal et al., 1999b; Carazzo and Jellinek, 2013), wind-induced overturning motions in ash clouds (Freret-Lorgeril et al., 2020), but also the periodical collapse of jets from overshoot regions (Gilchrist and Jellinek, 2021). Shear at the cloud base can also modulate the formation of ash fingers, notably through the creation of Kelvin-Helmholtz instabilities, or by inhibiting SDGIs (Farenzena and Silvestrini, 2017; Konopliv et al., 2018). It is also important to note the resemblance between ash fingers and mammatus that may form underneath volcanic clouds. The latter are rounded lobes, formed by a combination of ash-hydrometeor settling and evaporation/sublimation processes (Kanak et al., 2008; Ravichandran et al., 2020), with internal air velocities descending at greater speeds than individual particles (Durant et al., 2009), but mammatus do not propagate below the cloud base as discrete sedimentation columns, unlike ash fingers.

In this thesis, I focus on SDGIs formation mechanisms and resulting finger properties, as SDGIs are appropriate for describing the onset of ash fingers below volcanic

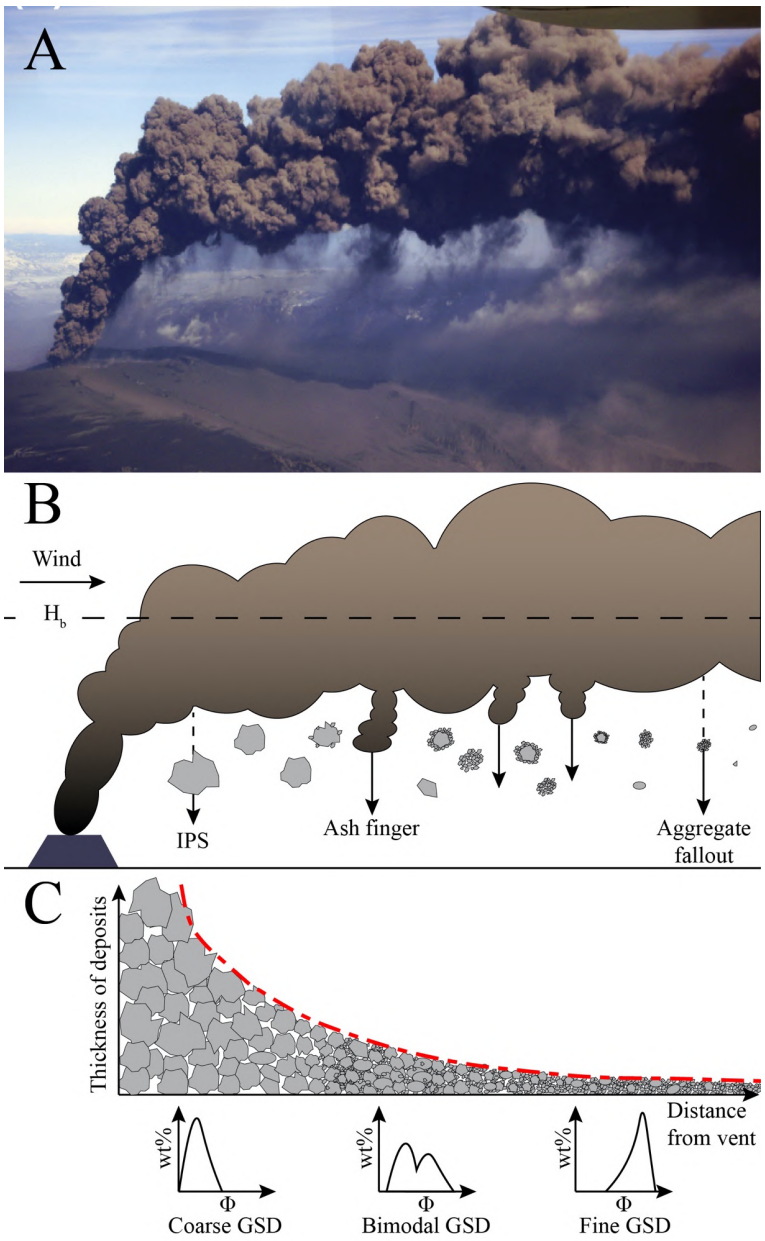

Figure 1.2: Sketch illustrating the sedimentation from a (weak) volcanic plume and collective settling mechanisms. **A.** Photograph of the 2010 eruption of Eyjafjallajökull from Eliasson (2020), with ash fingers observed at the base of the volcanic plume. **B.** Schematic representation of the plume shown in panel A. "IPS" denotes Individual particle Settling, and H_b is the height of the neutral buoyancy level. **C.** Illustration of expected gradual thinning and decrease in grainsize of tephra deposits. The grainsize distribution (GSD) is plotted in mass percentages (wt%) as a function of the particle diameter expressed in Φ units ($\Phi = -\log_2 d$, with d the particle diameter in mm).

ash clouds advected by the wind at the level of neutral buoyancy (Manzella et al., 2015; Scollo et al., 2017). Moreover, analysis of finger properties provides a simple, yet fundamental characterisation of the phenomenon, carefully applicable to fingers originating from other processes than SDGIs. Other formation mechanisms are described with additional details in Chapter 4. SDGIs result from particle settling across an interface in an initially stable density configuration where a particle suspension (i.e., volcanic cloud) is emplaced above a dense ambient fluid (i.e., underlying atmosphere). At the top of the dense fluid, the incorporation of particles generates a heavy Particle Boundary Layer (PBL) that becomes unstable, as it lies on particle free fluid with a lower bulk density (Hoyal et al., 1999b; Burns and Meiburg, 2015; Davarpanah Jazi and Wells, 2020). Rayleigh-Taylor-like instabilities (Sharp, 1984) develop, and the PBL detaches in the form of fingers.

1.1.2 Aeolian remobilisation of tephra deposits

Primarily deposited tephra can become mobile again under the action of several factors (e.g., water, ice, wind, human and animal activities) (Collins and Dunne, 1986; Manville et al., 2000), generating additional hazards and starting the *second life* of tephra. Deposited volcanic ash transported as a result of factors external to volcanic eruptions are called remobilised ash, and the process triggering this secondary transport are generally referred to as remobilisation. Volcanic ash can be remobilised even thousands of years after an eruption, and the duration of these effects depends principally on the availability (i.e., total volume) of tephra deposits (Dominguez et al., 2020b).

Aeolian remobilisation is one of the most recurrent and widespread remobilisation process. It poses several additional hazards to human health (e.g., through long-term exposure to high concentrations of respirable particles; Horwell and Baxter, 2006; Gudmundsson, 2011), agriculture (e.g., ash storms that can bury farmlands, or abrade vegetation; Wilson et al., 2011), and other aspects of society whose intensity notably depend on atmospheric and soil conditions (e.g., wind intensity, moisture, grainsize; level of compaction). Intensity of aeolian remobilisation can be classified as a function of visibility loss in distinct phenomena ranging from drifting ash to

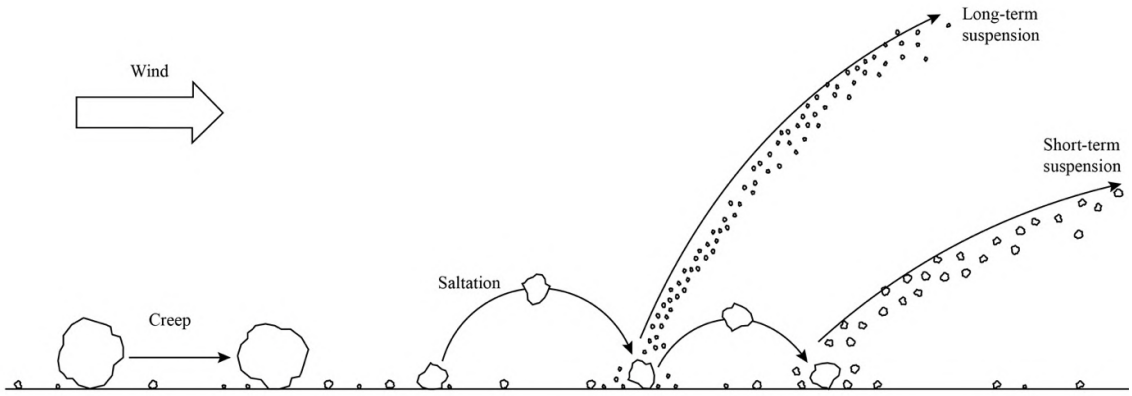

Figure 1.3: Aeolian remobilisation mechanisms (modified from Kok et al., 2012)

severe ash storms during which visibility is greatly reduced down to less than 200 m (Dominguez et al., 2020a).

It is important at this point to clearly separate remobilisation and resuspension. Whilst aeolian remobilisation refers to all secondary transport mechanisms of volcanic ash by the wind, aeolian resuspension only describes the process by which deposited volcanic ash re-enters in suspension under the action of the wind. In fact, similar to bedload transport in rivers, aeolian remobilisation also includes creep motion during which coarse grains roll and/or slide at the surface and saltation that transports particles by jumps (Zhang et al., 2021). Upon impact with the ground, saltating particles can trigger the lift-off and the eventual resuspension of smaller volcanic ash for short- or long- terms (Figure 1.3). The tendency for volcanic ash to become mobile in a wind field is classically quantified by the threshold wind friction velocity, that corresponds to the ratio of resisting gravitational and cohesive forces over driving aerodynamic forces (Shao and Lu, 2000). A particle lifts off the surface if the wind friction velocity (i.e., measure of the wind shear at the surface) becomes greater than the threshold wind friction velocity. This corresponds to particles in a given grainsize range for terrestrial conditions, as most easily remobilised particles are not too coarse (i.e., heavy), nor too fine (i.e., cohesive).

As highlighted during a 2019 workshop on wind-remobilisation processes of volcanic ash in Argentina (Jarvis et al., 2020), the characteristics of remobilised ash, and associated remobilisation mechanisms, still require laboratory and field measurements. In particular, there is a need to better assess the relation between remo-

bilisation intensity and terrain and deposit properties, as well as a need to develop strategies for field characterisation.

1.2 Methods employed in this thesis

Here, both analogue laboratory experiments and field investigations are used to characterise tephra sedimentation and aeolian remobilisation. Laboratory experiments are used to study analogue ash fingers developing underneath particle suspensions in water (Chapters 2, 3) and complement field observations (Chapter 4). Aeolian remobilisation is characterised in the field through a combination of sampling and imaging strategies presented in Chapter 5.

1.2.1 Experimental modelling

In order to better understand the formation of ash fingers and their dynamics, simple laboratory experiments in a small-scale water tank have been used. The experimental set-up used here is inspired by the experiments of Hoyal et al. (1999b), involving only two homogeneous layers initially separated by a barrier that is removed at the start of the experiments. In this configuration, the analogue of the volcanic ash cloud is a particle suspension that is placed on top of a dense sugar solution, analogue of the atmosphere at the base of a cloud spreading at the neutral buoyancy level. Particles are spherical glass beads, nearly monodisperse, and characterised by narrow grainsize distributions. Experiments take place in a quiescent environment in which the two layers are immobile.

Although not encompassing many aspects related to the sedimentation below volcanic ash clouds (e.g., absence of cloud spreading, monodisperse particles, narrow grainsize range, presence of rigid boundaries), such simplified experimental models can yield important results for the basic comprehension of natural phenomena. In fact, the complexity of natural systems requires modelers to carefully select the level of complexity adapted to the object or physical process studied, knowledge previously gained from past studies of this natural phenomenon, purpose of the model (i.e., hypothesis to test), and practical limitations in reproducing the size

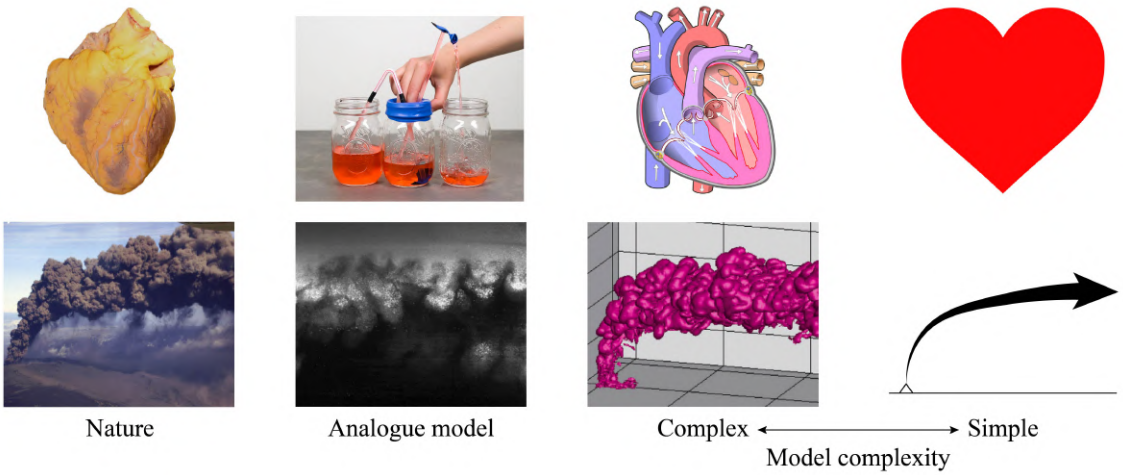

Figure 1.4: Variations in model complexity for the heart (top) and tephra fallout (adapted from van Zelst et al., 2022). Simple models, such the icon of the heart can be very useful, easy to understand, while capturing essential information (e.g., the basic shape of the heart with two ventricles). Images at the top are from https://commons.wikimedia.org/ and https://www.kiwico.com/diy/stem/anatomy-biology/pumping-heart, and bottom images are from Eliasson (2020), Koyaguchi and Suzuki (2013) and Scollo et al. (2017) from left to right.

and dynamics of the natural system. Simple models (in 1D or 2D) involving few controlling parameters, homogeneous initial conditions and fixed boundaries can be extremely useful if not oversimplified. For example, by varying specific parameters and neglecting others, simple models allow to identify main parameters involved in a problem independently. Conversely, a complex model allows further reconciliation with natural systems, but may become too complicated to be useful and/or feasible, depending on the studied phenomenon. Figure 1.4, adapted to the case of volcanic plumes from van Zelst et al. (2022), illustrates the difference between different degrees of complexities for studying the functioning of the heart or of volcanic ash sedimentation.

For large scale natural processes such as volcanic eruptions, experimental models are inevitably spatially and temporally simplified to be conceivable at the scale of a laboratory, even though large-scale experiments (Dellino et al., 2007; Ross et al., 2013; Lube et al., 2015) approach natural length scales. Hence, scaling analysis is a crucial step for ensuring similarity between small-scale models and large-scale volcanic phenomena when designing experiments in volcanology (Burgisser et al., 2005; Kavanagh et al., 2018; Roche and Carazzo, 2019). Accurate experiments are scaled

to correctly reproduce force ratios that are quantified by dimensionless numbers. Values of natural dimensionless numbers indicate the physical regimes of a natural system that needs to be reproduced by experiments, as determined by comparing natural and experimental dimensionless numbers. This procedure first requires the selection of relevant dimensionless numbers characterising the natural system. For example, for experiments aiming at reproducing viscous fluid flows, the Reynolds and Grashof numbers quantifying the importance of inertial over viscous forces and buoyant over viscous forces, respectively, can be investigated. Perfectly matching natural dimensionless numbers is nearly impossible in many cases. However, it is possible to identify the dynamical regimes associated with nature and experiments, and to understand the limitations of a model.

1.2.2 Areas studied

Eruptions from three volcanoes (Etna, Italy; Sabancaya, Peru and Sakurajima, Japan; Figure 1.5) were studied for improving the characterisation of natural ash fingers and aeolian remobilisation (analysed only at Sabancaya).

First, the sedimentation below volcanic plumes resulting from lava fountains produced at Mount Etna between 2011 and 2013 was studied based on operational videos provided by the Istituto Nazionale di Geofisica e Vulcanologia, Osservatorio Etneo (INGV-OE) that monitors the volcano. Mount Etna is located on Sicily island, in Italy (Figure 1.5A), and peaks at about 3300 m above sea level (a.s.l.). It is one of the most active volcano in the world, associated with multiple hazards, and it can be considered as an excellent natural laboratory for studying volcanic phenomena. Throughout its history, Mount Etna has mainly been associated with the emission of lava flows, frequently originating from the flanks of the edifice, but the number of explosive eruptions increased since 1986. 241 paroxysms characterised by strong Stombolian to lava fountaining activity happened at the summit craters between 1986 and 2021 (Andronico et al., 2021), generating high volcanic plumes spreading over hundreds of km and tephra fallouts. This poses significant hazards to populations living around the volcano (Scollo et al., 2013; Andronico et al., 2015), and notably to the city of Catania located about 28 km south of the summit (Figure

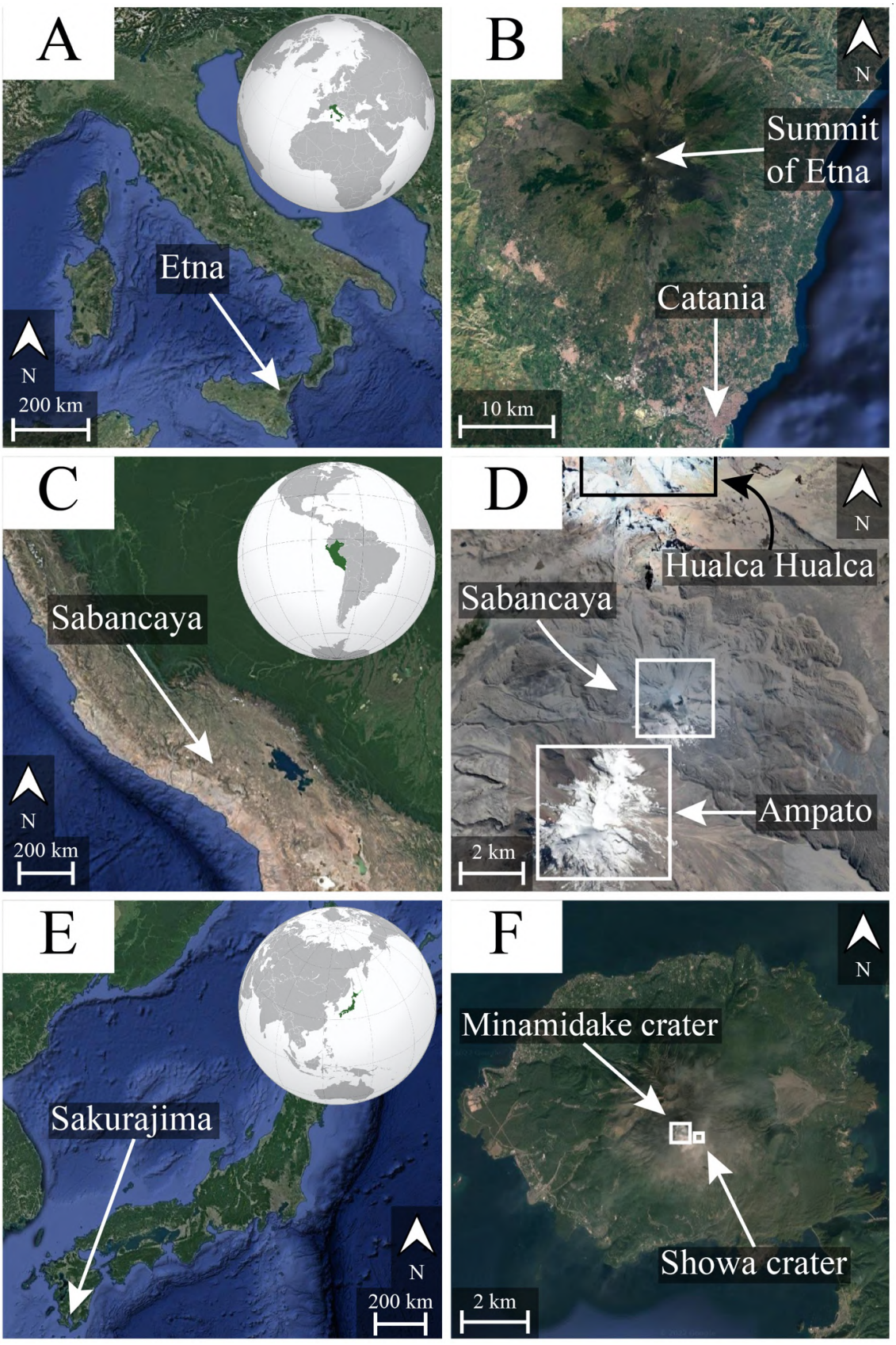

Figure 1.5: Location of study areas

1.5B). Between 2011 and 2013, 45 paroxysms occurred (Andronico et al., 2021), including the very intense 23 November 2013 eruption (Corradini et al., 2016; Poret et al., 2018) during which ash fingers have been observed (Andronico et al., 2015; Scollo et al., 2017).

Second, a field campaign was conducted from 27 July to 12 August 2018 at Sabancaya volcano (5970 m a.s.l.), in southern Peru (Figure 1.5C) for characterising tephra fallout and aeolian remobilisation processes, as well as tephra deposits and eruptive dynamics. Sabancaya volcano is part of a volcanic complex that also includes Hualca Hualca (6025 m a.s.l.) and Ampato volcanoes (Figure 1.5D), and Sabcancaya has been the only historically active volcano among this complex (Thouret et al., 1994; Juvigné et al., 1998; Gerbe and Thouret, 2004; Samaniego et al., 2016). Since 2016, the activity of Sabancaya volcano is characterised by frequent Vulcanian explosions typically reaching heights comprised between 1 and 4 km above the vent (Machacca Puma et al., 2021; Coppola et al., 2022), but tephra deposits from the ongoing eruption have not been studied yet. Additional information on the eruptive history and current volcanic activity at Sabancaya is reported in Chapter 5.

Finally, a field campaign was organised from 11 to 28 November 2019 at Sakurajima volcano (1117 m a.s.l.), on the island of Kyushu in southern Japan (Figure 1.5E), during which videos of tephra sedimentation were acquired. Sakurajima is also characterised by a persistent Vulcanian activity alternating between Minamidake and Showa craters (Figure 1.5F) since 1955 (Iguchi et al., 2013) that represents a long-lasting hazard to the nearby city of Kagoshima (Iguchi et al., 2020). Several explosions were recorded every day, reaching maximum plume heights of about 3 km above the vent during the campaign (Vecino et al., 2022). Sakurajima volcano can also be considered an excellent natural laboratory, due to the high frequency of explosions, accompanied by almost continuous ash venting, and the good accessibility of the area.

1.3 Thesis objectives and structure

This thesis aims to characterise different mechanisms (namely ash fingers and aeolian remobilisation) involved in the primary and secondary transport of volcanic ash. As mentioned in previous sections, ash fingers have the potential to significantly affect tephra sedimentation and deposits but are still poorly characterised. Hence, understanding the processes leading to the formation of ash fingers, and their dynamics, is crucial for improving our understanding of tephra dispersal and sedimentation and developing more efficient forecasting models. In fact, by increasing the fall velocity of fine particles that are entrained within rapidly descending currents, ash fingers can lead to premature deposition of volcanic ash and erroneous predictions of volcanic ash residence time and spatial distribution in the atmosphere. Very few quantitative measurements of finger characteristics have been performed so far, and rare examples include fingers observed during the 2010 eruption of Eyjafjallajökull by Manzella et al. (2015) and wind-induced fingers studied by Freret-Lorgeril et al. (2020) at Stromboli in 2015. Besides the lack of field data, the formation mechanism of ash fingers is unclear, resulting in impractical assessments of the conditions for which they develop and a more accurate description of the onset of ash fingers below volcanic plumes and clouds is required. This can be achieved through the combination of complementary analysis, and in particular through experimental and field characterisation of ash fingers. In order to obtain a better understanding of ash fingers, key open questions need to be addressed:

- How, where and when volcanic ash fingers form?
- What are the specific conditions favouring the development of ash fingers?
- How to distinguish ash fingers produced by different physical mechanisms?
- Is it possible to predict the velocity of ash fingers and, more generally, what are the key parameters controlling their dynamics?
- What are the particle sizes affected by ash fingers and their effect on tephra deposits?

- What is the possible relation between ash fingers and volcanic ash aggregation?

Similarly, aeolian remobilisation of volcanic ash requires additional experimental and field studies for constraining more accurately emission schemes. In particular, the field characterisation can be improved by:

- Studying aeolian remobilisation in various volcanic settings.
- Comparing and validating theoretical descriptions of aeolian remobilisation with field observations.
- Developing additional sampling and analysis strategies for characterising remobilised particles.

This thesis comprises four main chapters. **Chapters 2** and **3** present results from scaled analogue experiments aiming at characterising the formation and dynamics of ash fingers. Chapter 2 consists in a paper published in *Frontiers in Earth Sciences* (Fries, A., Lemus, J., Jarvis, P. A., Clarke, A. B., Phillips, J. C., Manzella, I. and Bonadonna, C. (2021). The Influence of Particle Concentration on the Formation of Settling-Driven Gravitational Instabilities at the Base of Volcanic Clouds. doi:10.3389/feart.2021.640090) that focuses on the control exerted by particle concentration on ash fingers resulting from settling-driven gravitational instabilities (SDGIs). In this work, various imaging techniques are employed separately in order to describe the configuration in which SDGIs arise. The length scales and dynamics of ash fingers are compared with existing theoretical relations and a criterion for the development of ash fingers is introduced and tested experimentally.

In addition to particle concentration, Chapter 3 includes the description of the influence of particle size on the tendency for particles to form fingers. Simultaneous particle imaging, Particle image Velocimetry (PIV) (Adrian, 2005) and Planar Laser Induced Fluorescence (PLIF) (Crimaldi, 2008) are used for a more complete characterisation of the properties of individual fingers. Results are extrapolated to volcanic clouds in order to constrain the conditions in which natural fingers may develop.

Chapters 4 and **5** describe results from field investigations. Previous observations and measurements of ash fingers are summarised and discussed in Chapter

4 that focuses on the field characterisation of ash fingers based on video recordings of volcanic ash sedimentation at Etna, Sabancaya and Sakurajima volcanoes. New quantitative measurements of the velocity and size of ash fingers are reported, considerably increasing the number of available data. From these measurements, maximum grainsizes potentially affected by ash fingers are derived and experimental scaling laws are tested to understand the mechanisms at the origin of ash fingers.

In Chapter 5, the field work conducted at Sabancaya volcano is presented. This Chapter links primary and secondary transport of tephra in the atmosphere. In fact, frequent and intense remobilisation phenomena are reported to occur at the same time fresh volcanic tephra is injected by Vulcanian explosions. Various sampling strategies are deployed to analyse primary tephra fallout and remobilised particles. Theories describing remobilisation mechanisms as a function of the grainsize are applied for enlightening field observation. The morphology of remobilised particles is compared with volcanic ash from primary fallout in order to identify potential signatures of remobilisation processes on the shape of volcanic ash. Besides, the activity of Sabancaya volcano is analysed, based on variations in repose times separating eruptions, airborne tephra sampling and tephra deposits.

Finally, the conclusions of this research, as well as future perspectives, are given in **Chapter 6**.

Chapter 2

The influence of particle concentration on the formation of settling-driven gravitational instabilities at the base of volcanic clouds[1]

2.1 Introduction

Many studies have highlighted that sedimentation from buoyant particle-laden currents (e.g., river plumes or volcanic ash clouds) is affected by collective settling mechanisms such as particle aggregation (Nicholas and Walling, 1996; Zimmermann-Timm, 2002; Costa et al., 2010; Durant and Brown, 2016) and settling-driven gravitational instabilities (Hoyal et al., 1999b; Parsons et al., 2001; Carazzo and Jellinek, 2012; Manzella et al., 2015). Both processes promote the scavenging of fine particles by increasing their fall velocities with respect to their individual settling rates. In particular, they can explain the fine-ash depletion observed in large volcanic clouds far from the source (Hoyal et al., 1999b; Carazzo and Jellinek, 2013; Durant, 2015; Gouhier et al., 2019). Many studies have already shown how particle aggregation can play a substantial role in enhancing fine ash sedimentation through the formation of clusters which might descend faster and closer to the vent than individual fine

[1]Published as: Fries, A., Lemus, J., Jarvis, P. A., Clarke, A. B., Phillips, J. C., Manzella, I. and Bonadonna, C. (2021). The Influence of Particle Concentration on the Formation of Settling-Driven Gravitational Instabilities at the Base of Volcanic Clouds. *Frontiers in Earth Science* 9, 640090. doi:10.3389/feart.2021.640090.

ash particles (Brown et al., 2012; Bagheri et al., 2016; Folch et al., 2016). However, less attention has been paid to settling-driven gravitational instabilities that can develop at the base of volcanic clouds and result in the formation of downward moving plumes, called ash fingers, within which fine ash particles fall faster than they do individually. Tephra dispersal and sedimentation can affect communities at multiple spatial and temporal scales (Jenkins et al., 2015; Bonadonna et al., 2021) including disruption to aviation (Guffanti et al., 2009; Prata and Tupper, 2009; Lechner et al., 2017), impact to public health (Horwell and Baxter, 2006; Gudmundsson, 2011) and damage to both residential buildings and critical infrastructures (Spence et al., 2005; Wilson et al., 2012). Therefore, understanding the processes controlling tephra sedimentation, including settling-driven gravitational instabilities, is fundamental for developing more efficient ash dispersal models and better managing the associated risk (Folch, 2012; Durant, 2015; Scollo et al., 2008).

Settling-driven gravitational instabilities develop at the base of particle suspensions from density differences generated by particles settling across the interface and their incorporation into the underlying fluid (Figures 2.1A,B). The configuration is an initially stable density stratification with a buoyant particle suspension (e.g., volcanic ash cloud) emplaced above a slightly denser fluid (e.g., atmosphere). The region immediately below the density interface becomes denser than the underlying layer when particles settle through it, forming a heavy, interfacial Particle Boundary Layer (PBL) (Burns and Meiburg, 2012, 2015; Yu et al., 2013; Davarpanah Jazi and Wells, 2020). Once the system is unstable, the PBL detaches and particle-laden bulbous plumes (called fingers) sink and protrude into the lower layer (Hoyal et al., 1999b). These fingers descend rapidly, driving particle sedimentation at faster velocities and rates than individual particle settling. In this paper, we refer to this finger-producing mechanism as settling-driven gravitational instabilities, where fingers are identified as the downward moving particle-laden plumes. We define the PBL as the heavy particle-laden layer formed below the initial density interface by the inclusion of particles in the dense underlying fluid.

Settling-driven gravitational instabilities can affect the sedimentation from buoyant flows that are associated with various natural systems including river (hypopy-

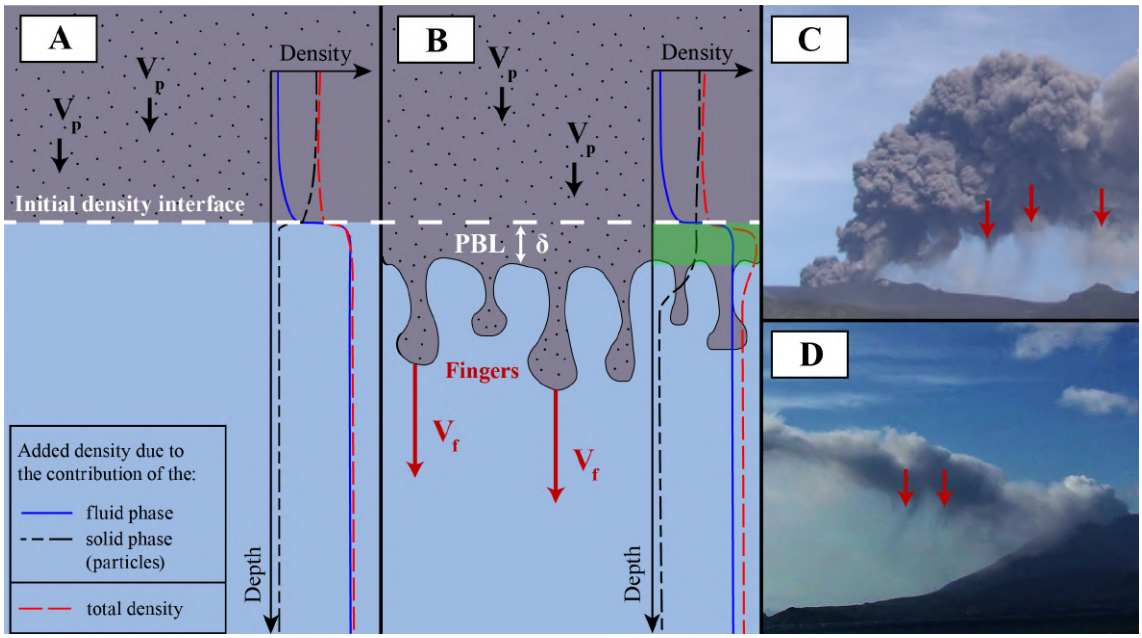

Figure 2.1: Schematic representation of the mechanism by which settling-driven gravitational instabilities arise. **(A)** The particle suspension (grey) initially overlies particle-free fluid (blue) and the density profile is stable. **(B)** Particles settle at their individual fall velocity (V_p) across the density interface between the particle suspension and the underlying, initially denser lower fluid, forming a dense Particle Boundary Layer (PBL) of thickness δ, highlighted in green, that contains density contributions from both the solid and fluid phases. Destabilization of the density stratification leads to the formation of fingers that rapidly descend at a speed $V_f > V_p$. Ash fingers have been observed at the base of volcanic clouds including **(C)** Eyjafjallajökull 2010, Iceland (Manzella et al., 2015), and **(D)** Sakurajima 2019, Japan. Red arrows highlight the presence of fingers. Note that more complex mechanisms than pure individual settling such as wind-driven stirring can also affect the particle delivery to the PBL in these natural examples and modify the density configuration that gives rise to ash fingers.

cnal) plumes (Hoyal et al., 1999b; Maxworthy, 1999; Parsons et al., 2001; Henniger and Kleiser, 2012; Davarpanah Jazi and Wells, 2016, 2020; Sutherland et al., 2018), magma chambers (Marsh, 1988), vertical tephra transport in oceans (Carey, 1997; Manville and Wilson, 2004; Jacobs et al., 2015, 2013) and volcanic clouds (Carazzo and Jellinek, 2012; Manzella et al., 2015; Scollo et al., 2017). Hence, several authors from different fields have investigated these instabilities through a combination of experiments, theoretical analyses and numerical simulations (Hoyal et al., 1999b; Cardoso and Zarrebini, 2001; Burns and Meiburg, 2012, 2015; Carazzo and Jellinek, 2012; Jacobs et al., 2013; Yu et al., 2013, 2014; Chou and Shao, 2016; Scollo et al., 2017). Whilst the instability mechanism here resembles the classical Rayleigh-Taylor instability which occurs when a dense fluid overlies a lighter one (Sharp, 1984; Linden and Redondo, 1991), the characteristics and dynamics differ in critical ways. A key difference is that this instability originates from the settling of particles out of the upper layer, forming a narrow region of excess density (the PBL). The interface between the upper layer and the PBL is gravitationally stable, which means that, unlike in classical Rayleigh-Taylor problems, the upper layer does not undergo overturning. Simultaneously, there is competition between the rate at which the PBL forms due to particle settling and the rate at which it is destroyed by gravitational instability with the lower layer. The finite-amplitude characteristics of the instability are therefore different.

In addition to particle settling, double diffusion, where two density-altering fluid properties diffuse at different rates, can also lead to the formation of an unstable interfacial region and associated fingers (Green, 1987; Chen, 1997; Hoyal et al., 1999a; Carazzo and Jellinek, 2013). A comparison between the diffusive and particle-settling fluxes allows differentiation between the two mechanisms (Green, 1987; Hoyal et al., 1999a; Carazzo and Jellinek, 2013); settling-driven gravitational instabilities can occur if the settling flux is greater than the diffusive flux. Both mechanisms are likely to coexist and to affect the sedimentation from volcanic clouds because of thermal diffusion and particle settling (Carazzo and Jellinek, 2013). However, in this paper, we focus on settling-driven gravitational instabilities which are more suitable for describing finger formation during the spreading of an ash cloud at

neutral buoyancy, once it is thermally equilibrated with the atmosphere (Manzella et al., 2015; Scollo et al., 2017). As we will show in Section 2.2.1, the particle flux into the PBL in our experiments is predominantly controlled by particle settling rather than double diffusion and we therefore only address gravitational instabilities arising because of particle settling across the interface.

Hoyal et al. (1999b) showed that the criterion for convection to start at the base of particle suspensions and for fingers to develop depends on the ratio between driving gravitational forces and resisting viscous forces as represented by the Grashof number

$$Gr = \frac{g'\delta^3}{\nu^2}, \tag{2.1}$$

where δ is the PBL thickness (Figure 2.1B), ν the kinematic viscosity, and $g' = g(\rho - \rho_a)/\rho_a$ the reduced gravity of the PBL, with $g = 9.81$ m s^{-2} the acceleration due to gravity, and ρ and ρ_a the densities of the PBL and of the ambient, respectively (a list of symbols can be found in Supplementary Table A2.1). By analogy with thermal convection, Hoyal et al. (1999b) proposed that the instability starts above a critical Grashof number of the order of 10^3. For given values of the reduced gravity and viscosity, this indicates that fingers develop only if the PBL can grow to a critical thickness $\delta_c = 10(\nu^2/g')^{(1/3)}$. Their experimental measurements further revealed that the instability wavelength (i.e., the spacing between fingers) and the finger width are proportional to the critical PBL thickness.

Another condition for the development of fingers due to settling-driven gravitational instabilities is that the particle-fluid mixture behaves as a continuum (Hoyal et al., 1999b). The particle and fluid motions can then be coupled through terms in their respective momentum equations (Harlow and Amsden, 1975; Valentine and Wohletz, 1989; Burgisser et al., 2005). In dilute mixtures, such as fingers, the degree of coupling can be assessed by calculating the Stokes and Sedimentation dimensionless numbers that quantify the relative strength of the forces the fluid and particles exert on each other (Crowe et al., 2011). For fingers to form, the coupling must be sufficiently strong for the finger velocity to be greater than the particle velocity. Carazzo and Jellinek (2012) showed that this last condition is met in numerous volcanic ash clouds, and effectively reduces to a dependence on particle size, with

fine ash particles (diameter $d < 100$ µm) promoting finger formation. In a series of aqueous analogue experiments with both glass beads and natural ash, Scollo et al. (2017) found that particle concentration and size exerted a major control on the instability and that no fingers formed for particle diameters greater than approximately 125 µm. Larger particles instead settled individually, sufficiently decoupled from the fluid phase. Finally, their experiments revealed that the ash composition did not significantly change finger dynamics, suggesting that, for a given ash size distribution, fingers can form underneath plumes regardless of the magma composition.

Ash fingers associated with settling-driven gravitational instabilities have been observed in various volcanic eruptions, e.g., Mount Redoubt, USA, 1990 (Hobbs et al., 1991); Ruapehu, New Zealand, 1996 (Bonadonna, 2005a); Soufrière Hills, Montserrat, 1997 (Bonadonna et al., 2002b); Eyjafjallajökull, Iceland, 2010 (Bonadonna et al., 2011; Manzella et al., 2015) (Figure 2.1C); Etna, Italy, 2013 (Andronico et al., 2015; Manzella et al., 2015); and Sakurajima, Japan, 2019 (Figure 2.1D). Their association with different eruptive styles suggests that settling-driven gravitational instabilities are a common, widespread phenomenon.

Despite these observations, quantitative field descriptions of ash fingers remain rare. During the 2010 Eyjafjallajökull eruption, Manzella et al. (2015) found the average downward finger velocity to be about 1 m s^{-1}, which is greater than the calculated settling velocities of individual ash particles finer than 100 µm (V_p<0.6 m s^{-1}). They also characterised the geometry of the instability by showing that the width and spacing of individual fingers appeared to be similar, as suggested previously by experimental studies (Hoyal et al., 1999b; Carazzo and Jellinek, 2012). Scollo et al. (2017) suggested that Mass Eruption Rates (MERs) greater than about 10^5 kg s^{-1} favour the formation of settling-driven gravitational instabilities, which is in good agreement with analogue experiments where the particle concentration corresponds to highly concentrated volcanic clouds. Finally, using a combination of radar and disdrometer measurements at Stromboli, Italy, Freret-Lorgeril et al. (2020) detected intermittent periods of higher particle concentration that they interpreted as fingers affecting the sedimentation from weak, short-lived plumes. Their work, along with

recent experiments on particle-laden currents (Davarpanah Jazi and Wells, 2020), suggests that the wind and the relative motion of the current may affect the formation of ash fingers, evidencing that settling-driven gravitational instabilities are not the only mechanism by which ash fingers can be produced. However, in our experiments that are performed in the absence of relative horizontal motion between the particle suspension and the ambient fluid (that are initially separated by a flat interface), we only consider the case of volcanic ash clouds with negligible wind shear effects for which the particle flux across the interface is dominated by individual settling, i.e., where the plume and fingers are advected at wind speed at the neutral buoyancy level and far from the source.

While previous studies have built the theoretical framework to assess the conditions necessary for the formation of settling-driven gravitational instabilities and focused mainly on the effect of the particle size, which is of primary importance, we only have limited insights into the effect of the particle concentration on the formation of settling-driven gravitational instabilities. We present new experiments, performed over a wide range of initial conditions, to investigate the velocity and size of fingers at different particle concentrations and compare our results with existing models on settling-driven gravitational instabilities (Hoyal et al., 1999b; Carazzo and Jellinek, 2012; Manzella et al., 2015). Additionally, we explore the potential of particle suspensions to develop fingers by introducing a new dimensionless number relating the suspension and characteristic PBL thicknesses. Despite significant progress in theoretical (Burns and Meiburg, 2012) and numerical (Burns and Meiburg, 2015) studies of the formation of settling-driven gravitational instabilities, uncertainties remain regarding the density configuration associated with the triggering of the instabilities. Although the presence of a heavy PBL below the particle suspension is widely accepted, the composition of the fluid phase and the particle concentration in this region remain poorly-described, despite their importance for the bulk density of the suspension and the dynamics of the resulting fingers. We have used Planar Laser Induced Fluorescence (PLIF) (Koochesfahani, 1984; Crimaldi, 2008) to measure the spatial and temporal evolution of the fluid phase density, specifically focusing on the PBL and fingers. Whilst previous experiments have focused

on the particle concentration and velocity fields, our PLIF measurements allow for a complete characterisation of the density configuration associated with the triggering of the instability. Once developed, settling-driven gravitational instabilities are thought to significantly increase the sedimentation rate below particle suspensions. We quantify the particle mass flux in the experiments at different particle concentrations. Experimental findings are finally discussed in relation to the sedimentation of fine ash from volcanic ash clouds.

2.2 Methods

2.2.1 Experimental configuration

The experiments are performed in an experimental water tank 30.1 × 30.1 × 50 cm^3 that is divided into two layers by a horizontal barrier (Manzella et al., 2015; Scollo et al., 2017) (Figure 2.2; H_1 = 5 - 21 cm and H_2 = 25 cm are the thicknesses of the upper and the lower layers, respectively). Initially, the density profile is stable. The upper layer (ash cloud analogue) is a mixture of particles and fresh water, with initial particle concentrations C_u ranging from 0.0007 to 10 g l^{-1} (mixture density from 997 to 1007 kg m^{-3}), and the lower layer (atmosphere analogue) is a denser sugar solution kept at a constant density of 1008 kg m^{-3} (sugar concentration of 29 g l^{-1}). Experiments are performed at ambient temperature. This experimental configuration is inspired by the classical work of Hoyal et al. (1999b) on settling-driven gravitational instabilities and experiments on Rayleigh-Taylor instabilities (Linden and Redondo, 1991; Dalziel, 1993). This minimalist design allows us to study the effect of particle concentration on settling-driven gravitational instabilities and finger dynamics in isolation from other processes and variables.

The particles are spherical glass beads, which are suitable for modelling the behaviour of natural ash (Manzella et al., 2015; Scollo et al., 2017). They have a median diameter D_{50} of 41.5 µm and a sorting $\sigma=(D_{84} - D_{16})/2$ (Inman, 1952) of 14 µm (see Supplementary Figure A2.1), as measured by laser diffraction using a BetterSizer S3 Plus. The particle density is measured, using Helium pycnometery with a Ultrapyc 1200e, to be 2519.2 ± 0.1 kg m^{-3}.

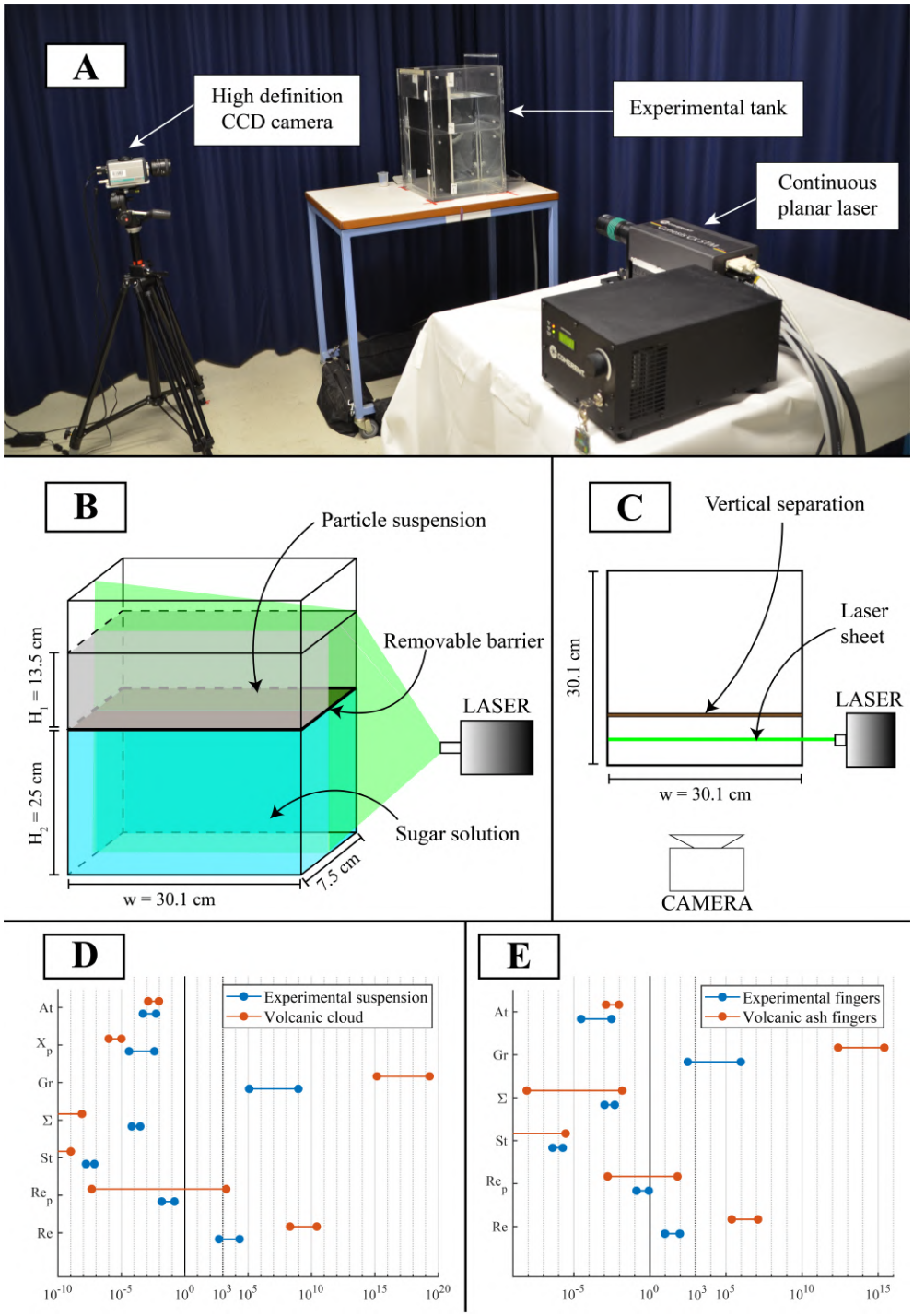

Figure 2.2: **(A)** Experimental apparatus. **(B)** Schematic of the tank configuration before barrier removal. The upper layer has a thickness H_1 that varies from 5 to 21 cm and is kept constant at 13.5 cm in type A experiments. In all experiments, the lower layer is a dense sugar solution with a thickness H_2 of 25 cm. The width of the tank w is 30.1 cm **(C)** Top view of the experimental configuration. The vertical separation and the laser plane are located 7.5 cm and 4.5 cm from the tank's front wall, respectively. **(D)** Comparison between experimental and natural dimensionless numbers (Re: Flow Reynolds number; Re_p: Particle Reynold number; St: Stokes number; Σ: Sedimentation number; Gr: Grashof number; X_p: Particle volume fraction; At: Atwood number) associated with ash clouds and **(E)** fingers. The vertical solid and dotted lines underline the values of 10^0 and 10^3 that are important for most dimensionless numbers.

Particles are kept in suspension by continuously mixing the upper layer top to bottom for 20 to 25 s with an agitator composed of a 23 × 7 cm^2 millimetric mesh, that is large enough to mix the entire upper layer and produce homogeneous and repeatable mixing. Mixing is stopped 5 s before the experiment begins. The separation between the two layers is then removed manually by sliding the barrier out of its slt in 0.9 to 1.3 s. A major challenge of this experimental configuration is that mixing is generated across the density interface when removing the barrier and is clearly visible in the first 10 s of the experiments, affecting the early development of settling-driven gravitational instabilities. The perturbation is particularly strong near the back wall of the tank, so we reduced the length of the tank to 7.5 cm with rigid vertical separators to attenuate the effect of the vorticity (Manzella et al., 2015; Scollo et al., 2017). After barrier removal, particles start settling into the lower partition of the tank (see 2.6; Supplementary Video A2.1). A continuous Nd:YAG planar laser (Genesis CX-SLM by Coherent) with a wavelength of 532 nm illuminates the experiments from the side of the tank and a sCMOS camera (HiSense Zyla by Dantec Dynamics), with 16 bit colour depth, is used to capture images of the experiments at 10 Hz with image dimensions of 1500×2100 pixels, resulting in a resolution of 55 px mm-1. We find that the sugar concentration is sufficiently small that it has negligible effect on the light intensity received by the camera.

Gravitational instabilities in our setup can theoretically develop through two different mechanisms, double diffusion and particle settling (Hoyal et al., 1999a,b; Burns and Meiburg, 2012). Double diffusive effects arise when two density-altering fluid properties (i.e., sugar and particles in the lower and the upper layers, respectively) diffuse at differential rates. The faster diffusion of one component relative to the other can lead to a local increase of the bulk density at the interface that triggers gravitational instabilities. The rate at which the bulk density increases in double-diffusive systems is therefore controlled by the diffusion of the fastest diffusing component. Conversely, settling-driven gravitational instabilities are generated by particles settling across the interface, causing the upper part of the lower layer (i.e., the PBL) to become heavier than the fluid below. Gravitational instabilities produced by particle settling are therefore controlled by both the vertical velocity

of the particles and the initial particle concentration of the upper layer. We determine the mechanism that provokes the formation of instabilities in our experiments by calculating the ratio of the double diffusive and settling fluxes, F_D and F_I, respectively, at the density interface (Green, 1987; Hoyal et al., 1999a; Carazzo and Jellinek, 2013).

$$F^* = \frac{F_D}{F_I}. \tag{2.2}$$

Replacing the fluxes by their expressions $F_D = \frac{1}{20}\rho_u(g\kappa_f\beta_m)^{1/3}(C_u/\rho_p)^{4/3}$ and $F_I = C_u g d^2(\rho_p - \rho_f)/18\mu$ (Hoyal et al., 1999a; Carazzo and Jellinek, 2013), where κ_f is the diffusion coefficient of the fastest diffusing substance, μ the dynamic viscosity of the fluid, C_u the initial particle concentration in the upper layer (in mass per unit volume), ρ_p the particle density, d the particle diameter, $\beta_m \approx (\rho_p - \rho_f)/\rho_p$ the volumetric expansion coefficient of a particle suspension and ρ_u and ρ_f the density of the particle suspension and of the fluid phase, respectively, equation (2.2) can be written as

$$F^* = \frac{9\mu\rho_u(\kappa_f\beta_m)^{1/3}}{10d^2(\rho_p - \rho_f)(\rho_p^2 g)^{2/3}}. \tag{2.3}$$

$F^* \gg 1$ means that double diffusion dominates the mass flux across the interface, whilst particle settling dominates for $F^* \ll 1$. In our experiment, the particles are the fastest diffusing substance, with a maximum hydrodynamic diffusion coefficient κ_p of 1.2 × 10-7 m^2 s^{-1} (Lee et al., 1992; Martin et al., 1994). We find that F^* is between 8 × 10^{-4} and 2 × 10^{-2} in our experiments, suggesting that settling is the principal mechanism provoking the formation of fingers, with a negligible contribution of double diffusive effects.

2.2.2 Scaling of experiments

Our experiments are dedicated to correctly reproducing the processes affecting ash sedimentation beneath volcanic clouds in a small, simplified configuration. The difference in complexity and scale between the natural phenomenon and small-scale experiments raises the problem of the applicability of the analogue experimental results. To address this, we perform a scaling analysis (Burgisser and Bergantz, 2002; Burgisser et al., 2005; Carazzo and Jellinek, 2012; Kavanagh et al., 2018;

Roche and Carazzo, 2019). Dimensionless numbers relevant to our problem are calculated for volcanic ash clouds and compared with particle suspensions (Figure 2.2D). We also compare the dynamical regimes of natural ash and experimental fingers based on dimensionless numbers (Figure 2.2E). The values of the parameters associated with volcanic clouds and fingers are obtained from the literature (Table 2.1; Burgisser et al., 2005; Carazzo and Jellinek, 2012; Manzella et al., 2015).

The Reynolds number $Re = \rho V L/\mu$, with μ the fluid dynamic viscosity and V and L the characteristic velocity and length scale of the flow, respectively, characterises the flow behaviour by comparing the inertial to viscous forces in the fluid. Re is greater in natural volcanic clouds and fingers, where it is far above the mixing transition ($Re >$ 1000-4000) and is fully turbulent. Hence, we can expect particle collisions and entrainment of the ambient fluid to be enhanced in natural ash fingers, compared with their experimental counterparts. However, the flows in both experiments and volcanic clouds are inertia-controlled, suggesting that they are comparable despite the fact that velocity fluctuations (i.e., turbulence) are greater in natural flows.

In situations involving particle settling in fluids, the particle Reynolds number $Re_p = \rho_f V_p d/\mu$ is used to assess the properties of the flow surrounding particles and the subsequent drag force acting on them. d is the particle diameter and V_p is the individual particle settling velocity given by the Stokes terminal velocity in the experiments

$$V_p = \frac{g d^2(\rho_p - \rho_f)}{18\rho_f \nu}. \tag{2.4}$$

At subcritical $Re_p < 3 \times 10^5$, the drag factor f, which assesses the importance of the fluid resistance exerted on the particles, can be expressed as a function of Re_p and two drag correction coefficients depending on the particle shape k_N and k_S by (Bagheri and Bonadonna, 2016a,b)

$$f = \frac{24 k_s}{Re_p}[1 + 0.125(Re_p k_N/k_S)^{2/3}] + \frac{0.46 k_N}{1 + \frac{5330}{Re_p k_N/k_S}}. \tag{2.5}$$

For multiphase flows involving particles, the Stokes St and Sedimentation Σ numbers quantify the momentum transfer between the fluid phase and the particles (Burgisser

et al., 2005; Roche and Carazzo, 2019). They are calculated as

$$St = \frac{(\rho_p - \rho_f)d^2}{18\mu f}\frac{\Delta U}{\delta_f})(1 + \frac{\rho_f}{2\rho_p}), \tag{2.6}$$

and

$$\Sigma = \frac{(\rho_p - \rho_f)d^2}{18\mu f}\frac{g}{\Delta U} = \frac{V_p}{\Delta U}, \tag{2.7}$$

with ΔU the characteristic velocity fluctuation over a characteristic distance δ_f. These two parameters allow us to assess the coupling between particles and fluid. When St $\ll 1$ and $\Sigma \ll 1$, particles are strongly coupled with the fluid. This is the case for both natural ash and experimental fingers, satisfying the assumption that particles remain coupled with the fluid for fingers to form (Hoyal et al., 1999b; Carazzo and Jellinek, 2012).

Previous studies have invoked a convective mechanism for finger formation whose initiation depends on the Grashof number Gr, which can be estimated using a combination of experimental and field observations (section 2.3.4). Our analysis shows that Gr is much greater in the natural systems than in the experiments but that, in both configurations, it exceeds the critical Grashof number $Gr_c = 10^3$ (Hoyal et al., 1999b) for the development of settling-driven gravitational instabilities.

For scaling the density ratio between the particle-laden layer and the underlying fluid, we calculate the Atwood number $At = (\rho - \rho_a)/(\rho + \rho_a)$. At is commonly used to parameterise the density difference between two fluid layers, notably in experiments on Rayleigh-Taylor instabilities (Dalziel, 1993; Wilson and Andrews, 2002). Here, $At \ll 1$ in all configurations, showing that the difference in density between the two layers is very small in nature as well as in experiments and that the instability develops from small initial density differences in both situations.

For settling-driven gravitational instabilities, the natural and experimental ranges of Re_p, At, St and Σ all overlap while they are different for Re and Gr, but above critical threshold values that ensure that experiments are comparable to the volcanic phenomenon. We also note that the dimensionless numbers systematically cover a wider range in nature than in experiments (Table 2.1). This can firstly be explained by the wide variety of eruptive source and atmospheric conditions which means erup-

tive clouds can be associated with a wide range of particle diameters, characteristic velocities and length scales. Moreover, a second explanation is that descriptions of ash fingers remain rare, meaning they are currently poorly constrained, with high associated uncertainties. Altogether, this scaling analysis shows that our experiments do a good job reproducing most dimensionless numbers associated with natural clouds and fingers, although the variability of natural phenomena means that they are associated with larger ranges of Re and Gr, potentially extending to greater values than in our experiments. However, it is inevitable that laboratory models of volcanic clouds cannot capture the full range of variability of the natural system (Carazzo and Jellinek, 2012; Kavanagh et al., 2018). Despite this, given that that the ranges of Re and Gr in both the experiments and natural clouds are close to or above expected transitional values (Reynolds, 1883; Hoyal et al., 1999b), we can regard our experiments as suitable analogues to study settling-driven gravitational instabilities at the base of volcanic clouds.

2.2.3 Imaging techniques

In order to independently obtain both the particle concentration C and fluid density fields, we imaged the particles using a set-up derived from Particle Image Velocimetry (PIV; Keane and Adrian, 1992; Grant, 1997; Adrian, 2005), and the fluid phase using Planar Laser Induced Fluorescence (PLIF; Koochesfahani, 1984; Crimaldi, 2008), in separate repeated experiments. These two techniques have previously been applied separately or simultaneously (Borg et al., 2001; Hu et al., 2002) to assess the particle concentration and velocity fields, as well as fluid properties such as temperature and density, in other aqueous experiments. Here we apply particle imaging and PLIF on separate experiments where we kept the experimental set-up in the same configuration, including identical starting conditions, i.e., particle size and concentration and fluid density contrast, as well as identical imaging conditions, i.e., camera and laser positions and settings. Ensuring the same experimental and imaging conditions is critical in order to enable the combination of the results given by the two techniques (Borg et al., 2001). Moreover, we ensured that results from PLIF experiments were reproducible before combining with results from particle-imaging

Parameter name (unit)	**Symbol**	**Volcanic cloud**	**Experimental suspensions**	**Ash fingers**	**Experimental fingers**
Characteristic velocity (m s^{-1})	V	50-150[c]	10^{-2}-10^{-1}	0.5-1.5[d]	5×10^{-3}-15×10^{-3}
Characteristic thickness (m) Cloud thickness or finger width	L	1200-3900[b]	0.05-0.21	142-194[d]	8×10^{-3}-2.5×10^{-2}
Gravitational acceleration (m s^{-2})	g	9.81	9.81	9.81	9.81
PBL thickness (m)	δ	70-100[d]	5×10^{-3}-10^{-2}	70-100[d]	5×10^{-3}-10^{-2}
PBL density (kg m^{-3})	ρ	0.1-1.32[d]	1008-1018	0.1-1.32[d]	1008-1018
Ambient density (kg m^{-3})	ρ_a	0.1-1.3[c],[d]	1008	0.1-1.3[c],[d]	1008
Fluid density (kg m^{-3})	ρ_f	0.1-1.3[c],[d]	997	0.1-1.3[c],[d]	997
Particle density (kg m^{-3})	ρ_p	750-2400[f]	2519.2	750-2400[f]	2519.2
Particle volume fraction	X_p	10^{-6}-10^{-5}[f]	4×10^{-5}-4×10^{-3}	-	-
Particle diameter (m)	d	10^{-6}-10^{-3}[c]	26×10^{-6}-57×10^{-6}	10^{-6}-10^{-3}[c]	26×10^{-6}-57×10^{-6}
Dynamic viscosity (Pa s)	μ	3×10^{-5}[c],[f]	10^{-3}[b],[c],[e]	3×10^{-5}[c],[f]	10^{-3}[b],[c],[e]
Kinematic viscosity (m^2 s^{-1})	ν	3×10^{-5}[a]	10^{-6}[b]	3×10^{-5}[a]	10^{-6}[b]
Characteristic velocity fluctuations (m s^{-1})	ΔU	2.5[b]	10^{-3}	0.125[b]	4×10^{-3}
Characteristic fluctuation lengthscale (m)	δ_f	120[b]	0.135	14[b]	8×10^{-3}
Stokes drag correction	k_S	1-2.5[g]	1[g]	1-2.5[g]	1[g]
Newton drag correction	k_N	1-10^3[g]	1[g]	1-10^3[g]	1[g]
Dimensionless numbers	**Formula**	**Volcanic cloud**	**Experimental suspensions**	**Ash fingers**	**Experimental fingers**
Reynolds (Re)[e]	$\frac{\rho V L}{\mu}$	10^8-10^{10}	10^2 -10^4	10^5-10^7	10^1-10^2
Particle Reynolds (Re_p)[c],[e]	$\frac{\rho_f V_p d}{\mu}$	10^{-8}-10^3	10^{-2}-10^{-1}	10^{-3}-10^2	10^{-1}-10^0
Stokes (St)[a]	$\frac{(\rho_p-\rho_f)d^2}{18\mu f}(\frac{\Delta U}{\delta_f})$ $[1+\frac{\rho_f}{2\rho_p}]$	10^{-16}-10^{-9}	10^{-8}-10^{-7}	10^{-13}-10^{-6}	10^{-7} – 10^{-6}
Sedimentation (Σ)[a]	$\frac{(\rho_p-\rho_f)d^2}{18\mu f}(\frac{g}{\Delta U})$	10^{-15}-10^{-8}	10^{-5}-10^{-4}	10^{-9}-10^{-2}	10^{-3}-10^{-2}
Grashof (Gr)[f]	$\frac{g'\delta^3}{\nu^2}$	10^{15}-10^{19}	10^5-10^8	10^{12}-10^{15}	10^2-10^6
Atwood (At)[d]	$\frac{\rho-\rho_a}{\rho+\rho_a}$	10^{-3}-10^{-2}	10^{-3}-10^{-2}	10^{-3}-10^{-2}	10^{-5}-10^{-3}

Table 2.1: Top - Typical dimensional parameter ranges for the variables used in the scaling analysis for both natural and experimental systems. Note that parameters associated with volcanic clouds (e.g. cloud thickness) can stray beyond the typical ranges given (Suzuki and Koyaguchi, 2009; Ansmann et al., 2010). Distinct values were considered for the particle-laden layer (volcanic ash cloud or particle suspension) and for the fingers. **Bottom -** Dimensionless numbers associated with natural processes and experiments. ([a]Burgisser and Bergantz, 2002; [b]Burgisser et al., 2005; [c]Carazzo and Jellinek, 2012; [d]Manzella et al., 2015; [e]Kavanagh et al., 2018; [f]Roche and Carazzo, 2019; [g]Bagheri and Bonadonna, 2016a

experiments (Supplementary Figure A2.2).

Particle imaging

We developed a calibration that links the particle concentration C to the light intensity scattered by particles and received by the camera sensor, with the assumption that the light intensity observed in the experiments is linearly related to the particle concentration. During calibrations, the water tank is first filled with a fluid of uniform and known particle concentration (ranging from 0 to 6 g l^{-1} at 0.5 g l^{-1} concentration steps). The tank is then illuminated with different laser powers of 0.50, 0.45, 0.40 and 0.35 W for each particle concentration. In order to erase short temporal variations in particle concentration, calibration images are acquired at 0.1 s intervals and then averaged over 10 s. Finally, we perform an individual pixel-by-pixel calibration relating pixel intensity to particle concentration for each laser power. The pixel digital level (i.e., received light intensity) is positively linearly correlated with the particle concentration and the coefficient of determination is high, $R^2 = 0.95$ (Figure 2.3A). However, the light intensity through the width of the experimental tank is dependent on the particle concentration and exponentially attenuates with x, the distance from the tank wall closest to the laser. Hence, the quality of the linear regression between light intensity and particle concentration diminishes with distance from the light source (Figures 2.3B,C). For accurate particle concentration measurements, we therefore calculate concentration only in pixels with a coefficient of determination $R^2 > 0.95$. This corresponds to the pixels located in the 12 cm of the tank closest to the laser, limiting the particle concentration measurements to approximately one third of the tank width. We assume that finger characteristics in this section are representative of those throughout the whole tank. Particle concentration measurements have already been employed to characterize settling-driven gravitational instabilities by Hoyal et al. (1999b) and Manzella et al. (2015). In both studies, the authors placed light sources behind or beside their experimental tanks and related light attenuation to the depth-averaged particle concentration in interrogation areas. With the present particle imaging scheme, we managed to improve the resolution of the concentration measurements

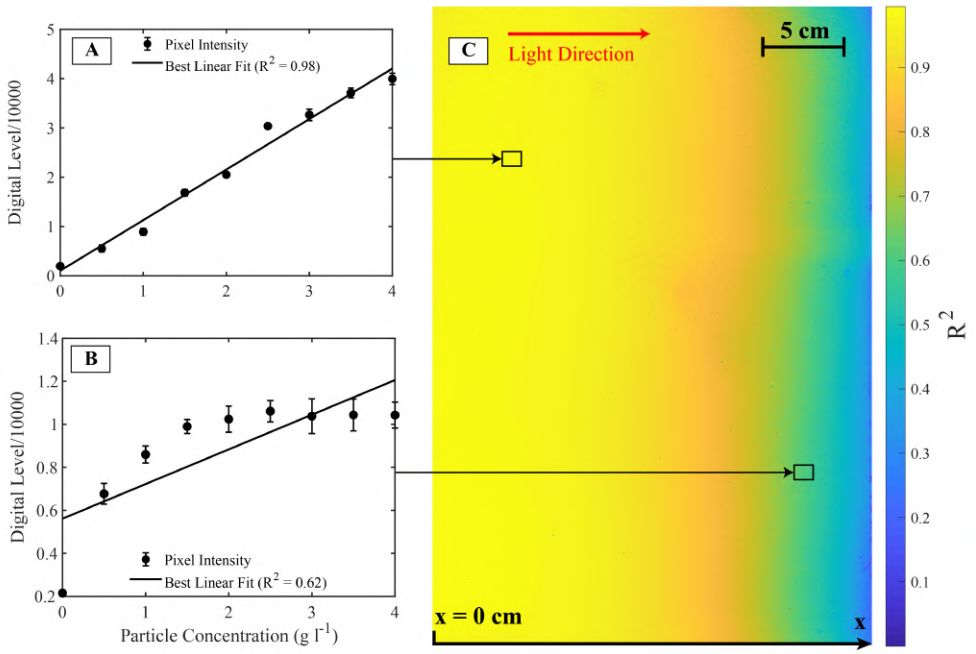

Figure 2.3: Calibration of the particle concentration for a laser power of 0.50 W. **(A)** Example of a linear relationship between particle concentration and the light intensity in one pixel. In this example, the coefficient of determination R^2 suggests a very good linear fit. **(B)** Example of a pixel with a low-quality linear regression. Vertical error bars in panels A and C represent the standard deviation of the averaged pixel digital level over 10 s. **(C)** Map of R^2 inside the tank. R^2 diminishes as a function of x (distance from the wall closest to the laser).

down to the pixel-scale, which corresponds to a resolution of 0.18 mm in the horizontal and vertical directions. Furthermore, our measurements within the laser plane differ from depth-averaged particle concentration measurements and offer a visualization of the 2D particle concentration. We compare our particle concentration measurements obtained using this novel calibration procedure against those of Manzella et al. (2015). The two measurement techniques are in good qualitative agreement (Supplementary Figure A2.3). It is worth noting that whilst particle concentration measurements in the lower layer, into which the laser light enters directly, are highly accurate, corresponding measurements in the upper layer are affected by the refractive index change between the sugar solution and the particle suspension.

Fluid phase imaging

Understanding the behaviour of the fluid phase associated with the occurrence of settling-driven gravitational instabilities is crucial to improving our general compre-

hension of the mechanisms driving the instability. In particular, it is important to quantify the contribution of the fluid phase on the generation of an unstable density profile associated with settling-driven gravitational instabilities. For this purpose, we applied the PLIF technique to a series of separate experiments. The PLIF approach yields quantitative, non-intrusive, measurements of fluid concentrations at high resolution (Koochesfahani, 1984; Crimaldi, 2008). It involves using a dye that generates fluorescence with an intensity linearly proportional to its concentration D when illuminated by a laser. In experiments on fluid mixing, by adding dye to one endmember, the fluorescence intensity can be used as a tracer, with the fluorescent dye concentration related to the proportion of dyed fluid (Linden and Redondo, 1991; Troy and Koseff, 2005; Dossmann et al., 2016). In the case presented here, mixing occurs between fluids of different density. The bulk density of the fluid phase thus changes during mixing and is quantified by the fluorescent dye concentration.

During our PLIF experiments, the upper layer is doped with Rhodamine 6G (R6G), a fluorescent dye with an absorption peak at 530 nm (Zehentbauer et al., 2014), close to the laser wavelength (532 nm), for a maximum absorption efficiency. The emission spectrum of R6G ranges from 510 to 710 nm with a peak at 560-580 nm, depending on the solvent (Zehentbauer et al., 2014). We isolate the R6G fluorescence from other light sources with a smaller wavelength (i.e., primary laser emission, particle scattering) by equipping the camera with a high-pass filter at 570 nm. This procedure allows us to image the R6G distribution only, as a proxy for the concentration of the upper fluid phase.

We perform a calibration in order to relate the local R6G dye concentration D to the digital level of individual pixels (i.e., fluorescence intensity). In PLIF measurements, the digital level F increases linearly with the R6G dye concentration D (Borg et al., 2001; Crimaldi, 2008)

$$F = (\phi \ \epsilon \ P \ a(r,\theta)\gamma(r,\theta)\Delta A)D + R, \tag{2.8}$$

in which ΔA is the pixel area, $a(r,\theta)$ the attenuation along the path, ϵ the dye absorption coefficient, P the laser power, ϕ the dye quantum efficiency, $\gamma(r,\theta)$ the spatial intensity distribution, R the residual light not related to R6G fluorescence,

and r and θ the radial and the angular components, respectively, of the 2D polar coordinates describing the position of points within the laser plane. Keeping the same particle concentration, fluorescent dye, laser properties, camera settings and experimental configuration in all calibrations and experiments, ΔA, $a(r,\theta)$, P, ϕ, ϵ, $\gamma(r,\theta)$ and R can reasonably be assumed to be constant. Equation (8) thus reduces to

$$F = pD + R, \tag{2.9}$$

where p and R are constants that can be determined by linear regression between F and D.

However, changing the particle concentration modifies the spatial intensity distribution because the particles have an attenuation effect on $a(r,\theta)$ and, therefore, the determination of p. In fact, complex optical effects including light scattering and shadowing take place in the presence of particles and the light intensity I decreases following approximately exponential curves, whose slope steepens with particle concentration (Figure 2.4A). Hence, in order to study the mixing between a particle-laden and a clear fluid, it is necessary to account for this effect (Borg et al., 2001). Whilst calibrations are performed with a uniform particle concentration, the spatial distribution of particles in the experiments can be very complex. Therefore, since the particle and R6G concentrations cannot be assessed simultaneously in this experimental set-up, we conduct PLIF calibrations using different particle concentrations. The difference between calibrations allows us to assess the uncertainty on measurements where the particle concentration is unknown. To obtain minimum uncertainties, we perform calibrations for particle concentrations of 0, 1 and 2 g l^{-1}, where the light intensity diminishes to a minimum of 33 % of its initial value (Figure 2.4A). The effect of particle concentration on R6G fluorescence through the width of the tank is shown in Figure 2.4B. It is clear that small particle concentration differences can drastically reduce the intensity of fluorescence by attenuating the spatial light distribution inside the tank.

We conduct PLIF calibrations varying the particle and R6G concentration whilst keeping a constant laser power of 1.15 W. The water tank is filled with a uniform dye concentration ranging from 0 to 8 µg l^{-1} for three particle concentrations: 0,

1 and 2 g l^{-1}. Calibration images are averaged over 10 s in order to erase short temporal variations in fluorescence intensity. For each pixel, we fit the digital level and the R6G concentration to equation (2.8) to determine p and R. In contrast with the particle concentration calibrations, the quality of the linear regression is good throughout the tank for a uniform particle concentration, where $a(r, \theta)$ is constant. However, the slope p is affected by the presence of particles as the fluorescence intensity diminishes with increasing particle concentration (Figure 2.4C), yielding an uncertainty on the measurements of R6G concentration and ultimately on the fluid density measurements. In the region of particular interest where the PBL forms, located within the first 5 cm below the barrier, we estimate the average uncertainty of the final fluid density measurement to be 0.1 and 0.8 kg m^{-3} for 1 and 2 g l^{-1} PLIF experiments, respectively (Supplementary Figure A2.4).

2.2.4 Experimental conditions

We performed two types of experiments, with different objectives. Type A experiments are each repeated at least three times with the aim of separately characterising (i) the fingers at different particle concentrations, and (ii) the density of the fluid phase (Table 2.2). In the first subset of type A experiments (A1-A10), we image the particles and vary the particle concentration from 1 to 10 g l^{-1}. In the second subset of type A experiments (A11-12), we repeat the same experiments but instead measure fluid phase properties using the PLIF technique, only with particle concentrations of 1 and 2 g l^{-1}. Type A experiments have a constant upper layer thickness of 13.5 cm and are imaged for 90-120 s after barrier removal.

In type B experiments, we explore the conditions that favour the formation of settling-driven gravitational instabilities by varying both the upper layer thickness (from 5 to 21 cm) and the particle concentration (from 7×10^{-4} to 3 g l^{-1}; Table 2.2). The maximum upper layer thickness is limited to 21 cm by the size of the water tank and we select the minimum thickness to be 5 cm in order to keep the upper layer much greater than the size of perturbations that could be induced by barrier removal. All type B experiments are particle-imaging experiments used to identify the presence or absence of settling-driven gravitational instabilities and are

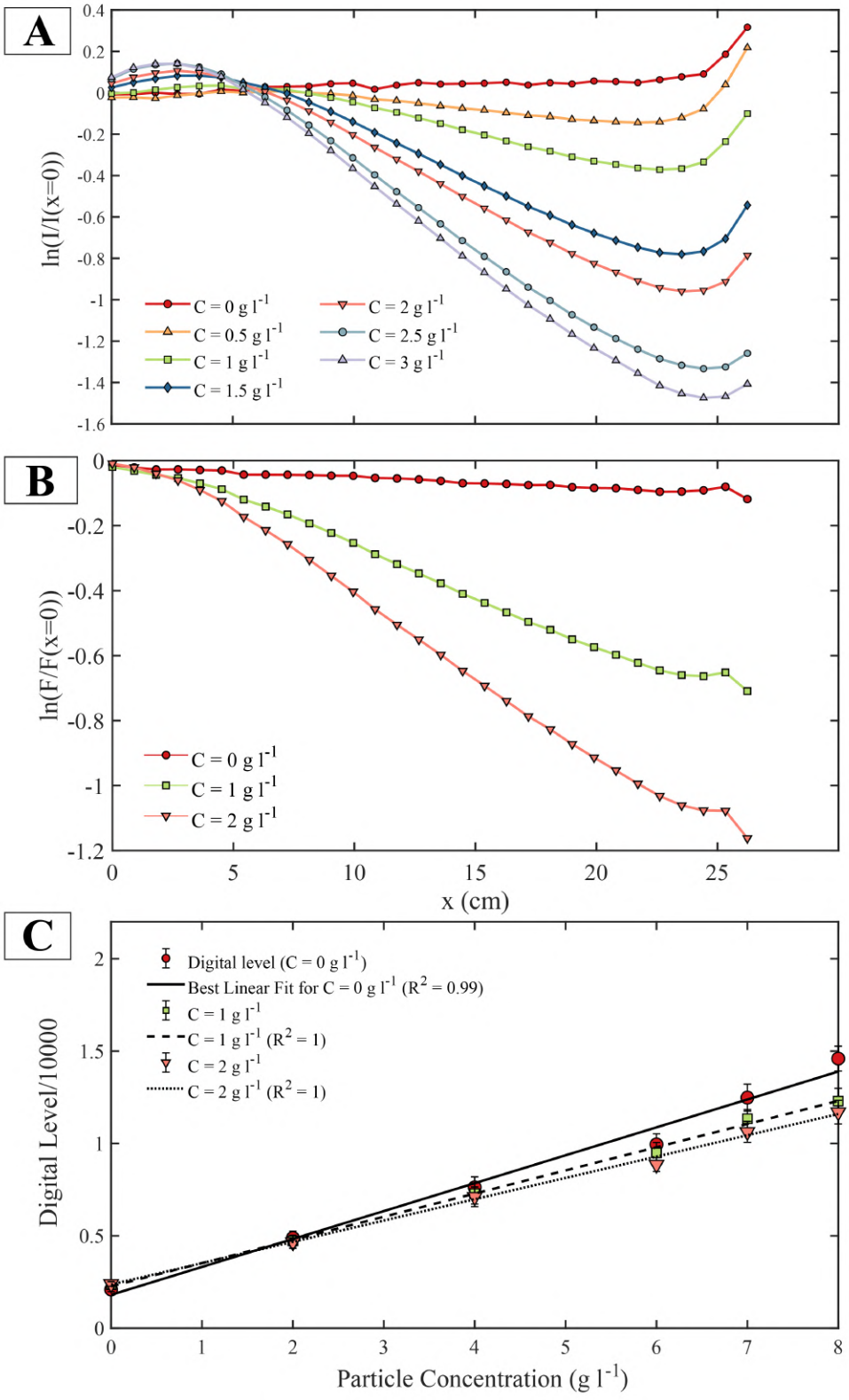

Figure 2.4: **(A)** Profile of light intensity I as a function of distance from the laser source x ($x = 0$ corresponds to tank wall closest to laser) for different particle concentrations (without R6G). **(B)** Decrease of fluorescence intensity F for selected particle concentrations in PLIF calibrations. Note that, in both **(A)** and **(B)**, intensity is expressed as a logarithm normalized with its value at $x = 0$. **(C)** Example of linear relation between R6G concentration and pixel digital level at different particle concentrations for a given pixel. The fluorescence intensity received by the camera diminishes with particle concentration, modifying the slope p. Vertical error bars in panels A and C represent the standard deviation of the averaged pixel digital level over 10 s.

imaged for at least 180 s after barrier removal.

2.2.5 Analytical procedure

For PLIF experiments (A11-12), we calculate the local concentration of upper fluid X_f that corresponds to the proportion of upper layer fluid (containing the fluorescent dye) within the fluid phase as $X_f = D/D_u$, with D the local dye concentration and D_u the initial R6G concentration of the upper layer. We then determine the fluid density ρ_f from the concentration of upper fluid as

$$\rho_f = X_f \rho_w + (1 - X_f)\, \rho_s, \tag{2.10}$$

where ρ_w is the density of fresh water (that initially forms the fluid phase of the upper layer) and ρ_s is the density of the sugar solution in the lower layer. Moreover, PLIF experiments provide reproducible results, with fluid density profiles very similar from one experiment to another. This allows us to reasonably combine the fluid phase density with the particle concentration, obtained in experiments A1-10, in order to calculate the bulk mixture density ρ_m as

$$\rho_m = X_p \rho_p + (1 - X_p)\, \rho_f, \tag{2.11}$$

with ρ_p the particle density and $X_p = C/\rho_p$ the particle volume fraction calculated from the measured particle concentration C. At the density interface, the reduced gravity is estimated as a function of ρ_m and ρ_s as

$$g' = g\frac{\rho_m - \rho_s}{\rho_s}. \tag{2.12}$$

For the PBL of density ρ, the reduced gravity is calculated as $g' = g(\rho - \rho_s)/\rho_s$.

Whilst PLIF experiments used to infer the fluid phase density involve only small particle concentrations of 1 and 2 g l^{-1}, we additionally calculate the bulk density in experiments involving higher particle concentrations by estimating the fluid phase density from $C_u = 2$ g l^{-1} PLIF experiments. To do so, we assume that the spatial distribution of the fluid phase is only weakly affected by the particle concentration.

Exp. number	**C (g l^{-1})**	**X_p**	**H_1 (cm)**	**L^***	**Sedim.**	**Number of repeats**	**Imaging techniques**
Type A experiments							
A1	1	4.0×10^{-4}	13.5	11.3	F	3	particle imaging
A2	2	8.0×10^{-4}	13.5	14.2	F	3	particle imaging
A3	3	1.2×10^{-3}	13.5	16.3	F	4	particle imaging
A4	4	1.6×10^{-3}	13.5	17.9	F	3	particle imaging
A5	5	2.0×10^{-3}	13.5	19.3	F	3	particle imaging
A6	6	2.4×10^{-3}	13.5	20.5	F	3	particle imaging
A7	7	2.8×10^{-3}	13.5	21.6	F	3	particle imaging
A8	8	3.2×10^{-3}	13.5	22.6	F	3	particle imaging
A9	9	3.6×10^{-3}	13.5	23.5	F	3	particle imaging
A10	10	4.0×10^{-3}	13.5	24.3	F	3	particle imaging
A11	1	4.0×10^{-4}	13.5	11.3	F	3	PLIF
A12	2	8.0×10^{-4}	13.5	14.2	F	3	PLIF
Type B experiments							
B1	0.0007	2.8×10^{-7}	13.5	1.0	IPS	1	particle imaging
B2	0.001	4.0×10^{-7}	21	1.8	IPS	1	particle imaging
B3	0.0056	2.2×10^{-6}	13.5	2.0	IPS	1	particle imaging
B4	0.009	3.6×10^{-6}	5	0.8	IPS	1	particle imaging
B5	0.018	7.5×10^{-6}	13.5	3.0	IPS	1	particle imaging
B6	0.02	8.0×10^{-6}	21	4.8	F	1	particle imaging
B7	0.02	8.0×10^{-6}	17	3.8	IPS	1	particle imaging
B8	0.045	1.8×10^{-5}	13.5	4.0	IPS	2	particle imaging
B9	0.05	2.0×10^{-5}	7.5	2.3	IPS	1	particle imaging
B10	0.05	2.0×10^{-5}	10	3.1	IPS	1	particle imaging
B11	0.05	2.0×10^{-5}	17	5.2	F	1	particle imaging
B12	0.05	2.0×10^{-5}	21	6.5	F	1	particle imaging
B13	0.087	3.5×10^{-5}	13.5	5.0	F	2	particle imaging
B14	0.1	4.0×10^{-5}	5	1.9	IPS	1	particle imaging
B15	0.1	4.0×10^{-5}	7.5	2.9	IPS	1	particle imaging
B16	0.1	4.0×10^{-5}	10	3.9	IPS	1	particle imaging
B17	0.1	4.0×10^{-5}	17	6.6	F	1	particle imaging
B18	0.1	4.0×10^{-5}	21	8.1	F	1	particle imaging
B19	0.15	6.0×10^{-5}	5	2.2	F	1	particle imaging
B20	0.15	6.0×10^{-5}	7.5	3.3	F	1	particle imaging
B21	0.15	6.0×10^{-5}	13.5	6.0	F	1	particle imaging
B22	0.25	1.0×10^{-4}	5	2.6	F	1	particle imaging
B23	0.25	1.0×10^{-4}	7.5	3.9	F	1	particle imaging
B24	0.25	1.0×10^{-4}	10	5.3	F	1	particle imaging
B25	0.36	1.4×10^{-4}	13.5	8.0	F	1	particle imaging
B26	0.5	2.0×10^{-4}	7.5	5.0	F	1	particle imaging
B27	0.5	2.0×10^{-4}	10	6.6	F	1	particle imaging
B28	1	4.0×10^{-4}	10	8.4	F	1	particle imaging
B29	3	1.2×10^{-3}	7.5	25	F	1	particle imaging
B30	3	1.2×10^{-3}	21	9.0	F	1	particle imaging

Table 2.2: List of experiments. All experiments are performed with spherical glass beads, with a median diameter of 41.5 µm, and a lower layer density of 1008 kg m^{-3}. Particle concentrations C and equivalent particle volume fractions X_p refer to the initial particle concentration in the upper layer. H_1 is the upper layer thickness and L^* a dimensionless number introduced in section 2.3.6 (equation 2.17). In the "Sedim." column, we indicate the presence of fingers by "F" whereas their absence (i.e. individual particle settling) is signaled by "IPS".

Given that the particle concentration can reach up to 10 g l^{-1}, this is a strong assumption that we can only test for $C_u = 1$ and 2 g l^{-1} PLIF experiments for which fluid phase density profiles are indeed very similar (Supplementary Figure A2.2).

Type A particle-imaging experiments (A1-10) are processed in order to quantify the effect of particle concentration on the dynamic and geometric properties of fingers. The finger velocity is obtained by manually tracking the front position (i.e., lowest position of the interface between the finger and the lower layer fluid) over time. We measure the PBL thickness throughout experiments using both visual observations and particle concentration profiles. At the lower boundary of the PBL there is an abrupt change in particle concentration that corresponds to the transition from the particle suspension to the particle-free lower layer. We therefore define the PBL base as the position where the vertical gradient of the particle concentration reaches its minimum value. Results show that the position of the lower PBL boundary (and therefore the PBL thickness) reaches a constant height after 10-20 s (Supplementary Figure A2.5), when the initial effect of barrier removal disappears. The PBL thickness is finally defined as the vertical separation between the initial density interface, represented by the barrier, and the lower PBL boundary (Figure 2.5). When fingers develop, they form distinct particle-rich columns that descend into the lower layer and are characterised by bright regions in the experiments. Along a horizontal transect crossed by fingers, the light intensity profile has a peak at each finger location (Supplementary Figure A2.6). We therefore determine the number of fingers by counting the most prominent peaks along a transect located 4 cm under the upper layer, where fingers are clearly developed. This counting procedure is sensitive to detection parameters such as the vertical position of the transect or threshold values for peak prominence, width, and separation. Therefore, in order to obtain repeatable results comparable to other studies, these parameters have been selected to reproduce manual finger detection (Scollo et al., 2017) within $\pm$ 1 finger. In contrast to previous methods, this allows us to quantify the temporal evolution of the number of fingers throughout the experiment duration. We assess the finger spacing λ and width W from visual observations (Figure 2.5). These geometrical parameters are measured 10-20 s after the experimental onset and at the

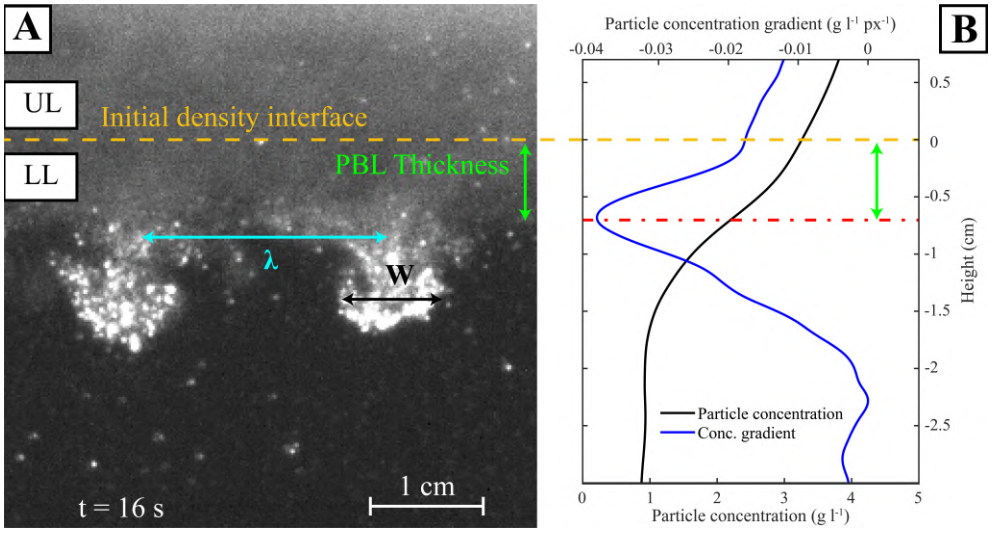

Figure 2.5: **(A)**Visualization of fingers' geometrical properties for experiment A5 (5 g l^{-1}) 16 s after removing the barrier. The yellow dashed line is located at the position of the initial density interface and separates the Upper Layer (UL) and the Lower Layer (LL). Green, black and blue arrows indicate the PBL thickness and finger width (W) and spacing (λ), respectively. **(B)** Variation in the particle concentration (black line) and its gradient (blue line) with height, in the region across the density interface 16 s after barrier removal. The lower boundary of the PBL is identified at the level where the particle concentration gradient reaches its minimum value (represented by the dotted red line).

same time as the PBL thickness, when the effect of barrier removal becomes small. λ corresponds to the distance separating two fingers and is measured at the base of the PBL, whilst W is measured at the head of the fingers (i.e., their thickest point). The uncertainty is quantified by the standard deviation from measurements of multiple fingers in each experiment. Key experimental measurements are summarised in Table 2.3.

Type B experiments are exclusively used to determine the presence or absence of fingers over a wider range of initial conditions than type A experiments. The presence of fingers is determined by visual identification of (i) downward-moving particle-laden plumes, with columnar or bulbous shapes, that form at the initial density interface and inside which particles move faster than individually and (ii) the tendency of fingers to initiate and maintain layer-scale convection in the lower partition of the tank (Hoyal et al., 1999b). We do not measure the evolution of particle concentration in type B experiments, for which the calibration presented in subsection 2.2.3 does not apply because of the low initial particle concentrations employed.

Parameter	Measurement	Method
PBL thickness δ	0.14-1.25 cm	Detection of the PBL thickness from analysis of the vertical particle concentration gradient
Finger width W	0.98-2.23 cm	Manual measurement of the width at finger's thickest point
Finger spacing λ	1.18-3.63 cm	Manual measurement of the distance separating adjacent fingers (at the level of the interface)
Maximum number of finger n	7-18	Detection of peaks in the digital level below the interface
Finger velocity V_f	0.34-1.38 cm s^{-1}	Manual tracking of the position of the finger front
Particle concentration in the PBL	0.8-9 g l^{-1}	Linear relation between the camera digital level and the particle concentration.
Concentration of upper fluid inside fingers	0-7 %	Linear relation between the camera digital level and fluorescent dye concentration
Time required to grow a PBL with excess density ≥ 0.15 kg m^{-3} t_i	54-4 s	Combination of measurements of the particle concentration measurements with estimations of the fluid phase density
Particle mass flux 20 cm below the barrier	0.21-2.60 g m^{-2} s^{-1}	Integration of the particle concentration profile at different times

Table 2.3: Summary of the measurements performed in type A experiments. The ranges of values are given by the difference between measurements performed at different particle concentrations.

2.3 Results

2.3.1 Evolution of particle concentration and mixture density with time: the formation of the PBL

Particles are initially contained in the upper part of the tank and they start sedimenting through the initial density interface after barrier removal. Subsequently, the average particle concentration decreases over time in the upper layer whilst it increases in the lower layer. In all experiments, we observe that the particle concentration in the PBL does not exceed that of the upper layer. Horizontally averaging the particle concentration at each time, we obtain particle concentration profiles for experiments A1-10. Particle concentration profiles are then combined with fluid phase density profiles (equation 2.10) to approximate the bulk mixture density profile (equation 2.11).

Figure 2.6A shows the evolution of bulk mixture density with time for experiment A8 (8 g l^{-1}; Table 2.2), chosen as an example since the relatively high particle concentration leads to a pronounced unstable density profile. Just after barrier removal ($t = 3$ s), the bulk density increases with depth in the experimental apparatus and the density profile is stable. However, particles sink below the interface and mix with the dense lower layer fluid. Consequently, an unstable heavy region associated with the PBL grows in thickness and density below the upper layer because of the added particle concentration. For experiment A8, this layer is particularly pronounced after the time $t = 12$ s, where it exceeds the density of the lower layer by about 1.3 kg m^{-3}.

An initial increase in density in the region immediately below the initial interface is observed in all experiments. Figure 2.6B shows the maximum excess density (i.e., difference between the density of the unstable region and that of the lower layer) versus initial upper layer particle concentration, for experiments A1 to A10 (Table 2.2). The maximum excess density gradually increases from 0.15 kg m^{-3} for a particle concentration of 1 g l^{-1} to 1.4 kg m^{-3} for a particle concentration of 10 g l^{-1}.

The perturbation to the system caused by the barrier removal at the experiment onset prevents us identifying the timescale of growth of the PBL thickness, which

is expected to be δ/V_p (Martin and Nokes, 1989). Because of this experimental limitation, we therefore quantify the timescale at which the density increases in the PBL by measuring t_i, the time to develop an unstable layer with excess density $\geq$ 0.15 kg m^{-3}. We find that t_i decreases with C (2.6; Supplementary Videos A2.2 and A2.3), with t_i = 40-60 s at C_u = 1 g l^{-1} and t_i = 4-6 s at C_u = 10 g l^{-1} (Figure 2.6C). Measurements are well fitted by the relation $t_i = (\alpha/g')$, where α = 0.2 m s^{-1} is an empirically-fitted constant, dimensionally homogeneous to velocity. By analogy with the expected timescale of PBL growth, we presume that the constant α, which governs the increase of the density inside the PBL, is inversely proportional to the individual settling speed of particles.

2.3.2 Fluid mixing driven by gravitational instabilities and entrainment within fingers

Unlike particles, the upper layer fluid phase is not significantly entrained inside the lower layer after barrier removal and fluid mixing between the upper and the lower layer is limited in proportion and vertical extent (Figure 2.7). However, we notice the development of a thin 2-3 cm mixing zone below the interface with intermediate concentrations of upper fluid (10-60 %). This zone is affected by disturbances created by the initial barrier removal. Below this zone, the spatial distribution of the concentration of upper fluid shows that only small amounts of upper fluid are entrained within fingers. This entrained fluid appears as thin leaks of upper fluid (similar to those observed by Parsons et al., 2001) with concentrations of upper fluid up to 6-7 % (Figure 2.7B). Once entrained downward, portions of the upper layer are seen to buoyantly rise back up once fingers reach the bottom of the tank (2.6; Supplementary Videos A2.4 and A2.5). On average, the concentration of upper fluid in the lower layer increases with time but remains low ($<$ 3 %) (Figure 2.7C). There is an initially rapid increase at the start of the experiment due to the removal of the barrier. This is then followed by small oscillations that are linked with the thickening and retraction of the PBL at the location where fingers are formed. This thickening induces a perturbation of the lower density interface that results in an increase of the average concentration of upper fluid. The PBL later retracts to its

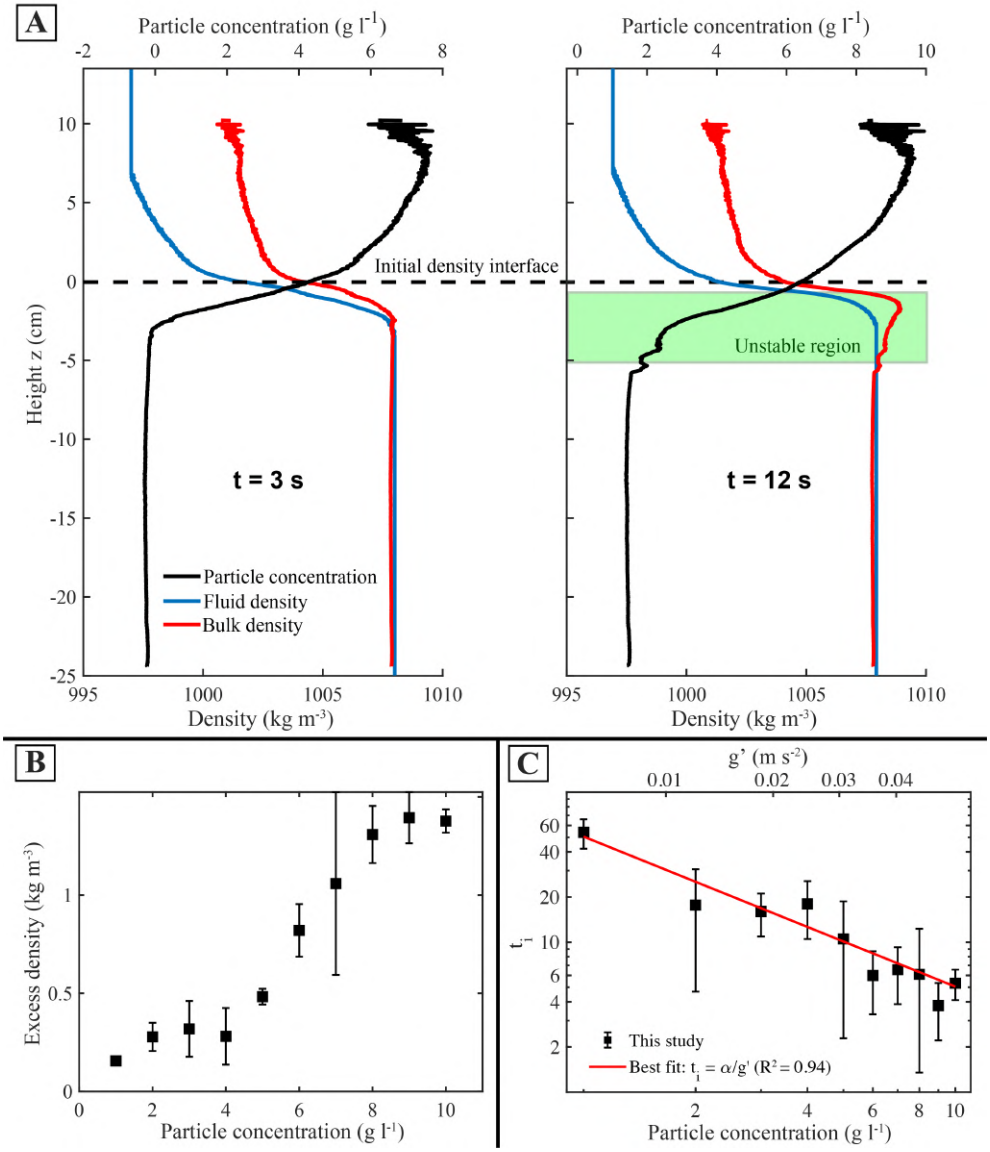

Figure 2.6: **(A)**Horizontally-averaged density and particle concentration profiles for experiment A8 (initial particle concentration is 8 g l^{-1}; Table 2.2), with the fluid phase density in blue, the particle concentration in black (axis above) and the bulk mixture density in red. The initial barrier position is represented by the dashed lines. Initially, at $t = 3$ s (left panel), the bulk stratification is stable. After some time $t = 12$ s (right panel), the PBL develops below the interface and leads to the formation of a dense unstable region highlighted in green. For clarity, the uncertainties associated with measurements of the fluid density (corresponding to 0.8 kg m^{-3} below the density interface) are not displayed on the figures. **(B)** Variation in the excess density with particle concentration for experiments A1 to A10 (Table 2.2). The particle concentration on the horizontal axis refers to the initial particle concentration of the upper layer, whereas the excess density is the maximum value for a given experiment. **(C)** Effect of particle concentration on the duration t_i required to attain an excess density ≥ 0.15 kg m^{-3} in the upper layer. Error bars correspond to the standard deviation associated with each particle concentration.

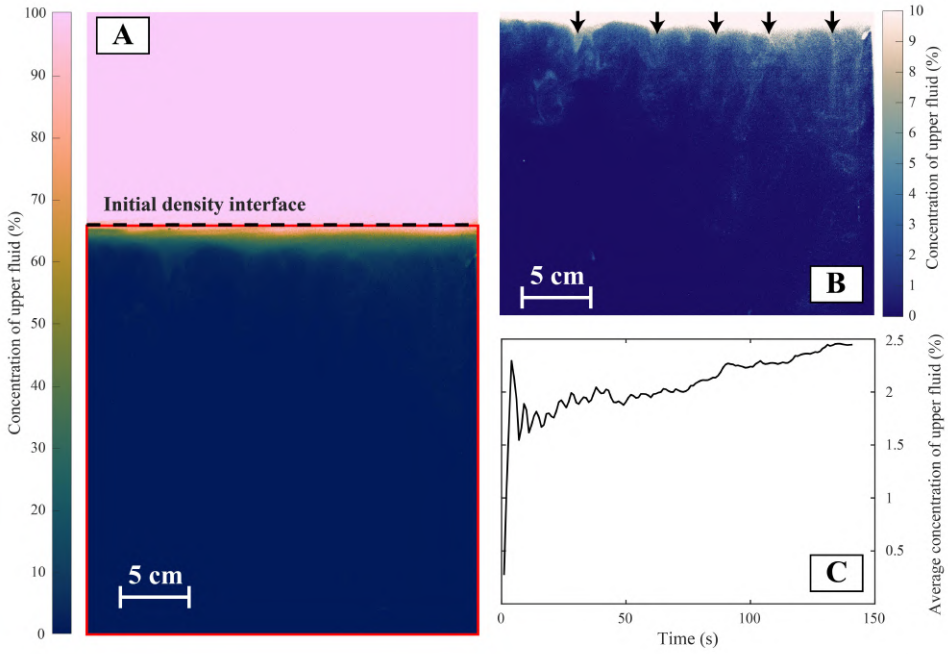

Figure 2.7: **A** Spatial distribution of upper fluid concentration 30 s after barrier removal in experiment A11 (1 g l^{-1}). The black dashed line indicates the position of the initial density interface and the red rectangle the portion of the experiment considered to be the lower layer. **(B)** Concentration of upper fluid in the lower partition of the tank with an adjusted colormap to highlight regions of upper fluid entrainment within fingers. Black arrows show the location of leaks. **(C)** Average concentration of upper fluid in the lower layer. Oscillations in the signal at the beginning of the experiment are initially due to the removal of the barrier and then PBL detachment (see 2.6; Supplementary Videa A2.4). The uncertainty on the measurement is estimated to be 17 %.

initial position after detachment of the fingers, resulting in a decrease in the average concentration of upper fluid.

2.3.3 Effect of particle concentration on finger velocity, number and temporal evolution

The average finger velocity increases with particle concentration (Figure 2.8), from 0.35 cm s^{-1} at $C_u = 1$ g l^{-1} to 1.4 cm s^{-1} for $C_u = 10$ g l^{-1}. We calculate the predicted characteristic finger velocity by combining the buoyancy and mass fluxes to obtain dimensions of velocity, as well as assuming that fingers have a circular cross section (Hoyal et al., 1999b; Carazzo and Jellinek, 2012)

$$V_f = g'^{2/5}\left(\frac{\pi V_p \delta^2}{4}\right)^{1/5}, \tag{2.13}$$

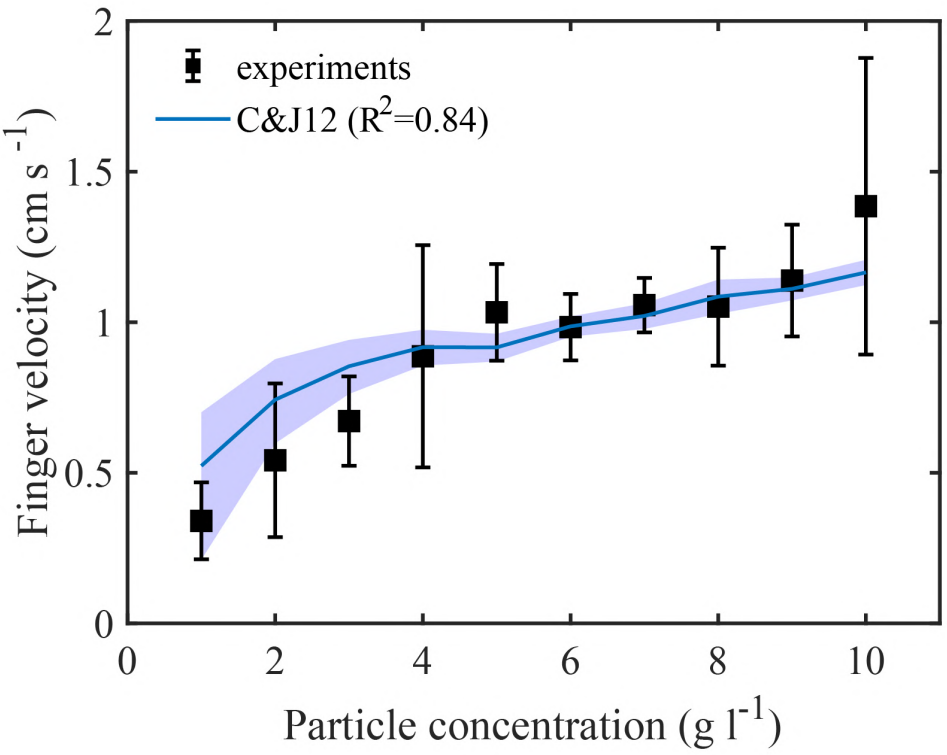

Figure 2.8: Finger velocity as a function of initial particle concentration. The blue line corresponds to the finger velocity calculated using equation (2.13) (Hoyal et al., 1999b; Carazzo and Jellinek, 2012) in combination with equation (2.12) to obtain the reduced gravity of the PBL. The blue region corresponds to finger velocities calculated with upper fluid concentrations ranging from 0 (upper limit) to 7 % (lower limit). Vertical error bars correspond to the standard deviation of the finger velocity measured in different experiments.

where V_p is given by equation (2.4) and $g^{'}$ is calculated using equation (2.12) and a maximum concentration of upper fluid in fingers of 7 % (Figure 2.8). The characteristic length of the instability δ is measured experimentally and estimated from volume conservation to be half the finger width, which is the length scale controlling finger dynamics (Hoyal et al., 1999b). The calculated evolution of finger velocity with initial particle concentration is in good agreement with the observed finger speed ($R^2 = 0.84$).

The evolution of the maximum number of fingers per unit width as a function of both particle concentration and time has been investigated (Figure 2.9). The number of fingers increases with particle concentration, with 0.25 fingers per cm formed on average at $C_u = 1$ g l^{-1} and 0.6 fingers per cm at $C_u = 10$ g l^{-1}. This new set of experiments agrees very well with the previous finding for the number of fingers

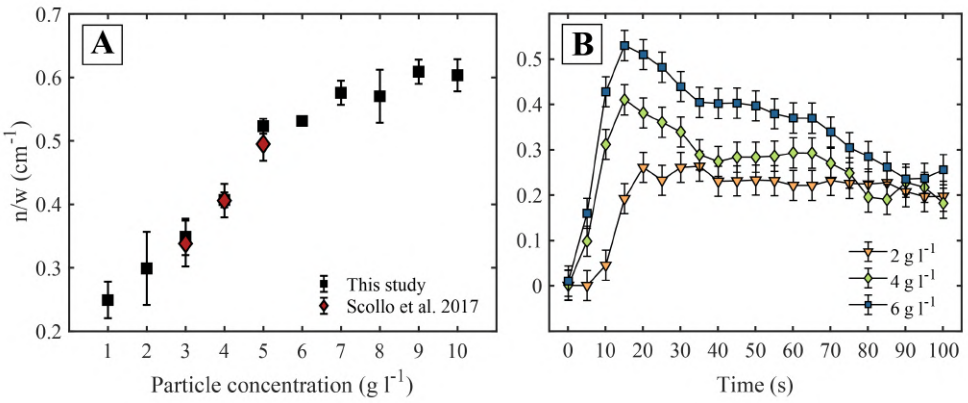

Figure 2.9: **(A)** Variation in the number of fingers per unit length (n/w) as a function of particle concentration, with n the number of fingers and w the width of the experimental tank (w = 30.1 cm in this study and w = 30.3 cm for Scollo *et al.* (2017)). Vertical error bars correspond to the standard deviation of the number of fingers measured in different experiments. **(B)** Evolution of the number of fingers per unit length as a function of time for selected particle concentrations. The uncertainty of 0.03 fingers cm^{-1} comes from the typical discrepancy of ± 1 fingers determined by comparing the automatic detection of fingers with visual observations.

(Scollo et al., 2017), while also expanding the previously-investigated concentration range (Figure 2.9A). We observe the occurrence of fingers from a few seconds after barrier removal. The maximum number of fingers is achieved 10 to 20 s after barrier removal and this timing weakly depends on the particle concentration (Figure 2.9B). For high particle concentrations, the number of fingers increases at a faster rate, reaching its maximum value quicker than for low particle concentrations. For example, whilst the number of fingers increases from 0 to a maximum of 0.53 fingers per cm in 10 s for C_u = 6 g l^{-1}, it takes 20 s to achieve the maximum number of fingers of 0.27 fingers per cm for C_u = 2 g l^{-1}. The number of fingers per unit length gradually decreases after reaching its maximum value (Scollo et al., 2017) and attains a nearly constant value of approximately 0.2 – 0.3 cm^{-1}, regardless of the initial particle concentration. This value is possibly related to the progressive depletion of particles from the upper layer and to the merging of fingers.

2.3.4 Finger length scales in experiments: PBL thickness, finger width and finger spacing

As expected for such settling-driven gravitational instabilities (Hoyal et al., 1999b; Carazzo and Jellinek, 2012), all characteristic length scales, which we measure 10 to 20 s after removing the barrier, are related to each other by a proportionality coefficient. We find finger width and spacing to scale as approximately two and three times the thickness of the PBL, respectively ($W \approx 2\delta$ and $\lambda \approx 3\delta$; Figure 2.10A-C) and that all these length scales decrease with the initial particle concentration (Figure 2.10D-E). From the definition of the Grashof number (equation 2.1), the PBL thickness is expected to scale as (Hoyal et al., 1999b; Carazzo and Jellinek, 2012)

$$\delta = (\frac{Gr\nu^2}{g'})^{1/3}. \tag{2.14}$$

Finger width and spacing should, therefore, scale similarly. Taking $Gr = Gr_c = 10^3$ provides an estimate of the critical PBL thickness (Turner, 1973; Hoyal et al., 1999b) above which convection can start (i.e., the minimum PBL thickness). This assumption, however, is found to underestimate the thickness of the PBL measured in experiments. It is therefore probable that the PBL continues to grow beyond this critical thickness. We find that a value $Gr = Gr_{\text{exp}} = 10^4$ provides a better fit between observations and equation (2.14). This is consistent with the results of Barnard (2021), who found $Gr_c = 10^4$ in an analogue experimental configuration. The agreement between the measurements and the model is good for the finger width and spacing, whilst equation (2.14) predicts the thickness of the PBL with less accuracy (Figure 2.10), which is characterised by more scattered data points due to the effect of barrier removal. Moreover, if we fit the measured characteristic length scales to scale with g'^m, we find m = -0.43 for the PBL thickness, for which the agreement with equation 2.14 is the lowest, whereas for the finger spacing and width, m = -0.38 and -0.35, which are closer to the predicted value of $-1/3$.

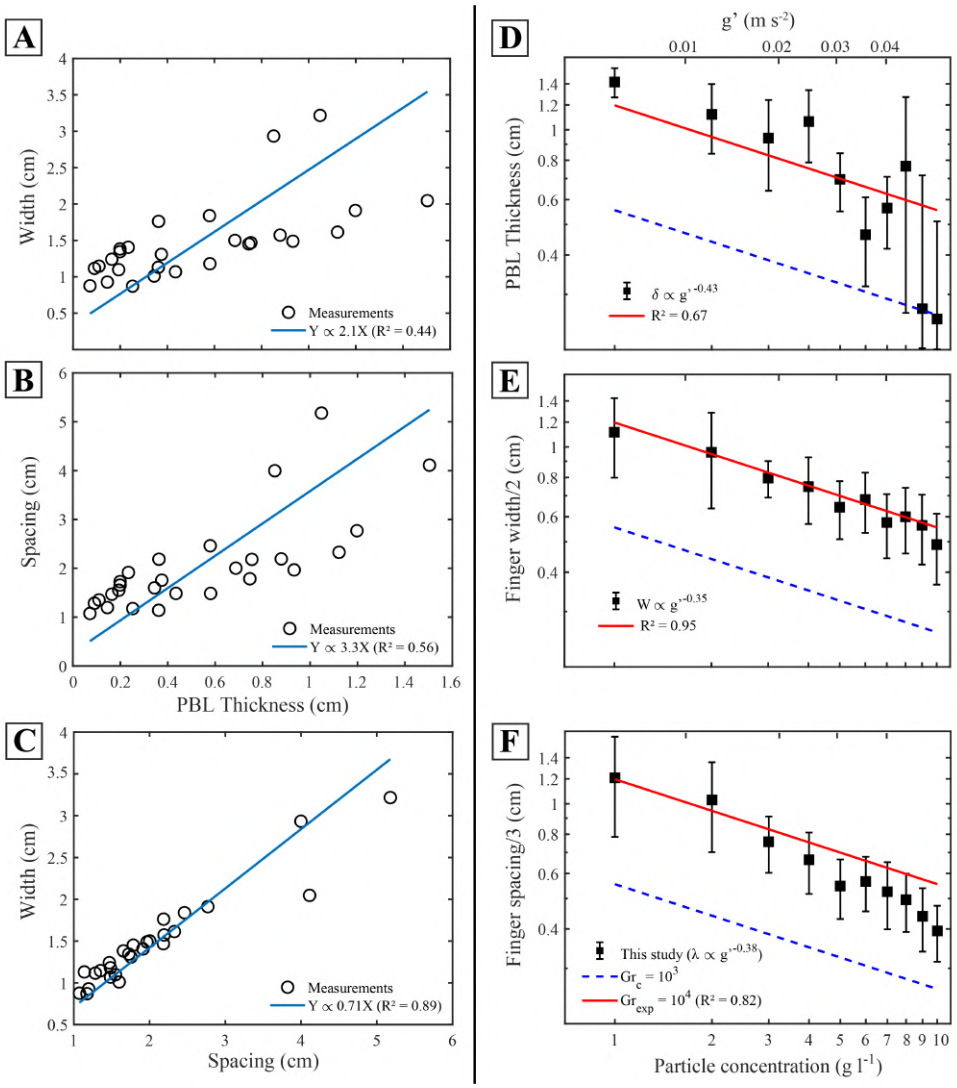

Figure 2.10: Comparison between fingers characteristic lengths for individual experiments. **(A)** Width (W) as a function of PBL thickness (δ). **(B)** Spacing (λ) against PBL thickness **(C)** Width against spacing. The blue lines show the proportionality relationships inferred between characteristic lengths: $W = 2.1\delta$; $\lambda = 3.3\delta$; $W = 0.71\lambda$. (**D-F**) Log-log plot of the characteristic length scales of the instabilities, measured 10 to 20 s after the beginning of the experiment, including **(D)** PBL thickness δ, **(E)** finger width W and **(F)** finger spacing λ, as functions of initial particle concentration, compared to the prediction of Hoyal et al. (1999b). The blue dashed line corresponds to $Gr_c = 10^3$ and the red solid line to $Gr_{\mathrm{exp}} = 10^4$. Vertical error bars correspond to the standard deviation of the sizes measured in different experiments.

2.3.5 Temporal evolution of the particle mass flux

The particle mass flux through a horizontal plane at depth l located below the upper layer can be calculated in the experiments as

$$F_{\text{exp}} = \frac{\Delta m}{A \Delta t}, \tag{2.15}$$

with $\Delta m = m_{t+\Delta t} - m_t$ the particle mass difference in the region below l measured in a time interval $\Delta t = 0.1$ s, and $A = 7.5 \times 30.1$ cm^2 the horizontal cross sectional area of the experimental domain. At any time, the mass of particles below l can be calculated by integrating the particle concentration profile (Figure 2.6) from the bottom of the tank $z = b$ ($z = 0$ corresponds to the height of the initial density interface) to $z = l$; $m_t = A \int_l^b C(z) dz$. This estimation of the mass does not account for the mass of particles accumulated at the bottom of the experimental tank and therefore only provides a lower limit on the particle mass flux.

Predicting the evolution of the particle mass flux in the presence of fingers is complex because a complete description requires: (i) information on the 3D evolution of the finger velocity and size with time and depth, (ii) a good knowledge of the duration necessary to produce fingers, and (iii) a description of the particle distribution and velocity field inside fingers. It is nonetheless possible to assess the time at which the particle mass flux is expected to increase (i.e. the time at which first particles reach a depth l). Assuming that particles are coupled with the flow within fingers that form instantaneously at the start of the experiment, first particles can reach a depth l after a time l/V_f, with V_f the vertical velocity of fingers given by equation (2.13). In contrast, first particles settling individually from the base of the upper layer at their Stokes velocity (equation 2.4) are expected to reach l after a time l/V_p.

Figure 2.11A shows the temporal evolution of F_{exp} measured at a depth $l = 20$ cm for $C_u = 1$, 3 and 5 g l^{-1}. Generally, experiments with high particle concentrations result in larger particle mass fluxes that start to increase quicker than in experiments at lower particle concentrations. For all particle concentrations, F_{exp} increases progressively from when fingers first arrive, before reaching a more stable

plateau. The particle mass flux starts to increase close to the time l/V_f (15-35 s), which is the expected arrival time for fingers, and much earlier than the expected arrival time of individual particles (143 s). F_{exp} continues to increase as more fingers reach $z = l$ and fingers become bigger through merging and entrainment of ambient fluid. The latter behaviour where F_{exp} fluctuates around a plateau that occurs once the number of fingers has stabilised (Figure 2.9B) and overturning has begun in the lower layer, homogenising the particle concentration. To compare different experiments, we average F_{exp} for 15 s after the plateau is attained and plot this value as a function of C_u (Figure 2.11B). We find that the particle mass flux increases with the initial particle concentration and that a power-law with a fitted exponent of 1.2 can be used to describe the relation between F_{exp} and C_u. In particular, we note that this exponent is independent of l and varies within the interval 1.2 ± 0.1. Theoretically, we can expect $F_{\text{exp}} \propto V_f C_u$. From equations (2.13) and (2.14), the finger velocity scales with $C_u^{4/15}$ so we therefore expect the particle mass flux to be proportional to $C_u^{19/15}$. The value of the exponent $19/15 \approx 1.27$ is close to the exponent of the power-law used to fit the evolution of F_{exp} with C_u in experiments and there is a good agreement between experimental measurements and the proportionality relation $F_{\text{exp}} \propto 0.14 C_u^{19/15}$.

2.3.6 Potential to form settling-driven gravitational instabilities

The tendency for settling-driven gravitational instabilities to develop below particle suspensions and to generate fingers has previously been shown to depend on the particle size. Carazzo and Jellinek (2012) compared the instability growth rate with the terminal fall velocity of individual particles and showed that fine ash promotes finger formation, whereas Scollo et al. (2017) experimentally demonstrated that coarse particle (> 125 µm) settled individually in water. When particles are sufficiently small, settling-driven gravitational instabilities can form below a particle-laden layer if the time scale of particle delivery to the PBL, given by H_c/V_p, with H_c the thickness of the particle-laden layer, is greater than the time necessary to grow an unstable PBL, given by δ/V_p. This condition is independent of the particle size (i.e. V_p). Assuming

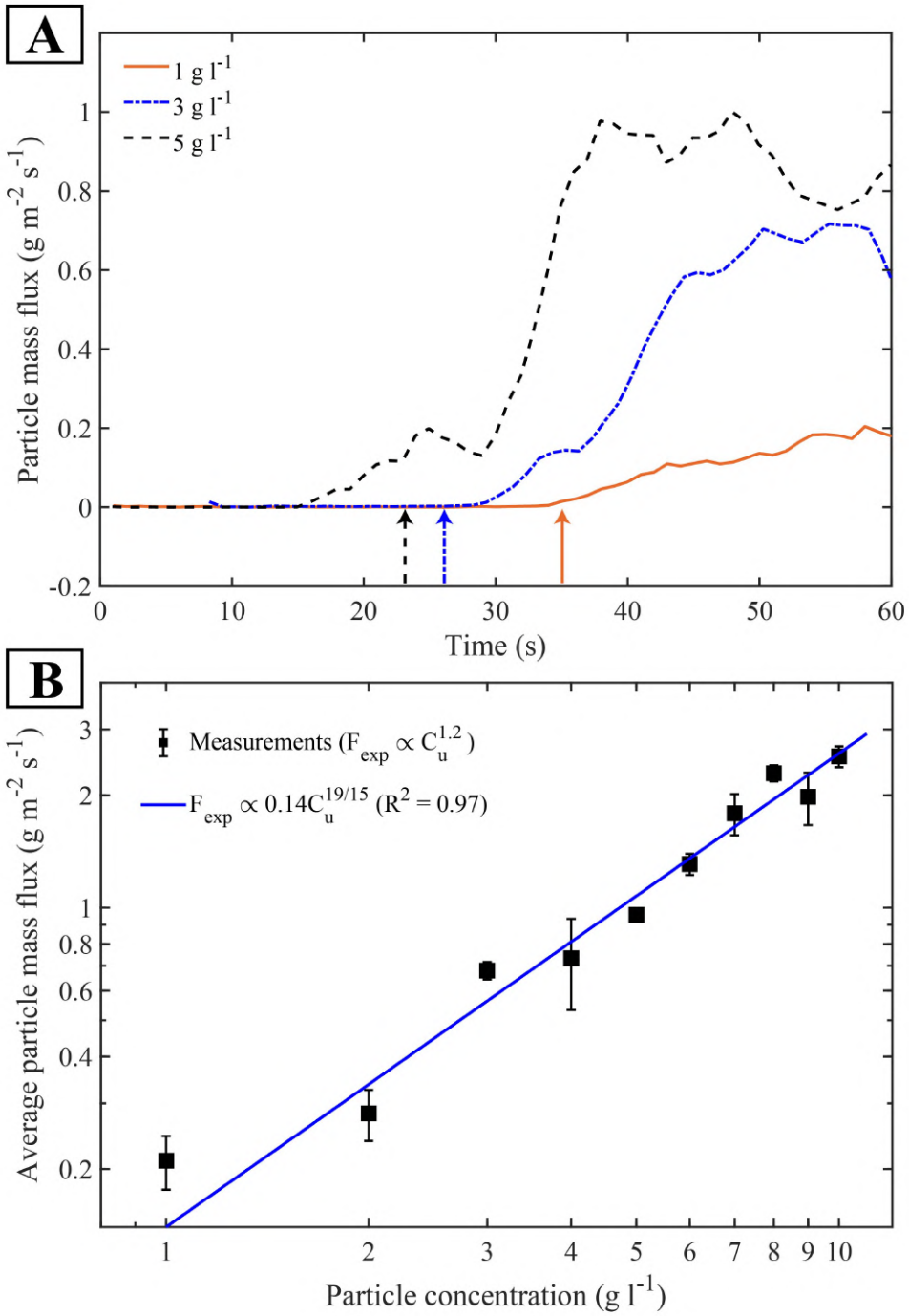

Figure 2.11: **(A)** Particle mass flux F_{exp} measured in experiments 20 cm below the upper layer from equation (2.15) for experiments A1, A3 and A6 (1, 3 and 6 g l^{-1}). The black, blue and orange arrows indicate the time l/V_f at which fingers are expected to arrive at depth l for initial particle concentrations C_u of 1, 3 and 6 g l^{-1}, respectively. Note that individually settling particles arrive at a depth 20 cm below the upper layer after a time t = 143 s that is beyond the limit of the horizontal axis **(B)** Variation in F_{exp} (averaged during 15 s after reaching a plateau value) with C_u in a log-log plot. The solid blue line shows the best fit between F_{exp} and C_u. Vertical error bars correspond to the standard deviation of the averaged particle mass flux measured in different experiments.

that the particle concentration is homogeneous in the particle-laden layer, and that its thickness remains constant and uniform, we can therefore assess the potential for instabilities to form by evaluating the dimensionless quantity

$$L^* = \frac{H_c}{\delta}. \tag{2.16}$$

Combining equations (2.12), (2.14) and (2.16), L^* can be expressed as

$$L^* = H_c\left(\frac{gX_p(\rho_p - \rho_a)}{\rho_a Gr\nu^2}\right)^{\frac{1}{3}} \tag{2.17}$$

$L^* \gg 1$ guarantees that the PBL can reach its characteristic thickness and that fingers can possibly develop. Conversely, $L^* \ll 1$ means that the particle-laden layer is substantially thinner than the critical PBL thickness, thus preventing finger formation. In our experiments, we consider $H_c = H_1$, $Gr = Gr_{\text{exp}} = 10^4$ and L^* consequently ranges from 11.3 to 24.3 in type A experiments, which all produced fingers (Table 2.2). In order to better constrain the conditions leading to the formation of fingers, we explore a wider range of initial particle concentration and upper layer thickness in type B experiments for which L^* varies from 0.8 to 25.

Figure 2.12 shows a regime diagram for experimental fingers as a function of upper layer thickness and initial particle concentration. Whilst fingers are observed in all the experiments performed at $L^* \geq 5$, experiments with $L^* \leq 2$ are characterised by individual particle settling and the absence of fingers (2.6; Supplementary Video A2.6). The domain defined by $2 < L^* < 5$ corresponds to a transition regime where fingers are either present or absent, depending mainly on the particle concentration, with higher particle concentrations favouring finger formation and their development, since they are more numerous and descending faster. We note that, as expected for settling-driven gravitational instabilities, high particle concentrations and thick upper layers favour the formation of fingers (Jacobs et al., 2015).

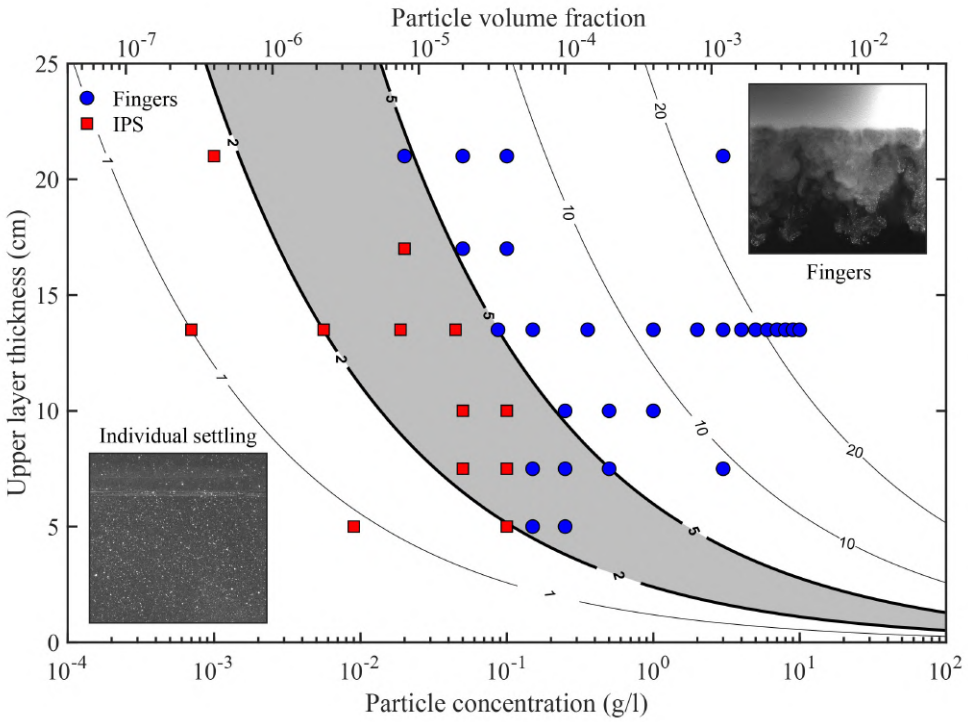

Figure 2.12: Contours of $L^* = H_c/\delta$ (equation 2.16) calculated for experiments as a function of the upper layer thickness and initial particle concentration. Calculation of L^* is performed with $Gr = Gr_{\text{exp}} = 10^4$. Blue circles and red squares correspond to experiments associated with fingers or individual particle settling (IPS), respectively (Table 2.2). The grey area $2 < L^* < 5$ indicates the transition between experiments with fingers and individual particle settling.

2.4 Discussion

2.4.1 Summary of the experimental results and comparison with previous studies

The combination of PLIF and particle imaging techniques in separate reproducible experiments provides an approximation of the bulk mixture density evolution with time. We report the formation of an unstable region in all type A experiments, which is more pronounced for high particle concentrations (Figure 2.6). From experimental observations of the evolution of the particle concentration and of the fluid and bulk mixture density, we summarise the mechanism leading to the onset of settling-driven gravitational instabilities as:

1. The initial density configuration is gravitationally stable, with a light particle-laden layer emplaced above a denser layer;

2. Particles settle across the interface from the upper layer and are incorporated in the dense lower layer fluid;

3. A thin region containing both particles and dense lower layer fluid grows below the original interface. This PBL becomes heavier than the underlying fluid because of the effect of added particles on the density of the lower layer fluid;

4. Settling-driven gravitational instabilities can occur when the thickness and density of the PBL increases causing its Gr to exceed $Gr_{\mathrm{exp}} = 10^4$, initiating convection and resulting in the formation of fingers.

This mechanism is consistent with theoretical scenarios describing the formation and the destabilisation of a dense particle-laden layer due to particle settling as illustrated in Figure 2.1 (i.e., the growing of the "nose region"; Burns and Meiburg, 2012, 2015; Yu et al., 2013; Davarpanah Jazi and Wells, 2020). It is worth mentioning that such a formation mechanism does not require the particle concentration inside the PBL to be greater than the initial particle concentration in the upper layer. The increase in bulk density inside the PBL is due to particles settling across the interface into the upper part of the dense lower layer that therefore becomes heavier than the

fluid below. This is in agreement with our experiments where we do not observe an increase of the particle concentration inside the PBL within the uncertainty of our measurements (Figure 2.6; Table 2.3). The fact that we do not observe an increase of the particle concentration across the interface is due to the lower layer being at most 1 % denser than the upper layer. Thus, in contrast with configurations involving large density differences (Carey, 1997; Manville and Wilson, 2004), particles are not significantly slowed at the interface by this density contrast and do not accumulate. Similarly, the density gradient created at the base of the upper layer (Figure 2.6A) because of barrier removal only causes negligible variations in the particle settling velocity and does not result in an increase of the particle concentration as reported by Blanchette and Bush (2005) for configurations with significant settling velocity variations.

Furthermore, our experiments suggest that fingers do not inject significant amounts of upper layer fluid into the lower layer and have an average concentration of upper fluid < 3 % (Figure 2.7). This observation indicates that settling-driven gravitational instabilities only weakly affect the transport of fluid phases from the upper to the lower layer, although we observe discrete fluid leaks with concentration of upper fluid up to 7 % injected through fingers propagating from the base of the upper layer (Table 2.3). The small upper fluid concentrations inside fingers suggest that their density, and hence their velocity, depends only weakly on the upper layer fluid density and is mainly controlled by the density of the lower layer fluid and the particle concentration inside fingers.

As in previous studies, we find that, along with particle size, particle concentration exerts a primary control on particle sedimentation and the formation of fingers (Del Bello et al., 2017; Scollo et al., 2017). Our results are in very good agreement with previous measurements of the number of fingers (Figure 2.9) (Scollo et al., 2017) and with theoretical estimates of the finger velocity (Figure 2.8) and characteristic lengths (Figure 2.10) (Hoyal et al., 1999b; Carazzo and Jellinek, 2012). This increases the confidence in these theoretical formulations of finger geometry and speed on an extended particle concentration range. However, we underline that the scaling relationships of equations (2.13) and (2.14) are not complete solutions

describing the complex flow mechanisms taking place in settling-driven gravitational instabilities. They are based on simplifying assumptions regarding the choice of a single length scale characterising finger dynamics. Moreover, they do not account for the complex particle-fluid and particle-particle interactions happening inside fingers and can therefore give only first order estimates of the size and velocity of both experimental and natural fingers.

We find that the critical thickness determined with Gr_c underestimates the observed PBL thickness (Figure 2.10D) and we report that the dimensions of the instabilities formed at different particle concentrations are consistent with a value of $Gr_{\mathrm{exp}} = 10^4$. This can be interpreted as evidence that the PBL continues to grow even after it reaches its critical thickness ($Gr = Gr_c$). Alternatively, this may also indicate that the effective PBL thickness is affected by barrier removal that initially modifies the flux of particles crossing the density interface by creating small scale eddies that quickly entrain particles below the interface. Even if we assess the dimensions and velocity of the fingers when the effects of the initial perturbation dissipate, this experimental issue can cause differences between the measured PBL thickness and the critical thickness which would develop in an ideal case. Hence, to predict the effective instability dimensions, one should first evaluate Gr from observations of the instabilities' characteristic lengths before using equation (2.14) to extrapolate the dimensions of the instability at different particle concentrations (i.e., different values of the reduced gravity).

2.4.2 Nature and size of volcanic ash fingers

We find the convective scaling law of Hoyal et al. (1999b), that works well for experiments, to greatly underestimate the dimensions of volcanic ash fingers by several orders of magnitude. For example, Manzella et al. (2015) estimated the width of ash fingers at Eyjafjallajökull 2010 to be about 170 m from visual observations. Based on observations of the fingers downward velocity, they also estimated the fine ash volume fraction to be in the range of 1×10^{-6} to 4×10^{-6} and the PBL bulk density to be approximately 1.31 kg m^{-3}. Using the values of the air kinematic viscosity υ = 3×10^{-5} m^2 s^{-1}, air density ρ_a = 1.30 kg m^{-3} and the Grashof number associated

with experiments $Gr_{\mathrm{exp}} = 10^4$, equation (2.14) only yields a finger width of a few centimetres when applied to the volcanic cloud of Eyjafjallajökull. This suggests that the characterisation of the PBL in nature is highly uncertain. Therefore, this law may not be appropriate for volcanic clouds. In addition to the challenges associated with the measurements of parameters such as the fine ash concentration in volcanic clouds and the PBL, a variety of mechanisms that are not described by our experiments or by those of Hoyal et al. (1999b) and that can form fingers can also explain these discrepancies. In fact, the PBL can purely grow by particle settling, as showed in Figure 2.1A and 2.1B for our experimental configuration, and is most likely to do so in the absence of other vertical fluid motions. Evidence for this mechanisms is perhaps suggested by lidar measurements during the 1991 Mount Redoubt eruption (Hobbs et al., 1991) that showed ash fingers forming at the flat base of the volcanic cloud about 150 km from the vent ("ash veils" in their Plate 1). However, other processes present in volcanic ash clouds can also affect the sedimentation of fine ash. These include jets from overshoot regions, internal waves, overturning motions inside the cloud, and wind-driven stirring (e.g. Carazzo and Jellinek, 2012; Freret-Lorgeril et al., 2020). In addition, Mammatus clouds, i.e., formations characterised by the development of lobes on the cloud base (Schultz et al., 2006), have also been observed at the base of volcanic clouds, e.g., Mt. St. Helens, USA, 1980 (Durant et al., 2009; Carazzo and Jellinek, 2012). However, even if they share visual and dynamic similarities with settling-driven gravitational instabilities, it remains unclear if there is any link between the two phenomena.

Another source of discrepancy with the experiments is related to the fact that, unlike volcanic clouds, experiments are performed in a confined and quiescent environment, without shear at the base of the particle suspension. Although our experiments can address the case where the plume and fingers are advected at wind speed (Scollo et al., 2017), the effect of shear on the base of volcanic clouds needs to be considered in future work in order to describe more adequately the formation and the size of ash fingers. The presence of shear at the base of the cloud can affect the formation of ash fingers for two main reasons: (i) shear can inhibit the formation of a PBL by producing eddies at the base the cloud that impede the sedimentation

of particles across the interface and (ii) it can create Kelvin-Helmoltz instabilities that will interact with settling-driven gravitational instabilities and possibly control the spatial distribution, dimensions and timing of ash fingers. Moreover, our experiments do not explore the effect of internal cloud dynamics on settling-driven gravitational instabilities. Whilst our experiments are in a transitional regime, volcanic ash clouds and ash fingers are fully turbulent and can contain vertical fluctuations that possibly affect the supply rate of particles to the PBL. We expect that more complete observations of ash fingers, combined with dedicated numerical simulations, will provide a better characterisation of ash finger sizes.

2.4.3 Conditions favouring the formation of volcanic ash fingers

Based on a new dimensionless number L^* (equations 2.16 and 2.17), we assess the possibility for the PBL to grow to its characteristic thickness and therefore constrain the conditions favouring the development of fingers. We can distinguish between three regimes in experiments: (i) fingers invariably form for $L^* \geq 5$ whereas, (ii) they never form for $L^* \leq 2$ and (iii) are either present or absent for $2 < L^* < 5$ which corresponds to a transition regime. In general, our analysis indicates that fingers are more likely to form below thick particle-laden layers associated with large particle concentrations, which correspond to $L^* \geq 5$. Calculating L^* in volcanic ash clouds is more complex and requires a good characterisation of the PBL thickness and of the eruptive parameters associated with volcanic eruptions. For instance, measurements of the fine ash concentration in volcanic clouds remain uncertain, as in situ characterisation of volcanic ash is often associated with the very edge of volcanic clouds due to flight restrictions of aircraft (Weber et al., 2012; Eliasson et al., 2014, 2016; Fu et al., 2015). Because of these caveats, we are not able to reliably quantify the value of L^* for natural volcanic ash clouds.

However, both the cloud thickness and the particle concentrations are related to the MER (Wilson et al., 1978; Sparks, 1986), suggesting that eruptions with high MERs are more prone to develop ash fingers (Scollo et al., 2017). Whilst L^* depends on both the particle concentration and the thickness of the upper layer

(i.e., volcanic cloud), other parameters also affect the occurrence of settling-driven gravitational instabilities and the production of fingers. For example, particle size has been shown to exert a major control on the tendency to form fingers, with small particles more likely to settle collectively than coarse particles (Carazzo and Jellinek, 2012; Scollo et al., 2017). Hence, although L^* provides a good characterisation of the particle concentrations and cloud thicknesses that are associated with fingers, it is not sufficient to obtain a complete characterisation of the conditions favouring the generation of settling-driven gravitational instabilities. L^* needs to be considered along with other parameters, such as the particle size and the cloud velocity, in order to assess the potential of volcanic ash clouds to produce fingers.

2.4.4 Experimental limitations and perspectives

As with all experimental studies, a number of limitations must be considered when interpreting the data.

First, because of the additional light scattering effect of particles, we only measure the fluid density field in PLIF experiments for low particle concentrations (1 and 2 g l^{-1}), with relatively large uncertainties ($\pm$ 0.8 kg m^{-3} on average below the initial density interface). Future combined PLIF and particle imaging will allow simultaneous measurement of the particle spatial distribution and fluid density (Borg et al., 2001; Dossmann et al., 2016), thus accounting for the effect of particles on fluid density measurements. The combination of these two techniques would therefore contribute to reduce the uncertainty associated with fluid density measurements and provide estimates of the fluid phase properties for particle concentrations $>$ 2 g l^{-1}.

Second, measurements of the PBL thickness are initially affected by a disturbance to the density interface generated when removing the barrier. We therefore measure the PBL thickness after it reaches a constant value once the initial perturbation disappears (Supplementary Figure A2.5). The initial perturbation could be reduced by using a thinner composite barrier (Dalziel, 1993; Lawrie and Dalziel, 2011) and a motorised barrier removal system (Davies Wykes and Dalziel, 2014) in order to obtain a better description of the initial growth of the PBL.

Third, the scaling of the finger size with the Grashof number works well when applied to experiments but not when applied to volcanic ash clouds. As described in section 2.4.2 differences between the experimental configuration and volcanic clouds can explain this discrepancy, in addition to the challenges associated with the measurement of relevant parameters in natural eruption. Experiments involving particle-laden currents instead of an immobile particle suspension will contribute to better understand this discrepancy and the scaling of natural ash fingers, along with efforts in numerical simulations of the processes. In fact, the scaling analysis in section 2.2.2 notably revealed that volcanic clouds are associated with a wider range of dimensionless numbers than our experiments and that Re and Gr can be orders of magnitude greater in nature (Table 2.1). This shows that volcanic clouds are much more turbulent than the analogue particle suspensions in the experiments, that are emplaced in a quiescent environment. Contrarily to the experiments, we can therefore expect turbulent motions inside the clouds to have a more pronounced effect on ash sedimentation, in particular by modulating the flux of particles entering the PBL, as described in section 2.4.2. The discrepancy between Grashof numbers associated with the experimental and natural configuration is related to the difficulty of measuring the PBL thickness below volcanic clouds. We expect that a more complete characterisation of the parameters associated with volcanic clouds will contribute to better assess the size of the PBL and evaluate the relevance of the scaling presented in our experimental study.

Finally, laboratory experiments, unlike volcanic plumes, exist in a confined space affected by boundary conditions and the formation of return flows (Roche and Carazzo, 2019). In our experiments, boundary conditions have an impact on convection in the lower layer, which has only a limited effect on measurements of finger characteristic velocity and dimensions, especially in the early part of the experiments, and a negligible influence on finger formation. Despite these uncertainties however, we can infer useful and rigorous interpretations of the results.

2.5 Conclusions

Our experiments provide new insights into the development of an unstable particle-laden layer from an initially stable configuration because of particle settling across the interface. The use of PLIF has revealed that the fluid phase in the upper layer is not substantially affected by the instability and the subsequent propagation of fingers. Additionally, our experiments confirm and expand previous experimental findings and theoretical predictions concerning the increase of both finger number and speed with respect to particle concentration and the decrease of PBL and fingers size. Estimations of the particle mass flux also suggest that fingers are associated with a quicker deposition of fine particles. Finally, we propose a new dimensionless number L^* in order to assess the potential of settling-driven gravitational instabilities to occur at the base of volcanic ash clouds. In summary:

- Settling-driven gravitational instabilities in a quiescent environment arise from small density anomalies generated by particle settling across the interface and being incorporated in the denser underlying fluid (i.e., the sugar solution in experiments and the atmosphere for volcanic clouds). The bulk mixture becomes denser in this region (PBL) and destabilizes the density configuration by generating a dense layer above a lighter fluid. A gravitational instability originates and, when the PBL exceeds its critical thickness (dependent on the particle concentration), fingers begin intruding into the lower layer.

- Our new experiments validate previous results (Scollo et al., 2017) and extend them to a larger particle concentration range (from 1 to 10 g l^{-1}). Both the number of fingers and the finger velocity increase with particle concentration of the suspension, and, therefore, the importance of ash fingers on fine ash settling is expected to increase with the mass loading of ash clouds.

- Experiments show that the particle mass flux increases quicker below high particle concentration suspensions than below particle suspensions with low particle concentrations because of the presence of fingers.

- Experimental results suggest that the characteristic lengths of the instabil-

ity scale with the finger Grashof number, with $Gr_{\text{exp}} = 10^4$ in experiments. Natural ash fingers, however, may exhibit a different scaling.

- The potential to form settling-driven gravitational instabilities at the base of particle suspensions can be quantified through $L^* = H_c/\delta$ that depends on the thickness of the suspension and on the particle concentration. Our experimental results suggest that fingers form at $L^* \geq 5$ (thick upper layer and high particle concentration) and that particles settle individually at L^* ≤ 2 (thin upper layer and low particle concentration), with a transitionary regime for $2 < L^* < 5$. Volcanic eruptions associated with large MERs as well as thick ash clouds and high particle concentrations are expected to favour the production of fingers associated with settling-driven gravitational instabilities; however, the characterization of associated PBL and ash concentrations is still too uncertain for calculating accurate values of L*.

Author contributions for Chapter 2

Costanza Bonadonna, Irene Manzella, Amanda B. Clarke, and Jeremy C. Phillips were involved in designing the project. Allan Fries conducted experiments and data analysis under Paul A. Jarvis and Costanza Bonadonna supervision. Allan Fries elaborated the manuscript. All authors have contributed to data interpretation as well as the editing and finalisation of the paper.

2.6 Appendix A2

Notations used in Chapter 2

Notation		Units
a	dimensionless attenuation	-
c_d	fluorescent dye concentration	kg m^{-3}
d	particle diameter	m
f	drag factor	-
g	acceleration due to gravity	m s^{-2}

Notation		**Units**
$g^{'}$	reduced gravity	m s^{-2}
k_N	Newton drag correction	-
k_S	Stokes drag correction	-
m	exponent on reduced gravity	-
n	number of fingers	-
p	slope of the linear regression between I and c_d	m^3 kg^{-1}
r	radial component of the polar coordinates	m
t	time	s
t_i	duration required to develop an unstable region	s
w	experimental tank width	m
C	particle concentration	kg m^{-3}
D_{50}	median particle diameter	m
D_{16}	16^{th} percentile diameter	m
D_{84}	84^{th} percentile diameter	m
F	camera digital level (fluorescence)	-
H_1	upper layer thickness	m
H_2	lower layer thickness	m
H_c	cloud thickness	m
I	Dimensionless light intensity	-
L	characteristic flow thickness	m
L^*	ratio between the cloud and the PBL thickness	m
P	dimensionless laser power	-
R	residual light effect on digital level	-
V	characteristic flow velocity	m s^{-1}
V_f	finger velocity	m s^{-1}
V_p	particle settling velocity	m s^{-1}
W	finger width	m
X_f	fluid mixing ratio	-
X_p	particle volume fraction	-
At	Atwood number	-

Notation		Units
Gr	Grashof number	-
Re	Reynolds number	-
Re_p	particle Reynolds number	-
St	Stokes number	-
α	empirical scaling parameter for the time	m s^{-1}
β	spatial intensity distribution (angular)	rad^{-1}
γ	spatial intensity distribution (radial)	m^{-1}
δ	PBL thickness	m
δ_f	characteristic fluctuation lengthscale	m
ϵ	fluorescent dye absorption coefficient	m^2 kg^{-1}
λ	finger spacing	m
μ	fluid dynamic viscosity	kg m^{-1} s^{-1}
θ	angular component of the polar coordinates	rad
ν	fluid kinematic viscosity	m^2 s^{-1}
ρ	PBL density	kg m^{-3}
ρ_a	ambient density	kg m^{-3}
ρ_f	fluid density	kg m^{-3}
ρ_p	particle density	kg m^{-3}
ρ_s	sugar solution density	kg m^{-3}
ρ_w	water density	kg m^{-3}
σ	sorting parameter (Inman, 1952)	m
ϕ	fluorescent dye quantum efficiency	-
ΔA	pixel area	m^2 rad
ΔU	characteristic velocity fluctuations	m s^{-1}
Σ	sedimentation number	-

Table A2.1: List of symbols

Supplementary Figures

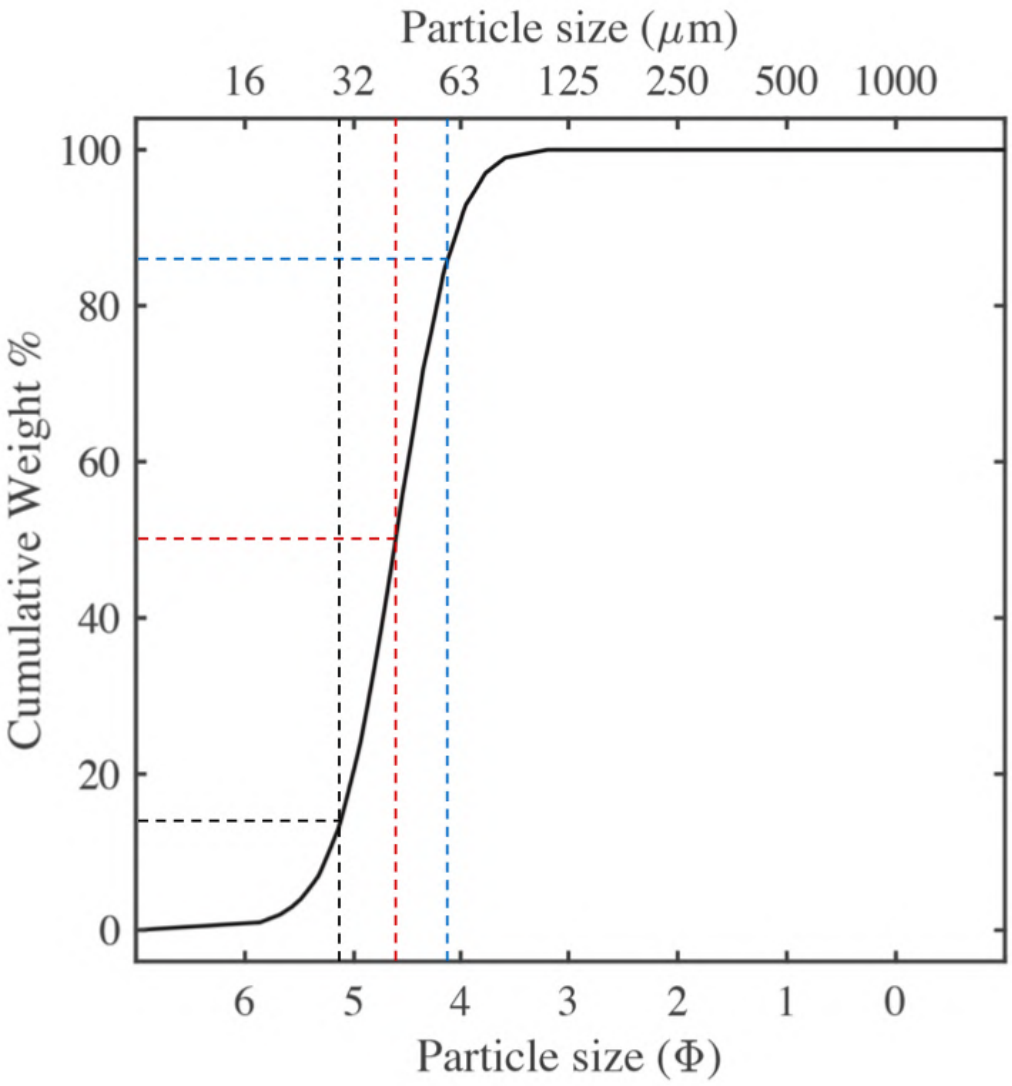

Figure A2.1: Cumulative grain size distribution of the glass beads used in the experiments (D_{50} = 41.5 µm, σ = 14 µm). The grain size distribution was obtained by laser diffraction using a BetterSizer S3 Plus. The dotted black, red and blue lines respectively indicate the 14_{th}, 50_{th} and 86_{th} percentiles.

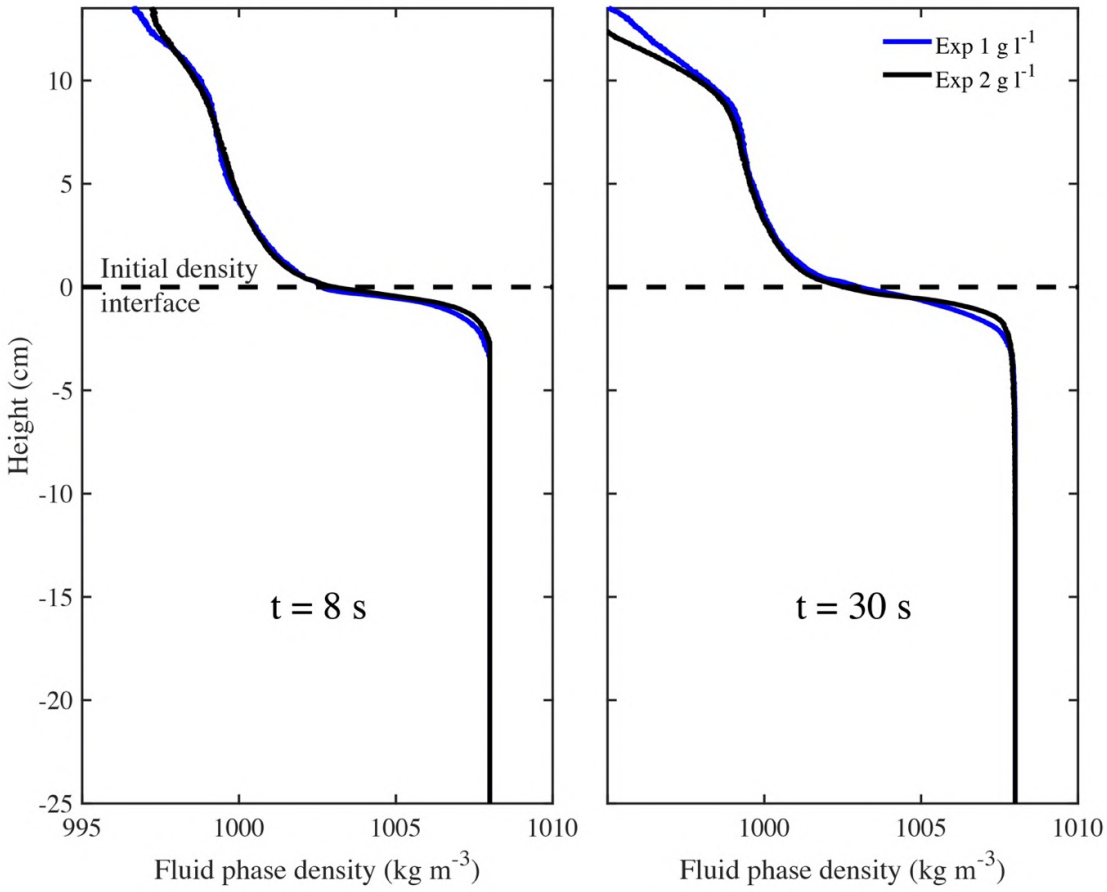

Figure A2.2: Comparison of the fluid density profiles for experiments A11 and A12 (with particle concentrations of 1 and 2 g l^{-1}, respectively). Results are very similar and reproducible.

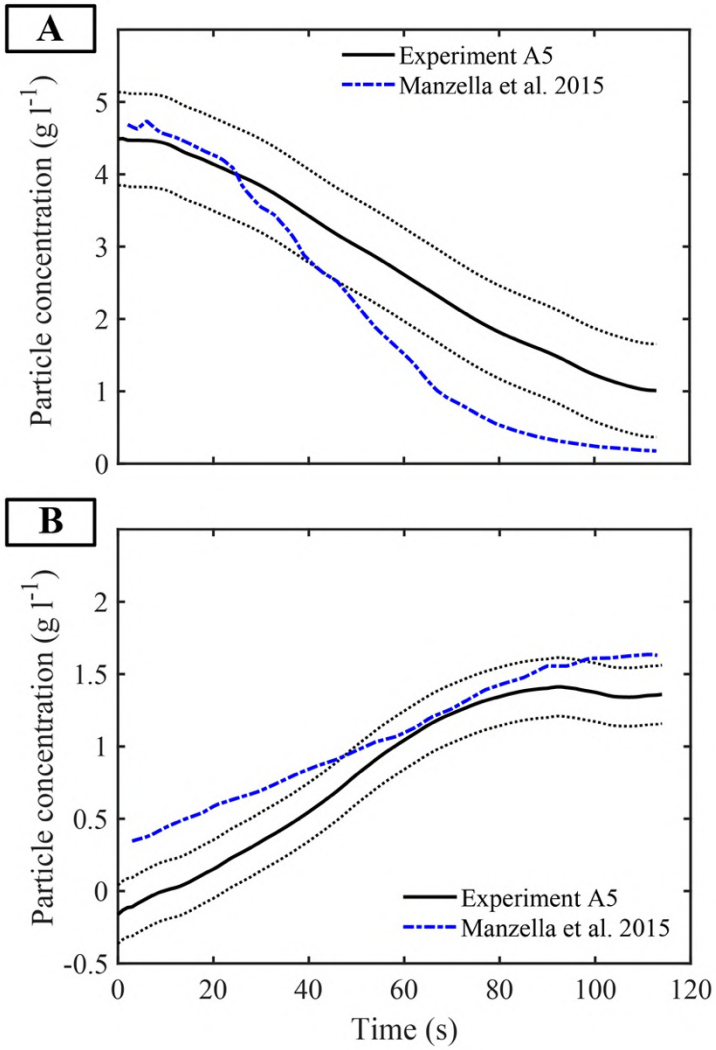

Figure A2.3: Temporal evolution of the average particle concentration in experiment A5 (5 g l^{-1}) compared with the results of Manzella et al. (2015) obtained in the same conditions, using a different imaging technique, for **(A)** the upper layer and **(B)** the lower layer. Dashed lines correspond to error limits. They are estimated using uniform suspensions, with a known particle concentration, that are imaged in the experimental configuration. The average error is given by the difference between the known particle concentration and the particle concentration inferred from the calibration. The average relative error is 10 to 15 % of the particle concentration, depending on the laser power.

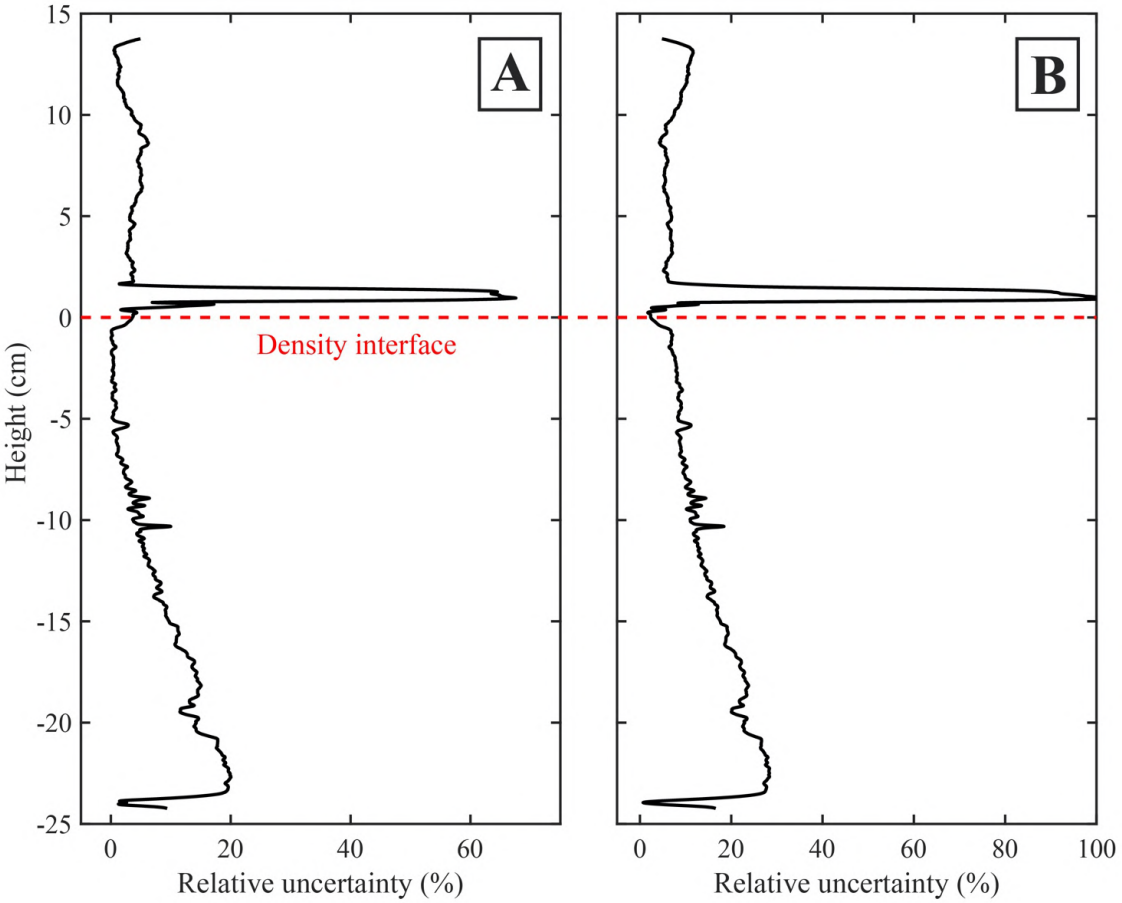

Figure A2.4: In PLIF experiments, the spatial particle distribution cannot be assessed, meaning that the particle concentration in a given volume can vary from 0 g l^{-1} up to the initial upper-layer concentration. Therefore, to assess the uncertainty of PLIF measurements, we use the calibration to infer the R6G concentration of uniform suspensions having different particle concentrations, ranging from 0 to 2 g l^{-1}, whilst keeping the same R6G concentration of 8 µg l^{-1}. The relative uncertainty is then obtained by calculating the difference between horizontally averaged R6G concentration measurements performed on particle suspensions with those performed on particle-free solutions. This difference is 7 % (0.7 % in the first 5 cm below the barrier) between 0 and 1 g l^{-1} suspensions and 13 % (7 % in the first 5 cm below the barrier) between 0 and 2 g l^{-1}. Therefore, in the region of interest where the PBL grows, R6G concentration measurements are associated with an uncertainty dependent on the input particle concentration which is 0.7 % and 7 % of the initial R6G concentration for 1 and 2 g l^{-1} experiments, respectively. For our experimental conditions where the fluid phase density varies from 997 kg m^{-3} in the upper layer to 1008 kg m^{-3} in the lower layer, the uncertainty in the determination of R6G concentrations results in an average uncertainty in fluid density of 0.08 kg m^{-3} for 1 g l^{-1} experiments and of 0.77 kg m^{-3} for 2 g l^{-1} experiments. The relative uncertainty on R6G concentration measurements as a function of height is shown for **(A)** 1 g l^{-1} experiments and **(B)** $\geq$ 2 g l^{-1} experiments. The peak in uncertainty located above the position of the initial density interface is an artifact and due to light extinction on the barrier track.

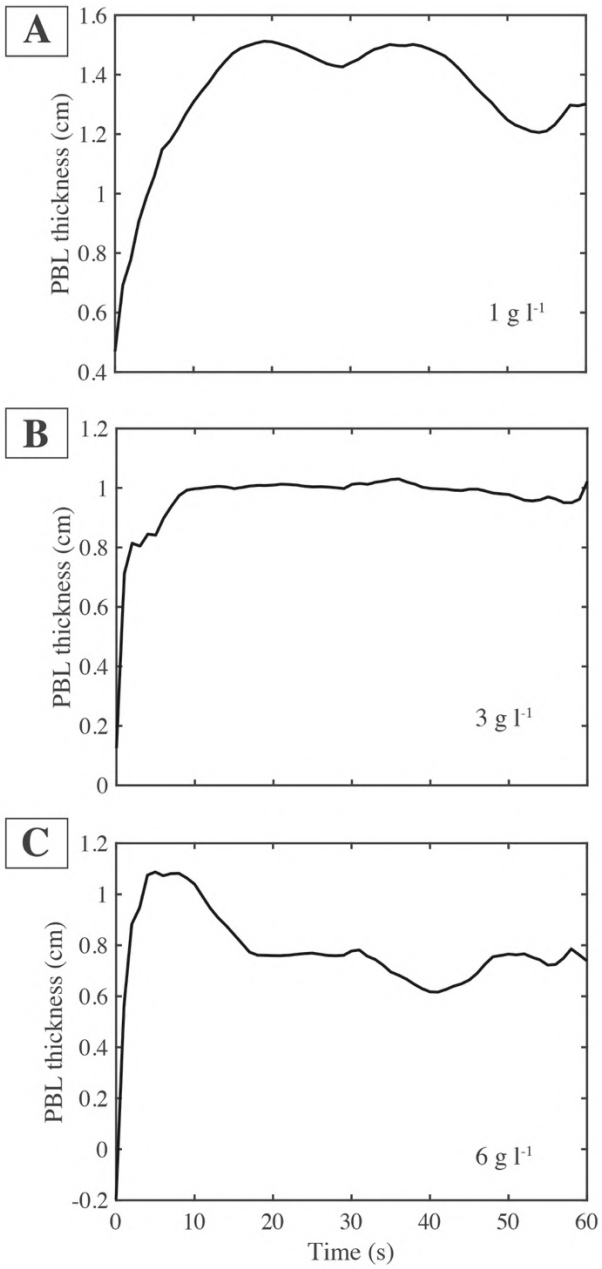

Figure A2.5: Automatic determination of the PBL thickness based on the localization of the minimum particle concentration gradient during experiment 1 (**A.** 1 g l^{-1}), 3 (**B.** 3 g l^{-1}), 6 (**C.** 6 g l^{-1})

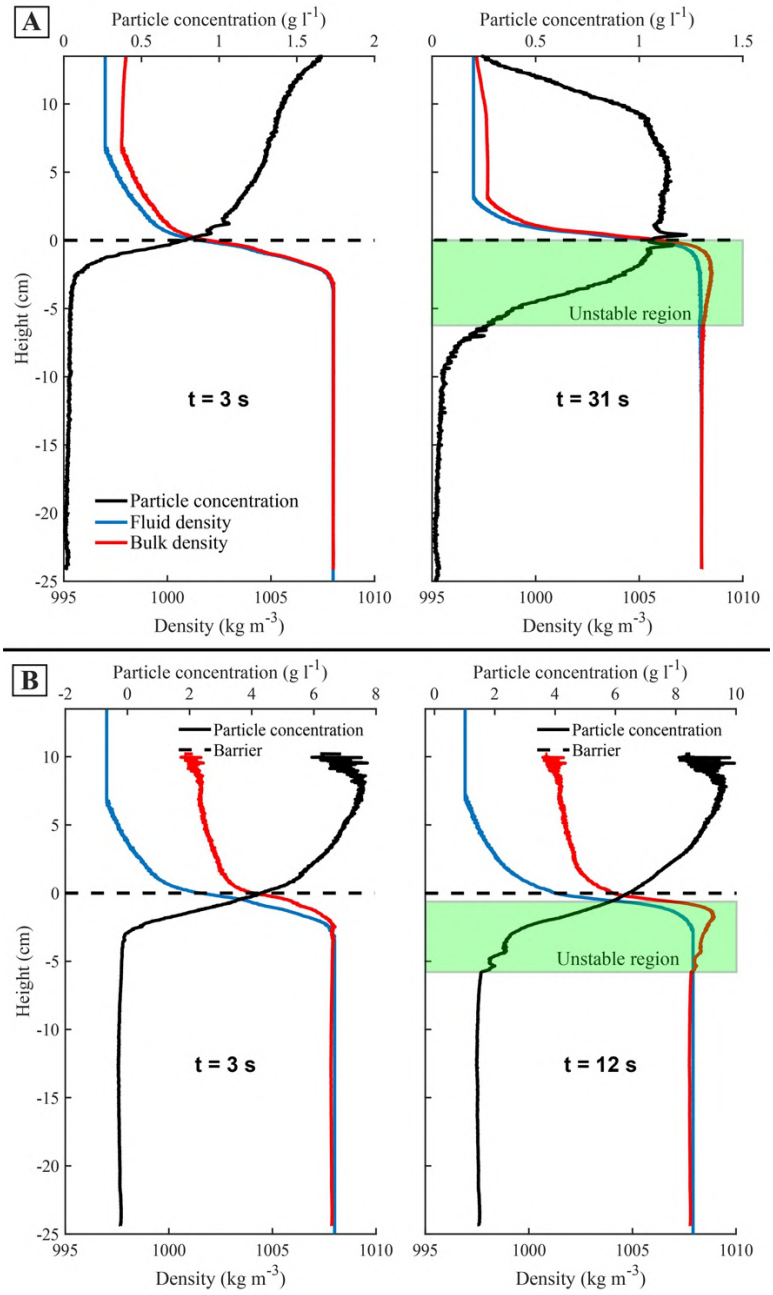

Figure A2.6: Horizontally averaged density and particle concentration profiles, with the fluid phase density in blue, the particle concentration in black (axis on the top) and the bulk mixture density in red. The initial position of the barrier is represented by the dashed lines. A dense unstable region highlighted in green develops below the interface after a certain time t. **(A)** 2 g l^{-1} experiment (small peaks in particle concentration are due to reflection of the laser sheet on the barrier) **(B)** 8 g l^{-1} experiment.

Supplementary Videos

Links to supplementary videos:

- Supplementary Video A2.1: https://archive-ouverte.unige.ch/unige:163115/ATTACHMENT04
- Supplementary Video A2.2: https://archive-ouverte.unige.ch/unige:163115/ATTACHMENT05
- Supplementary Video A2.3: https://archive-ouverte.unige.ch/unige:163115/ATTACHMENT06
- Supplementary Video A2.4: https://archive-ouverte.unige.ch/unige:163115/ATTACHMENT07
- Supplementary Video A2.5: https://archive-ouverte.unige.ch/unige:163115/ATTACHMENT08
- Supplementary Video A2.6: https://archive-ouverte.unige.ch/unige:163115/ATTACHMENT09

Chapter 3

Control of particle size and concentration on the onset of settling-driven gravitational instabilities at the base of volcanic clouds and resulting finger dynamics[1]

3.1 Introduction

Particle settling across the interface between a buoyant particle-laden fluid and a denser particle-free ambient can result in the formation of settling-driven gravitational instabilities (SDGIs) (Hoyal et al., 1999b; Manzella et al., 2015). Even if the configuration is originally gravitationally stable, mixing of particles and denser fluid below the initial density interface generate a narrow region of excess density (Burns and Meiburg, 2015; Davarpanah Jazi and Wells, 2020; Fries et al., 2021). This heavy particle boundary layer (PBL) develops under the base of the buoyant particle-laden fluid and detaches in the form of fingers (i.e., downward moving currents) within which particles collectively descend faster than individually. The formation of fingers from SDGIs consequently has the potential to enhance the sed-

[1]To be submitted to *Journal of Geophysical Research* as: Fries, A., Lemus, J., Jarvis, P. A., Clarke, A. B., Phillips, J. C., Manzella, I. and Bonadonna, C. : Control of particle size and concentration on the onset of settling-driven gravitational instabilities at the base of volcanic clouds and resulting finger dynamics.

imentation from buoyant particle suspensions and particle-laden flows in various geophysical settlings.

SDGI-driven fingers have been widely observed within volcanic ash clouds with significant implications for the vertical transport of fine ash in the atmosphere (Hobbs et al., 1991; Bonadonna et al., 2002b, 2011; Carazzo and Jellinek, 2012; Manzella et al., 2015; Scollo et al., 2017). Collective settling has also been observed to impact ash sedimentation at the ocean-atmosphere interface (Carey, 1997; Manville and Wilson, 2004; Jacobs et al., 2013). Even though particle aggregation has often been considered as the main collective settling process to reduce the residence of fine ash in the atmosphere (e.g., Costa et al., 2010; Rose and Durant, 2011; Brown et al., 2012), recent studies have demonstrated how SDGI-driven fingers have a similar potential. In fact, particle aggregation and SDGIs are expected to be closely linked, even though their interaction is still poorly characterised (e.g. Carazzo and Jellinek, 2012). Manzella et al. (2015) provided a rare quantitative description of the ash fingers formed during the 2010 eruption of Eyjafjallajökull (Iceland). They find that ash fingers descended at an average vertical velocity of about 1 m s^{-1}, which surpasses the terminal fall velocity of individual ash particles finer than 200 µm collected upon deposition on the ground. Ash fingers were found to impact in the same area of sedimentation as different types of particle aggregates (Manzella et al., 2015).

In recent decades, analogue experiments and numerical simulations have advanced our comprehension of the processes by which ash fingers can be generated. In fact, other mechanisms than SDGIs can also potentially result in fingering instabilities. This includes double diffusive instabilities that originate from the differential diffusion of two components that affect the fluid density (Green, 1987; Hoyal et al., 1999a; Carazzo and Jellinek, 2013). However, if the particle settling flux is significantly greater than that due to double diffusion, SDGIs are the dominant mechanism producing ash fingers (Hoyal et al., 1999b). Although both mechanisms could possibly coexist in natural settings (Carazzo and Jellinek, 2013; Carazzo et al., 2013), here we focus on SDGIs that are appropriate to describe ash sedimentation beneath volcanic clouds in thermal equilibrium with the atmosphere at the level

of neutral buoyancy and far from the source (Manzella et al., 2015; Scollo et al., 2017). Close to the source, the delivery of particles to the PBL can be modulated by mechanisms other than solely particle settling (Eliasson et al., 2016; Eliasson, 2020; Freret-Lorgeril et al., 2020; Gilchrist and Jellinek, 2021).

Improving the characterisation of ash fingers and defining the conditions in which they form is necessary in order to refine our understanding of fine ash sedimentation from volcanic clouds (Durant, 2015). In particular, whilst it is accepted that ash fingers are associated with small particle sizes and high particle concentrations (Carazzo and Jellinek, 2012; Scollo et al., 2017; Fries et al., 2021), the actual conditions for which ash fingers can develop remain uncertain. In addition, all experiments associated with SDGIs have been carried out in aqueous environments. As a result, all resulting characterisation is difficult to apply to natural volcanic clouds. In this work we extrapolate the experimental results to a real volcanic setting based on the field observations of Manzella et al. (2015) and theoretical analysis. Moreover, the detailed structure of individual fingers, as well as their evolution in time, has not been sufficiently described yet.

This contribution is motivated by two main objectives. First, we investigate the particle sizes and concentration associated with the formation of SDGIs and compare our results with existing criteria predicting the development of fingers, both in the experiments (water environment) and below volcanic ash clouds (air environment). Second, we describe the density configuration from which fingers originate with higher accuracy than previous experiments (Fries et al., 2021), and we provide detailed measurements of fingers physical properties using an innovative combination of Particle Imaging (PI), Planar Laser Induced Fluorescence (PLIF; Koochesfahani, 1984; Crimaldi, 2008) and Particle Image Velocimetry (PIV; Grant, 1997; Adrian, 2005). In particular, we characterise particle velocity within fingers through PI and PIV measurements and assess the associated coupling with fingers. Concentration and vorticity are also characterised to investigate the relation between SDGI-driven fingers and particle aggregation. Finally, we analyse the evolution of the fingers width with time that is quantified by the entrainment coefficient.

3.2 Background

3.2.1 Measures of the tendency for SDGIs to form

It has been shown that the development of fingers from SDGIs depends on the Grashof number Gr (Hoyal et al., 1999b), which represents the ratio between driving gravitational and retarding viscous forces. In simple analogue experiments making use of separate particle imaging and PLIF, Fries et al. (2021) have illustrated how SDGIs can arise from very small density differences. They report that fingers form when the PBL reaches a critical thickness

$$\delta = \left(\frac{Gr_c \nu^2}{g^{'}} \right)^{1/3}, \tag{3.1}$$

with $Gr_c = 10^4$ the critical Grashof number, ν the ambient fluid kinematic viscosity and g' the reduced gravity of the PBL defined as

$$g^{'} = \frac{(\rho_{PBL} - \rho_a)}{\rho_a} g, \tag{3.2}$$

where $g = 9.81$ m s^{-2} is the gravitational acceleration and ρ_{PBL} and ρ_a are the densities of the PBL and the ambient, respectively. The observed value of $Gr_c = 10^4$ is an order of magnitude larger than that used in previous characterisations of the onset of SDGIs, which was that $Gr_c = 10^3$ (Hoyal et al., 1999b), based on an analogy with the critical Rayleigh number above which thermal convection initiates. However, recent numerical simulations (Lemus et al., 2021) and experiments (Barnard, 2021) also point towards $Gr_c \approx 10^4$ for collective settling.

An additional necessary condition for the onset of SDGIs below particle-laden fluids of thickness H is that $L^* = H/\delta$ must be much greater than one. This means that only particle-laden fluid layers sufficiently thick to sustain a critically unstable PBL can produce SDGIs. Fries et al. (2021) find SDGIs develop for $L^* > 5$, whilst individual particle settling (IPS) dominates for $L^* < 2$. For $2 \leq L^* \leq 5$, a transitional regime exists where either SDGIs or IPS dominate, with higher particle concentrations associated with SDGIs.

The tendency of SDGIs to develop also depends on the particle size, as demon-

strated by analogue experiments (Scollo et al., 2017) and numerical simulations (Lemus et al., 2021) that have shown how only particles smaller than a threshold size are observed to settle collectively within fingers (size threshold in water is 125 µm for particle concentration of the order of 1 g l^{-1}). This observation is consistent with previous theoretical works, which consider that fingers can form only if the timescale over which individual particles settle is much greater than the onset of the instability. This criterion is expressed through the dimensionless number B_1 that corresponds to the ratio between the growth rate of the instability V_i and the settling velocity of individual particles V_p (Marsh, 1988; Carey, 1997; Fiske et al., 1998; Manville and Wilson, 2004; Carazzo and Jellinek, 2012; Jacobs et al., 2015)

$$B_1 = \frac{V_i}{V_p}. \tag{3.3}$$

Values of $B_1 \gg 1$ ensure that SDGIs can form before particles settle, whereas values of $B_1 \ll 1$ imply that IPS is much faster than the development of the instability, such that the latter is therefore inhibited. The growth rate of SDGIs has been estimated from the growth rate of Rayleigh-Taylor instabilities as (Whitehead and Luther, 1975; Carazzo and Jellinek, 2012)

$$V_i = \frac{(\rho_{PBL} - \rho_a)\, g\delta^2}{3\mu}, \tag{3.4}$$

with μ the ambient dynamic viscosity. We have used adapted settling laws for describing the sedimentation of particles as a function of the particle Reynolds number Re_p (Bonadonna et al., 1998). For high Re_p, the individual particle settling velocity is estimated as

$$V_p \approx \sqrt{\frac{3.1 g \rho_p}{\rho_a}}, (Re_p > 500). \tag{3.5}$$

At intermediate values of Re_p, the settling velocity is approximated by

$$V_p \approx d \left(\frac{4 g^2 \rho_p^2}{225 \mu \rho_a} \right)^{1/3}, (0.4 < Re_p < 500). \tag{3.6}$$

Low Re_p ($Re_p < 0.4$) particles are considered to settle at their Stokes velocity (equa-

tion 3.7)

$$V_p = \frac{gd^2\left(\rho_p - \rho_a\right)}{18\mu}, \tag{3.7}$$

with d and ρ_p the particle diameter and density, respectively.

Jacobs et al. (2015) have derived an alternative formulation of B_1 considering that instabilities develop if the timescale for collective settling is greater than the timescale for individual particle settling. In this formulation, the growth of the instability is controlled by the balance between gravitational forces and inertial drag rather than viscous drag. The timescale for collective settling τ_c is estimated from the late-time growth rate of Rayleigh-Taylor instabilities (Linden and Redondo, 1991; Ristorcelli and Clark, 2004):

$$\tau_c = \sqrt{\frac{\delta}{\beta A_{PBL} g}}, \tag{3.8}$$

where β is a dimensionless parameter that depends on the density ratio and A_{PBL} is the dimensionless Atwood number of the PBL defined as $A_{PBL} = (\rho_{PBL} - \rho_a)/(\rho_{PBL} + \rho_a)$. Here we take $\beta = 0.03$, in the range of values estimated by experimental and numerical investigations (Linden and Redondo, 1991; Dimonte et al., 2004; Jacobs et al., 2015). The ratio of these two timescales yields the dimensionless number B_2 that can be written

$$B_2 = \frac{\tau_i}{\tau_c}, \tag{3.9}$$

with τ_i the timescale for individual particle settling. The tendency of fingers to exclusively affect fine particles also demonstrates that fingers can form and persist only if the particles and the flow are sufficiently coupled, i.e., if the characteristic velocity of laminar fingers, V_f, defined from the mass and buoyancy flux as

$$V_f = g^{'\left(\frac{2}{5}\right)} \left(\frac{\pi V_p \delta^2}{4}\right)^{1/5}, \tag{3.10}$$

is much greater than the individual settling velocity of the particles V_p (Hoyal et al., 1999b). It is, therefore, possible to define another dimensionless number character-

ising the formation of SDGIs

$$B_3 = \frac{V_f}{V_p}. \tag{3.11}$$

The dimensionless numbers B_1, B_2 and B_3 described here are all defined as a ratio between a characteristic velocity, or timescale, of SDGIs (or resulting fingers) and the individual particle velocity. They, therefore, all share similarities. Values much greater than one are favourable for the development of SDGIs, whilst IPS dominates for values lower than unity. For particles settling at their Stokes velocity, they are all inversely proportional to the particle diameter raised to an exponent ~ 2. Significant differences between B_1, B_2 and B_3 arise from the dependence of the growth rate of the instability (or the velocity of resulting fingers) on the particle concentration that has an influence on the density of the PBL and, consequently, on the reduced gravity, the thickness of the PBL and the Atwood number. Although B_1, B_2 and B_3 all quantify the tendency for SDGIs to develop, they have subtly different physical meanings. B_1 quantifies if the growth rate of SDGIs controlled by the balance between gravitational and viscous forces is greater than the velocity of individually settling particles, whilst B_2 assesses if the growth rate of SDGIs controlled by the balance between gravitational forces and inertial drag is greater than the timescale over which particles settle from the particle suspension (Jacobs et al., 2015). B_1 and B_2 therefore represent similar numbers, with the growth of SDGIs slowed by either viscous (B_1) or inertial (B_2) forces. Separately, B_3 quantifies if particles are sufficiently coupled with the flow for fingers to form (Hoyal et al., 1999b). Hence, despite the analogies existing between B_1, B_2 and B_3, these numbers are independent and target different aspects of the onset of instabilities. B_1 and B_2 are relevant for different physical regimes, but B_3 is a complementary number that can be combined with both B_1 and B_2 for assessing the conditions for the onset of SDGIs and fingers.

In recent work, Lemus et al. (2021) used numerical modelling to study the formation of fingers in an aqueous environment with small density differences between the particle-laden fluid and the underlying dense ambient that reproduces the experiments of Manzella et al. (2015), Scollo et al. (2017) and Fries et al. (2021). Varying the particle size in their simulations, they find that fingers only form for particle diameters where $V_f > V_p$. Their results, therefore, agree with the formulation of

B_3, with the additional detail that fingers resulting from SDGIs can form even if V_f is only greater (rather than much greater) than V_p; i.e., $B_3 > 1$. Here we aim to test the existing criteria for the development of SDGIs in water and scale our results to natural volcanic ash clouds. To do so, we compare the values of the above dimensionless numbers B_1, B_2 and B_3 (equations 3.1, 3.9 and 3.11) with observations of the conditions under which SDGIs initiate in simple analogue experiments during which we vary the particle concentration and size. B_1, B_2 and B_3 are then calculated for volcanic ash clouds in order to evaluate the possibility of SDGIs and ash fingers to occur.

3.2.2 Coupling between particles and the flow within fingers

The behaviour of particles within fingers and the complex interactions between particles and the fluid phase can be characterised by the combination of the Reynolds (Re), Stokes (St) and sedimentation (Σ) numbers (Burgisser et al., 2005). For fingers, these dimensionless numbers are defined as (Burgisser et al., 2005; Burgisser and Bergantz, 2002; Carazzo and Jellinek, 2012)

$$Re = \frac{V_f \delta}{\nu}, \tag{3.12}$$

$$St = \frac{(\rho_p - \rho_a) d^2 V_f}{18 f \mu \delta}, \tag{3.13}$$

and

$$\Sigma = \frac{(\rho_p - \rho_a) d^2 g}{18 f \mu V_f} = \frac{V_p}{V_f} = \frac{1}{B_3}, \tag{3.14}$$

with f the drag factor approximately equal to 1 for our experimental conditions (Fries et al., 2021). V_f and δ are respectively chosen as the characteristic velocity and length scales of the flow (and of its fluctuations).

Re, i.e., the ratio of inertial over viscous forces in the flow, indicates the fluid dynamical regime of the flow. The flow is fully turbulent if $Re \geq 10^4$, transitional for $1 < Re < 10^4$ and laminar for $Re \leq 1$. St corresponds to the ratio of the particle response time over the time scale of the flow motion (i.e., the balance between the inertial and viscous forces on a particle) and Σ is the balance between gravity and

viscous forces applied on a particle (Roche and Carazzo, 2019). Particles with $St > 1$ are decoupled from the fluid phase, increasing the turbulence intensity of the flow, whilst $St < 1$ indicates that particles are dynamically coupled with the fluid phase and tend to reduce the turbulence intensity of the flow (Burgisser et al., 2005). The settling of particles is governed by gravity for $\Sigma > 1$ and controlled by the flow motion for $\Sigma < 1$. For fingers, the definition of B_3 (equation 3.11) corresponds to the reciprocal of Σ (equation 3.14). The formation of fingers from SDGIs is therefore favoured for $\Sigma < 1$ and inhibited for $\Sigma > 1$.

The combination of St and Σ quantifies the complete dynamic behaviour of particles within fingers (Burgisser et al., 2005; Carazzo and Jellinek, 2012; Roche and Carazzo, 2019). For $St < 1$ and $\Sigma < 1$, there is a strong coupling between the particles and the fluid phase, and particles are well mixed within the flow, whereas particles are decoupled from the fluid phase and settle for $St > 1$ and $\Sigma > 1$. A strong two-way coupling between the fluid phase and particles develops for $St \approx 1$ and $\Sigma \approx 1$, $St < 1$ and $\Sigma > 1$, or $St > 1$ and $\Sigma < 1$. This can create transient particle gathering and the formation of mesoscale structures with higher particle concentrations (Burgisser et al., 2005; Carazzo and Jellinek, 2012). In our experiments, we therefore quantify both St and Σ in order to assess the coupling of particles and the flow within fingers.

3.2.3 Structure and physical characterisation of fingers

Once SDGIs are initiated, fingers start to propagate underneath the particle-laden fluid. In confined environments, layer-scale convection starts shortly after the intrusion of the first fingers and induces mixing in the layer underneath the particle-laden fluid (Hoyal et al., 1999b; Manzella et al., 2015). Whilst the evolution of fingers during the late layer-scale convection stage partially depends on the dimensions of the system (i.e., the thicknesses of the particle-laden layer and of the ambient; Lemus et al., 2021), the properties of fingers formed initially are principally controlled by the characteristics of the particles and the initial density configuration. Equations (3.1) and (3.10), that respectively describe the characteristic size and velocity of fingers, have been validated against measurements of the size and the front velocity

of fingers in experiments (Scollo et al., 2017; Fries et al., 2021) and numerical simulations (Lemus et al., 2021). The results suggest that the size of fingers is proportional to the thickness of the PBL from which they originate by detachment. The size and velocity of fingers is, therefore, related to the density difference between the PBL (that depends on the particle concentration) and the underlying ambient. Hence, by analogy with thermal convection (Turner, 1973), it has been measured that the characteristic size of ash fingers varies as $\delta \propto g'^{-1/3}$, with the finger size diminishing with increasing particle concentrations (Hoyal et al., 1999b; Fries et al., 2021).

It has been postulated in previous studies on SDGIs that the particle concentration increases in the PBL and fingers with respect to the initial concentration within the particle suspension (Carazzo and Jellinek, 2012; Manzella et al., 2015; Scollo et al., 2017). Although this is certainly the case when the density and/or viscosity difference between the particle suspension and the ambient is high enough to considerably hinder the settling of particles at the interface (such as fingers formed below the air/water interface; Carey, 1997; Manville and Wilson, 2004), the experimental measurements of Fries et al. (2021) and the numerical simulations of Lemus et al. (2021) reveal that the particle concentration in the PBL does not increase when the differences in density and viscosity are small. The PBL becomes heavier than the fluid below when dense particles settle on top of the dense underlying ambient, adding their contribution to the mixture density (Fries et al., 2021; Lemus et al., 2021). However, the particle concentration and density within fingers has not been accurately constrained in experiments yet, despite its relevance for the sedimentation of particles in natural systems, and notably below volcanic ash clouds. In fact, besides its importance for the formation of ash fingers, the particle concentration is also one of the main factor influencing particle aggregation (Rose and Durant, 2011; Brown et al., 2012; Durant and Brown, 2016), i.e., another major process enhancing the sedimentation of volcanic ash by increasing the associated terminal fall velocity due to particles binding into larger aggregates. Manzella et al. (2015) reported, during the 2010 eruption of Eyjafjallajökull, that ash fingers reached the ground at a distance also characterised by the occurrence of volcanic ash aggregates, highlighting that the two phenomena (i.e., formation of fingers and aggregation) can

happen conjointly. This observation additionally suggests that aggregation could occur within ash fingers, as the particle concentration may increase, leading to higher probabilities of particle collisions.

The PBL can be described as analogous to a thermal boundary layer by further comparing SDGIs with thermal convection, and fingers that form are accordingly analogous to thermals detaching from the boundary layer. This analogy has been explored by several authors that studied the behaviour of sediment thermals (Rahimipour and Wilkinson, 1992; Ruggaber, 2000; Bush et al., 2003; Zhao et al., 2014; Freret-Lorgeril et al., 2020); i.e., thermal-like particle clouds formed by the rapid release of dense particles into a fluid. The particle clouds follow three stages of motion according to Rahimipour and Wilkinson (1992). Particles first accelerate as a solid body in an initial acceleration phase. The behaviour and structure of particle clouds then become similar to that of thermals, with strong internal circulation and characteristic vortex ring structures. This is in line with the observations of Scollo et al. (2017) who used PIV measurements to observe the creation of vortices during finger propagation across the initial density interface. During this self-preserving phase, it can be assumed that the sediment thermals reach a state of self-similarity in which all lengths are in proportion (Ruggaber, 2000). Thermals gradually increase in size and decelerate due to turbulent entrainment. The internal circulation ultimately ceased during the dispersive phase, as the velocity of the sediment thermal approaches that of individually settling particles. Fingers resulting from SDGIs share similarities with sediment thermals. However, contrarily to fingers produced by SDGIs, previously-studied sediment thermals have initial densities much higher than that of the ambient fluid, as groups of closely packed dense particles are instantaneously released in a fluid medium.

3.3 Methods

3.3.1 Experimental set-up

We perform experiments in a simple experimental configuration that involves an isothermal water tank $30.1 \times 30.1 \times 50.0$ cm^3 divided horizontally, by a removable

barrier, into an upper particle suspension and a lower, denser sugar solution with constant thicknesses of 13.5 and 25.0 cm, respectively (Figure 3.1A). In this configuration, the two layers are static, with no motion in between them. Similarly to previous studies that have used the same experimental apparatus (Manzella et al., 2015; Scollo et al., 2017; Fries et al., 2021), the length of the water tank is limited to 7.5 cm with rigid vertical separations in order to attenuate the vorticity generated at the back of the water tank upon the removal of the barrier. All experiments are performed at room temperature. The upper particle suspension is composed of a buoyant mixture of glass spheres and fresh water, whilst the lower layer has a constant density of 1008 kg m^{-3}, attained with a sugar concentration of 29 g l^{-1}. The density of the lower layer is always greater than the density of the particle suspension, which results in an initially gravitationally-stable configuration. Before the start of an experiment, particles are manually dispersed in the upper layer with an agitator until a homogeneous particle concentration C_u is attained. The experiments begin ($t = 0$ s) with the manual removal of the barrier that allows particles to settle across the initial density interface into the top of the lower layer. As described in the experiments of Fries et al. (2021), and as reported in most similar setups (Linden and Redondo, 1991; Dalziel, 1993), a major experimental issue with the start of the experiments is that a perturbation of the interface is initially generated when removing the barrier, affecting the early stage (first 10 s) of the experiments.

The experiments are scaled to represent an analogue volcanic ash cloud (i.e., the upper particle suspension) emplaced at the level of neutral buoyancy over a dense atmosphere (i.e., the lower sugar solution). Readers can refer to the work of Fries et al. (2021) for a complete scaling analysis (Chapter 2.2.2). The most important dimensionless numbers involved in scaling this problem are the Reynolds (Re), Atwood (A_u), Grashof (Gr), Stokes (St) and sedimentation (Σ) numbers that respectively characterise the flow behaviour, the density ratio between the upper and lower layers, the balance of gravitational over viscous forces, and the degree of coupling between the particles and the fluid phase (St and Σ). In both experiments and natural volcanic clouds, the flows are controlled by inertia (i.e., $Re > 1$), although Re is typically much greater in the natural system than experiments, signifying a

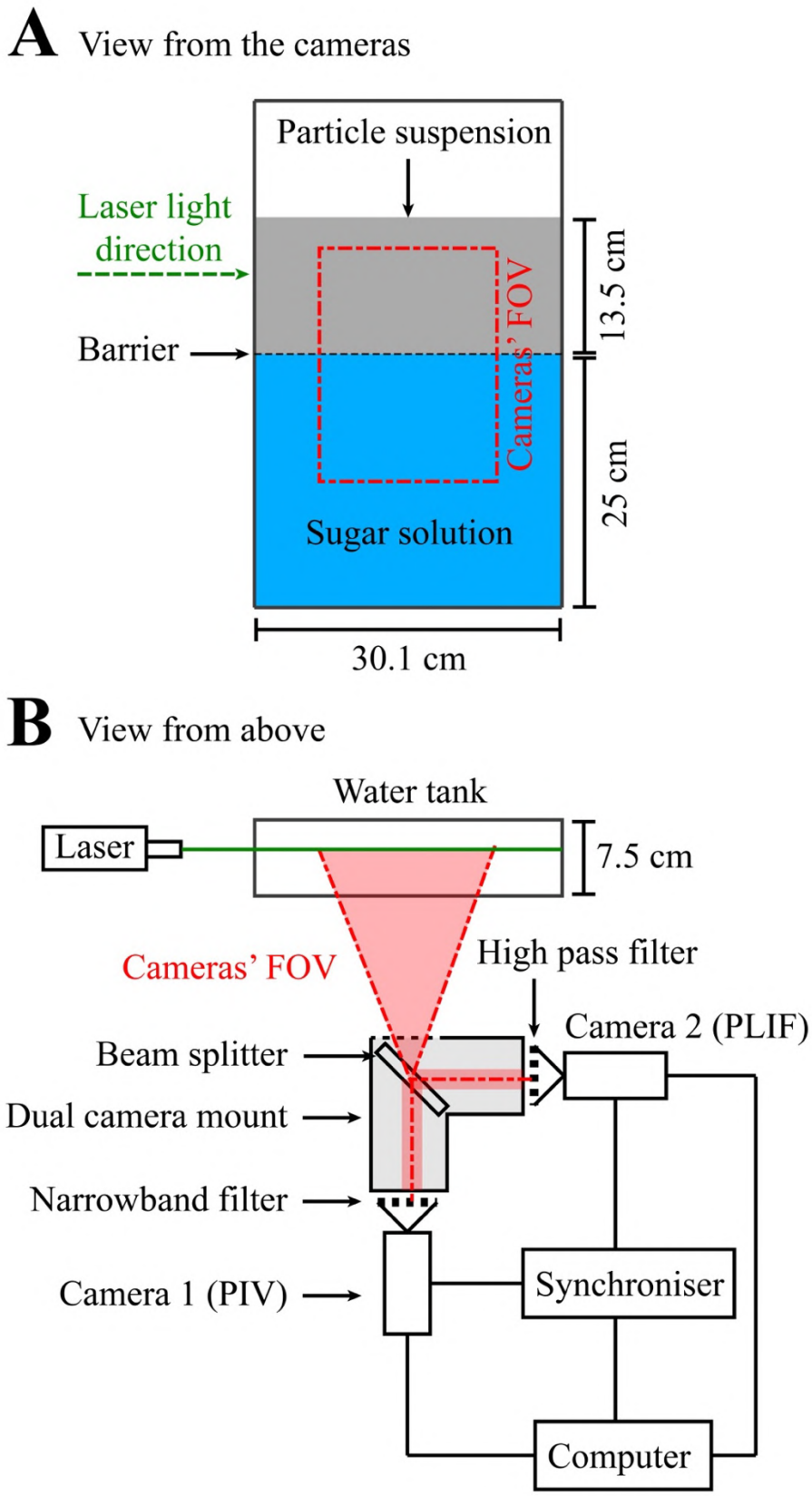

Figure 3.1: Sketch of the experimental set up. **A.** View from the cameras. **B.** View from above. In both sketches, the fields of view (FOV) of the cameras is illustrated by the red area that is 22.8×17.4 cm^2

greater degree of turbulence. In fact, whilst natural fingers are fully turbulent ($Re \geq 10^4$; Fries et al., 2021), the experimental fingers are in the transitional regime ($Re \approx 10^2$). A_u is $\ll 1$ in all configurations, as the density difference between the two layers is very small in both nature and in experiments. We find values of Gr greater than the critical Grashof number for the initiation of SDGIs ($Gr_c = 10^4$) in volcanic clouds and their analogues. Finally, for experiments where SDGIs form (i.e., for the fine particle sizes and high particle concentrations), St and Σ are both < 1 in the natural and experimental fingers. As discussed above in *Section 3.2.2*, this implies that particles are strongly coupled with the fluid (Burgisser et al., 2005; Carazzo and Jellinek, 2012).

3.3.2 Imaging techniques

Our experiments are illuminated from the side of the water tank with a continuous 532 nm Nd:YAG planar laser (Coherent Genesis CS-SLM) at a constant power of 1 W. Two sCMOS cameras (HiSense Zyla by Dantec Dynamics) are used to acquire image pairs at a frame rate of 4 Hz and with a pixel depth of 16 bits, with an interval of 20 ms between pair images. Both cameras are equipped with Nikon Nikkor 35 mm f/2D lenses. Our experimental setup is designed to simultaneously image both the particles and the fluid phase. To do so, one camera is fitted with a narrow band filter centred around the wavelength of the laser to isolate the light scattered by the particles, whilst the other camera is equipped with a high-pass filter at 570 µm that obstructs the primary laser wavelengths and, thus, the light scattered by the particles. Moreover, in order to combine the results of the two cameras, it is crucial to ensure that they capture the same spatial field of view (FOV) (Borg et al., 2001) and that their acquisition is synchronised. Both cameras are therefore mounted on a Dantec Dynamics dual camera mount, which uses a beam splitter (i.e., a partially-silvered mirror) to present identical FOVs to both cameras. For both cameras, 1600 × 2100 pixel images have been acquired, covering the centre of the experimental water tank as shown in Figure 3.1A, at a resolution of 92 px mm^{-1}. The two cameras are synchronised within a maximum of 10 µs by a BNC 575 synchroniser. Figure 3.1B schematically illustrates the setup employed for imaging

the experiments.

Images captured by the first camera, which detect the light scattered by particles, are used for PIV analysis, described below (in Section 3.3.4) and for determining the local particle concentration in the experiments. In order to measure the latter, we use a calibration identical to that of Fries et al. (2021), that is based on a linear relation between the particle concentration C and the pixel digital level (i.e., the pixel brightness). To determine the calibration, we perform a set of calibration experiments where, first, the water tank is filled with a uniform particle concentration ranging from 0 to 3 g l^{-1}, at 0.5 g l^{-1} concentration steps. Second, calibration images are acquired and averaged over 10 s. Finally, we perform a linear regression between the known particle concentration and the pixel digital level for each pixel. However, the quality of this regression is found to decrease with distance from the laser (Figure 3.2A). In later analysis, we therefore estimate C only in pixels with a coefficient of determination $R > 0.95$.

The density of the fluid phase is assessed independently, but simultaneously, with the second camera. We apply the PLIF imaging technique in order to measure the density of the fluid phase at high resolution. This is based on the linear relation between the concentration of a fluorescent dye (here Rhodamine 6G; R6G) and the pixel digital level. In our case, R6G is only added in the particle suspension in order to trace the fluid phase of the upper layer and measure its proportion in the tank (Linden and Redondo, 1991; Dossmann et al., 2016; Fries et al., 2021). Because the upper and the lower layer fluids have different densities, it is, therefore, possible to infer the fluid phase density from PLIF measurements in any pixel, in both the upper and lower layers. R6G has a peak fluorescence wavelength between 560 and 580 nm (Zehentbauer et al., 2014). The camera is, therefore, equipped with the high-pass filter at 570 nm that is sensitive to the fluorescent emission from R6G, whilst the primary laser light and scattering from the particles is filtered out. Quantitative PLIF measurements necessitate a prior calibration that relates the fluorescent dye concentration D to the pixel digital level (i.e., to the fluorescence intensity F). Similarly to the particle concentration calibration, the PLIF calibration is performed by filling the tank with fluid of a uniform R6G concentration. Images are averaged

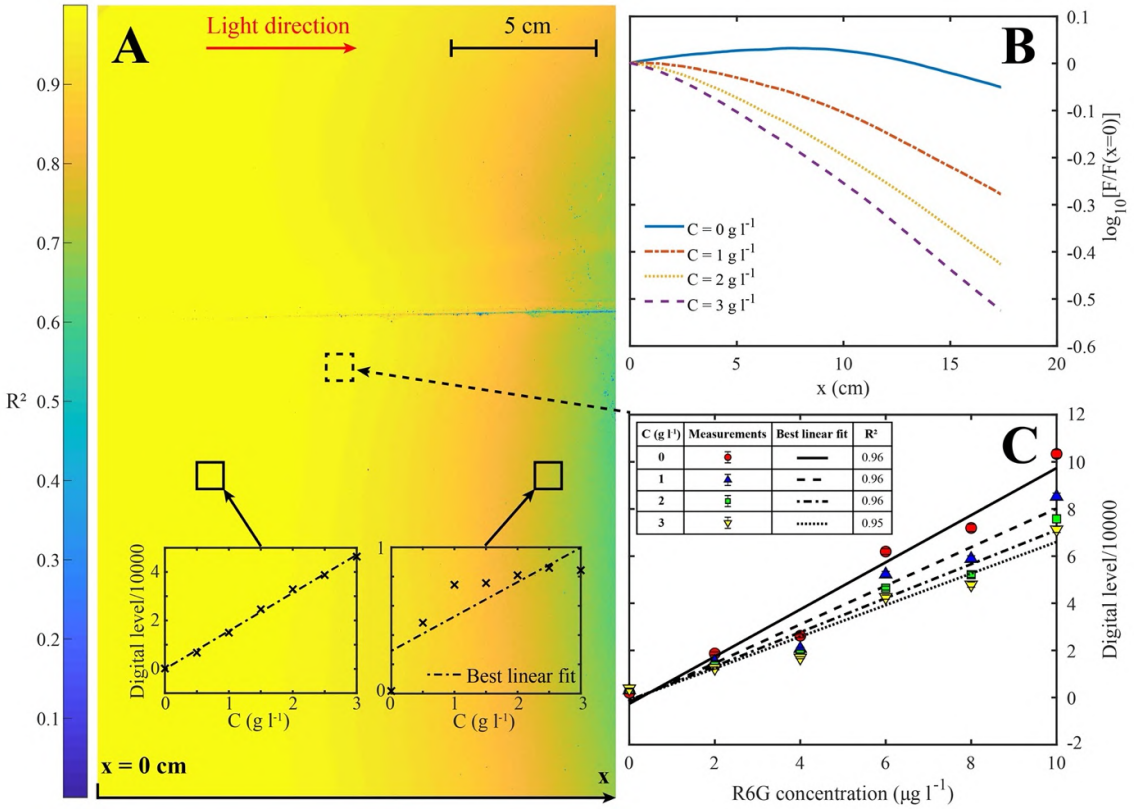

Figure 3.2: **A.** Variation in the quality of the linear relation for PI, quantified through the coefficient of determination R^2, between the particle concentration C and the pixel digital level. The insets show the calibration of two individual pixels: close to the tank wall (i.e., the light source) on the left there is a good linear regression between C and the pixel digital level whilst this is not the case further from the light source. The squares indicate the region in which the pixels presented in the insets are located. **B.** Spatial variation in the vertically averaged fluorescence intensity F received by the sensor of the camera for different particle concentrations. **C.** Calibration of the PLIF imaging technique for an individual pixel (located in the region within the dashed square) and different particle concentrations.

over 10 s and, for each pixel, we perform a linear regression between D and F. The quality of the linear regressions is good throughout the entire tank, with an $R > 0.95$, in contrast to the calibration for the particle concentration. However, adding particles to the fluid doped with R6G has a clear attenuation effect on the spatial distribution of F (Figure 3.2B) due to the additional interactions between the particles and the laser light. At a given distance x from the wall of the tank through which the laser light arrives, higher values of C are associated with lower values of F. Hence, we calibrate the PLIF measurements for the particle concentrations used in the experiments; i.e., from 0 to 3 g l^{-1}, with 1 g l^{-1} steps (Figure 3.2C).

For both the determination of the particle concentration and PLIF measurements, it is important to mention that the calibrations are performed with homogeneous particle and R6G concentrations that are uniformly distributed in the entire experimental tank. In subsequent experiments, the initial configuration differs from calibrations, as only the upper layer initially contains particles and R6G. Moreover, the concentrations of particles and R6G are not homogeneous throughout the entire duration of the experiments. These differences lead to subtle changes in the pixel digital level recorded by the cameras and, therefore, to uncertainties in the estimation of both the particle concentration and PLIF measurements.

3.3.3 Experimental conditions

The experiments are divided into two types. In the first type of experiments (experiments E1-E16; Table 3.1), we have investigated the triggering conditions for SDGIs. In particular, we have varied both the particle concentration and the particle size in order to address the conditions favourable for the occurrence of SDGIs and compare these results with the values of B_1, B_2 and B_3. We select a wide range of parameters for complementing the conditions explored in previous works (Scollo et al., 2017; Fries et al., 2021). During these experiments, we only image the particles (Particle Images – PI; Table 3.1) to observe their settling behaviour (i.e., individual or collective sedimentation), and we do not apply PIV analysis, nor the PLIF imaging technique.

The second type of experiments (experiments D1 – D3; Table 3.1) makes use

Exp. number	C_u (g/l)	X_p × 10^{-4}	D_{10} (µm)	D_{50} (µm)	D_{90} (µm)	L^*	B_1	B_2	B_3	St	Σ	Type of sedim.	Number of repeats	Imaging techniques
Triggering of SDGIs														
E1	0.01	0.04	21.0	30.1	45.0	2	81	0.7	0.9	10^{-6}	1.1	IPS	1	PI
E2	0.05	0.2	21.0	30.1	45.0	4	139	2.1	2.9	10^{-5}	0.3	SDGIs	1	PI
E3	0.5	2	23.6	40.7	64.8	9	163	5.3	3.3	10^{-4}	0.3	SDGIs	1	PI
E4	0.5	2	61.6	87.3	124.4	9	36	1.2	1.0	10^{-4}	1.0	IPS	1	PI
E5	0.5	2	76.1	108.7	153.8	9	23	0.8	0.7	10^{-3}	1.4	IPS	1	PI
E6	1	4	61.6	87.3	124.4	11	45	1.8	1.2	10^{-3}	0.8	SDGIs	1	PI
E7	1	4	76.1	108.7	153.8	11	29	1.2	0.8	10^{-3}	1.2	SDGIs	1	PI
E8	1	4	102.9	143.5	201.0	11	17	0.7	0.5	10^{-3}	2.0	IPS	1	PI
E9	2	8	61.6	87.3	124.4	14	56	2.9	1.4	10^{-3}	0.7	SDGIs	1	PI
E10	2	8	76.1	108.7	153.8	14	36	1.9	1.0	10^{-3}	1.0	SDGIs	1	PI
E11	2	8	102.9	143.5	201.0	14	21	1.1	0.6	10^{-3}	1.7	IPS	1	PI
E12	3	12	61.6	87.3	124.4	16	65	3.8	1.6	10^{-3}	0.6	SDGIs	1	PI
E13	3	12	76.1	108.7	153.8	16	42	2.5	1.1	10^{-3}	0.9	SDGIs	1	PI
E14	3	12	102.9	143.5	201.0	16	24	1.4	0.7	10^{-3}	1.4	SDGIs	1	PI
E15	3	12	152.0	238.6	336.6	16	9	0.5	0.3	10^{-2}	3.3	IPS	1	PI
E16	12	48	152.9	230.1	312.7	26	15	1.4	0.5	10^{-2}	2.0	IPS	1	PI
Fingers characteristics														
D1	1	4	23.6	40.7	64.8	11	206	8.5	4.1	10^{-4}	0.2	SDGIs	7	PI, PIV & PLIF
D2	2	8	23.6	40.7	64.8	14	259	13.4	4.9	10^{-4}	0.2	SDGIs	7	PI, PIV & PLIF
D3	3	12	23.6	40.7	64.8	16	297	17.6	5.4	10^{-4}	0.2	SDGIs	8	PI, PIV & PLIF

Table 3.1: List of experiments. We have varied both the initial particle concentration of the upper layer C_u (i.e., the particle volume fraction X_p) and the size of the particles, here characterised by the median diameter D_{50} and the 10^{th} and 90^{th} percentiles of the distributions D_{10} and D_{90}, respectively . The dimensionless numbers L^*, B_1, B_2 and B_3 that quantify the tendency to develop fingers are calculated for the experiments, as well as St and Σ that quantify the coupling between the flow and particles. We distinguish between experiments associated with settling-driven gravitational instabilities (SDGIs) and individual particle settling (IPS). The imaging techniques applied are particle imaging (PI), particle image velocimetry (PIV) and planar laser induced fluorescence (PLIF).

of a complete set of imaging techniques applied simultaneously with the aim of describing SDGIs and the resulting fingers in detail. We image the particles (PI) and additionally use the PIV technique for obtaining the particle velocity field and PLIF measurements for analysing the properties of the fluid phase (Table 3.1). In order to apply the PLIF imaging technique, the upper layer in the second type of experiments is dyed with a uniform R6G concentration of $D_u = 8$ µg l^{-1}. Only one particle size fraction (median diameter, D_{50}, of 40.7 µm) is used in these experiments over a narrow range of particle concentrations of 1, 2 and 3 g l^{-1}. These experiments are repeated at least 7 times in order to increase the number of individual fingers that can be studied. The detailed list of experimental conditions is given in Table 3.1. All experiments are performed in the same experimental configuration (Figure 3.1) and imaged for at least 120 s after the removal of the horizontal barrier that marks the start of the experiments.

In both types of experiments, the particles are spherical glass beads with a density ρ_p of 2519.2 ± 0.1 kg m^{-3} measured with a Helium pycnometer (Ultrapic 1200e). Different particle classes with unimodal grainsize distributions have been obtained by sieving. The grainsize distributions of the particle classes are obtained by laser diffraction using a BetterSizer S3 Plus. They are described by the median diameter D_{50} and the 10^{th} and 90^{th} percentiles of the grainsize distribution D_{10} and D_{84}, respectively. The main parameters describing the different particle classes are given in Table 3.1.

3.3.4 Data analysis

For the first type of experiments, we use the images to determine the settling mechanisms of the particles leaving the particle suspension. In our experiments, which involve slowly diffusing substances, i.e., where the formation of fingers is triggered by SDGIs rather than by double-diffusive effects (see Fries et al., 2021for a more complete analysis), the presence of fingers is considered as the evidence of the onset of SDGIs. Fingers are identified based on visual observations of downward moving particle-laden plumes and on the tendency of fingers to initiate layer-scale convection in the lower layer (Hoyal et al., 1999b; Manzella et al., 2015; Lemus et al., 2021).

The second type of experiments makes use of a more complete set of imaging techniques and, consequently, of more advanced analysis. For each pixel, we calculate the concentration of upper fluid X_f from D and D_u

$$X_f = \frac{D}{D_u}. \tag{3.15}$$

The density of the fluid phase ρ_f in a given pixel can therefore be inferred from X_f, the density of fresh water $\rho_w = 997$ kg m^{-3}, that initially constitutes the fluid phase of the upper layer, and the density of the underlying sugar solution ρ_s

$$\rho_f = X_f \rho_w + (1 - X_f)\, \rho_s. \tag{3.16}$$

Simultaneously, we obtain the particle concentration from the calibration described in Section 3.3.2. Hence, it is possible to calculate the bulk mixture density ρ_m from the particle volume fraction $X_p = C/\rho_p$ as

$$\rho_m = X_p \rho_p + (1 - X_p)\, \rho_f. \tag{3.17}$$

Additionally, we use the images of the particles for PIV analysis (Grant, 1997; Adrian, 2005), performed with the Dantec Dynamic Studio Software using the built-in Adaptive PIV algorithm. The PIV technique provides an estimation of the particle velocity field based on the cross-correlation of a defined interrogation area (IA) between two pair images. Similarly to Scollo et al. (2017), we use an adaptive PIV iterative process that progressively diminishes the size of the IAs from 64 $\times$ 64 to 16 $\times$ 16 pixels. It should be noted that we are using PIV to obtain the velocity field of the dense, dispersed particle phase, which differs from its typical application that involves using neutrally buoyant particles to quantify the velocity field of a fluid (Hassan et al., 2020).

The particle velocity field obtained with the PIV analysis is extracted from the Dynamic Studio software and treated separately. For our 2D data, we calculate the component of the vorticity perpendicular to the laser plane (i.e., the plane on which

the particles are imaged) as

$$\omega = \frac{\partial V}{\partial x} - \frac{\partial U}{\partial z}, \tag{3.18}$$

with x and U the horizontal position and velocity, respectively, and z and V their vertical counterparts. Vorticity is constrained as an indication of the potential of particles to collide within fingers, and, therefore, to enhance particle aggregation (Scollo et al., 2017). Turbulent flows generate eddies with sizes comprised between the characteristic scale of the flow down to the Kolmogorov length scale (Burgisser et al., 2005) and are, therefore, associated with non-zero, fluctuating ω (Scollo et al., 2017). Here, ω is used to quantify the vortical motion of particles within and around fingers (i.e., the direction and strength of vortices). In our experiment, we assess ω at the scale of individual fingers in order to document their structure; broader measurements of ω have been performed by Scollo et al. (2017) across the initial density interface. The absolute value of ω scales with the local angular rate of rotation in the flow and its sign indicates the sense of rotation. With our system of coordinates clockwise rotations are characterised by positive values of ω. Whilst fingers are 3D structures, we are not able to estimate the other components of the vorticity in this setup. However, as fingers essentially propagate downward in the z direction, and seemingly have an axisymmetric geometry (Yu et al., 2014), we consider that we are able to document the most significant flow dynamics with the planar velocity field (Scollo et al., 2017).

From our second set of experiments, we have selected 16 individual fingers for further, more detailed, analysis (Table 3.2). The properties of fingers (i.e., the particle and fluid concentration, the mixture density and the velocity field) are averaged for time intervals varying from 10 to 21 s, which correspond to the durations between the formation of a finger and the onset of strong horizontal motions. In fact, we choose to analyse fingers that propagate in the vertical direction, without being significantly affected by horizontal displacements generated by the convection in the lower layer. These fingers are continuously fed particles from the upper layer before completely detaching from the PBL. As such, the growing fingers can be modelled either as negatively-buoyant starting plumes or sediment thermals (Turner, 1962; Bush et al., 2003; Zhao et al., 2014; Freret-Lorgeril et al., 2020). An important

quantity that describes the evolution of such flows is the entrainment coefficient that corresponds to the ratio U_e/V_c, where U_e is the radial entrainment velocity inside the thermal and V_c the centreline vertical velocity (Morton et al., 1956). For thermals, the entrainment coefficient α_e corresponds to the mean slope of half-spread

$$\alpha_e = \frac{r}{h}, \tag{3.19}$$

with r the radius and h the height of the thermal (Morton et al., 1956; Turner, 1962, 1969; Peñas et al., 2021). The finger geometry is estimated from time-averaged images (Figure 3.3). First, we select the background image that corresponds to the time before the finger starts to propagate below the particle suspension (Figure 3.3A). Second, the background is subtracted from images with developing fingers (Figure 3.3B,C). Third, images of fingers are time-averaged (Figure 3.3D) and binarized, considering a threshold digital level that corresponds to 2.5 % of the maximum pixel digital level of the time-averaged image (Figure 3.3E). Finally, r and h are measured on the binary image, by manually tracing the edge of the finger (Figure 3.3F).

3.4 Results

3.4.1 Onset of SDGIs

Particles in our experiments are all characterised by $St < 1$ (Table 3.1), suggesting that they are dynamically coupled with the fluid phase. The value of Σ, therefore, determines the behaviour of particles with respect to the flow within fingers. $\Sigma < 1$ (and $St < 1$) is associated with the formation of SDGIs. In this case, particles are well-mixed within fingers and fully coupled with the fluid phase. Conversely, $\Sigma > 1$ (and $St < 1$) is associated with IPS, as particles would settle or be expelled from the flow within fingers, even if their trajectories would be affected by the motion of the fluid phase. For $\Sigma \approx 1$ (and $St < 1$), either SDGIs or IPS are observed.

In Figure 3.4, we compare the values of the dimensionless numbers B_1, B_2 and B_3 (equations 3.1, 3.9 and 3.11, respectively) with observations of the conditions in

Finger number	Exp. number	C_u (g l^{-1})	$C_{\max}$ (g l^{-1})	$C_{\max}$ $/C_u$	$V_{\max}$ (mm s^{-1})	$V_{\max}$ $/V_p$	α_e	t_f (s)
F1	D1	1	0.27	0.27	-14.6	-10.4	0.19	21
F2	D1	1	0.49	0.49	-20.4	-14.6	0.16	16
F3	D1	1	0.31	0.31	-8.5	-6.1	0.23	10
F4	D1	1	0.62	0.62	-16.0	-11.4	-	21
F5	D1	1	0.31	0.31	-15.9	-11.4	0.23	16
F6	D1	1	0.29	0.29	-12.0	-8.6	-	20
F7	D2	2	0.54	0.27	-12.4	-8.9	0.27	10
F8	D2	2	1.05	0.53	-14.1	-10.1	0.30	12
F9	D2	2	0.51	0.26	-10.9	-7.8	0.21	16
F10	D3	3	1.95	0.65	-14.2	-10.1	0.19	12
F11	D3	3	1.84	0.61	-20.6	-14.7	-	14
F12	D3	3	1.37	0.46	-15.7	-11.2	0.19	10
F13	D3	3	1.75	0.58	-12.6	-9.0	0.60	10
F14	D3	3	0.77	0.26	-26.3	-18.8	0.40	10
F15	D3	3	0.97	0.32	-10.2	-7.3	0.23	10
F16	D3	3	1.07	0.36	-18.2	-13.0	0.46	11
Mean				0.41	-14.2	-10.8	0.28	14
(Standard deviation)				(0.15)	(3.5)	(3.2)	(0.13)	(4)

Table 3.2: List of individual fingers properties. C_u is the initial particle concentration of the particle suspension and $C_{\max}$ the maximum particle concentration measured within time-averaged fingers. Similarly, V_p is the individual settling velocity of the particles and $V_{\max}$ the maximum downward vertical velocity measured in time-averaged fingers with the PIV technique. α_e is the entrainment coefficient that has not been estimated for merging fingers (F4, F6 and F11). Finally, t_f is the duration for which fingers properties have been averaged. The median diameter of the particles is 40.7 µm for all the fingers selected.

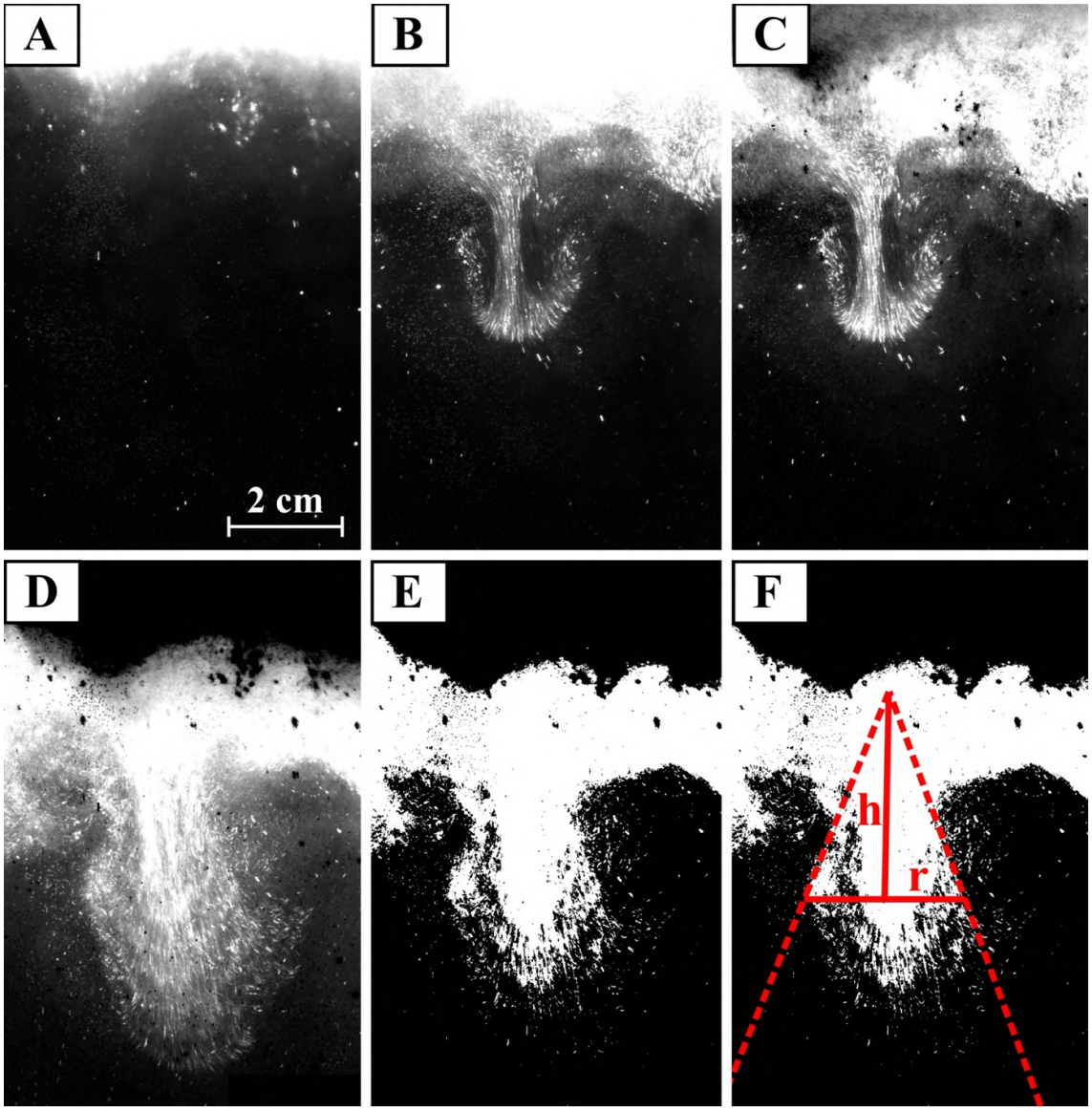

Figure 3.3: Image processing for estimating the entrainment coefficient associated with an individual finger (example of finger F14; Table 3.2). **A.** Background image. **B.** Instantaneous image of a developing finger from which **C.** the background is subtracted. **D.** Time-averaged image. **E.** Binary image of the time-averaged finger **F.** Manual measurement of the radius r and height h of the finger.

which SDGIs develop in our experiments and in previous experimental (Scollo et al., 2017; Fries et al., 2021) and numerical (Lemus et al., 2021) studies performed in the same configuration. The values of B_1, B_2 and B_3 are estimated as functions of both the particle concentration of the suspension and the size of the particles. First, the reduced gravity is calculated by equation (3.2), considering that the density of the PBL is

$$\rho_{PBL} = X_p \rho_p + (1 - X_p)\, \rho_f. \tag{3.20}$$

The density of the fluid phase is calculated from equation (3.16), with $X_f = 0.07$, as supported by the PLIF measurements of Fries et al. (2021). The reduced gravity values are then used to estimate the PBL thickness with equation (3.1). For these aqueous systems, the fluid kinematic viscosity is 1×10^{-6} m s^{-2}.

We report that SDGIs preferentially form in association with fine particle sizes and high particle concentrations, which confirms previous experimental findings (Carazzo and Jellinek, 2012; Jacobs et al., 2015; Scollo et al., 2017; Lemus et al., 2021). This corresponds to high values of B_1, B_2 and B_3, as expected from the definition of the criteria ensuring the onset of SDGIs for B_1, B_2, $B_3 \gg 1$. Alternatively, coarse particle sizes and low particle concentrations lead to IPS (i.e., small values of B_1, B_2 and B_3). We have also highlighted how the particle size threshold above which particles preferentially settle individually rather than within fingers increases for increasing particle concentration. The relative importance of the particle size and concentration on the development of SDGIs is reflected in the slopes of B_1, B_2 and B_3 contour lines plotted in a particle concentration-size diagram such as Figure 3.4. Breaks in slope correspond to the transition between low Re_p particles (equation 3.6) and intermediate Re_p (equation 3.7). Steep contour lines indicate that the particle size is of primary importance over the particle concentration, whilst gentler slopes imply that the particle concentration plays a more prominent role.

The contour line $B_1 = 1$ is found to inaccurately describe the transition from SDGIs to IPS. Indeed, we observe IPS even though $B_1 \geq 9$ for all experiments (Table 3.1). As illustrated by the line $B_1 = 100$, the contour lines of B_1 are also too steep to separate the SDGI and IPS experiments (Figure 3.4). This suggests that the definition of B_1 fails to account for the relative importance of the particle size

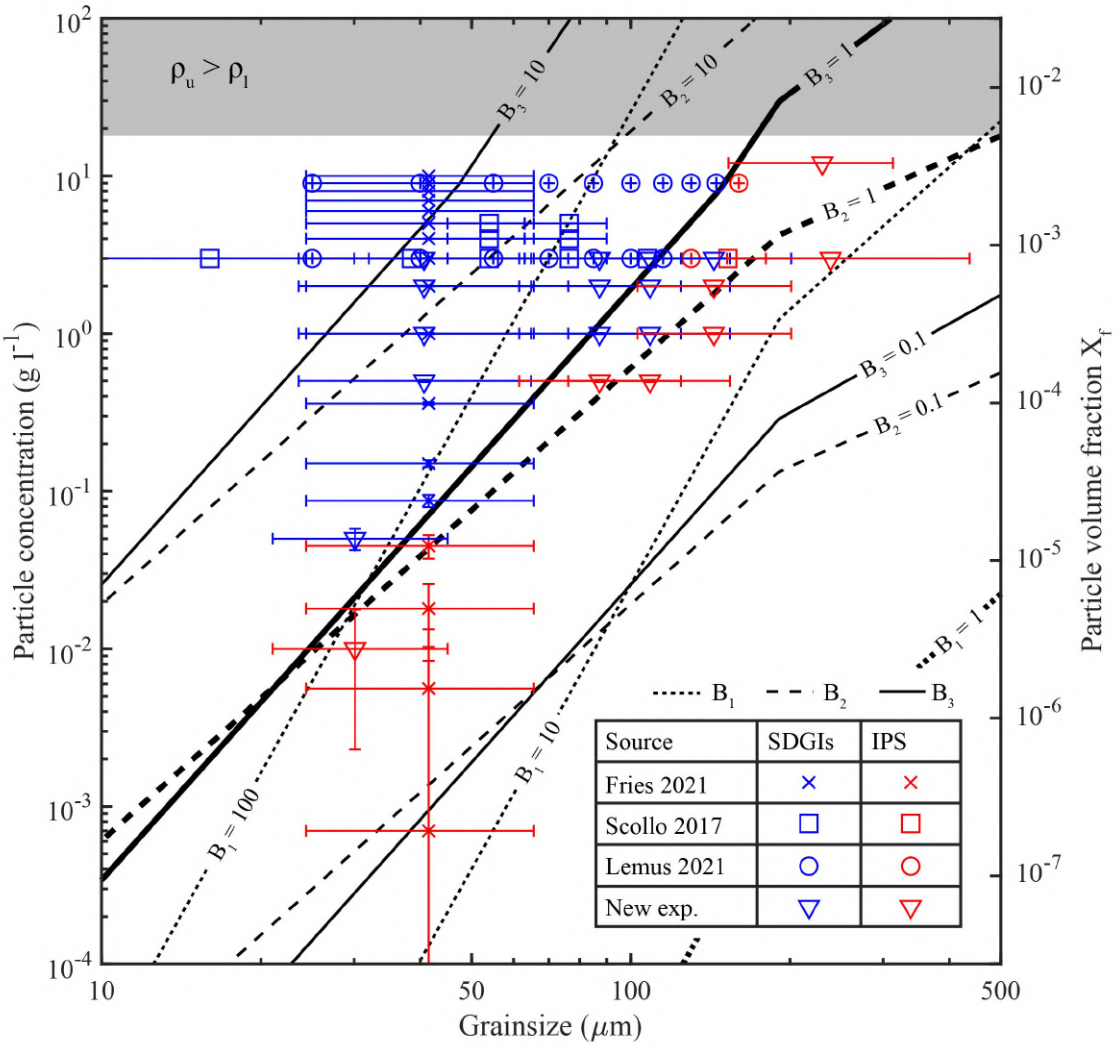

Figure 3.4: Comparison between the conditions at which the sedimentation is governed by either SDGIs or IPS and the contours of the dimensionless numbers B_1 (dotted lines), B_2 (dashed lines) and B_3 (solid line) predicting the onset of SDGIs as a function of the particle concentration and the grainsize. The contour lines B_1, B_2 and $B_3 = 1$ are highlighted with greater thicknesses, as they theoretically quantify the transition from SDGIs to IPS. Observations of SDGIs are reported in blue and the experiments/simulations for which IPS dominates are reported in red. The dataset comprises measurements in identical system configurations from Scollo et al. (2017) (squares), Fries et al. (2021) (crosses), Lemus et al. (2021) (circles; numerical simulations) and additional experiments presented in this study (triangles). The horizontal error bars extend to the 10^{th} and 90^{th} percentiles of the grainsize distribution and the markers are positioned at the median diameter. Vertical error bars correspond to the uncertainty on the particle concentration, derived from both the uncertainty on the mass and volume measurements. On the top of the figure, the grey region indicates the particle concentrations for which the initial density of the upper layer ρ_u is greater than the density of the lower layer ρ_s, and, therefore, corresponds to a Rayleigh-Taylor unstable configuration.

and concentration on the onset of SDGIs by underestimating the effect of particle concentration. The contour lines $B_2 = 1$ and $B_3 = 1$, however, adequately distinguish the dataset into SDGIs for B_2, $B_3 > 1$ and IPS for B_2, $B_3 < 1$. Values close to 1 give more transitional results, notably with values of $1 < B_2 \leq 1.4$ associated with IPS for 3 experiments, and values of $0.7 \leq B_3 < 1$ associated with SDGIs for 2 experiments (Table 3.1). Both B_2 and B_3 correctly capture the relative influence of particle size and concentration. However, for numerical simulations (Lemus et al., 2021) and for the experiments of Scollo et al. (2017), only the contour line $B_3 = 1$ predicts the onset of SDGIs consistently.

3.4.2 Development of SDGIs and of associated fingers

Images of the particles are treated in order to obtain the distribution of the particle concentration inside the water tank (Figure 3.5). As described in *Section 3.3.2*, the particle concentration cannot be obtained throughout the entire images because the linear regression between the particle concentration and the pixel digital level is not valid far from the laser source. Particle concentration maps are horizontally averaged for obtaining particle concentration profiles. At the beginning of the experiments (t = 3 s), fingers already start to form below the initial density interface. Interestingly, the particle concentration increases below the upper layer as particles settle on top of the initially particle-free lower layer, but particles do not accumulate (i.e., the particle concentration in the PBL does not exceed the initial particle concentration of the upper layer). Fingers later develop and descend in the lower layer as discrete columns of particles (t = 12 s). As they descend, fingers become larger through entrainment of the surrounding fluid and merging (t = 30 s). In the final stage of the experiments, fingers still form below the upper layer and the lower layer becomes more homogeneous because of the mixing induced by layer-scale convection (t = 70 s). The particle concentration profile is, therefore, more uniform in the lower layer. In the upper layer, we observe the creation of a gradient in the particle concentration due to sedimentation that progressively removes particles from the top part of the particle suspension. The particle concentration at the density interface therefore becomes greater than at the top of the upper layer, without exceeding the initial

particle concentration.

Simultaneously, PLIF images are used to calculate the concentration of upper fluid and the fluid phase density in the experiments with equations (3.15) and (3.16), respectively (Figure 3.6). The fluid density is seen to remain relatively unchanged with time as fingers only entrain small amounts of upper fluid within them (Fries et al., 2021). Despite this, some descending columns with greater upper fluid concentrations are visible in the images and correspond to fingers entering the lower layer. This is further evidenced in images showing the difference between the concentration of upper fluid at a certain time and at $t = 0$ s. At $t = 70$ s, the measured concentration of upper fluid erroneously increases in the upper layer, due to the decrease of the particle concentration that diminishes the attenuation effect of the particles on PLIF measurements. Because of the mixing induced at the start of the experiments by the barrier removal, the fluid density profile does not exhibit a perfect step transition from the density of fresh water in the upper layer to the density of the sugar solution in the lower layer. The density of the fluid phase instead transitions smoothly, but rapidly, across the interface from the density of fresh water to the density of the sugar solution. Based on the profiles, the density of the fluid phase is found to remain uniform in the lower layer.

Combining simultaneous particle imaging and PLIF visualisation techniques allows us to obtain the mixture density ρ_m in the experiments with equation (3.17) (Figure 3.7). The density configuration is initially stable and ρ_m increases gradually with depth across the interfacial region ($t = 3$ s). As already described in previous works (Burns and Meiburg, 2012, 2015; Yu et al., 2013; Davarpanah Jazi and Wells, 2020; Fries et al., 2021; Lemus et al., 2021), the PBL grows below the interface, combining both the contribution of the particles and of the dense lower layer fluid to ρ_m. The density configuration, therefore, becomes unstable, with a layer of higher density emplaced above a lighter ambient. Similarly to Fries et al. (2021), we find the density difference between the PBL and the ambient fluid to be very small. In fact, the density of the particle-fluid mixture in the PBL is only 0.01 to 0.1 % higher than that of the ambient density. Fingers grow ($t = 12$ s) and descend ($t = 30$ s) in the lower layer as negatively buoyant plumes. Later in the experiments ($t = 70$ s),

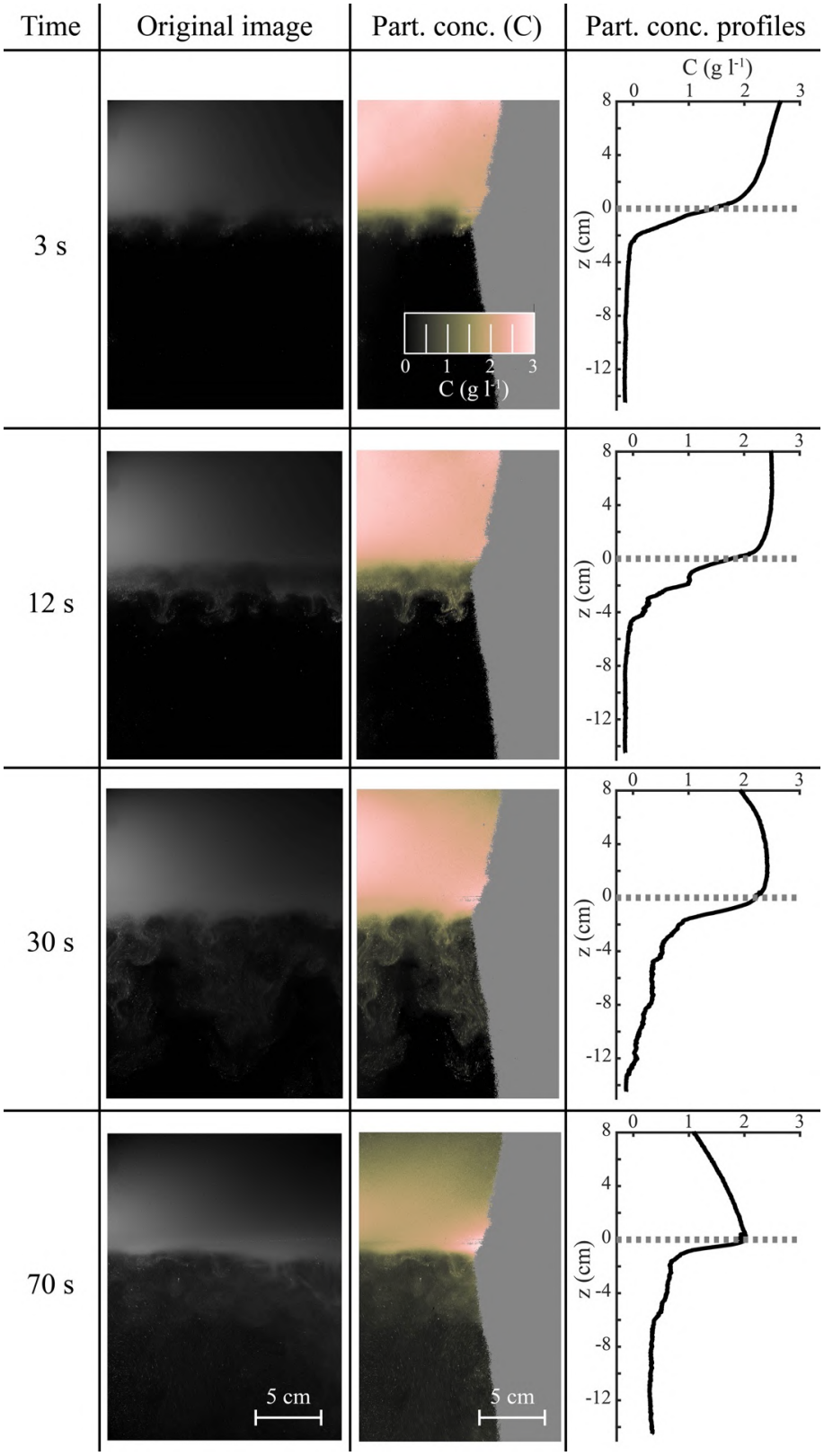

Figure 3.5: Image processing for obtaining the particle concentration map and profile inside the experimental tank at four different times, for experiment D3 (3 g l^{-1} and D_{50} = 40.7 µm Table 3.1). Pixels for which the particle concentration cannot be calculated appear in grey (i.e., pixels associated with $R^2 \leq 0.95$). The dashed grey line represents the initial position of the density interface at $z = 0$ cm.

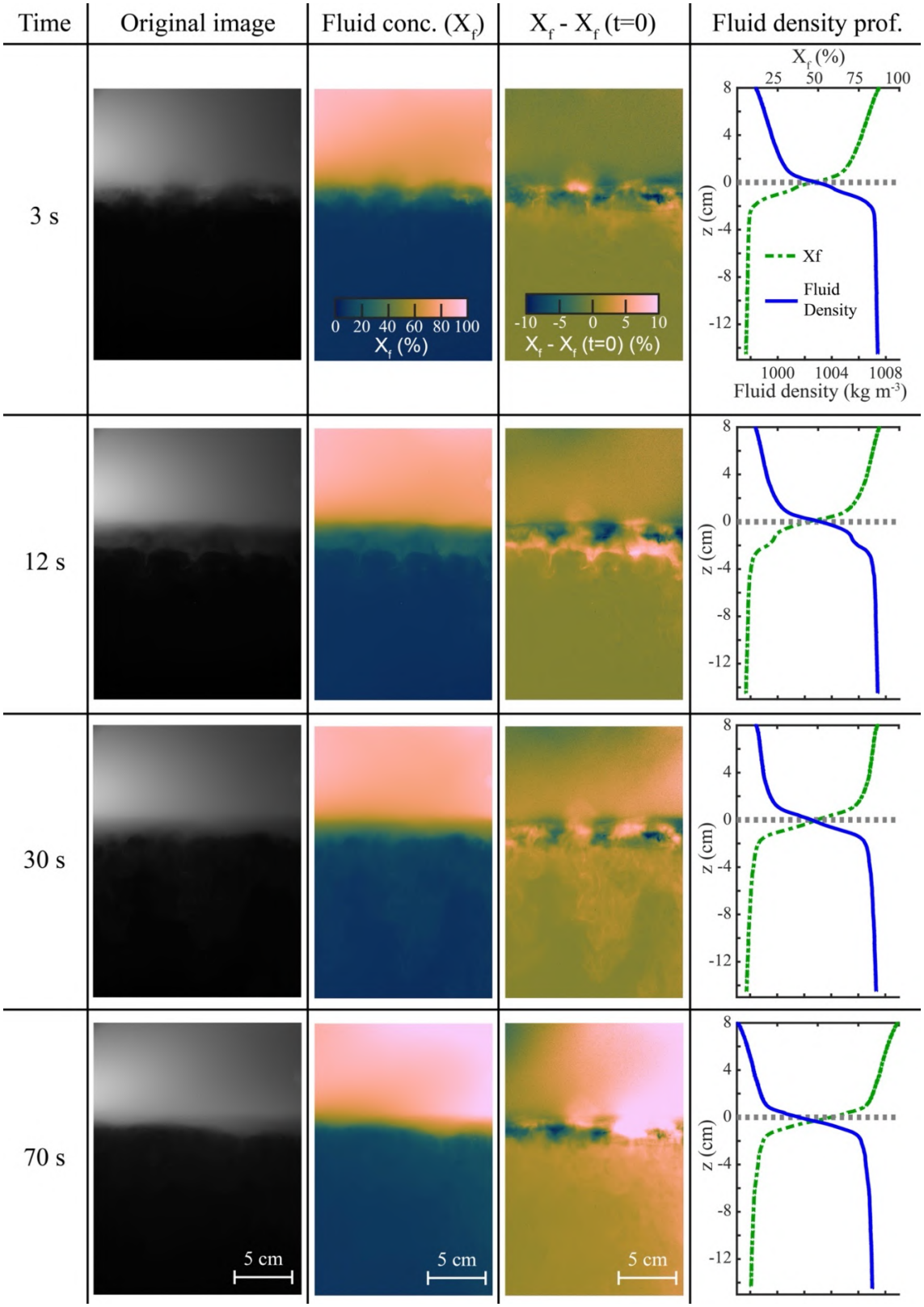

Figure 3.6: Image processing used to infer the concentration of upper fluid concentration X_f (equation 3.12) in the experiments and the density of the fluid phase ρ_f (equation 3.13) for experiment D3 (3 g l^{-1} and D_{50} = 40.7 µm; Table 3.1) at four different times. Changes in the upper fluid concentration with respect to the initial state $X_f - X_f(t = 0)$ are highlighted. The dashed grey line represents the initial position of the density interface at $z = 0$ cm.

the lower layer is mixed by convection and the density stratification becomes more stable.

3.4.3 Dynamics of individual fingers

Fingers start to form in the first 10 s following the removal of the barrier and rapidly evolve as they descend in the lower layer (Figure 3.8). First, fingers detach from the upper layer in the form of small columns ($t = 7$ s; Figure 3.8A) that expand vertically and radially with time. For all particle concentrations studied here, the entrainment coefficient α_e (equation 3.19) that quantifies this change is found to significantly vary (Table 3.2), with a mean value of 0.28 ± 0.13, a minimum of 0.16 and a maximum of 0.60. The radial expansion is related to strong internal circulation and the creation of a vortex ring that develops in the head region ($t = 12$ s; Figure 3.8B). At this stage fingers resemble sediment thermals in the self-preserving phase (Rahimipour and Wilkinson, 1992). They adopt a characteristic mushroom shape, similarly to Rayleigh-Taylor bubbles formed for fluids with nearly equal densities (Sharp, 1984; Kull, 1991; Waddell et al., 2001; Chou and Shao, 2016). As fingers descend, the particle-laden columns connected to the base of the upper layer gradually thins ($t = 12$ s; Figure 3.8C) and the particle concentration diminishes in this region ($t = 19$ s; Figure 3.8D). The maximum particle concentration within time-averaged fingers $C_{\max}$ does not exceed that of the particle suspension and is consistently found to be between $0.25C_u$ and $0.66C_u$, with a mean value of $C_{\max} = 0.41C_u$ (Table 3.2).

The merging of fingers happens through interactions between their respective vortex rings. This is illustrated in Figure 3.9 which makes use of the PIV technique to obtain the particle velocity field. A first finger grows below the interface and develops a characteristic vortex ring, whilst a second smaller finger forms beside ($t = 31$ s; Figure 3.9A,D). The vortex rings of the two fingers later interact and merge, causing the entrainment of the smaller finger into the bigger one ($t = 35$ s; Figure 3.9B,E). As a result, a thicker finger is formed ($t = 39$ s; Figure 3.9C,F). Finger merging is also promoted by the lateral motion induced at the density interface when convection in the lower layer initiates.

As seen above in *Section 3.4.2*, fingers develop from very small density differences

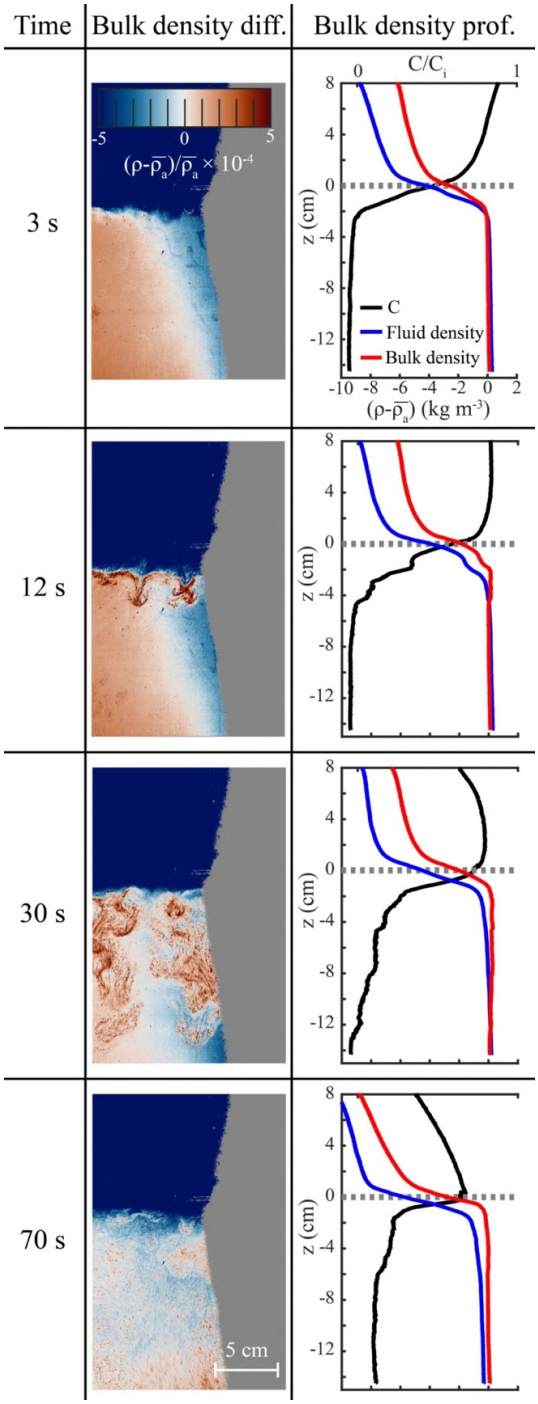

Figure 3.7: Mixture density maps normalised by the ambient density of the sugar solution in the lower layer $(\rho_m - \overline{\rho_a})/\overline{\rho_a}$ for experiment D3 (3 g l^{-1} and $D_{50} = 40.7$ µm; Table 3.1) at three different times. ρ_m is the mixture density derived from equation (3.14) and $\overline{\rho_a}$ is the average fluid density of the lower layer at time t. Blue colours indicate mixture densities lower than the density of the lower layer whilst the regions of higher density appear in red. An artificial lateral variation in the measurement of ρ_m is created in the lower layer at $t < 70$ s, due to the initial absence of particles, contrarily to calibrations. Corresponding particle concentration C (black line) and density profiles are shown in the right column. Densities are expressed as the density difference $\rho - \overline{\rho_a}$, with ρ the density of the mixture (red line) or of the fluid phase (blue line). The grey areas correspond to the pixel for which C cannot be determined and the dashed grey line represents the initial position of the density interface at $z = 0$ cm.

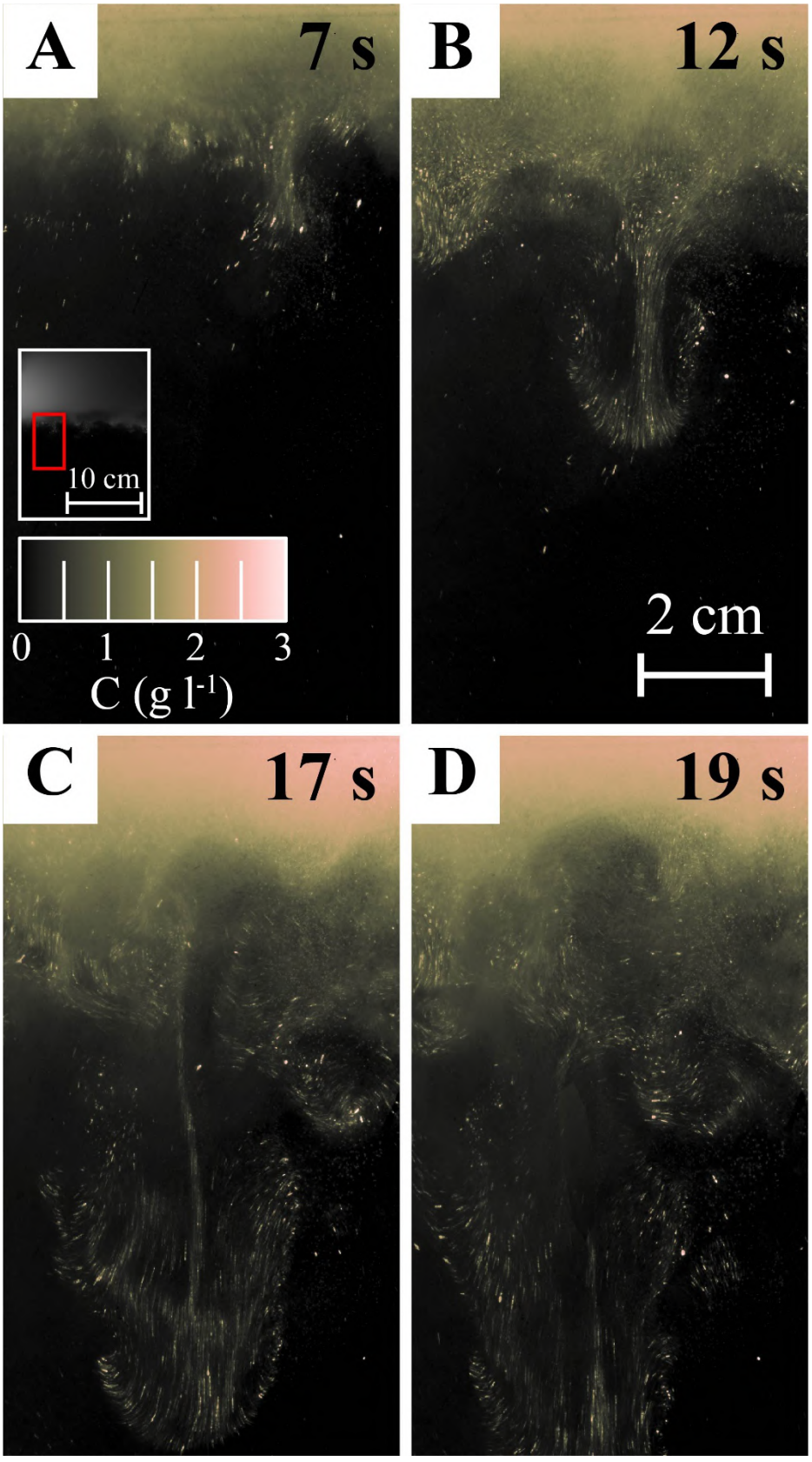

Figure 3.8: False-colour image of the particle concentration field showing the evolution of the particle concentration within a single finger (F14: 3 g l^{-1} and D_{50} = 40.7 µm; Table 3.2) at times **A.** t = 7 s, **B.** t = 12 s , **C.** t = 17 s and **D.** t = 19 s. The region encased in red in the inset of panel A indicates the imaged region of the experiment.

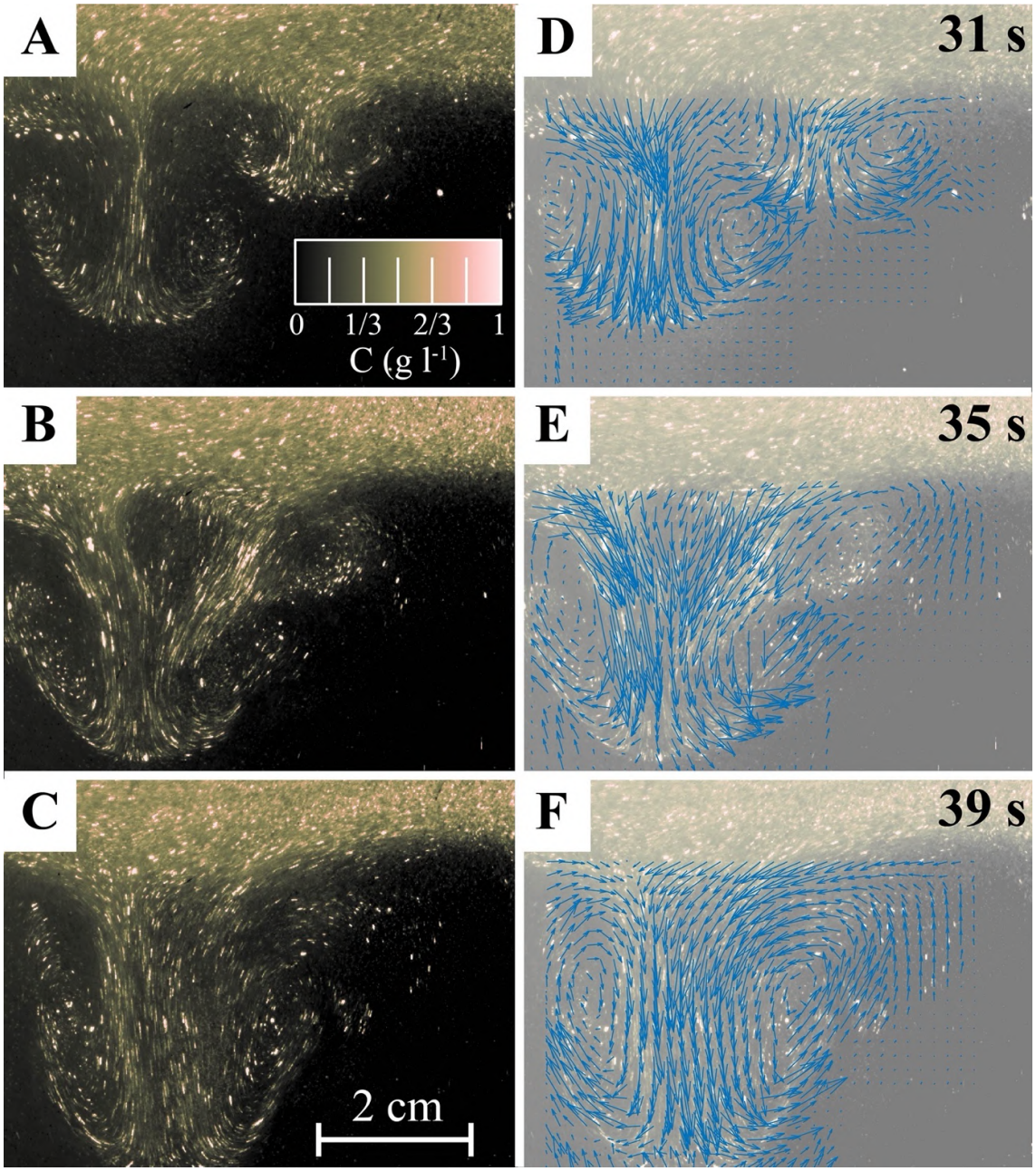

Figure 3.9: Distribution of the particle concentration (left panels **A.**, **B.**, and **C.**) and velocity field (right panels **D.**, **E.**, **F.**) associated with the merging of two fingers (F4: 1 g l^{-1} and D_{50} = 40.7 µm; Table 3.2).

generated at the base of the initial density interface. This is demonstrated at the scale of a finger in Figure 3.10. Fingers incorporate both the contributions of the particles (Figure 3.10A,B) and of the dense lower layer fluid phase. This makes them negatively buoyant, driving their propagation below the interface, with particle-fluid mixture densities 0.01 – 0.1 % greater than the ambient density (Figure 3.10C,D). PIV measurements are also used to assess the particle velocity field (Figure 3.10E,F) and in particular $V_{\max}$, the maximum value of the vertical component of the particle velocity. Within fingers, $V_{\max}$ corresponds to the maximum vertical velocity of the flow, as particles are fully coupled with the fluid phase. Comparison with the individual settling velocity of the particles V_p shows that $V_{\max}$ is greater than V_p by an order of magnitude within fingers (Figure 3.10G,H), with a mean value $V_{\max}/V_p$ equal to -10.8 $\pm$ 3.2 (Table 3.2). This indicates that the particle settling velocity is considerably enhanced within fingers, and we find $V_{\max}$ to even exceed the characteristic finger front velocity V_f (equation 3.10) by up to a factor of 4 (V_f/V_p = -4.1, -4.9 and -5.4 for particle concentrations of 1, 2 and 3 g l^{-1}, respectively). In fact, the flow velocity is not homogeneous within fingers, as it decreases toward the thick propagation front and increases in narrower regions where particles are channelized downward (Figure 3.10G,H).

The distribution of the time-averaged normalised particle concentration $C/C_{\max}$ within fingers is found to be nearly symmetrical around the centreline that is defined as the position at which the particle concentration reaches a maximum (Figure 3.11A). Small heterogeneities can be related to the short period available for averaging the particle concentration, as fingers develop rapidly and are not maintained for durations greater than 30 s in our experimental setup. The normalised particle velocity V/V_p presents two minima (Figure 3.11B), which can be linked to the presence of the ring vortex that slightly enhances the flow velocity around the centreline. In 2D, the ring vortex appears as two counter-rotating vortices (i.e., regions characterised by vorticity values of opposing signs) (Figure 3.11C). As expected for fingers developing from the detachment of a PBL with a thickness δ, $C/C_{\max}$, V/V_p and ω all reach zero over a radial length scale comparable to δ.

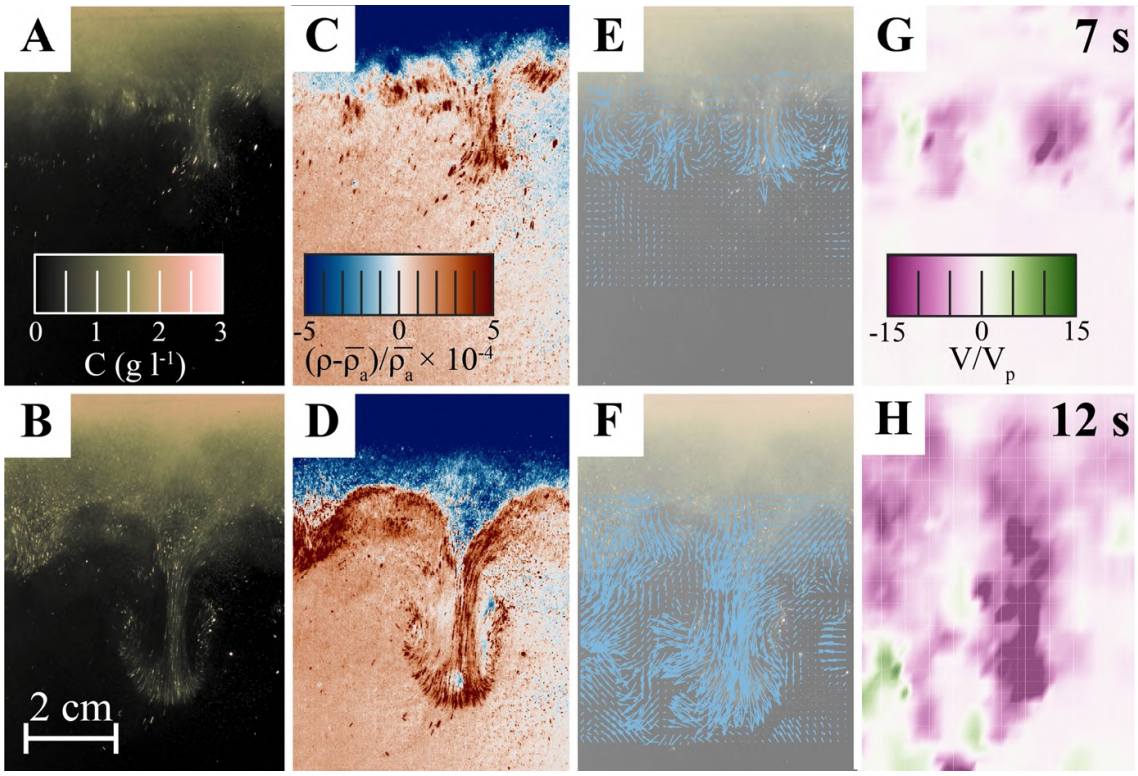

Figure 3.10: Particle concentration (**A.** and **B.**), normalised mixture density (**C.** and **D.**), particle velocity field (**E.** and **F.**) and vertical component of the particle velocity V normalised by the individual particle settling speed V_p (**G.** and **H.**) associated with the development of a finger in experiment D3 (F14: 3 g l^{-1} and D_{50} = 40.7 µm; Table 3.2). In **G.** and **H.**, purple colours indicate downward motions at speeds greater the particle individual settling rate and green colours are found for upward motions. Panels on the top (**A.**, **C.**, **E.**, **G.**) are associated with the formation of a finger at t = 7 s and panels at the bottom (**B.**, **D.**, **F.**, **H.**) correspond to the same finger at t = 12 s.

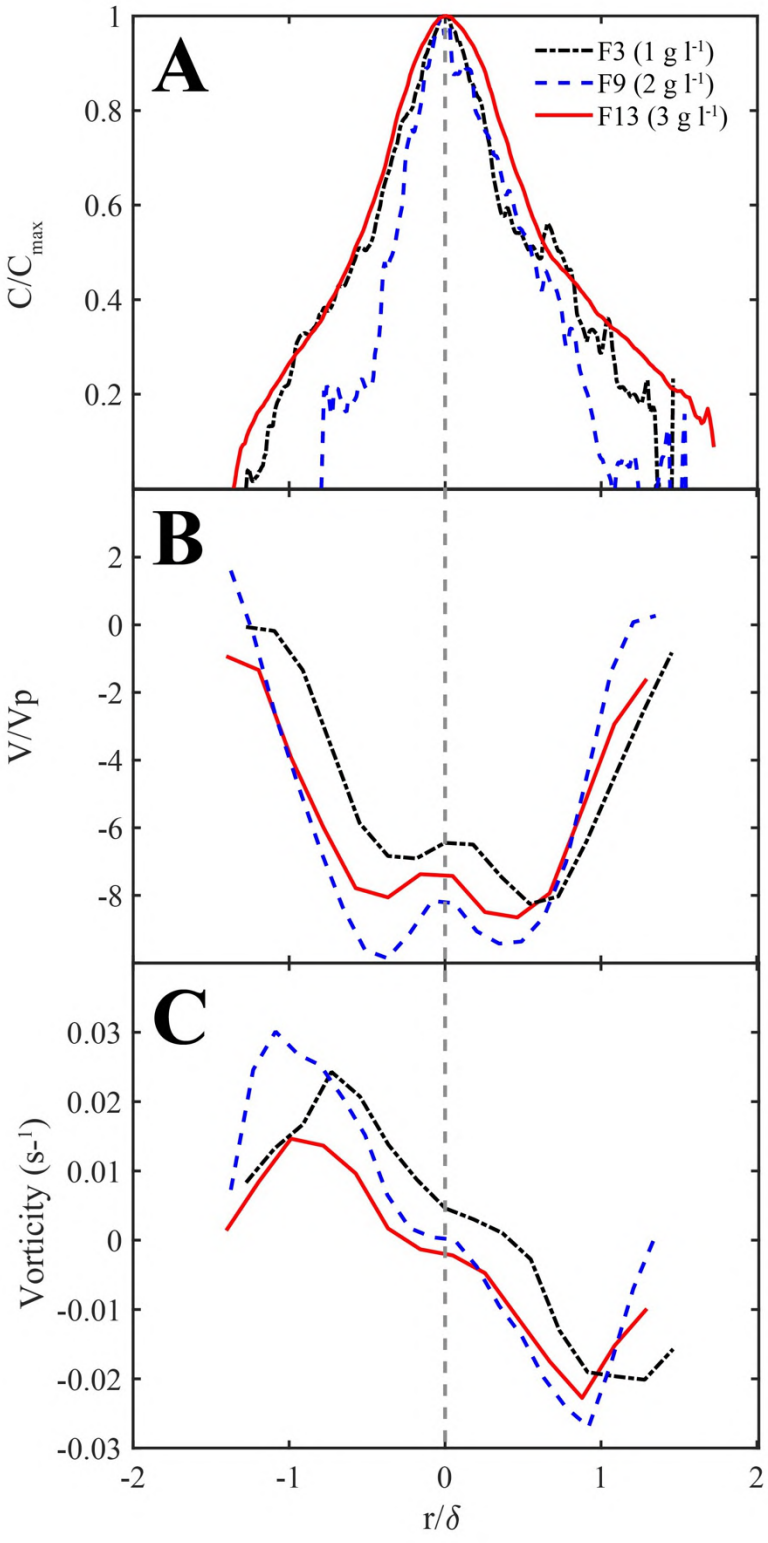

Figure 3.11: Time-averaged radial profiles of (**A.**) the normalised particle concentration, (**B.**) normalised vertical velocity and (**C.**) vorticity for three selected fingers F3, F9 and F13 (respectively 1, 2 and 3 g l^{-1} and D_{50} = 40.7 µm; Table 3.2). Profiles are acquired at a depth ranging between 1 and 3.6 cm below the density interface. Here, we normalise the horizontal distance from the centreline r by the characteristic size of the PBL δ (equation 3.1). $r/\delta = 0$ corresponds to the position of the finger centreline which is represented by the grey dashed line. The particle concentration is normalised to its maximum value along the centreline $C_{\max}$.

3.5 Discussion

3.5.1 The onset of SDGIs

Previous work has already established that high particle concentrations and fine grainsizes favour the formation of SDGIs below particle suspensions (Marsh, 1988; Manville and Wilson, 2004; Carazzo and Jellinek, 2012; Jacobs et al., 2015; Scollo et al., 2017; Fries et al., 2021; Lemus et al., 2021). Here, we quantify the potential onset of SDGIs over a wide range of particle concentrations and sizes based on the dimensionless numbers B_1, B_2 and B_3 derived in this work (equations 3.1, 3.9 and 3.11) .

The criterion $B_1 > 1$ is found to overestimate the parameter range for which SDGIs develop. Additionally, the contour lines of B_1 cannot separate the conditions where SDGIs are observed from IPS. A first possible explanation for this discrepancy is that the growth rate of the instability V_i (equation 3.4) used to derive the formulation of B_1 is an approximation for a system in which the viscosity of the fluid propagating as fingers is negligible compared to the ambient (Whitehead and Luther, 1975; Carazzo and Jellinek, 2012). In our experimental configuration, as well as below volcanic ash clouds, the fluids have nearly identical viscosities and this assumption is therefore not valid. Secondly, this discrepancy indicates that the growth of SDGIs is not controlled by the balance between gravitational forces and viscous drag, but rather slowed by inertial drag.

Our results suggest that the criteria $B_2 > 1$ (i.e., the timescale for the descent of instabilities controlled by the balance between gravitational and inertial drag is shorter than the timescale for the settling of individual particles; Jacobs et al., 2015) and $B_3 > 1$ (i.e., the characteristic velocity of fingers is greater than the particles individual settling velocity V_p) can most adequately predict the conditions for which SDGIs form in our experimental configuration (Figure 3.4). Under these conditions, particles are fully coupled with the flow within fingers (i.e., St < 1 and $\Sigma < 1$; with Σ the reciprocal of B_3). Conversely, IPS dominates for $B_2 < 1$ and $B_3 < 1$. As described in *Section 3.4.1*, fingers are associated with a Reynolds number much greater that unity both in experiments and below volcanic ash clouds (Jacobs et al.,

2013; Scollo et al., 2017; Fries et al., 2021). Inertial drag forces must, therefore, be considered for estimating the finger velocity, as confirmed by the good agreement between the value of B_2 and the experimental observations. On the other hand, the characteristic finger velocity, derived from the combination of the fingers mass and buoyancy fluxes (Hoyal et al., 1999b), provides a good estimation of the finger front velocity, already tested for our experimental configuration (Fries et al., 2021). This is additionally supported by the good predictive capability of B_3 for the formation of SDGIs.

Although both depending on the individual settling velocity of the particles, the values of B_2 and B_3 are independent and assess different conditions for predicting the tendency of SDGIs to for. However, they are both able to predict the onset of SDGIs in experiments with a satisfactory accuracy. For values close to unity, IPS are yet reported for $B_2 > 1$, whilst SDGIs are reported for $B_3 < 1$ (Table 3.2). B_2, therefore, slightly overestimates the conditions for which SDGIs form and B_3 slightly underestimate these conditions. However, the onset of SDGIs in numerical simulations (Lemus et al., 2021) is much more consistently predicted by B_3 values than B_2 values and the size threshold $d \approx 125$ µm for the formation of SDGIs reported by Scollo et al. (2017) for particle concentrations on the order of 1 g l^{-1} is better predicted by B_3 as well, giving additional confidence in the criterion based on B_3. Although B_3 is found to be more efficient than B_2 for quantifying the tendency to form SDGIs, the combination of both numbers provides accurate bounds on the conditions associated with SDGIs in aqueous environments. B_2 and B_3 can, therefore, be considered together for a more complete characterisation of the conditions favouring SDGIs.

3.5.2 Application to volcanic ash clouds

By analogy with the experiments and the simulations involving the sedimentation of well-sorted dense particles in an initially-quiescent aqueous environment, it is possible to predict the type of sedimentation for volcanic ash clouds (collective – SDGI or individual – IPS) based on the values of B_2 and B_3 in the atmosphere. Similarly to analogue configurations in water, the size threshold separating the formation of

SDGIs from IPS is expected to be positively correlated with the ash concentration within volcanic clouds. Figure 3.12 shows the contour lines of B_2 and B_3 as a function of the concentration (i.e., the particle volume fraction) and the diameter of volcanic ash. B_2 and B_3 have been calculated for high, intermediate and low Re_p particles by combining equations (3.5), (3.6) and (3.7) for the velocity of individually-settling particles with equations (3.8) and (3.10) giving the velocity of collective settling. We have selected conditions representative of volcanic ash clouds, with $\rho_a = 1.3$ kg m^{-3} the air density, $\rho_p = 1550$ kg m^{-3} the density of volcanic ash collected during the 2010 Eyjafjallajökull eruption (Bonadonna et al., 2011), $\mu = 1.8 \times 10^{-5}$ Pa s the dynamic viscosity of the air, $H = 1$ km the characteristic thickness of the volcanic ash cloud and $\delta = 90$ m the characteristic PBL thickness (Manzella et al., 2015). As for experiments, the values of B_2 and B_3 increase with increasing particle volume fractions and finer grainsizes, indicating that high concentrations of fine volcanic ash promote the formation of SDGIs. For a particle volume fraction of 10^{-6} characteristic of volcanic ash clouds produced by small to moderate eruptions (Carazzo and Jellinek, 2012; Manzella et al., 2015), the transition from IPS to SDGIs is found to happen around a diameter $d \approx 250$ µm in the atmosphere, in good agreement with the measurements of Manzella et al. (2015) who found fingers to affect particles < 200 µm during the 2010 eruption of Eyjafjallajökull. Interestingly, this size threshold is higher than in a water environment for the same particle volume fraction ($d \approx 20$ µm; Figure 3.4) due to inertial effects that become much more important than viscous forces. Results additionally suggest that the relative influence of the particle concentration against the particle size increases with Re_p, as illustrated by the contour lines of B_2 and B_3 that become more horizontal for increasing Re_p in Figure 3.12.

Figure 3.12 can only describe the case of the 2010 eruption of Ejyafjallajökull (Manzella et al., 2015) adequately. Hence, for other volcanic ash clouds, the regime diagram presented in Figure 3.12 only provides a general approximation of the conditions for which ash fingers can form. In fact, the calculation of B_2 and B_3 for volcanic ash clouds is associated with several caveats.

Both the estimations of B_2 and B_3 require the preliminary determination of

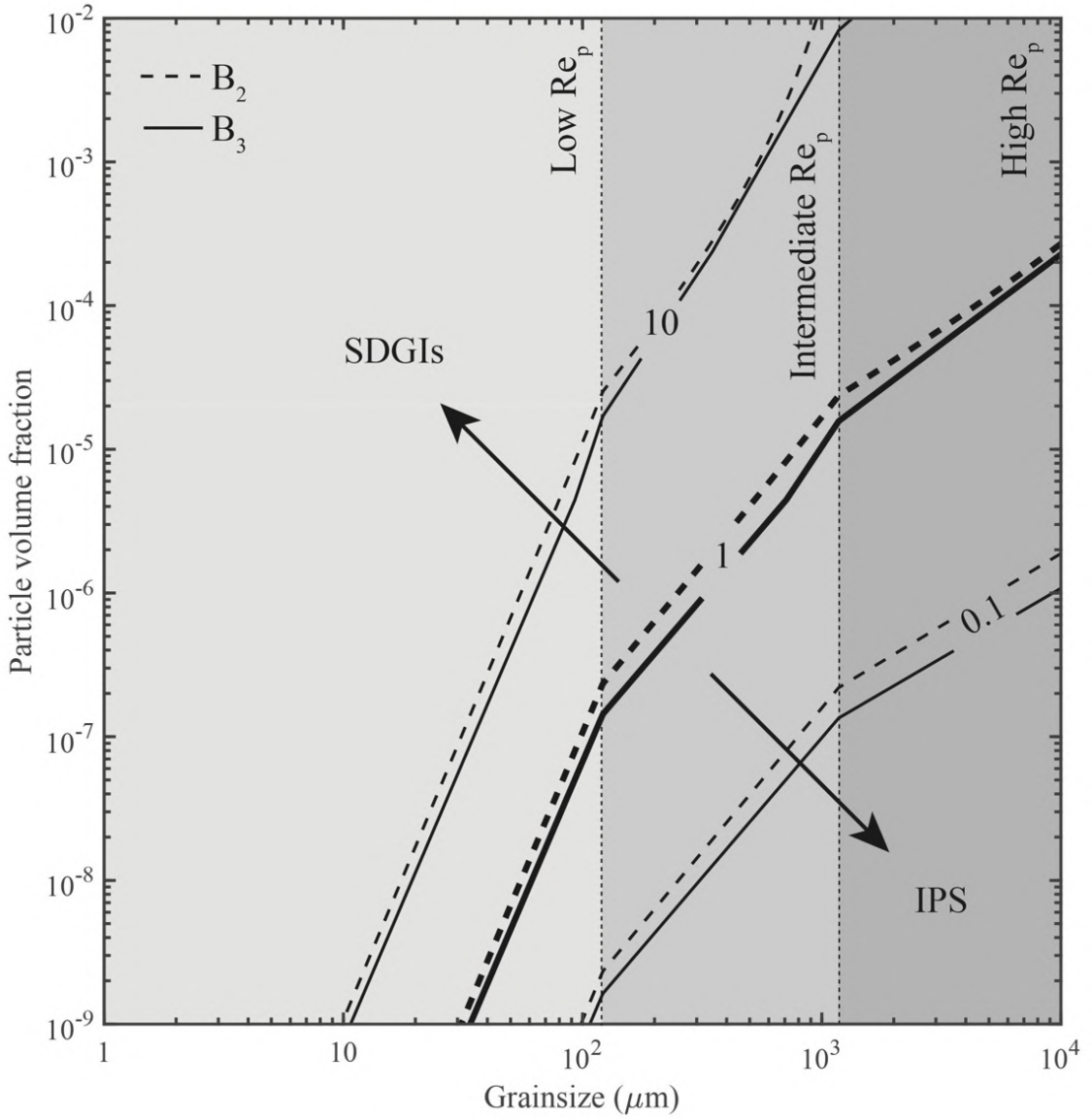

Figure 3.12: Contours of B_2 (dashed lines) and B_3 (solid lines) calculated as functions of ash concentration and grainsize for conditions representative of the 2010 volcanic cloud of Eyjafjallajökull (Manzella et al., 2015). The contour lines are divided in three distinct regions based on the grainsize d, with low Re_p particles ($d < 120$ µm), intermediate Re_p particles (120 µm $< d <$ 1200 µm) and high Re_p particles ($d >$ 1200 µm).

δ. However, whilst δ can be accurately predicted in aqueous experiments using equation (3.1) (Hoyal et al., 1999b), applying this definition to volcanic ash clouds results in greatly underestimating the observed size (i.e., width and spacing) of ash fingers by 4 orders of magnitude (Manzella et al., 2015; Fries et al., 2021). These important discrepancies can be explained by uncertainties in measuring parameters associated with volcanic ash clouds (such as the ash concentration) that lead to erroneous results using equation (3.1), and by the experimental simplifications that do not account for a variety of mechanisms affecting volcanic ash clouds. In fact, the experimental configuration is simplified in order to examine the fundamental mechanisms through which SDGIs develop. In particular, we only consider two uniform and static fluid layers separated by an initially flat interface in a confined environment. Volcanic ash clouds are much more complex systems that involve a wide variety of atmospheric processes that can affect the deposition of volcanic ash, including the role of hydrometeors that can influence both the formation of volcanic ash aggregates (Textor et al., 2006) and the cloud mass loading (Durant et al., 2008, 2009). Additionally, other processes which have the potential to modulate the sedimentation of fine volcanic ash, such as wind-driven stirring (Freret-Lorgeril et al., 2020) are neglected in our experimental configuration. Moreover, volcanic ash clouds spread laterally in the atmosphere, creating shear velocity profiles which can affect the formation of SDGIs (Farenzena and Silvestrini, 2017; Konopliv et al., 2018). These processes highlight the need for future studies dedicated to evaluating their effects on SDGIs and improving understanding of ash fingers with more realistic parameterisation. Here, we therefore chose to evaluate the values of B_2 and B_3 by taking direct measurements of the size of ash fingers observed during the 2010 eruption of Eyjafjallajökull (Manzella et al., 2015). This is a major limitation, as we are not able to quantify the evolution of the PBL thickness as a function of eruptive parameters. Another important caveat is that the experimental observations and numerical simulations reported in Figure 3.4 are all associated with monodisperse and relatively well-sorted particle suspensions whilst natural volcanic clouds contain a wide range of particle sizes. The effect of polydispersity on SDGI formation and evolution also needs to be considered in future works. Finally, parameters other

than the particle concentration and the grainsize play a role in the development of SDGIs and should consequently be taken into account. The variation of atmospheric parameters, notably as a function of the cloud's altitude, can have a significant influence on the values of B_2 and B_3 (Carazzo and Jellinek, 2012). As already shown in previous works (Jacobs et al., 2015; Fries et al., 2021), the thickness of the particle suspension (cloud) is also particularly important, with thick suspensions favouring the formation of SDGIs. This corresponds to values greater than 5 for the dimensionless number L^* that represents the ratio of the particle suspension over the PBL thickness (Fries et al., 2021).

3.5.3 Characterisation of individual fingers

The simultaneous application of the PIV and PLIF imaging techniques allows us to investigate the internal structure of fingers, with more accuracy and in more detail than in the previous experimental setup, where particle imaging and PLIF were used separately (Fries et al., 2021). As described in previous studies (Burns and Meiburg, 2015; Davarpanah Jazi and Wells, 2020; Fries et al., 2021; Lemus et al., 2021), fingers result from the destabilisation of the PBL through a SDGI that arises from a very small density difference (Figure 3.8). Once they descend below the initial density interface, the heavy-particle laden fluid rolls up along the sides of the fingers and a ring vortex develops at their front. This gives fingers a characteristic mushroom shape (Figure 3.8B), similar to the structures observed for Rayleigh-Taylor instabilities (Sharp, 1984; He et al., 1999; Waddell et al., 2001; Ramaprabhu and Andrews, 2004; Chou and Shao, 2016), with strong internal circulations as described for sediment thermals (Rahimipour and Wilkinson, 1992; Ruggaber, 2000; Bush et al., 2003; Zhao et al., 2014). In 2D, the ring vortex appears as two vortices with sizes scaling as δ, and we do not observe the creation of eddies over multiple length scales as expected for fully turbulent flows (Burgisser et al., 2005). This is in line with the Reynolds number of experimental fingers that is characteristic of a transitional regime. Contrarily to experiments on sediment thermals, we do not observe an initial acceleration phase during which particle clouds behave as solid bodies, as the density of fingers is initially much lower than that of sediment

thermals. The ring vortex is observed to efficiently entrain the surrounding fluid into the fingers as well as favouring the merging of nearby fingers (Figure 3.9). As a result, the width of fingers gradually increases, especially in the head region (i.e., propagation front), whilst the column that connects growing fingers to the PBL thins with time (Figure 3.8). On average, fingers can be considered as relatively radially symmetrical (Figure 3.11). In 2D, the ring vortex appears as two counter-rotating vortices on the side of the fingers. The downward velocity V of particles within fingers is found to be an order of magnitude greater than V_p, showing that fingers considerably enhance sedimentation (Figure 3.10; Table 3.2). Interestingly, we also observe that V is greater than the finger front velocity V_f (equation 3.10; Hoyal et al., 1999b). This suggests that particles decelerate when reaching the head region.

Furthermore, we quantify the entrainment coefficient α_e and report a mean value $\alpha_e = 0.28 \pm 0.13$ (Table 3.2). However, considerable variations are found in the values of α_e that varies from 0.16 to 0.60. This is possibly linked to the fact that fingers do not descend purely vertically and can be affected by small horizontal variations due to the convection of the lower layer. Moreover, the determination of α_e implies subjective choices, notably for defining the edge of fingers (Figure 3.4). The mean value of α_e is nonetheless close to the value of 0.25 ± 0.1 found for thermals (Turner, 1969; Escudier and Maxworthy, 1973) and sediment thermals (Bush et al., 2003) that share similarities with fingers. Entrainment within fingers controls the evolution of their width and of their buoyancy, as measured by Freret-Lorgeril et al. (2020) who report the expansion of finger width with time from Doppler radar observations below volcanic ash clouds. Hence, it has implications regarding the longevity of fingers below the initial density interface and for the associated deposits (Bush et al., 2003; Zhao et al., 2014). Better constraining α_e in future studies is therefore crucial for a more complete characterisation of the evolution of fingers with time and depth. To do so, numerical simulations and experiments involving single fingers (similarly to the experiments on sediment thermals; Rahimipour and Wilkinson, 1992; Bush et al., 2003) could be explored.

Finally, we report that the particle concentration within the PBL (Figure 3.5)

and fingers (Table 3.2) does not become greater than the initial particle concentration of the particle-laden layer C_u. Indeed, the maximum particle concentration $C_{\max}$ within fingers is found to be a fraction of C_u, with mean $C_{\max}/C_u$ values of 0.41 $\pm$ 0.15. This suggests that the probability for particle collisions and the formation of aggregates does not increase within fingers. However, similarly to Scollo et al. (2017), we find vorticity to increase around the finger centrelines, in association with strong internal circulations and the formation of a ring vortex. This observation suggests that particle collisions can nonetheless happen within fingers, notably through interactions between eddies such as the ones highlighted during the merging of two fingers (Figure 3.9), especially because natural volcanic ash fingers are fully turbulent contrarily to their experimental counterparts. Dedicated experiments and numerical simulations involving wider grainsize distributions would be necessary to further investigate the complex relationship between fingers and particle aggregation.

3.6 Conclusions

Our experimental results confirm previous findings that showed how both particle concentration and size exert a primary control on the formation of fingers resulting from SDGIs. In addition, we characterise the conditions for the potential onset of SDGIs both in water (experiments) and in the atmosphere (natural volcanic clouds) based on the two parameters B_2 (ratio of the timescale for individual particle settling over the timescale for collective settling controlled by inertial drag over) and B_3 (ratio of the finger characteristic velocity over the velocity of individual particles). In particular, we find that:

1) fingers form preferentially for $B_2 > 1$, and $B_3 > 1$ at which particles are fully coupled with the flow within fingers, as indicated by the Stokes and sedimentation numbers ($St < 1$ and $\Sigma < 1$);

2) individual particle settling dominates at lower particle concentrations and for coarser grainsizes (i.e., $B_2 < 1$, or $B_3 < 1$);

3) particle size threshold for the formation of SDGI-driven fingers increases with particle concentration and is different in water and in air. As an example, for a characteristic particle volume fraction of 10^{-6}, particles < 20 µm are associated with B_2 and $B_3 > 1$ in water and can be entrained within fingers, whilst coarser grainsizes (< 250 µm) can be affected by SDGIs in the atmosphere below natural volcanic ash clouds. It is important to note that the extrapolation of experimental results to volcanic ash clouds to identify favourable conditions for the development of fingers based on B_2 and B_3 is difficult and needs to be considered as a first order approximation. In fact, volcanic ash clouds are significantly more complex than our experiments and other parameters, such as cloud thickness and atmospheric conditions, should also be accounted for in addition to the ash concentration and size.

Furthermore, under conditions appropriate for finger formation we observe that:

1) SDGIs arise from very small density differences resulting from the settling of particles at the top of the dense lower layer. In fact, the density of the destabilising layer and fingers is only 0.01 to 0.1 % greater than the density of the ambient fluid in experiments;

2) the mushroom shape that fingers develop during descent is associated with the formation of a vortex ring, as illustrated by PIV measurements on a 2D plane that evidence the presence of two counter-rotating vortices on the side of fingers. This is consistent with Rayleigh-Taylor structures (Sharp, 1984) that are produced for fluids of similar densities;

3) the radius of individual fingers increases with time through entrainment of the ambient fluid and is characterised by an entrainment coefficient of 0.28 ± 0.13, in good agreement with the entrainment coefficient for sediment thermals in the self-preserving phase (0.25 ± 0.1; Bush et al., 2003);

4) particle concentration, flow velocity and vorticity profiles are approximately symmetrical around finger centrelines and particles are fully coupled with the finger fluid;

5) the velocity within fingers is not homogeneous, with the narrow column feeding the finger head being faster with the potential to exceed the finger front velocity by a factor 4. In general, the velocity of particles entrained within fingers exceeds the individual settling velocity by one order of magnitude;

6) even if the particle concentration within fingers is not found to increase with respect to the upper layer, strong circulation within fingers has the potential to promote particle collisions, especially because of the interactions between eddies. The turbulence of natural volcanic ash fingers can further increase this potential.

Author contributions for Chapter 3

Allan Fries performed the experiments and analysed results. The manuscript was elaborated by Allan Fries and edited by all authors.

3.7 Appendix A3

Notations used in Chapter 3

Notation		**Units**
d	Particle diameter	m
f	Drag factor	
g	Gravitational acceleration	m s^{-2}
g'	Reduced gravity	m s^{-2}
h	Height of finger	m
r	Radius of a finger	m
t	Time	s
x	Horizontal position	m
z	Vertical position	m
A_{PBL}	Atwood number of the PBL	
A_u	Atwood number of the upper layer	
B_1	Ratio V_i over V_p	

Notation		Units
B_2	Ratio τ_i over τ_c	
B_3	Ratio V_f over V_p	
C	Particle concentration	kg m^{-3}
$C_{\max}$	Maximum particle concentration	kg m^{-3}
C_u	Particle concentration of the upper layer	kg m^{-3}
D	Fluorescent dye concentration	kg m^{-3}
D_u	Fluorescent dye concentration of the upper layer	kg m^{-3}
F	Fluorescence intensity	
Gr	Grashof number	
Gr_c	Critical Grashof number	
H	Thickness of the particle-laden layer	m
L^*	Ratio of the particle-laden layer over the PBL thickness	
R^2	Coefficient of determination	
Re	Reynolds number	
Re_p	Particle Reynolds number	
St	Stokes number	
U	Horizontal velocity	m s^{-1}
U_e	Radial entrainment velocity	m s^{-1}
V	Vertical velocity	m s^{-1}
V_c	Centreline vertical velocity	m s^{-1}
V_f	Characteristic finger velocity	m s^{-1}
V_i	Growth rate of the instability	m s^{-1}
$V_{\max}$	Maximum vertical velocity within fingers	m s^{-1}
V_p	Individual particle settling velocity	m s^{-1}
X_f	Concentration of upper fluid	
X_p	Particle volume fraction	
α_e	Entrainment coefficient	
β	Constant plume growth parameter	
δ	PBL thickness	m
μ	Dynamic viscosity	Pa s

Notation		**Units**
ν	kinematic viscosity	$m^2\ s^{-1}$
ρ_a	Ambient density	$kg\ m^{-3}$
ρ_f	Density of the fluid phase	$kg\ m^{-3}$
ρ_m	Bulk mixture density	$kg\ m^{-3}$
ρ_p	Particle density	$kg\ m^{-3}$
ρ_{PBL}	PBL density	$kg\ m^{-3}$
ρ_s	Density of the sugar solution	$kg\ m^{-3}$
ρ_w	Density of fresh water	$kg\ m^{-3}$
τ_c	Timescale for collective settling	s
τ_i	Timescale for individual particle settling	s
ω	Vorticity	s^{-1}
Σ	Sedimentation number	

Table A3.1: List of symbols

Chapter 4

Formation and characteristics of rapidly descending ash-laden currents below volcanic clouds.[1]

4.1 Introduction

Fragmentation associated with explosive volcanic eruptions generates particles of various sizes ranging from blocks and bombs (diameter $d > 64$ mm) to lapilli ($2 < d < 64$ mm) and ash ($d < 2$ mm). These fragments are collectively called tephra when ejected into the atmosphere, irrespective of their size. Whilst large blocks and bombs typically decouple from the upward-moving eruption column and follow ballistic trajectories (Biass et al., 2016b; Taddeucci et al., 2017; Massaro et al., 2022), lapilli and ash may ascend within the volcanic plume and are dispersed by winds further from the source (Carey and Sparks, 1986; Bonadonna et al., 2015b). The residence time, and consequently the travel distance, of tephra in the atmosphere is strongly dependent on the particle terminal fall velocity that is controlled by their physical properties, including their size, density and shape (Bonadonna et al., 1998; Mele et al., 2011; Bagheri and Bonadonna, 2016a; Saxby et al., 2018). In general, large and dense tephra particles settle close to the vent, whereas smaller and lighter particles are transported further downwind. Volcanic ash can, therefore, travel hundreds to thousands of kilometres in the atmosphere before settling (Prata,

[1]To be submitted to *Journal of Volcanology and Geothermal Research* as: Fries, A., Lemus, J., Jarvis, P. A., Scollo, S. and Bonadonna, C. : Hands on ash fingers: formation and characteristics of rapidly descending ash-laden currents below volcanic clouds.

2009; Cashman and Rust, 2020). Resulting tephra fallout deposits typically thin with increasing distance from the vent, and the size of deposited tephra typically diminishes with distance from the vent (Pyle, 1989; Bonadonna and Costa, 2012).

Collective sedimentation processes and specific atmospheric conditions can modulate the longevity of volcanic ash in the atmosphere (Del Bello et al., 2017; Gouhier et al., 2019), as well as the properties of tephra deposits. Fine volcanic ash ($d < 63$ 100 µm) commonly settles as aggregates that deposit much faster than individual particles (Rose and Durant, 2011). Conversely, depending mainly on the aggregate type (Brown et al., 2012; Bagheri et al., 2016) and porosity, particle aggregation has the potential to delay the sedimentation of coarser volcanic ash (Rossi et al., 2021). In many cases, the occurrence of secondary thickness maxima in tephra deposits can be attributed to the effect of particle aggregation (Scasso et al., 1994; Bonadonna and Phillips, 2003; Tsuji et al., 2020) that is also characterised by bimodal grainsize distributions due to the breaking of particle clusters upon impact (Carey and Sigurdsson, 1982; Bonadonna et al., 2011). Additionally, it has also been showed that topographically induced vertical oscillations in the wind velocity can impact the deposition of volcanic ash by increasing the particle terminal fall velocity (Poulidis et al., 2017, 2021; Takemi et al., 2021). Hence, these orographic effects can also explain the occurrence of some secondary thickness maxima in mountainous regions (Watt et al., 2015; Eychenne et al., 2017; Poulidis et al., 2018).

Instabilities forming beneath volcanic ash clouds can generate rapidly descending particle-laden currents (called ash fingers) that also have the potential to prematurely scavenge fine volcanic ash in the atmosphere, as fingers propagate at speeds greater than the terminal fall velocity of their constitutive particles (Carazzo and Jellinek, 2012, 2013; Manzella et al., 2015). Ash fingers take the form of approximately vertical columns, similar in appearance to virga, precipitation shafts or microburst (Houze et al., 1993) observed at the base of meteorological clouds, within which volcanic ash settle collectively at speeds greater than their individual terminal fall velocity. However, the characterisation of natural ash fingers and their formation mechanism remains incomplete since very few measurements of their properties have been reported.

The atmospheric dispersal and subsequent sedimentation of volcanic ash represent potentially severe hazards affecting human societies over wide spatial and temporal scales (Blong, 1984; Jenkins et al., 2015; Bonadonna et al., 2021). In fact, volcanic ash fall can be life-threatening and cause immediate damage to buildings and infrastructures in areas close to active volcanoes (Spence et al., 2005; Wilson et al., 2012, 2015; Jenkins et al., 2015). Even very far from the source, volcanic ash can notably disrupt air traffic and have heavy economic repercussions (Mazzocchi et al., 2010; Alexander, 2013; Guffanti and Tupper, 2015; Prata and Rose, 2015). In order to mitigate these impacts, accurate Volcanic Ash Transport and Dispersal Models (VATDMs) have been instituted for forecasting the spatial distribution of volcanic ash in the atmosphere (Searcy et al., 1998; Bonadonna et al., 2012). For simulating volcanic ash transport, VATDMs combine atmospheric models with the parameterisation of volcanic clouds, including the characterisation of the source (e.g., eruptive parameters) and sink (e.g., sedimentation) terms. Although some VATDMs have already reached a high level of complexity (Hurst and Davis, 2017; Folch et al., 2020; Beckett et al., 2022), notably with regards to the possibility to account for volcanic ash aggregation, the description of the sink term can be improved by implementing additional physical processes affecting the settling speed of volcanic ash (Bonadonna et al., 2012; Durant, 2015). In particular, VATDMs would benefit from the quantitative description of instabilities forming underneath volcanic ash clouds that lead to the development of ash fingers. To do so, a good preliminary understanding of these phenomena and of their effect on tephra sedimentation is required.

In this work, we first review previous observations of downward-moving ash-laden currents formed below volcanic ash clouds, and we summarise the mechanisms that have been proposed to explain the formation of ash fingers. We then present new field measurements of ash fingers. Finally, using a supplementary catalogue of previously-studied volcanic eruptions, we quantify the conditions promoting the onset of ash fingers.

4.2 Current understanding of ash fingers

4.2.1 Observations

The destabilisation of volcanic ash cloud undersides has been observed during various eruptions, leading to the formation of descending particle-laden currents. All of these observations, and associated references, are presented in Table 4.1. Although previous publications have used various terms to describe these currents (e.g., "ash veils", Hobbs et al., 1991; "streak fallouts", Eliasson et al., 2014; Eliasson, 2020; "sediment thermals", Freret-Lorgeril et al., 2020; Figure 4.1), in this work we refer to these currents as "ash fingers" (Bonadonna et al., 2002b; Carazzo and Jellinek, 2012; Andronico et al., 2015), irrespective of the formation mechanism. Mammatus are also considered in the following review, but their specificities require us to separate them from other phenomena in the terminology (see in sections 4.2.1 and 4.2.2).

Volcano	Year	Observed features	Methods used	W (m)	λ (m)	V_f (m s^{-1})	References
Soufrière Hills	1997	Ash fingers	Visual observations	-	-	-	Bonadonna et al. (2002b)
Ruapehu	1996	Ash fingers	Visual observations	-	-	-	Bonadonna (2005a)
Etna	2013	Ash fingers	Visual observations	-	-	-	Andronico et al. (2015); Scollo et al. (2017)
Eyjafjallajökull	2010	Ash fingers	Visual observations and correlation with tephra deposits	142 – 194	120 – 240	0.5 – 1.5	Bonadonna et al. (2011); Manzella et al. (2015)
Mount Redoubt	1990	Ash veils and mammatus	Lidar detections	250 – 300	350 – 400	-	Hobbs et al. (1991)
Sakurajima	2013	Streak fallouts	Visual observation and particle concentration measurements	666	-	0.34	Eliasson et al. (2014)
Grímsvötn	2004	Streak fallouts	Visual observations	-	-	-	Eliasson et al. (2014)
Sakurajima	2019	Ash fingers	Visual observations	-	-	-	Fries et al. (2021)
Stromboli	2015	Wind-driven ash fingers	Visual observations, disdrometer and Doppler radar	100 – 600	-	0.55 – 1.92	Freret-Lorgeril et al. (2020)
Mount Saint Helens	1980	Mammatus	Visual observations	250 – 8000	-	3	Schultz et al. (2006); Durant et al. (2009)

Table 4.1: Summary of observations and measurements of ash fingers. W is the finger width, λ the spacing between fingers and V_f the finger downward velocity. For the 1980 eruption of Mount Saint Helens, the values of W and V_f are averages for mammatus lobes, as reported by Schultz et al. (2006). W and λ have been estimated from Plate 1 of Hobbs et al. (1991) for the 1990 eruption of Mount Redoubt.

Ash fingers and gravitational instabilities

Few authors have described sedimentation within ash fingers. First, Bonadonna et al. (2002b) noticed the presence of "finger-like protrusions" in the sedimentation of volcanic ash from the September 1997 eruption of Soufrière Hills (Montserrat) volcano (Figure 4.1A). In June 1996, Bonadonna (2005a) described "instability structures" potentially enhancing the deposition of fine volcanic ash below a weak volcanic plume from Ruapehu (New-Zealand) (Figure 4.1B). Andronico et al. (2015) and Scollo et al. (2017) later presented the development of ash fingers affecting sedimentation from the 23 November 2013 lava fountain of Etna volcano (Italy) (Figure 4.1C).

One of the most complete characterisation of natural ash fingers has been performed by Manzella et al. (2015) for the 4 May 2010 eruption of Eyjafjallajökull (Iceland) (Figure 4.1D). From high-resolution videos, they estimated that ash fingers formed at the base of the volcanic ash cloud at a distance $\approx$ 1.4 km from the vent, and reached the ground approximately 10 km downwind. Fingers had average widths of 168 $\pm$ 26 m, and spacings of 180 $\pm$ 60 m. They find that ash fingers propagated at 1 $\pm$ 0.5 m s^{-1} downward and at 8.5 $\pm$ 0.8 m s^{-1} horizontally, which is consistent with a volcanic plume spreading at 7.9 $\pm$ 1.3 m s^{-1}. The vertical speed of fingers corresponded to the terminal fall velocity of ash particles with diameters $d \approx 200$ µm, as calculated with the model of Ganser (1993), and to particle volume fractions of $1 \times 10^{-6} - 4 \times 10^{-6}$ within fingers. Additionally, tephra sedimentation and resulting deposits are extensively documented for this eruption (Bonadonna et al., 2011). Aggregates (coated particles and fragile ash clusters) that broke on impact with the ground occur at $\approx$ 10 km from the vent, as well as bimodal deposits with a coarse ($d \approx 500$ µm) and a fine ($d \approx 150$ µm) mode. The origin of the fine grainsize mode in bimodal deposits is interpreted as either the result of aggregates breaking upon impact, or of fine particles being transported within fingers at speeds higher than their terminal fall velocity. The coincidence of both particle aggregation and ash fingers reaching the ground approximately 10 km from the vent also raised the question of a possible relation between the two phenomena, notably as particle aggregation could happen both in the volcanic plume and in ash fingers.

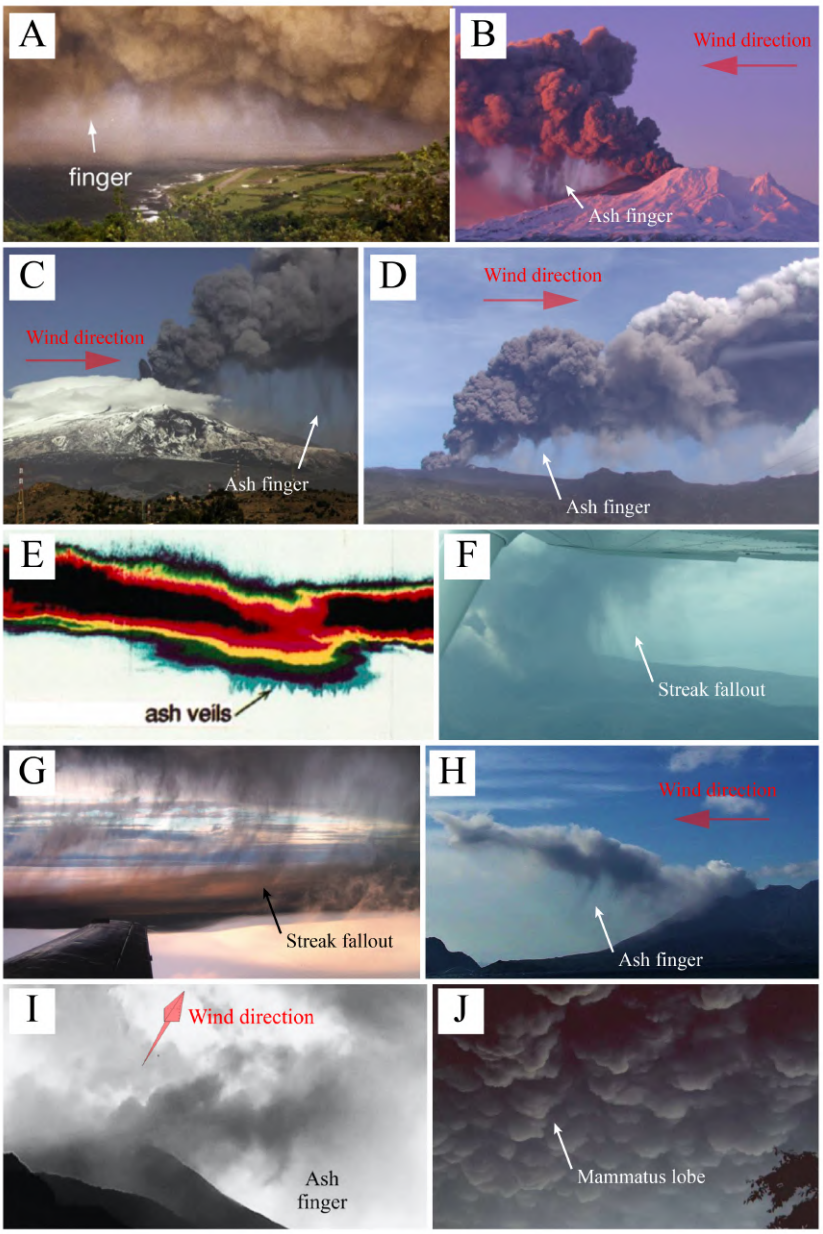

Figure 4.1: Ash fingers reported below volcanic ash clouds in previous publications at **(A)** Soufrière Hills, Montserrat, in September 1997 (Bonadonna et al., 2002b; modified by Carazzo and Jellinek, 2012), **(B)** Ruapehu, New Zealand, in June 1996 (Bonadonna, 2005a; picture from Scollo et al., 2017), **(C)** Etna, Italy, in November 2013 (Andronico et al., 2015; Scollo et al., 2017), **(D)** Eyjafjallajökull, Iceland, in May 2010 (Bonadonna et al., 2011; Manzella et al., 2015), **(E)** Mount Redoubt, USA, in January 1990 (Hobbs et al., 1991), **(F)** Sakurajima, Japan, in July 2013 (Eliasson et al., 2014), **(G)** Grímsvötn, Iceland, in November 2004 (Eliasson et al., 2014), **(H)** Sakurajima, in November 2019 (Fries et al., 2021), **(I)** Stromboli, Italy, in September – October 2015 (Freret-Lorgeril et al., 2020). **(J)** Mammatus formed below the ash cloud of Mount Saint Helens, USA, in May 1980 (Schultz et al., 2006). Panel E is a false-colour image of lidar backscattering measurements, black/red and blue/white indicating high and low backscatter values, respectively.

Ash veils

Using lidar backscattering measurements, Hobbs et al. (1991) reported the occurrence of "ash veils" in the ash fallout from the 1990 eruptions of Mount Redoubt volcano (USA). These ash fingers formed underneath the volcanic plume, approximately 130 to 180 km downwind of the source. Although their properties have not been further characterised, we can estimate from their measurements (Figure 4.1E) that ash fingers were approximately 250 to 300 m wide, and that the spacing between them was about 350 – 400 m.

Streak fallouts

From visual observations at Sakurajima volcano (Japan) in 2013 (Figure 4.1F), and during the 2004 Grímsvötn eruption (Figure 4.1G), Eliasson et al. (2014) have recognised "streak fallouts" below volcanic ash clouds that appeared as discrete sedimentation columns. Additional airborne measurements of the particle concentration were performed during campaigns at Sakurajima using optical particle counters onboard observation aircraft. Eliasson et al. (2014) report ash fingers width of 666 m, and calculate average descent velocities of 0.34 m s^{-1} based on the mass flow within ash fingers. This corresponds to the terminal fall velocity of 66 µm grains. From their measurements, we can estimate that the maximum particle concentration detected during their flights in ash fingers was approximately 50 mg m^{-3}. We also note that, in 2019, Fries et al. (2021) (Chapter 2) also identified the occurrence of ash fingers at Sakurajima (Figure 4.1H).

Fingering sediment thermals

Freret-Lorgeril et al. (2020) revealed the presence of "fingering sediment thermals" in the sedimentation of weak short-lived plumes from Stromboli volcano (Italy) in 2015. They used detailed Doppler radar time series to highlight the presence of discrete reflectivity features in tephra fallouts interpreted as ash fingers, confirmed by complementary visual observations (Figure 4.1I). The fingers' widths increased with time, ranging from $\approx$ 100 to $\approx$ 600 m, and their downward velocities were estimated at 0.55 – 1.92 m s^{-1}, corresponding to the terminal fall velocity of 100

– 300 µm particles. Moreover, Freret-Lorgeril et al. (2020) derived maximum ash concentrations of 681 mg m^{-3} based on disdrometers that recorded the fallout of 230 – 690 µm particles at velocities 0.7 – 3.2 m s^{-1} on the ground.

Mammatus clouds

Observations of mammatus below volcanic ash clouds are documented by Schultz et al. (2006) and Durant et al. (2009). Mammatus are descending pouch-like lobes (i.e., finger-like structures) occurring on the underside of a wide variety of clouds (e.g., cumulonimbus, altocumulus, altostratus, stratocumulus, cirrus, and volcanic ash clouds; Schultz et al., 2006). From their review of available mammatus observations, Schultz et al. (2006) indicate that the width of individual mammatus lobes is 250 m to 8 km, with average values of 1 – 3 km. Mammatus fields can both appear in small cloud sections, or over hundreds of kilometres, for durations ranging from 15 minutes to several hours. The vertical extent of mammatus is ≈ 0.5 km below clouds' base, and typical descending current motion is ≈ 3 m s^{-1}. Mammatus were also described on the underside of the volcanic ash clouds of Augustine volcano (USA) in March 1986 and Mount Saint Helens (USA) on 18 May 1980 (Schultz et al., 2006) (Figure 4.1J). More recently, mammatus have been distinguished below the ash cloud produced by Grímsvötn on 21 – 28 May 2011 (Prata et al., 2017). In their study of the 1980 Mount Saint Helens eruption, Durant et al. (2009) have highlighted the presence of a distal mass deposition maxima ≈ 300 km from the vent in the same region where mammatus lobes were observed and aggregates deposited. Moreover, they show that the settling rate of particles < 100 µm was greatly enhanced through aggregation favoured by the conditions resulting from the formation of mammatus lobes and rapid cloud subsidence that largely exceeded the terminal fall velocity of individual volcanic ash particles.

4.2.2 Formation mechanisms of ash fingers and mammatus

As seen above, ash fingers can take several forms and different formation mechanism have been proposed. These formation mechanisms are not necessarily contradictory, but instead apply to different types of eruptions, under different conditions, and

for different regions of volcanic ash clouds. Whilst individual particle settling (IPS) of coarse tephra (i.e., blocks, lapilli) dominates in regions closest to the source of volcanic plumes, Figure 4.2 proposes a general overview of the ash finger formation mechanisms described in previous studies for strong, vertical (Figure 4.2A), and weak, wind-bent (Figure 4.2B) volcanic plumes.

Sediment waves

Close to the source of strong, typical Plinian eruption columns, Gilchrist and Jellinek (2021) have studied the formation of periodic "sediment waves" (SWs) with exhaustive particle-laden jet experiments. SWs are intermittent annular waves carrying downward particles and entrained jet fluid around the volcanic jet faster than the particle terminal fall velocity. The frequencies of jet oscillations and SW formation overlap, indicating that SWs originate from the periodic collapse of the jet mixture, notably from the overshoot region. SWs can transport coarse tephra to the ground at greater rates than individual fallout and entrain smaller particles as well, with implications for the plume structure and proximal deposits of Plinian eruptions, including the formation of multiply-layered ash clouds upon dilution of SWs through entrainment of the surrounding fluid. Although SWs differ from ash fingers, they are presented in this work, as they have the potential to enhance volcanic ash sedimentation close to volcanic jets through collective settling in descending gravity currents.

Settling-driven gravitational instabilities (SDGIs)

Further from the vent, the volcanic tephra cloud spreads downwind at the level of neutral buoyancy H_b (Sparks, 1986; Bonadonna and Phillips, 2003). In this context, ash fingers can originate from settling-driven gravitational instabilities (SDGIs) (Carazzo and Jellinek, 2012; Manzella et al., 2015; Scollo et al., 2017; Fries et al., 2021; Lemus et al., 2021) that are alternatively called more generally "convective instabilities" in a number of earlier publications (Bonadonna et al., 2002b; Bonadonna, 2005a; Bonadonna et al., 2011). SDGIs arise from the settling of dense particles across an interface between a particle suspension (or particle-laden current) and an

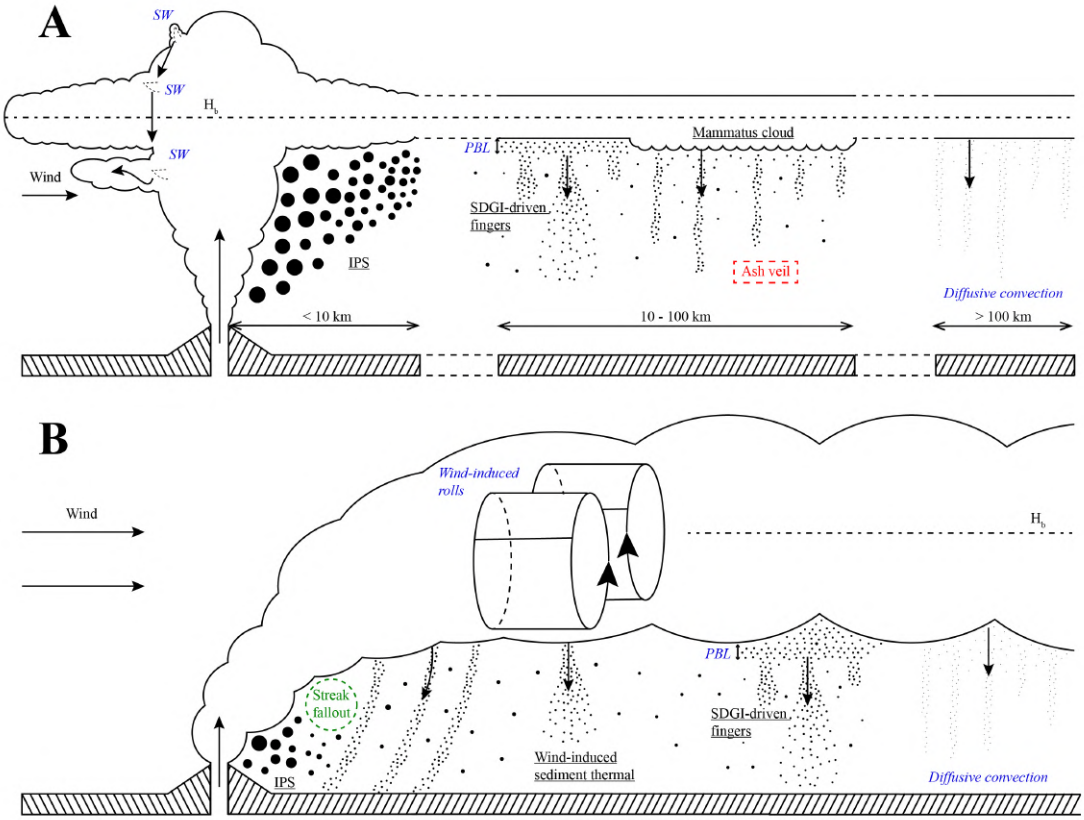

Figure 4.2: Overview of ash finger and mammatus observations and formation mechanisms for **(A)** strong (vertical), and **(B)** weak (bent-over) volcanic plumes. Acronyms and symbols are: IPS for Individual Particle Settling, SW for Sedimentation Wave, PBL for Particle Boundary Layer, SDGI for Settling-Driven Gravitational Instability and H_b for the height at which the volcanic plume reaches the level of the neutral buoyancy. Black underlined font indicates mechanisms that have been directly observed and modelled experimentally and/or numerically. Blue italic font is for processes and features supported by theoretical, experimental, and/or numerical investigations and indirect observations. In green (circled), we report mechanisms that are theorised and directly observed, but without experimental and/or numerical validation. Finally, in red (in rectangles), are features that are directly observed, without supporting theoretical, experimental or numerical models.

underlying denser ambient (Hoyal et al., 1999b). Although the configuration is initially gravitationally stable, with a light fluid emplaced above a denser one, settling of particles into the top of the dense lower layer creates an increase in the bulk density below the initial interface that triggers a Rayleigh-Taylor-like instability (Sharp, 1984) and the onset of fingers.

Depending on the density contrast between the particle suspension and the denser ambient, settling particles are either slowed at the interface and accumulate, for high density and viscosity contrasts (Carey, 1997; Manville and Wilson, 2004; Jacobs et al., 2013), or are not significantly slowed, for smaller contrasts (Fries et al., 2021; Lemus et al., 2021). In the first case, particle accumulation results in the formation of a dense interfacial layer with greater particle concentrations than the upper particle suspension. This is notably seen for volcanic ash settling at the top of water bodies, where particles are considerably slowed at the air-water interface (Carey, 1997; Manville and Wilson, 2004; Jacobs et al., 2013). In the second case, the particle concentration does not increase across the interface between fluids of similar densities and viscosities. However, the bulk density of the particle-fluid mixture increases below the particle suspension as particles settle and are incorporated in a denser ambient. This is evidenced for simple two-layer experimental configurations (Fries et al., 2021) and numerical simulations (Lemus et al., 2021) modelling the settling of a particle suspension on top of a denser ambient in water, and supported by theoretical scenarios describing the growth of a heavy "nose region" below particle suspensions (Burns and Meiburg, 2012, 2015; Yu et al., 2013; Davarpanah Jazi and Wells, 2020). Here, the dense particle-laden layer that destabilises and detaches as fingers is called the Particle Boundary Layer (PBL), regardless of its particle concentration. It is worth mentioning that SDGIs can affect particle deposition in a variety of natural settings other than volcanic ash clouds and especially riverine plumes (Hoyal et al., 1999b; Maxworthy, 1999; Parsons et al., 2001; Henniger and Kleiser, 2012; Davarpanah Jazi and Wells, 2016; Sutherland et al., 2018).

Formation of mammatus clouds

Several mechanisms have been advanced to explain the formation of mammatus clouds (Schultz et al., 2006). Among them, the most important mechanisms have been identified as (i) ash-hydrometeor evaporation/sublimation, (ii) ash-hydrometeor settling, and (iii) cloud-base detrainment instability (CDI) (Schultz et al., 2006; Kanak et al., 2008; Durant et al., 2009). Ash-hydrometeor evaporation/sublimation mechanisms involve the formation of a cold air layer at the cloud base due to the absorption of latent heat when water droplets or ice crystals fall into dry air and evaporate or sublimate, respectively. This cold air layer at the cloud base then descends as mammatus lobes once it becomes denser than the underlying atmosphere. Similarly to SDGIs, ash-hydrometeor settling at the cloud base can generate an instability and the subsequent formation of descending finger-like structures (Ravichandran et al., 2020). (iii) CDI arises from the spontaneous mixing of moist air in underlying warm, dry air (Emanuel, 1981; Kanak et al., 2008). This subtly differs from ash-hydrometeor evaporation/sublimation mechanism because hydrometeors are introduced in dry air by mixing induced by shear, rather than by fallout (Schultz et al., 2006). Interestingly, mammatus lobes have been reported to form under ash plumes from Mount Redoubt in 1990, and the "ash veils" observed by Hobbs et al. (1991) could be reminiscent of bursting mammatus lobes (Schultz et al., 2006).

Diffusive convection

Very far from the vent, diffusive convection can result in double-diffusive fingers that affect the finest fraction of volcanic ash (Carazzo and Jellinek, 2013). Double-diffusive fingers are thin, elongated, descending structures formed as a result of the differential diffusion of density-altering components. A classic example of double-diffusive fingers are "salt fingers" that originate in oceans at the boundary between warm, salty layers and underlying colder, fresher water (Turner, 1967). Even if the initial density configuration is stable in this case, rapid diffusion of heat and simultaneous slow diffusion of salt leads to the formation of a heavy, unstable layer that is both cold and salty, causing the onset of fingering instabilities. This process can also affect particle suspensions, or particle-laden plumes, when the rapid diffusion of

heat and fine, slowly settling particles are involved and may be treated as the slow-diffusive component in the system (Green, 1987; Chen, 1997; Hoyal et al., 1999a; Parsons et al., 2001). Double-diffusive fingers also have the potential to enhance particle sedimentation. For volcanic ash clouds, diffusive convection can arise from the differential diffusion of slowly-diffusing very fine particles and rapidly-diffusing heat (Carazzo and Jellinek, 2013).

Streak fallouts

Weak volcanic plumes, bent over by the wind, are associated with the majority of ash fingers observations. Close to the vent, where volcanic plumes raise in the atmosphere, "streak fallouts" (i.e., ash fingers) are interpreted by Eliasson et al. (2014) and Eliasson (2020) as the result of the cooling of lower parts of rising volcanic plumes that start much hotter than the environment. In this case, ash fingers form when volcanic ash loading exceeds the maximum carrying capacity of the density stratification inside the cloud that can be expressed as a function of temperature difference between the plume and the atmosphere.

Wind-induced ash fingers

Wind-induced ash fingers can form if volcanic ash in a cloud settles slower than the horizontal wind velocity, as described by the conceptual model of Freret-Lorgeril et al. (2020), based on both natural observations at Stromboli and simple qualitative experiments. First, wind-driven organisation of the ash cloud happens when subjected to sufficiently strong winds, with the development of counter rotating rolls comparable in size to the cloud thickness. Second, these wind-induced rolls enhance the delivery of particles to the cloud base, producing a dense basal layer, especially where the rolls converge. Third, similarly to SDGIs, gravitational instabilities initiate below this dense particle-laden layer (i.e., PBL) resulting in the formation of ash fingers. Fourth, fingers entrain ambient fluid, expand and decelerate during descent, as described for sediment thermals (Rahimipour and Wilkinson, 1992; Bush et al., 2003; Zhao et al., 2014). Finally, a new generation of fingers forms below the first one.

Differences between weak and strong volcanic plumes

Streak fallouts and wind-induced processes are not expected to form beneath strong volcanic plumes, whilst SW formation is limited to strong Plinian columns. Mammatus clouds have not been observed below weak volcanic plumes, although their formation is possible in theory for favourable atmospheric conditions. Finally, SDGIs and diffusive convection can potentially trigger the formation of ash fingers for both strong and weak volcanic plumes.

4.2.3 Quantitative constraints on the onset and properties of ash fingers

For all formation mechanisms, a common characteristic of resulting ash fingers is that they inevitably have to propagate faster than the individual terminal fall velocity of their constitutive particles (Durant et al., 2009; Carazzo and Jellinek, 2012; Eliasson et al., 2014; Manzella et al., 2015; Scollo et al., 2017; Freret-Lorgeril et al., 2020). In other terms, the downward velocity of ash fingers V_f must be greater than the terminal fall velocity of individual particles V_p. Classically, this criterion is evaluated using the ratio (Marsh, 1988; Hoyal et al., 1999b; Carazzo and Jellinek, 2012; Chapter 3)

$$B = \frac{V_f}{V_p}, \tag{4.1}$$

where the finger velocity can be estimated from the combination of the buoyancy and volume fluxes as (Hoyal et al., 1999b; Carazzo and Jellinek, 2012)

$$V_f = \left(\frac{g X_p \left(\rho_p - \rho_a\right)}{\rho_a}\right)^{2/5} \left(\frac{\pi V_p \delta_f^2}{4}\right)^{1/5}, \tag{4.2}$$

with $g = 9.81$ m s^{-2} the gravitational acceleration, X_p the particle volume fraction, ρ_p and ρ_a the particle and ambient (air) density, respectively, and δ_f the finger characteristic length scale that corresponds to the thickness of the destabilizing particle-laden layer (i.e., the PBL) δ_{PBL}. Fingers can form only if $B > 1$. This is an intuitive condition, as particles would leave the current and inhibit the formation of ash fingers otherwise ($B < 1$). In fact, ash fingers can form only if their constitutive

particles are fully coupled with the descending flow, i.e., for dimensionless Sedimentation (Σ) and Stokes (St) numbers below 1 (Burgisser et al., 2005; Carazzo and Jellinek, 2012; Scollo et al., 2017; Roche and Carazzo, 2019; Fries et al., 2021). Σ is the reciprocal of B

$$\Sigma = \frac{V_p}{V_f} = \frac{1}{B}, \tag{4.3}$$

whilst St is defined as

$$\mathrm{St} = \frac{(\rho_p - \rho_a) d^2 V_f}{18 f \mu \delta}, \tag{4.4}$$

with f the drag factor and μ the ambient dynamic viscosity.

The second shared consideration is that ash fingers are gravity currents originating from density differences between the volcanic ash cloud and the underlying atmosphere, similarly to Rayleigh-Taylor-like fingering instabilities (Sharp, 1984; Völtz et al., 2001) which occur at the interface between fluids of different densities, when a dense fluid is emplaced above a lighter one. These density differences lead to unstable density configurations that trigger instabilities at the cloud base and, ultimately, the formation of fingers (Durant et al., 2009; Carazzo and Jellinek, 2012, 2013; Eliasson et al., 2014; Manzella et al., 2015; Scollo et al., 2017; Freret-Lorgeril et al., 2020). Critical differences in the proposed scenarios for the onset of ash fingers lie in the processes explaining the source of the density differences.

Sediment waves

SW descending around jet columns periodically originate from the overshoot region of rising particle-laden jets (Gilchrist and Jellinek, 2021). Hence, depending on the jet regime, the characteristic frequency for SWs f_{SW}, defined as

$$f_{SW} = \frac{V_{SW}}{\lambda_{SW}}, \tag{4.5}$$

with V_{SW} the descent speed of SWs and λ_{SW} the distance between successive SWs, overlaps with either that of the overshoot oscillations or the fountain collapse frequency. This can be used to diagnose if descending currents around volcanic jets are SWs, by comparing their frequency of occurrence with that of overshoot oscillations or fountain collapse.

Settling-driven gravitational instabilities

The conditions leading to the destabilisation of a PBL produced by particle settling across a density interface depend on the ratio between destabilising gravitational forces and resisting viscous forces (Hoyal et al., 1999b; Carazzo and Jellinek, 2012). This is quantified through the dimensionless Grashof number Gr that can be written as

$$Gr = \frac{gX_p\left(\rho_p - \rho_a\right)\rho_a\delta_{PBL}^3}{\mu^2}, \tag{4.6}$$

when particles are the density-altering component. Above a critical Grashof number $Gr_c = 10^4$ in aqueous experiments (Fries et al., 2021), the PBL detaches, leading to convection. Hence, the PBL becomes unstable only if it can reach a critical thickness δ_c that diminishes as a function of the particle volume fraction (Jacobs et al., 2015). This criterion can be expressed through the dimensionless number

$$L^* = h\left(\frac{gX_p\left(\rho_p - \rho_a\right)\rho_a}{Gr_c\mu^2}\right)^{1/3}, \tag{4.7}$$

that corresponds to the ratio of the cloud thickness h over δ_c (Fries et al., 2021). At $L^* \gg 1$, the cloud is sufficiently thick to sustain an unstable PBL, whereas a critically thick PBL cannot grow below clouds characterised by $L^* \approx 1$, or $L^* < 1$. As a consequence, thick volcanic ash clouds, containing large quantities of volcanic ash, are expected to favour the development of ash fingers, in contrast with thin ash-poor volcanic clouds.

SDGIs generate fingers from the detachment of the PBL. As a result, the length scales of ash fingers originating from SDGIs are expected to be proportional to the PBL thickness δ_{PBL} (Hoyal et al., 1999b; Carazzo and Jellinek, 2012; Manzella et al., 2015; Scollo et al., 2017). The width of individual fingers W, and the spacing between them λ, have been measured to be approximately twice and thrice the PBL thickness, respectively (i.e., $W \approx 2\delta_{\mathrm{PBL}}$, $\lambda \approx 3\delta_{\mathrm{PBL}}$ and $\lambda \approx 3W/2$) (Fries et al., 2021).

Diffusive convection

As described by Green (1987), Hoyal et al. (1999a) and Carazzo and Jellinek (2013), diffusive convection can happen below particle-laden clouds if

$$R_T = \frac{\alpha_T \Delta T}{\beta_m \Delta C_m} < \left(\frac{\kappa_T}{\kappa_p}\right)^{3/2} , \tag{4.8}$$

with R_T the stability ratio, α_T the volumetric expansion coefficient for some density-altering component, e.g., heat or a solute, ΔT and ΔC_m the temperature and particle concentration (expressed as a mass fraction) difference between the cloud and the atmosphere, β_m the volumetric expansion coefficient for a particle suspension, κ_T and κ_p the diffusion coefficients of heat and particles, respectively. Typical values of these parameters suggest that criterion of equation (4.8) is largely respected for particles smaller than 10 µm in volcanic ash clouds (Carazzo and Jellinek, 2013). Moreover, double-diffusive fingers contribute to the sedimentation below volcanic ash clouds if the diffusive convective flux of particles crossing the interface F_D is high enough compared to the flux by individual particle settling F_I. This is quantified by the ratio

$$F^* = \frac{F_D}{F_I}. \tag{4.9}$$

Diffusive convection dominates for $F^* > 100$, whereas individual particle settling governs sedimentation for $F^* < 0.01$. Both processes are important for $0.01 < F^* < 100$ (Carazzo and Jellinek, 2013). Based on particle size and concentration measurements obtained from a variety of remote sensing techniques, Carazzo and Jellinek (2013) show that F^* ranges between 0.01 and 100 for several volcanic ash clouds, with increasing F^* as a function of time and distance from the vent.

Streak fallouts

Eliasson et al. (2014) and Eliasson (2020) hypothesise that the onset of ash fingers below hot, rising, volcanic plumes (i.e., "streak fallouts") is an instability process that cannot be predicted in the time domain but that the conditions leading to the formation of streak fallouts can be described theoretically. In this context, ash fingers potentially arise if the volume fraction of volcanic ash X_p becomes greater than the

maximum transportable particle concentration (or maximum carrying capacity) C_{mp} that can be defined as the ratio (Eliasson, 2020)

$$C_{\mathrm{mp}} = \frac{\Delta T}{T_p}, \tag{4.10}$$

with T_p the plume temperature. The volcanic plume is stably stratified for $X_p < C_{mp}$, whereas ash fingers rapidly jettison the excess volcanic ash under the form of "streak fallouts" for $X_p > C_{mp}$ and $X_p \approx C_{mp}$. When volcanic plumes reach H_b, and become neutrally buoyant due to the diminution of the plume temperature and removal of excess mass load, the formation of ash fingers ceases as X_p becomes smaller than C_{mp}, explaining why ash fingers are predominantly observed close to volcanic vents (Eliasson, 2020).

Wind-induced fingers

Wind-induced rolls in a volcanic ash cloud which form over a timescale t_w can only modulate the sedimentation of particles settling over a lower, or similar timescale t_p (Freret-Lorgeril et al., 2020). These timescales can be expressed as a function of the cloud thickness h, horizontal wind velocity V_w, and particle individual settling velocity V_p, resulting in the following criterion for the development of wind-induced fingers

$$t_w = \frac{h}{V_w} \gtrsim t_p = \frac{h}{V_p}. \tag{4.11}$$

If this condition is satisfied, wind-induced ash fingers can develop from a distance

$$d_0 = t_w V_c \approx t_w V_w = h \tag{4.12}$$

from the vent, with V_c the cloud horizontal velocity that can be approximated by the wind velocity for clouds advected at the wind speed. In this case, wind-induced ash fingers are expected to start forming at the distance similar to the cloud thickness, as suggested by Freret-Lorgeril et al. (2020) for the 4 May 2010 volcanic plume of Eyjafjallajökull (Manzella et al., 2015) and the 23 November 2013 eruption of Mount Etna (Scollo et al., 2017).

Mammatus

Mammatus lobes can appear under specific conditions below volcanic ash clouds. Observations of mammatus under volcanic ash clouds are all associated with the presence of dry underlying air layers and possibly high water contents in the clouds (Schultz et al., 2006). These conditions favour the occurrence of evaporation/sublimation at the cloud base and are in good agreement with broader studies on the formation of mammatus clouds. Using 3D numerical simulations, Kanak et al. (2008) found that evaporation/sublimation at the cloud base is essential for the formation of mammatus that developed without settling, but not without evaporation/sublimation. Ravichandran et al. (2020) investigated in more detail the formation of mammatus by the combination of settling and evaporation/sublimation. They find that the size of the hydrometeors is a crucial factor controlling the structure of mammatus clouds. Whilst well-defined mammatus lobes developed for large hydrometeors ($d > 25$ µm), only stringy cloud structures, similar to double-diffusive fingers, developed for small hydrometeors ($d < 25$ µm). Furthermore, Kanak et al. (2008) have demonstrated that the CDI criterion (i.e., the liquid-water or ice-water static energy of the underlying warm, dry air is higher than that of the air in the cloud) is a necessary condition for the formation of mammatus. However, not all of their simulations satisfying the CDI criterion produced mammatus. The CDI criterion is, therefore, not a sufficient criterion. In summary, whilst the CDI criterion must be satisfied for mammatus clouds to form, evaporation/sublimation below the cloud base is the main mechanism driving the production of mammatus, with additional contribution from ash-hydrometeor settling that affects mammatus structures as a function of the particle size (lobes for $d > 25$ µm and filaments for $d < 25$ µm). For volcanic ash clouds, this implies that mammatus require a dry underlying atmosphere to form, and is favoured by the nucleation of ice (Durant et al., 2009), with coarse ash-hydrometeor particles promoting the development of well-defined mammatus lobes.

4.2.4 Summary and objectives of this study

We have summarised above the observations of ash fingers reported in the scientific literature (Figure 4.1 and Table 4.1), and we have presented the main mechanisms invoked to explain their formation and properties (Figure 4.2). Whilst previous studies agree that ash fingers are vertical density currents resulting from an increase of the cloud base density, several explanations are advanced to describe the conditions leading to this increase (i.e., oscillations from the overshoot region of volcanic jets, particle settling, double diffusion, cloud cooling, wind-driven internal cloud rolls, or evaporation/sublimation for mammatus clouds). The tendency to form ash fingers can be estimated from considerations depending on the formation mechanism that are summarised in section 4.2.3. However, as quantified by the dimensionless numbers B (equation 4.1), Σ (equation 4.3) and St (equation 4.4), a general condition for fingers to develop is that particles stay coupled to the flow within fingers (Hoyal et al., 1999b; Carazzo and Jellinek, 2012; Manzella et al., 2015; Scollo et al., 2017; Freret-Lorgeril et al., 2020).

The aim of this study is to provide additional characterisation of natural ash fingers based on visual observations in order to improve our general understanding. Where possible, these new measurements will be compared with theoretical considerations from previous studies in order to analyse the conditions leading to the formation of ash fingers and suggest probable formation mechanisms. Finally, the additional measurements will refine our comprehension of the ash fingers properties and their potential effect on volcanic ash sedimentation.

4.3 Methods

4.3.1 Field observations

In order to better constrain the conditions leading to the formation of ash fingers, we have collected additional information on the eruptions associated with observations of ash fingers or mammatus presented in Table 4.1. We have also included the May 2011 eruption of Grímsvötn during which mammatus have been observed (Prata et al., 2017). Additionally, we have complemented our investigation with

2 explosive events from Etna volcano where ash fingers were not observed (Scollo et al., 2017). These 2 eruptions are a low intensity explosive event that happened on 15 November 2010 and a lava fountain produced on 12 August 2011 (Scollo et al., 2012; Mereu et al., 2018). All additional information is presented in Table 4.2, combining measurements of the eruptive (i.e., top plume height H_t, plume thickness h, Mass Eruption Rate (MER), volume fraction of volcanic ash in the plume X_p) and atmospheric (i.e., horizontal wind speed V_w) parameters. We have used published data, notably the Independent Volcanic Eruption Source Parameter Archive (IVESPA) (Aubry et al., 2021), in order to obtain these parameters. When not directly available, the cloud thickness has been approximated from the plume top height as $h \approx 0.3H_t$ (Sparks, 1986). The volume fraction of volcanic ash in the plume has been calculated as a function of the ash concentration C and density ρ_p as $X_p = C/\rho_p$. Ash concentrations were measured using a variety of techniques including radar (Harris et al., 1981; Harris and Rose, 1983; Marzano et al., 2006), lidar (Scollo et al., 2012; Mereu et al., 2018), disdrometer (Freret-Lorgeril et al., 2020) and VATDM (Tesche et al., 2012) observations. The concentration inside ash fingers produced during the May 2010 eruption of Eyjafjallajökull was estimated from the finger velocity and width (Manzella et al., 2015). We consider an average density of 2600 kg m^{-3} for volcanic ash based on observations from Bonadonna et al. (2011) (averaged density for pumice fragments < 125 µm).

Volcano	Date	H_t (km a.v.)	h (km)	MER (kg s^{-1})	X_p	V_w (m s^{-1})	Obs.	References
Mount Saint Helens	18/05/1980	22.5	7.5	2.0×10^7	3.3×10^{-6}	16.4	Mammatus	Harris et al. (1981); Harris and Rose (1983); Carey and Sigurdsson (1985); Schultz et al. (2006); Durant et al. (2009); Aubry et al. (2021)
Ruapehu	17/06/1996	5.5	1.8	8.8×10^4	-	21.2	Ash fingers	Bonadonna (2005a); Aubry et al. (2021)
Grímsvötn	01/11/2004	9.0	3.0	3.7×10^6	1.5×10^{-6}	26.6	Ash fingers	Marzano et al. (2006); Eliasson et al. (2014)
Eyjafjallajökull	04/05/2010	2.9	2.0	2.0×10^5	1.5×10^{-6}	11.0	Ash fingers	Ripepe et al. (2013); Manzella et al. (2015)
Grímsvötn	21/05/2011	18.5	6.2	1.3×10^6	1.5×10^{-6}	6.6	Mammatus	Tesche et al. (2012); Prata et al. (2017)
Etna	15/11/2010	1.0	0.3	-	1.6×10^{-9}	-	-	Scollo et al. (2012); Mereu et al. (2018)
Etna	12/08/2011	5.9	1.9	-	6.9×10^{-9}	-	-	Scollo et al. (2017); Mereu et al. (2018)
Sakurajima	27/07/2013	-	-	-	1.9×10^{-8}	-	Ash fingers	Eliasson et al. (2014)
Stromboli	01/10/2015	-	-	-	2.5×10^{-7}	-	Ash fingers	Freret-Lorgeril et al. (2020)

Table 4.2: Main eruptive parameters associated with previously studied eruptions. H_t is the top plume height in km above the vent (a.v.), h the plume thickness, MER the Mass Eruption Rate, X_p the particle volume fraction and V_w the horizontal wind velocity. A "-" in the column "Obs." means that instabilities were not observed.

For characterising the properties of ash fingers, we have analysed 3 visible-wavelength videos (resolution of 704 × 608 px) of lava fountains associated with the occurrence of ash fingers at Etna volcano. The lava fountains occurred on 12 April 2012, 04 April 2013 and 23 November 2013. Except for the 23 November 2013 explosive activity, previous publications did not report the formation of ash fingers during these events. Videos were provided by the Istituto Nazionale di Geofisica e Vulcanologia, Osservatorio Etneo (INGV-OE) that operates a camera network for monitoring the activity of Etna volcano (Scollo et al., 2014, 2019). They were all acquired from the city of Catania (ECV camera), about 26 km south of the vent.

Furthermore, we have conducted two field campaigns at Sabancaya (Peru) and Sakurajima volcanoes in July to August 2018 and November 2019, respectively, in order to further analyse the properties of ash fingers, the conditions favouring their development and the characteristics of associated tephra deposits. We chose Sabancaya and Sakurajima because both volcanoes are characterised by persistent Vulcanian explosions (Iguchi et al., 2013; Machacca Puma et al., 2021) that generate transient volcanic ash plumes at a high frequency and are, therefore, excellent for studying tephra sedimentation, with several explosions per day during our campaigns. At Sabancaya volcano, that summits at 5970 m above sea level (a.s.l.), explosive activity started in November 2016 and is still ongoing up to the time of writing (March 2022). Explosions happened at a typical frequency of 21 explosions per day during our field campaign (Chapter 5), reaching heights of 1 – 4 km above the vent (a.v.) (Manrique et al., 2018; Coppola et al., 2022). The density of volcanic ash emitted during this period has been estimated at about 2700 kg m^{-3} using Helium pycnometry (Aguilar, 2019; Chapter 5). Similarly, Sakurajima volcano (1117 m a.s.l.) has exhibited persistent Vulcanian activity since 1955 (Iguchi et al., 2013), typically producing several explosions per day that reached maximum heights of about 3 km a.v.l. during our campaign (Vecino et al., 2022). The activity additionally included almost continuous ash venting between explosions. During this period, the density of volcanic ash has been measured at 2400 – 2700 kg m^{-3} from water pycnometry (Freret-Lorgeril et al., 2022). At Sabancaya and Sakurajima, we have acquired visible-wavelength videos of the volcanic ash plumes at a resolution of 1980

× 1080 px and a frame rate of 50 Hz using Canon Legria HF G40 and Sony HD-SR8e cameras. 17 ash plumes have been selected for analysis, including 6 plumes at Sabancaya and 11 plumes at Sakurajima. Ash fingers have been recognised in 1 video from Sabancaya and 8 videos from Sakurajima. We have also analysed the grainsize of tephra deposited at locations close to the location where fingers reached the ground. At Sabancaya, the most surficial ground layer was sampled (Chapter 5) whilst falling tephra were collected in rectangular plastic trays at Sakurajima (Vecino et al., 2022). For both volcanoes, the grainsize was obtained by a combination of sieving and laser diffraction techniques (Chapter 5; Vecino et al., 2022).

The main characteristics of the videos studied in this work are presented in Table 4.3. For INGV-OE videos, the optical parameters of the ECV camera are sourced from the work of Snee (2021) who studied tephra plumes coupled to lava fountains at Etna volcano between 2011 and 2013 from visible video analysis. At Sabancaya and Sakurajima volcanoes, cameras have variable positions around the volcanoes and we have directly measured the altitude z_{cam}, orientation and inclination ϕ_i of the cameras prior to the acquisition of the videos. The horizontal fields of view θ_h of each video have been estimated using the same methodology as Snee (2021). This consists of first drawing a line in Google Earth from the position of the camera that represents the horizontal projection of the camera line of sight, as determined from the camera orientation. A second line representing the right or left boundary of the videos is then drawn by adjusting the ground level view in Google Earth to match the images acquired by the camera. The angle between these two lines corresponds to $\theta_h/2$, and the vertical field of view is calculated as

$$\theta_v = \theta_h \frac{N_i}{M_i}, \tag{4.13}$$

where M_i and N_i are respectively the width and height of the images. With this procedure, the uncertainty on the determination of θ_h is estimated by drawing multiple lines to adjust video margins to the ground level view in Google Earth. For our videos, maximum uncertainties are $\sim 2°$. From Google Earth data, the geographic coordinates of the vent have been determined, as well as its altitude z_{vent}, that has been estimated at 5.9 and 0.9 km a.s.l. for Sabancaya and Sakurajima, respectively.

Finally, volcanic plumes at Etna, Sabancaya and Sakurajima were bent over by the wind that, therefore, played a significant role in the dynamics of the plumes. We have estimated the wind direction and horizontal velocity V_w at the time of the eruptions from the ECWMF ERA 5 reanalysis dataset (Hersbach et al., 2020) at the level of the vent and at the plume top height. V_w in Table 4.3 corresponds to the average value of these estimations obtained at the two different levels.

Plume	**Volcano**	**Date**	**Time (UTC)**	**Camera**	$\mathbf{M_i}$ **(px)**	$\mathbf{N_i}$ **(px)**	$\mathbf{z_{cam}}$ **(m)**	$\mathbf{z_{vent}}$ **(km)**	$\mathbf{j_{vent}}$ **(px)**	$\mathbf{d_i}$ **(km)**	$\mathbf{V_w}$ **(m s^{-1})**	$\upsilon_\mathbf{w}$	$\phi_\mathbf{i}$	$\theta_\mathbf{h}$	$\theta_\mathbf{v}$	**Obs.**
Etna-1	Etna	12/04/2012	14:00	Canon VC-C4R	704	608	35	3.1	107	26.2	21.4	6.3	11.7	18.0	15.5	F
Etna-2	Etna	03/04/2013	13:45	Canon VC-C4R	704	608	35	3.1	107	26.2	43.8	36.9	11.7	18.0	15.5	F
Etna-3	Etna	23/11/2013	09:43	Canon VC-C4R	704	608	35	3.1	107	26.2	30.0	12.2	11.7	18.0	15.5	F
Sab-1	Sabancaya	29/07/2018	17:56	Canon HF G40	1920	1080	5024	5.9	275	4.4	5.6	5.1	23	38.0	21.4	-
Sab-2	Sabancaya	29/07/2018	18:56	Canon HF G40	1920	1080	5024	5.9	275	4.4	5.6	6.9	23	38.0	21.4	-
Sab-3	Sabancaya	30/07/2018	14:37	Canon HF G40	1920	1080	5010	5.9	318	5.5	4.2	43.4	18	80.0	45.0	-
Sab-4	Sabancaya	30/07/2018	14:57	Canon HF G40	1920	1080	4553	5.9	318	5.5	4.0	8.0	18	80.0	45.0	-
Sab-5	Sabancaya	31/07/2018	14:42	Canon HF G40	1920	1080	4553	5.9	338	8.0	7.4	56.2	20	68.0	38.3	-
Sab-6	Sabancaya	01/08/2018	16:50	Canon HF G40	1920	1080	5026	5.9	339	4.4	6.2	27.0	22	75.0	42.2	F
Sak-1	Sakurajima	15/11/2019	05:29	Canon HF G40	1920	1080	31	0.9	88	4.8	6.5	76.6	30	58.0	32.6	-
Sak-2	Sakurajima	17/11/2019	02:12	Sony HD-SR8e	1920	1080	0	0.9	196	6.7	8.9	22.5	12	28.0	15.8	-
Sak-3	Sakurajima	17/11/2019	02:52	Canon HF G40	1920	1080	0	0.9	448	6.7	9.3	29.4	10	36.0	20.3	F
Sak-4	Sakurajima	17/11/2019	04:49	Canon HF G40	1920	1080	0	0.9	430	6.7	10.4	30.1	12	69.0	38.8	-
Sak-5	Sakurajima	17/11/2019	05:54	Canon HF G40	1920	1080	0	0.9	150	6.7	10.9	30.9	14	30.0	16.9	F
Sak-6	Sakurajima	17/11/2019	07:32	Canon HF G40	1920	1080	0	0.9	151	6.7	10.8	31.8	14	30.0	16.9	F
Sak-7	Sakurajima	17/11/2019	07:43	Canon HF G40	1920	1080	0	0.9	151	6.7	10.8	30.9	14	30.0	16.9	F
Sak-8	Sakurajima	19/11/2019	03:34	Canon HF G40	1920	1080	0	0.9	348	11.3	13.7	41.1	10	30.0	16.9	F
Sak-9	Sakurajima	19/11/2019	07:07	Canon HF G40	1920	1080	0	0.9	429	12.2	13.9	36.7	5	24.0	13.5	F
Sak-10	Sakurajima	19/11/2019	07:54	Canon HF G40	1920	1080	0	0.9	460	12.2	13.8	37.6	5	30.0	16.9	F
Sak-11	Sakurajima	24/11/2019	06:43	Canon HF G40	1920	1080	0	0.9	267	11.3	8.7	17.4	10	78.0	43.9	F

Table 4.3: Main parameters of the videos studied in this work. Symbols are M_i for the image width, N_i for the image height, z_{cam} for the altitude of the camera, z_{vent} for the altitude of the reference point, j_{vent} for the vertical position of the reference point in the image, d_i for the distance between the camera and the image plane, υ_w for the angle between the orientation of the camera and the wind direction, ϕ_i for the camera inclination and θ_h and θ_v for the horizontal and vertical fields of view, respectively. "F" and "-" entries in the column "Obs." denote that ash fingers were observed or not, respectively.

4.3.2 Video analysis

Videos are used to measure the evolution of the volcanic plumes' height and thickness with time. For eruptions associated with observations of ash fingers, we additionally measure the fingers' width, spacing and front position. Measuring the finger front position allows us to quantify both the distance at which fingers form and reach the ground, as well as their downward velocity. When not directly observed, the distance at which fingers reach the ground is estimated based on their initial position, vertical velocity and wind speed (Manzella et al., 2015). Figure 4.3 is a sketch showing the different properties that have been quantified from the video analysis. Prior to measurements, we remove lens distortion effects using the Camera Calibration Toolbox for Matlab which estimates the camera's intrinsic parameters (Zhang, 1999). We then process the images similarly to Manzella et al. (2015), by accentuating the contrast between the volcanic plume and the background in order to facilitate analysis. All measurements are performed manually with ImageJ on video frames extracted at time steps Δt ranging from 2 to 10 s. Original results (in px) are then converted to metric units thanks to a geometrical calibration corrected to account for the dispersion of the plumes along the wind direction (Scollo et al., 2014; Bombrun et al., 2018; Snee, 2021).

Following the method developed by Snee (2021), we apply the procedure described hereafter in order to calibrate the videos. First, we perform a geometrical calibration based on the camera properties (Table 4.3) by considering that the points of interest to be on a vertical image plane passing through the vent and perpendicular to the line of sight of the camera (Figure 4.4). This image plane is located at a distance d_i from the camera. In this framework, the altitude of a point P_1 located at a pixel height j_1 is given by (Valade et al., 2014; Bombrun et al., 2018; Snee, 2021; Simionato et al., 2022)

$$z_1 = z_{cam} + \frac{d_i}{2}\left[\tan\left(\phi_i - \frac{\theta_v}{2} + (j_1 - 1)\,\delta\theta_v\right) + \tan\left(\phi_i - \frac{\theta_v}{2} + j_1\delta\theta_v\right)\right], \quad (4.14)$$

with $\delta\theta_v = \theta_v/N_i$ the vertical angle subtended by an individual pixel. Similarly, the

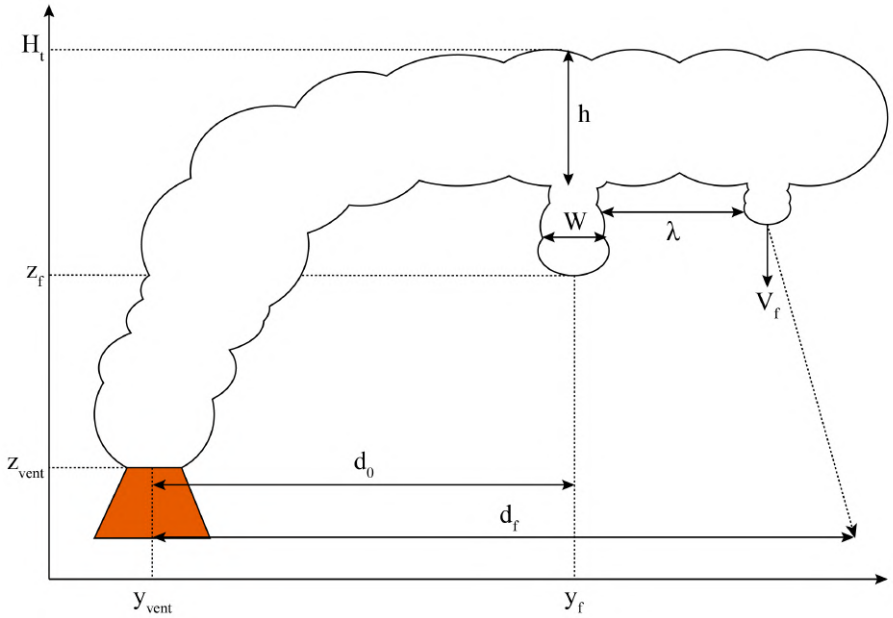

Figure 4.3: Properties measured from video analysis. z_{vent} and z_f are the altitudes of the vent and of the finger front, respectively. Similarly, y_{vent} and y_f are the horizontal positions of the vent and of the finger front, with d_0 the distance between the vent and the first finger formed beneath the plume. d_f is the distance between the vent and the position where fingers reach the ground. H_t and h are the plume top height and thickness, respectively. W, λ and V_f are the finger width, spacing and vertical velocity.

distance b_1 between P_1 and the vent is calculated as (Snee, 2021)

$$\begin{aligned} b_1 = \frac{d_i}{2}[&\tan(-\frac{\theta_h}{2} + (i_1 - 1)\delta\theta_h) + \tan(-\frac{\theta_h}{2} + i_1\delta\theta_h) \\ &- \tan(-\frac{\theta_h}{2} + (i_{vent} - 1)\delta\theta_h) - \tan(-\frac{\theta_h}{2} + i_{vent}\delta\theta_h)], \end{aligned} \tag{4.15}$$

with i_1 and i_{vent} the horizontal location of P_1 and of the vent in the image, respectively, and $\delta\theta_h = \theta_h/M_i$ the horizontal angle subtended by an individual pixel.

Finally, we adjust the initial geometrical calibration to correct for the plume dispersal along the direction of the wind (Scollo et al., 2014; Snee, 2021). In the case a weak volcanic plume is bent into the direction of the wind, as is the case in the videos that we have analysed, a new vertical plane passing through the vent, and parallel to the average wind direction, needs to be defined. This new wind-oriented plane forms an acute angle υ_w with the image plane (Figure 4.5). Depending on the position of the point of interest in the image plane (i.e., left or right of the vent) and on the wind direction (i.e., wind going away or towards the camera), it is possible to define 4 scenarios for which the wind correction requires specific adaptations (Snee,

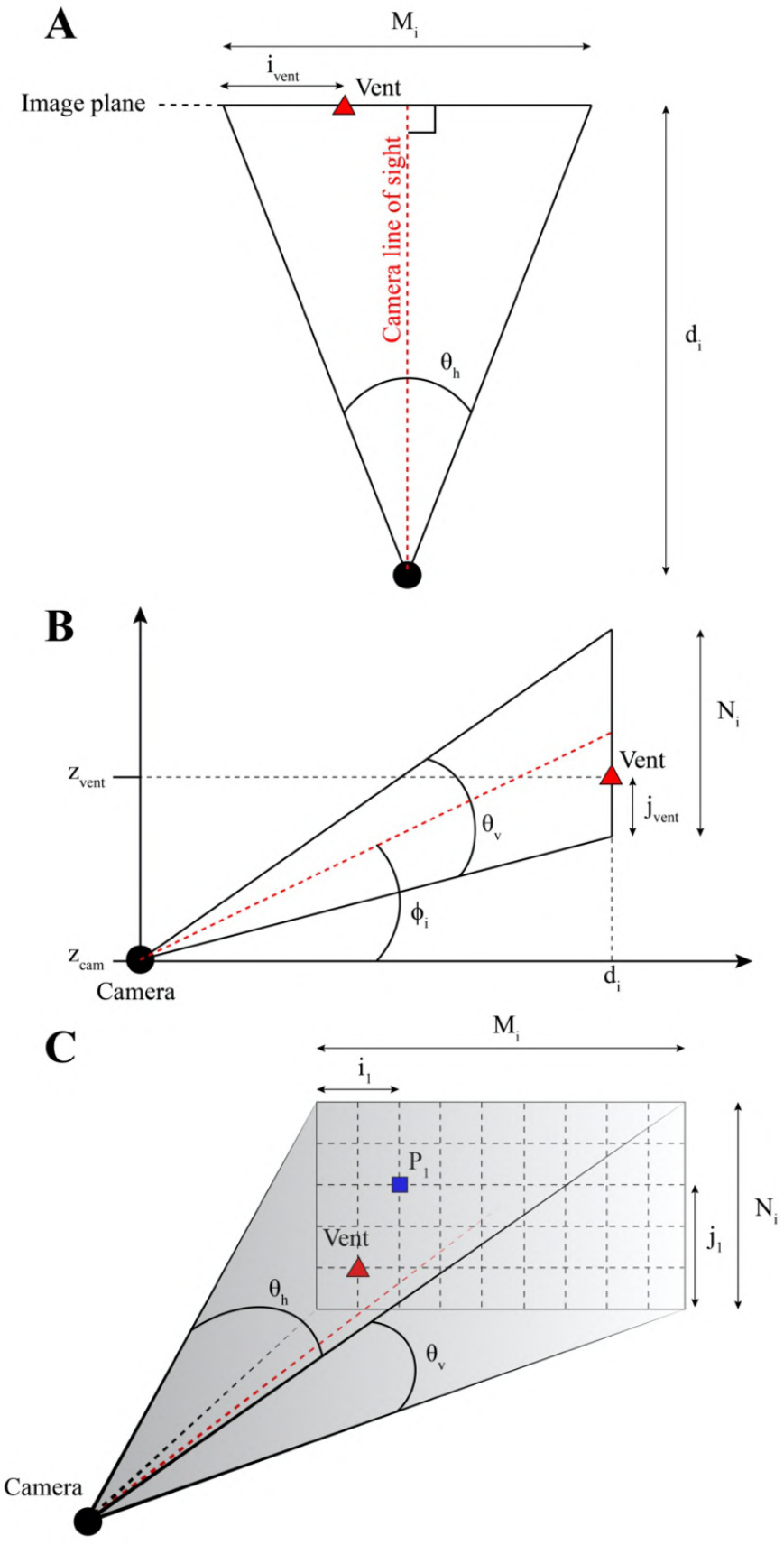

Figure 4.4: Geometrical calibration. **A.** Top view. **B.** Side view. **C.** Visualisation of a point of interest P_1 located on the image plane. Modified from Snee (2021)

2021). Here, we only present one scenario where the point of interest is located to the right of the vent from the camera's perspective, and the wind is directed away from the camera (Figure 4.5). Detailed calculations and additional configurations are described by Snee (2021). In order to perform the wind correction, P_2 is defined as the projection of P_1 onto the wind-oriented plane and a horizontal distance d_h therefore separates P_1 and P_2. The coordinates of P_2 equal to those of P_1 shifted by horizontal offsets Δx and Δy (Figure 4.5A), and a vertical offset Δz (Figure 4.5B). Hence, the distance b_2 between the vent and P_2 and the altitude z_2 of P_2 can be calculated as

$$b_2 = \sqrt{(b_1 + \Delta x)^2 + \Delta y^2}, \tag{4.16}$$

$$z_2 = z_1 + \Delta z, \tag{4.17}$$

where b_1 and z_1 are calculated using equations (4.15) and (4.14), respectively. In the configuration presented in Figure 4.5, the horizontal and vertical offsets are (Snee, 2021)

$$\Delta x = -\frac{b_1 \sin(\upsilon_w)}{\cos\left(\alpha_h - \frac{\theta_h}{2} + \upsilon_w\right)} \sin\left(\frac{\theta_h}{2} - \alpha_h\right), \tag{4.18}$$

$$\Delta y = \frac{b_1 \sin(\upsilon_w)}{\cos\left(\alpha_h - \frac{\theta_h}{2} + \upsilon_w\right)} \cos\left(\frac{\theta_h}{2} - \alpha_h\right), \tag{4.19}$$

$$\Delta x = \Delta y \tan\left(\phi_i - \frac{\theta_v}{2} - \alpha_v\right), \tag{4.20}$$

with $\alpha_h = i_1 \delta\theta_h$ and $\alpha_v = j_1 \delta\theta_v$.

4.3.3 Data analysis

Measurements calibrated to account for the plume distortion due to the wind are used to derive the main properties of the volcanic plume and of the ash fingers. The plume top height H_t is the highest point of the plume, and the vertical difference in altitude between H_t and the plume base corresponds to the plume thickness h. We evaluate the distance d_0 at which the first finger is observed to form as the distance between the vent and the front of the finger closest to the vent. The finger width is determined from the difference between the horizontal distances separating the vent and the left and right edges of an individual finger (equation 4.16). Similarly

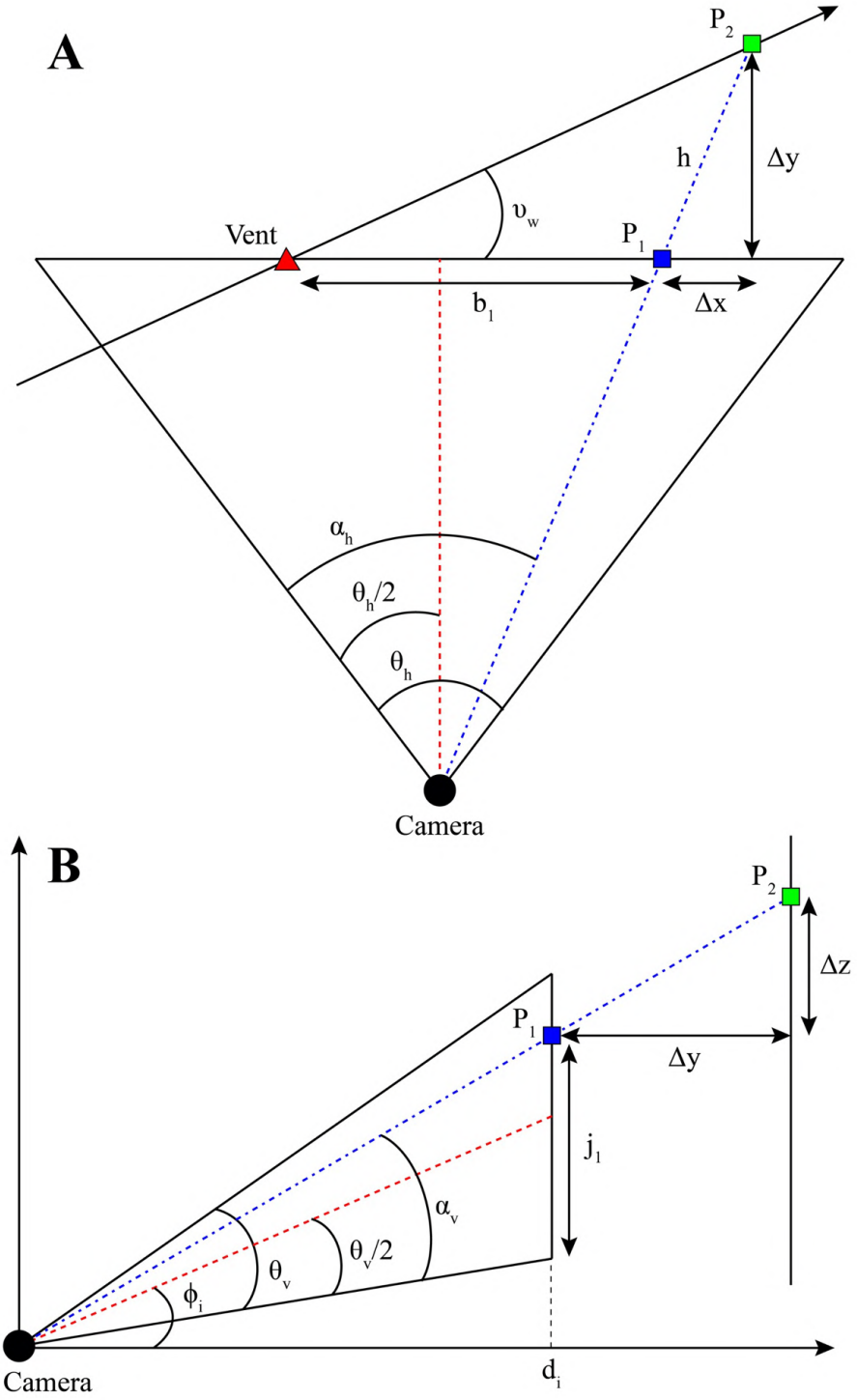

Figure 4.5: Wind calibration. **A.** Top view. **B.** Side view. Modified from Snee (2021)

the spacing corresponds to the difference in distance from the vent between two consecutive fingers. The downward finger velocity is estimated from the evolution of the finger front altitude with time

$$V_f = \frac{\Delta z_f}{\Delta t}, \tag{4.21}$$

where Δz_f is the change in vertical position of the finger front over a time step Δt separating consecutive analysed images.

Given that fingers can only incorporate particles with individual fall velocities V_p lower than V_f (i.e., $B > 1$, St < 1 and $\Sigma < 1$; equations 4.1, 4.3 and 4.4), we calculate the maximum particle diameter $d_{\max}$ which can be entrained by ash fingers as the particle diameter for which $V_p\,(d_{\max}) = V_f$ (Carazzo and Jellinek, 2012; Manzella et al., 2015; Freret-Lorgeril et al., 2020; Lemus et al., 2021). V_p increases with increasing particle diameter d, but the precise functional dependence depends on the particle Reynolds number (Bonadonna et al., 1998)

$$Re_p = \frac{V_p d \rho_a}{\mu}. \tag{4.22}$$

For low Re_p (< 0.4), V_p is the Stokes settling velocity. $d_{\max}$ can therefore be determined as

$$d_{\max} = \sqrt{\frac{18 \mu V_f}{g\,(\rho_p - \rho_a)}}\ , \quad (Re_p < 0.4). \tag{4.23}$$

For intermediate Re_p ($0.4 < Re_p < 500$), $d_{\max}$ is calculated as

$$d_{\max} = V_f \left(\frac{4 g^2 \rho_p^2}{225 \mu \rho_a} \right)^{-1/3}, \quad (0.4 < Re_p < 500). \tag{4.24}$$

At high Re_p (> 500), $d_{\max}$ becomes

$$d_{\max} = \frac{V_f^2 \rho_a}{3.1 g \rho_p}, \quad (Re_p > 500). \tag{4.25}$$

We have selected a typical density for volcanic ash $\rho_p = 2600$ kg m^{-3}, and representative atmospheric density values $\rho_a = 0.9$, 0.7 and 1.2 kg m^{-3} for Etna, Sabancaya and Sakurajima, respectively. The air dynamic viscosity has been assumed to be

1.8×10^{-5} kg m^{-1} s^{-1} for all cases.

Finally, following Manzella et al. (2015), we estimate the particle volume fraction of volcanic ash particles smaller than $d_{\max}$ as a function of the finger velocity and width. Under the assumption that ash fingers propagate at a velocity determined by equation (4.2), as validated for aqueous experiments (Hoyal et al., 1999b; Carazzo and Jellinek, 2012; Scollo et al., 2017; Fries et al., 2021), the particle volume fraction within fingers is

$$X_p = \frac{2V_f^2 \rho_a}{\sqrt{\pi}\delta_f g(\rho_p - \rho_a)}. \tag{4.26}$$

The characteristic length scale of ash fingers δ_f is approximated as half the finger width. For the calculation of equation (4.26), we chose identical values of ρ_p and ρ_a as those selected for calculating $d_{\max}$ (equation 4.23, 4.24 and 4.25).

4.4 Results

4.4.1 Properties of volcanic ash fingers

Figure 4.6 shows an example of an analysis performed for a plume at Sakurajima volcano (Sak-9; Table 4.3). Additional examples for Etna and Sabancaya volcanoes can be found in Supplementary material (Figure A4.1 for Etna and Figure A4.2 for Sabancaya). Error bars on W and z_f result from the uncertainties associated with the determination of θ_h and d_i. For all videos studied here, ash fingers are observed below weak volcanic plumes bent over by the wind. For sustained plumes (i.e., lava fountains at Etna volcano), ash fingers form continuously underneath the plume, whilst the formation of ash fingers ceases rapidly (in the order of 1 – 10 min) for transient volcanic events (i.e., Vulcanian explosions at Sabancaya and Sakurajima volcanoes). Ash fingers propagate downward until reaching the ground or disappearing as a result of dilution in the atmosphere, and analyses are limited in some cases by the ability to trace individual ash fingers, especially at Etna volcano, where videos are of low resolution. As illustrated in Figure 4.6, the width of ash fingers is not observed to increase with time and the decrease in z_f is found to be approximately linear (i.e., constant V_f) for the duration of the analysis, which is

Plume	**H_t (km a.v.)**	**h (km)**	**d_0 (km)**	d_f **(km)**	λ **(m)**	**W (m)**	**V_f (m s^{-1})**	**d_{max} (μm)**	**X_p**
Etna-1	3.6	0.9	0.9	5.1	436	244	3.7	412	2.2×10^{-6}
Etna-1	3.6	2.7	1.9	4.8	376	84	5.5	613	1.4×10^{-5}
Etna-2	2.1	1.3	1.2	4.5	471	168	4.3	487	4.5×10^{-6}
Etna-3	3.3	2.3	2.1	11.9	352	94	1.8	203	1.4×10^{-6}
Etna-3	3.3	3.3	3.0	-	373	101	-	-	-
Sab-1	1.2	0.4	-	-	-	-	-	-	-
Sab-2	1.6	0.5	-	-	-	-	-	-	-
Sab-3	1.6	1.1	-	-	-	-	-	-	-
Sab-4	2.0	1.3	-	-	-	-	-	-	-
Sab-5	0.5	0.7	-	-	-	-	-	-	-
Sab-6	1.6	0.5	1.0	-	-	134	-	-	-
Sab-6	1.6	0.9	1.4	-	-	97	-	-	-
Sab-6	1.6	0.5	1.1	2.1	213	87	5.1	529	9.5×10^{-6}
Sak-1	1.2	0.8	-	-	-	-	-	-	-
Sak-2	0.9	0.8	-	-	-	-	-	-	-
Sak-3	1.2	0.9	1.8	3.0	-	50	3.6	444	1.4×10^{-5}
Sak-4	2.7	1.3	-	-	-	-			
Sak-5	0.9	0.8	1.6	4.2	-	151	1.7	211	1.0×10^{-6}
Sak-6	0.7	0.4	1.7	3.9	-	119	2.2	272	2.2×10^{-6}
Sak-7	0.5	0.4	1.5	4.7	-	83	2.2	272	3.1×10^{-6}
Sak-8	1.0	0.5	1.0	2.9	304	81	3.3	404	7.1×10^{-6}
Sak-8	1.0	0.5	1.0	3.4	-	131	2.0	354	1.6×10^{-6}
Sak-8	1.0	-	-	-	-	-	2.9	243	-
Sak-9	0.4	-	-	-	-	111	-	-	-
Sak-9	0.4	0.7	1.3	3.4	252	79	4.2	518	8.5×10^{-6}
Sak-10	0.6	-	-	-	302	186	3.1	390	2.9×10^{-6}
Sak-11	0.2	0.9	5.5	6.2	314	149	2.6	325	2.5×10^{-6}

Table 4.4: Results of the video analysis (H_t: top plume height above vent, h: plume thickness, λ: spacing between fingers, W: finger width, V_f: finger velocity, $d_{\max}$: calculated maximum diameter of volcanic ash constituting ash fingers, X_p: calculated volume fraction inside ash fingers). "-" entries mean that observations were not usable for measurements/calculations

limited by the time taken by ash fingers to reach the ground. Average measurements of the properties of volcanic ash plumes (i.e., H_t and h) and ash fingers (i.e., d_0, λ, W and V_f) are summarised in Table 4.4.

Comparison with previously-studied ash fingers (Table 4.1) is shown in Figure 4.7. The error bars correspond to the standard deviation of the properties measured as a function of time. λ (Figure 4.7A) and W (Figure 4.7B), with average values of 304 ± 123 m and 123 ± 83.4 m, are found to cover similar ranges to those reported for the 2010 eruption of Eyjafjallajökull (Manzella et al., 2015), 1990 eruption of Mount Redoubt (Hobbs et al., 1991) and 2015 plumes of Stromboli (Freret-Lorgeril et al., 2020). However, our measurements of V_f (Figure 4.7C) are all found to be

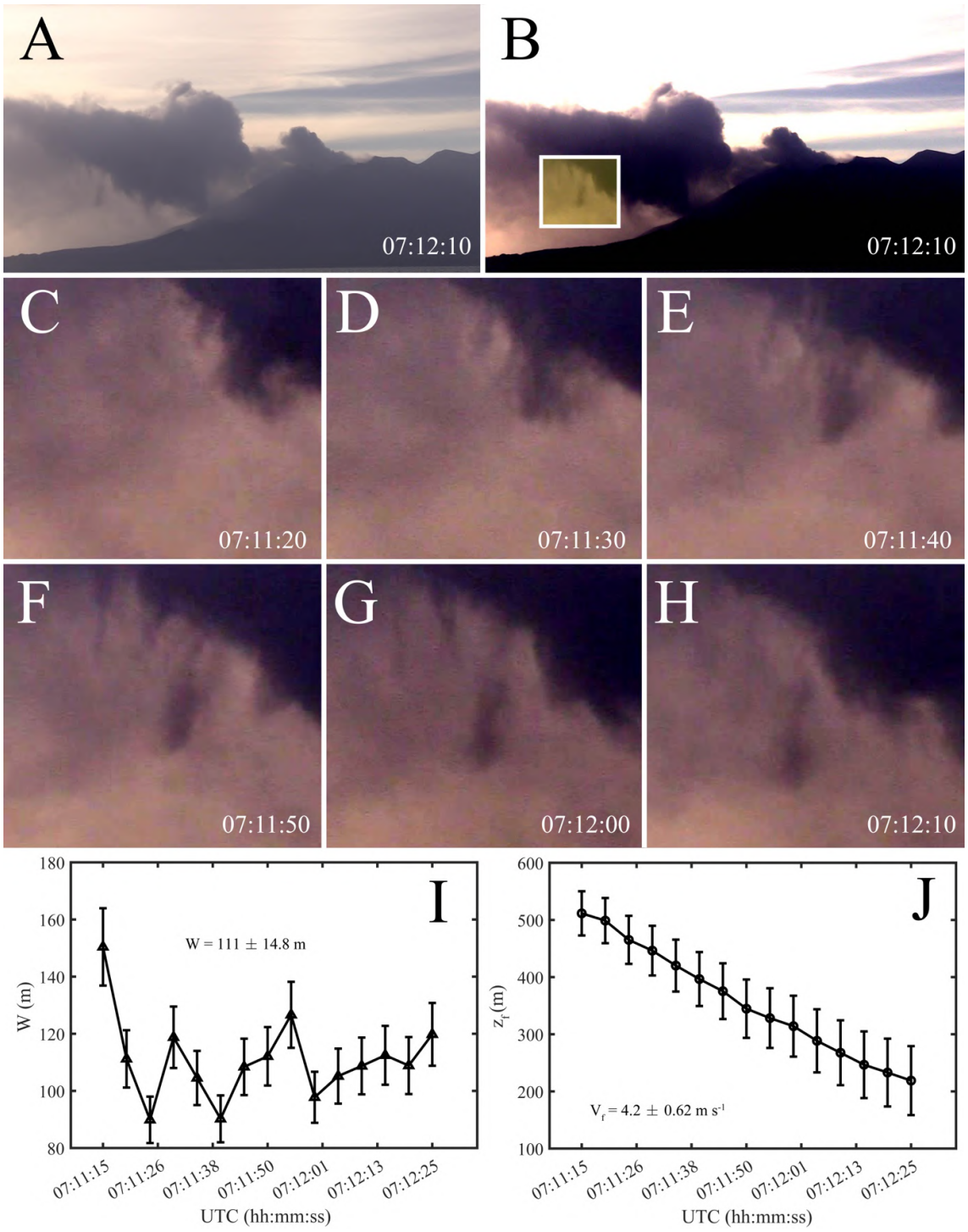

Figure 4.6: Example of a finger analysis (for plume Sak-9; Table 4.3). **A.** Original image. **B.** Processed image with increased contrast. **C-H.** Detailed view of an individual ash finger corresponding to the region highlighted by the yellow window in panel B. **I.** Evolution of the finger width W with time. **J.** Evolution of the finger front altitude z_f with time.

greater than previous estimates (Eliasson et al., 2014; Manzella et al., 2015; Freret-Lorgeril et al., 2020), with maximum values up to 5.5 ± 1.2 m s^{-1}, a minimum of 1.7 ± 0.3 m s^{-1} and a mean of 2.4 ± 1.6 m s^{-1}. Except for λ, that is greater at Etna than at Sakurajima and Sabancaya, the properties of ash fingers are not found to differ according to the type of eruption.

The maximum diameter of volcanic ash that can potentially be entrained into ash fingers ($d_{\max}$) increases as a function of V_f (equations 4.23-4.25). Since our estimates of V_f are greater than those reported in previous studies, our derived $d_{\max}$ are coherently larger (Figure 4.8A). The uncertainties associated with the calculation of $d_{\max}$ result from the uncertainties on V_f measurements. We find a minimum value of $d_{\max} = 203 \pm 48$ µm and a maximum at $d_{\max} = 613 \pm 130$ µm. The average value for the ash fingers studied here is $d_{\max} = 378 \pm 125$ µm. Whilst the minimum value of $d_{\max}$ compares well with those of Manzella et al. (2015) and Freret-Lorgeril et al. (2020) who found $d_{\max} \approx 200$ µm, the maximum value of $d_{\max}$ is approximately the triple the previous estimates. It is interesting to note that our measurements of V_f at Sakurajima, and, therefore, values of $d_{\max}$ are one order of magnitude greater than those of Eliasson et al. (2014) although we have studied very similar plumes at the same volcano. These differences are possibly linked to the contrasting techniques that have been employed for estimating V_f.

The particle volume fraction within fingers X_p also increases with increasing V_f, but is also a function of the finger characteristic length scale (equation 4.26). Hence, uncertainties on X_p originate from both uncertainties on V_f and W. We find a mean value $X_p = (5.3 \pm 4.6) \times 10^{-6}$, with a minimum and a maximum of $(1.0 \pm 0.1) \times 10^{-6}$ and $(1.4 \pm 0.2) \times 10^{-5}$, respectively (Figure 4.8B). Similarly to $d_{\max}$, we present X_p values greater than those reported in previous studies (Table 4.2). Although Eliasson et al. (2014) and Freret-Lorgeril et al. (2020) used techniques independent of V_f to measure X_p, it is worth mentioning that a correlation between X_p and V_f, consistent with our estimates, is apparent in their data.

Calculated $d_{\max}$ values are compared with the grainsize of tephra deposited on the ground for plumes at Sabancaya and Sakurajima volcanoes in Figure 4.9. For Sabancaya, fingers were observed to reach the ground in an area located 2.1 km

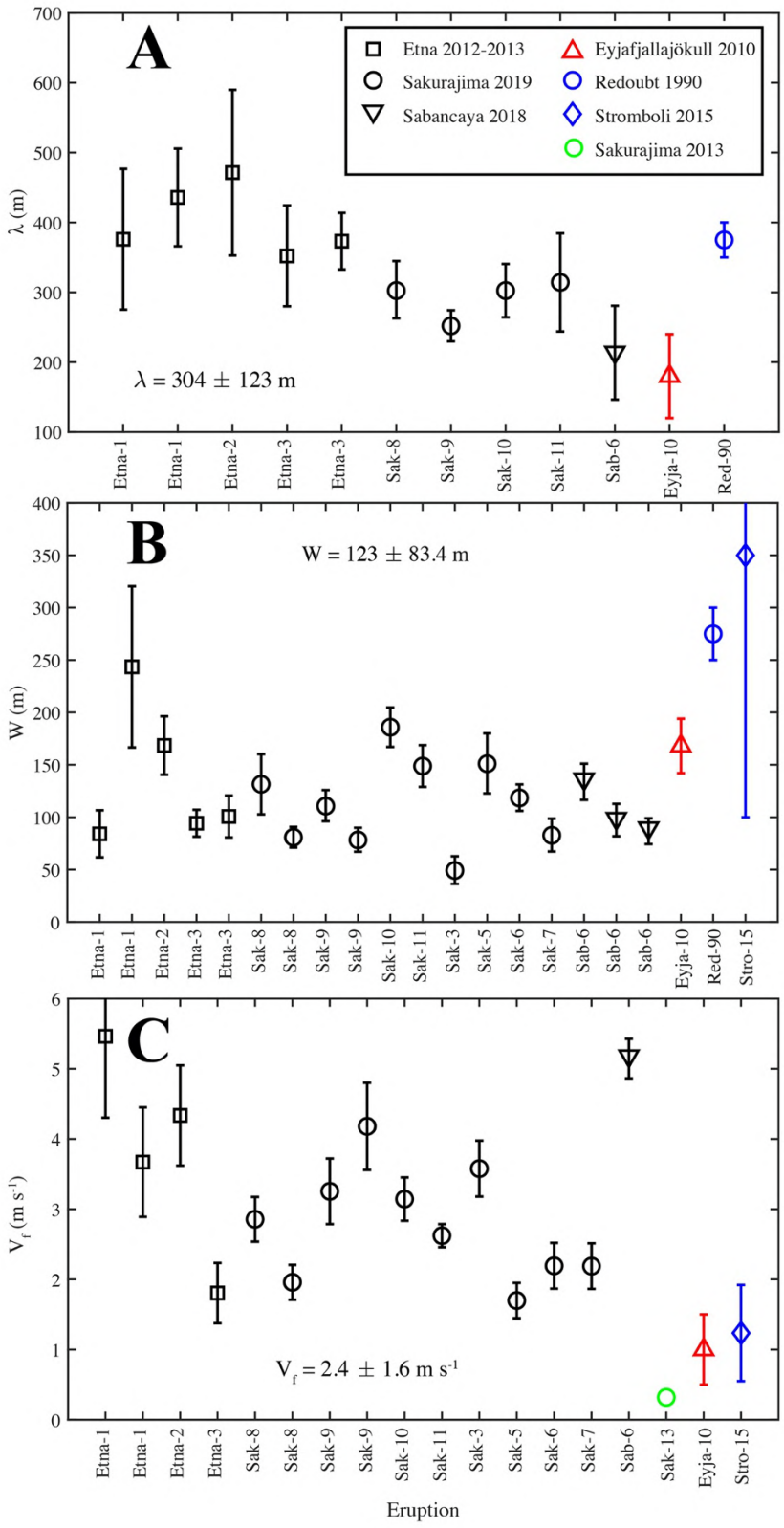

Figure 4.7: Properties of ash fingers: **A.** spacing λ, **B.** width W and **C.** downward velocity V_f. In black are results from this study, with the names of the plumes corresponding to those of Table 4.3. Red triangles, blue circles, blue diamonds and green circles correspond to the observations of Manzella et al. (2015), Hobbs et al. (1991), Freret-Lorgeril et al. (2020) and Eliasson et al. (2014), respectively (Table 4.1).

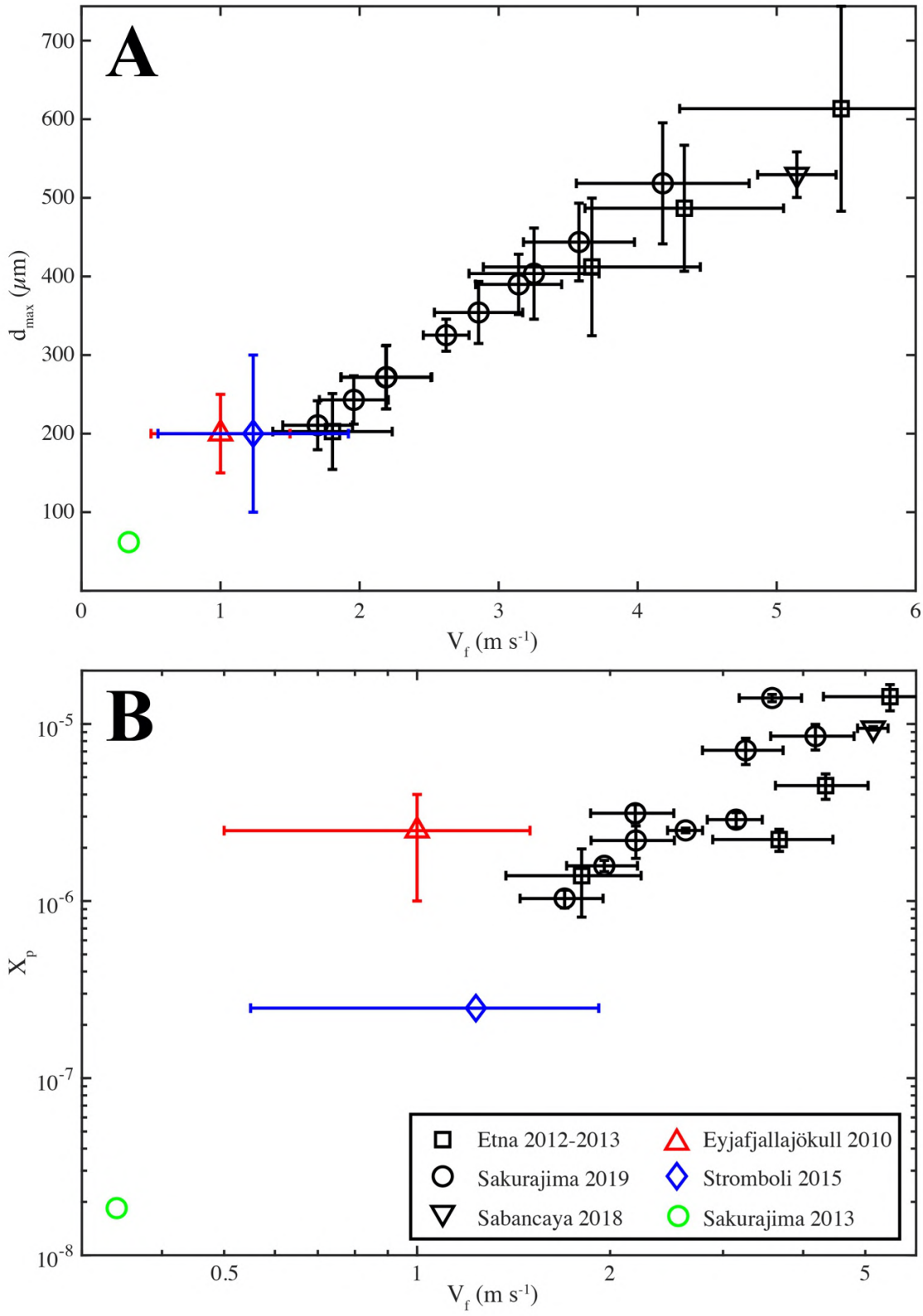

Figure 4.8: Variations in (**A**) the maximum particle diameter $d_{\max}$ and (**B**) particle volume fraction X_p as a function of the finger velocity V_f. In black are results from this study. Red triangles, blue diamonds and green circles correspond to the measurements of Manzella et al. (2015), Freret-Lorgeril et al. (2020) and Eliasson et al. (2014), respectively (Tables 4.1, 4.2).

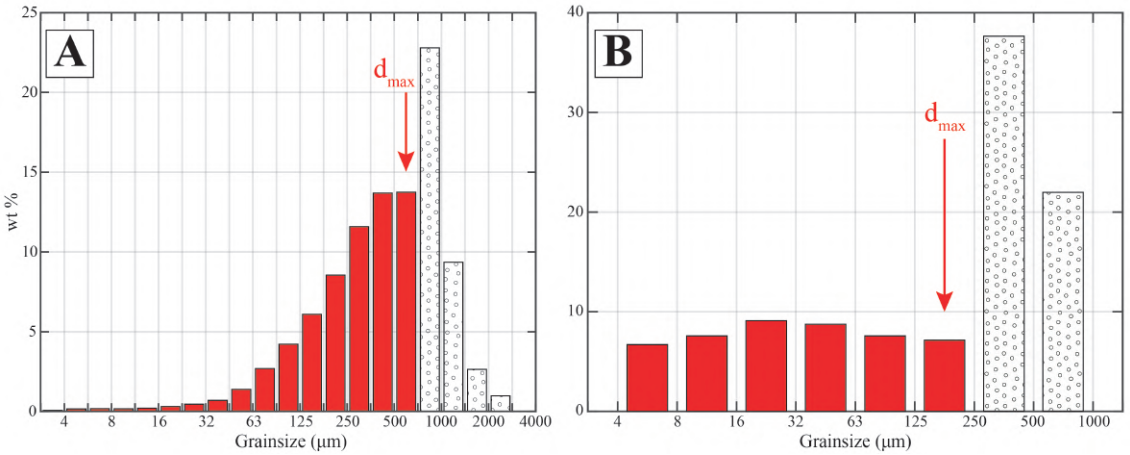

Figure 4.9: Comparison between d_{max} and the grainsize distribution (in weight percentage, wt%) of tephra collected at the locations fingers reached the ground for (**A**) Sabancaya (Sab-6 plume; Table 4.4) and (**B**) Sakurajima (Sak-5 plume; Table 4.4) volcanoes. The value of d_{max} is represented by a red arrow. Size fractions finer than d_{max} are highlighted in red (i.e., particles having potentially settled within ash fingers), whilst size fractions larger than d_{max} are represented by the dotted areas (i.e., particles that rather settled individually).

south-east of the vent on the 01 August 2018 (Sab-6; Tables 4.3 and 4.4). Surficial tephra deposits were collected 2.0 km south-east of the vent during the July to August 2018 field campaign. Deposits are characterised by a coarse (710 - 1000 µm) grainsize mode and a finer ($<$ 710 µm) grainsize distribution tail. For plume Sab-6, d_{max} is estimated at 529 µm from visual observations. This suggest that a substantial fraction of the particles composing the fine grainsize distribution tail could have settled within ash fingers, whilst coarser particles would have detach from the flow winthin fingers and rather settled individually. For Sakurajima, fingers were observed to reach the ground in an area located 4.2 km north of the vent on the 17 November 2019 (Sak-5; Tables 4.3 and 4.4). On the same day, falling tephra were collected 4.5 km north of the vent (Vecino et al., 2022). Particles are characterised by a bimodal grainsize distribution, with a fine (16 - 32 µm) and a coarse (250 - 500 µm) grainsize mode. For plume Sak-5, d_{max} is estimated at 211 µm, adequately separating the fine and coarse grainsize modes. The presence of the fine grainsize mode can also be explained by the presence of particle clusters composed of a coarse core ($>$ 90 µm) and a shell of fine material ($<$ 90 µm) that were observed to break upon impact with the ground at the same location (Vecino et al., 2022).

4.4.2 Scaling of volcanic ash fingers and conditions favouring their formation

If ash fingers originate from the detachment of a critically unstable PBL, as described for SDGIs (Hoyal et al., 1999b; Carazzo and Jellinek, 2012; Manzella et al., 2015; Scollo et al., 2017; Fries et al., 2021), their characteristic length is expected to decrease with increasing particle concentrations. In fact, based on equation (4.6), the critical thickness of the PBL can be calculated as

$$\delta_c = \left(\frac{Gr_c \mu^2}{g X_p \left(\rho_p - \rho_a\right) \rho_a} \right)^{1/3}, \tag{4.27}$$

where the critical Grashof number is evaluated at $Gr_c = 10^4$ for simple configurations in water (Fries et al., 2021; Lemus et al., 2021). W is expected to scale as $2\delta_c$. We show the variation in W as a function of X_p in Figure 4.10, for our measurements (Table 4.4) and data from previous publications (Table 4.1 and 4.2) (Eliasson et al., 2014; Manzella et al., 2015; Freret-Lorgeril et al., 2020). Measurements are compared with equation (4.27) predicting the value of δ_c. Although, as previously mentioned by Fries et al. (2021), equation (4.27) is found to greatly underestimate the length scale of ash fingers, we report a strong negative correlation between W and X_p. Interestingly, the best fit ($R^2 = 0.75$) suggests that W decreases as $X_p^{-1/3}$, as expected from equation (4.27), but with a discrepancy of about two orders of magnitude ($W \approx 100 \times \delta_c$). Here, we are not able to measure X_p independently of W, but equations (4.26) and (4.27) are nonetheless derived from separate expressions. Moreover, the best fit is also coherent with the data of Eliasson et al. (2014) and Freret-Lorgeril et al. (2020), who measured the particle concentration and W separately.

We have seen in Section 4.2.2 that ash fingers may originate from various mechanisms for given conditions that imply different scaling laws between the properties of ash fingers. Although we have not been able to measure the plume temperature, thought to be important for the onset of diffusive convection or of streak fallouts, nor directly estimated the particle concentration within the volcanic plume, we have quantified the geometrical properties of ash fingers. We can therefore compare these

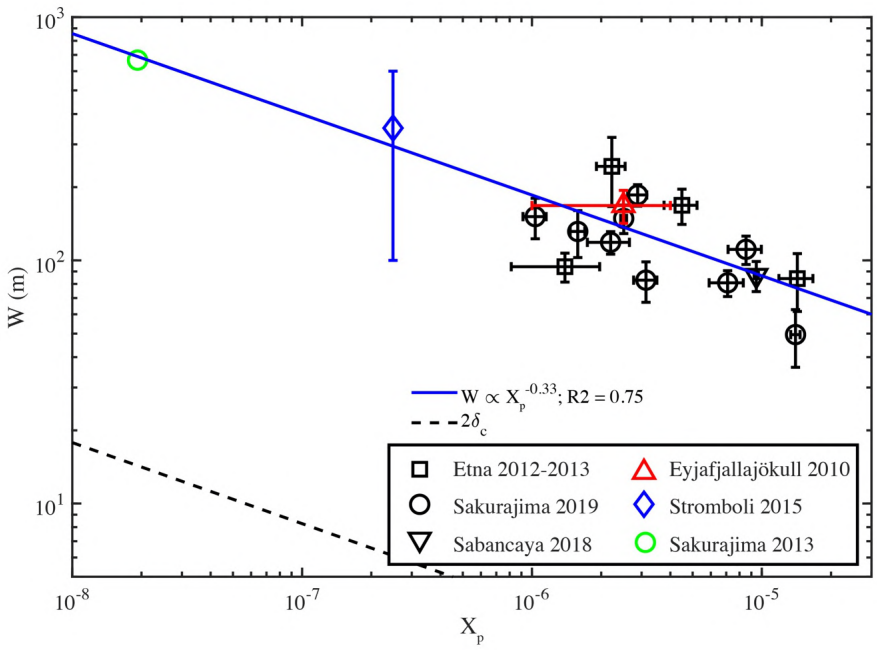

Figure 4.10: Comparison between the finger width W and the particle volume fraction X_p. Our data are presented in black. Red triangles, blue diamonds and green circles represent the measurements of Manzella et al. (2015), Freret-Lorgeril et al. (2020) and Eliasson et al. (2014), respectively (Tables 4.1, 4.2). The blue line corresponds to the best fit $W = X_p^m$, with m the fitted exponent. The dashed black line represents theoretical estimates based on $W = 2\delta_c$ (equation 4.27).

geometrical characteristics with the available scaling laws presented in section 4.2.3 in order to examine the processes at the source of observed ash fingers. In particular, our investigation focuses on SDGIs and wind-induced formation mechanisms. Figure 4.11A shows the variation of λ as a function of W. Theoretical and experimental constraints suggest that λ and W are proportional to each other (Hoyal et al., 1999b; Carazzo and Jellinek, 2012; Scollo et al., 2017; Fries et al., 2021), with $\lambda \approx 3W/2$. Including previous observations of Manzella et al. (2015) and Hobbs et al. (1991), the coefficient of determination $R^2 = 0.55$ confirms a poor agreement between measurements and the scaling $\lambda \approx 3W/2$. In Figure 4.11B, we compare the plume thickness h with d_0 the distance at which the first finger is observed to form. For fingers produced at Etna volcano, we find that h and d_0 are similar ($R^2 = 0.73$), whilst d_0 is systematically greater than h at Sabancaya and Sakurajima volcanoes. This suggests that ash fingers potentially form after a characteristic time t_w for the turnover of wind-induced rolls (equation 4.12), consistently with the analysis of Freret-Lorgeril et al. (2020) who revealed the existence of such scaling at Stromboli

in 2015, Eyjafjallajökull in 2010 (Manzella et al., 2015; represented in Figure 4.11B) and Etna in November 2013.

Although the number of observations is limited, we evaluate the influence of h, X_p, H_t and V_w on the formation of volcanic ash fingers. In Figure 4.12A, our measurements and previous observations (Table 4.2) are compared with the contour lines of L^* (equation 4.7; Fries et al., 2021). As expected for SDGIs, we find that thick volcanic ash clouds and high particle concentrations (i.e., $L^* \gg 1$) favour the development of ash fingers, whereas their onset is inhibited for thin clouds and low particle concentrations. In particular, we find that $L^* \geq 15$ guarantees the formation of ash fingers. For $L^* < 15$, the particle concentration controls the formation of ash fingers that form only for $X_p > 1 \times 10^{-6}$. Figure 4.12B shows the occurrence of ash fingers as a function of both the top plume height H_t and the horizontal wind velocity V_w. Ash fingers are observed predominantly for high V_w, typically greater than 10 m s^{-1}. It is also clear in Figure 4.12 that mammatus clouds form preferentially for high volcanic ash clouds ($H_t > 15$ km; Table 4.2).

4.5 Discussion

4.5.1 New measurements of ash fingers and implications for volcanic ash sedimentation

After reviewing previous observations, we propose to use the term "ash fingers" to describe all ash-laden currents descending below volcanic ash clouds in the form of discrete sedimentation columns driven by density differences, irrespective of the formation mechanism. Mammatus share similarities with ash fingers, but are not reported to extend below the base of volcanic ash clouds (Schultz et al., 2006; Durant et al., 2009). Hence, the term "ash fingers" adequately describes "ash veils" (Hobbs et al., 1991), "gravitational instabilities" (Manzella et al., 2015; Scollo et al., 2017), "convective instabilities" (Bonadonna et al., 2002b; Bonadonna, 2005a), "streak fallouts" (Eliasson et al., 2014; Eliasson, 2020), and "sediment thermals" (Freret-Lorgeril et al., 2020), but not mammatus. Within this framework, observed phenomena (i.e., ash fingers) can be separated from the processes responsible for their generation.

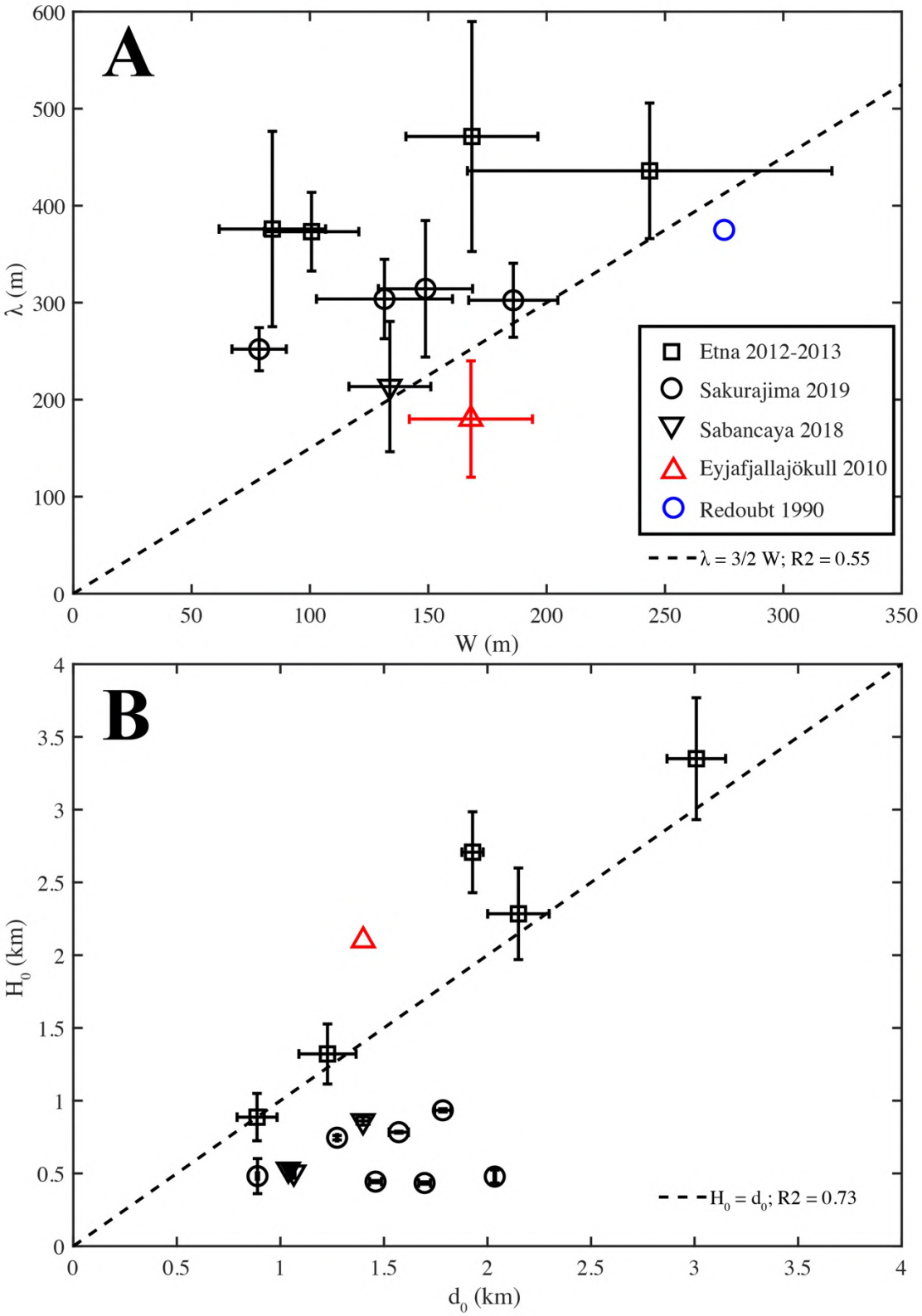

Figure 4.11: Geometrical comparisons between (**A**) the spacing between ash fingers λ and the finger width W and (**B**) the plume thickness h and the distance between the vent and the closest finger d_0. In black are results from this study. Red triangles and blue circles indicate the observations of Manzella et al. (2015) and Hobbs et al. (1991), respectively (Table 4.1). Dashed black lines indicate geometrical scaling laws expected for SDGIs (panel A) and wind-induced fingers (panel B).

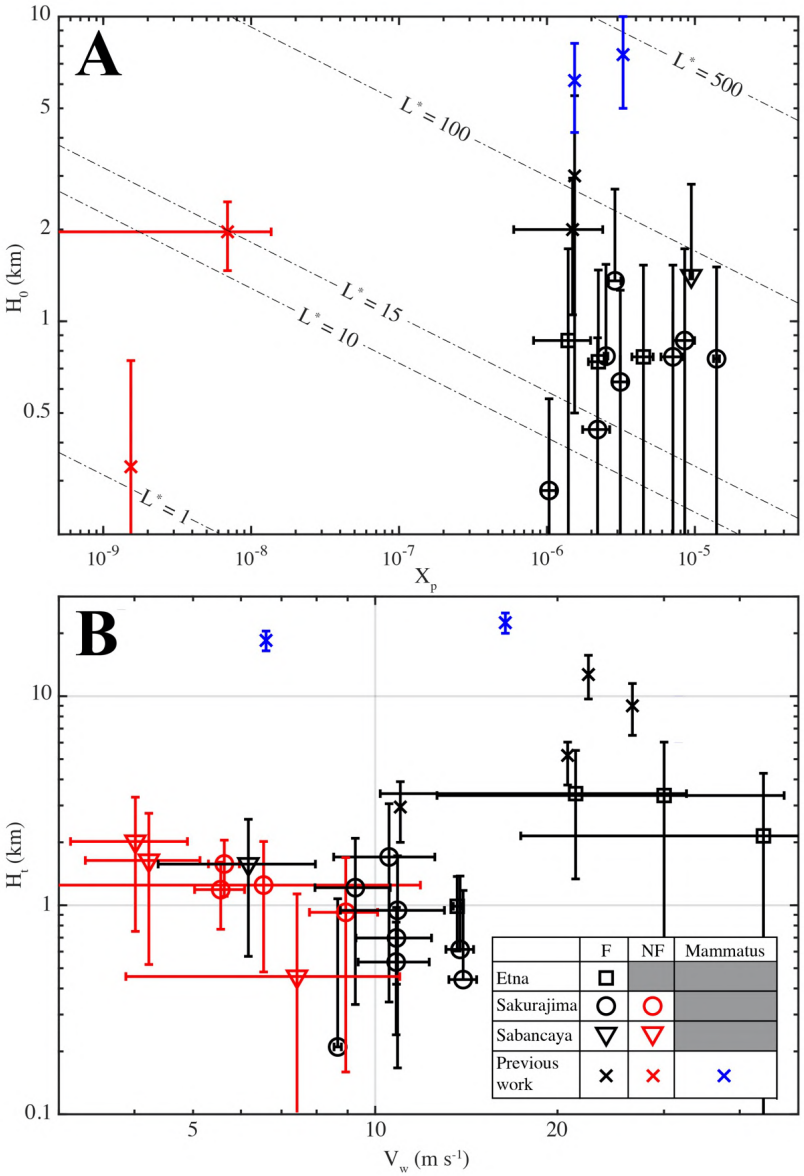

Figure 4.12: Conditions associated with the development of ash fingers. **A.** Influence of the particle volume fraction X_p and plume thickness h on the formation of ash fingers compared with contours of L^* (equation 4.7). **B.** Influence of the horizontal wind speed V_w and plume top height H_t on observations of ash fingers. Squares, circles and triangles represent results from this study and crosses are results from previous studies. Black markers indicate conditions associated with the observations of ash fingers (F), red markers show the conditions for which ash fingers are not observed (NF), and blue markers represent mammatus clouds.

The formation mechanisms all involve the creation of a dense, unstable, layer at the base of volcanic ash clouds resulting from either particle settling (Carazzo and Jellinek, 2012; Manzella et al., 2015; Scollo et al., 2017; Fries et al., 2021), double diffusive processes (Carazzo and Jellinek, 2013), temperature differences (Eliasson et al., 2014; Eliasson, 2020) or wind-induced stirring (Freret-Lorgeril et al., 2020). However, it remains essential to assess the mechanisms responsible for the formation of ash fingers, as different mechanisms result in different scaling laws and dynamics (see section 4.2.3).

Quantitative descriptions of ash fingers remain rare (Table 4.1), despite their frequent occurrence and their potential effect on tephra sedimentation that can greatly enhance the deposition of fine volcanic ash (Carazzo and Jellinek, 2012; Durant, 2015; Manzella et al., 2015). Here, we have used visible-wavelength videos in order to further characterise ash fingers and the conditions for which they form. Our results considerably increase the number of measurements for ash fingers, notably through direct assessments of their velocity V_f, width W and spacing λ (Figure 4.7; Table 4.4), associated with measurements of the plume top height H_t, thickness h and distance between the vent and closest ash fingers d_0 (Figure 4.11; Table 4.4). These results extend previously-determined properties, especially for V_f that is consistently found to be greater than in preceding studies (Figure 4.7).

Our new measurements of V_f imply that particles coarser than previously thought can be affected by collective settling within ash fingers. This is quantified by $d_{\max}$ for which $V_p\left(d_{\max}\right) = V_f$ (equations 4.23-4.25). Previous estimations have reported maximum $d_{\max}$ values of about 200 µm (Manzella et al., 2015; Freret-Lorgeril et al., 2022). Here, we find minimum and maximum $d_{\max}$ values of, 203 ± 48 µm and 613 ± 130 µm respectively, with a mean $d_{\max} = 378 \pm 125$ µm (Figure 4.8). This increases the maximum diameter of volcanic ash that can be entrained with ash fingers by a factor 3. Hence, ash fingers have the potential to further enhance the sedimentation of volcanic ash, notably for sizes as large as ≈ 600 µm.

$d_{\max}$ values were compared to the grainsize distributions of tephra deposited on the ground for two plumes at Sabancaya and Sakurajima volcanoes (Figure 4.9). For Sabancaya, surficial tephra deposits were sampled in order to identify if the

presence of ash fingers left a characteristic signature in deposits. A fine tail in the grainsize distribution can be linked to fine particles transported within ash fingers that would, therefore, settle closer to the vent than expected. However, the absence of direct sampling below the plume (Sab-6; Tables 4.3 and 4.4) limits the interpretation of these deposits that resulted from the accumulation of several fallouts, but also because other mechanisms such as particle aggregation could also have resulted in similar grainsize distribution. The comparison is more straightforward for Sakurajima, where tephra particles were directly collected in dedicated trays below Sak-5 plume (Tables 4.3 and 4.4). Alike Manzella et al. (2015), the grainsize distribution of the particles is bimodal, with a fine grainsize mode (16 - 32 µm) that can be explained by the sedimentation of fine volcanic ash within ash fingers, but also within the shell of particle clusters (Vecino et al., 2022). Ash fingers and particle aggregation affect the same grainsizes and have nearly identical effects on tephra sedimentation, by driving the premature fall of fine volcanic ash. Hence, clearly distinguishing between the two processes based on the characteristics of tephra deposits was not possible for this plume.

4.5.2 Scaling of ash fingers and conditions favouring their development

As expected for fingers produced by SDGIs, the size of ash fingers is found to decrease as a function of the particle concentration ($W \propto X_p^{-1/3}$; Figure 4.10). We also find a poor agreement ($R^2 = 0.55$) between the characteristic length scales of ash fingers and the scaling $\lambda = 3W/2$ derived for SDGIs (Figure 4.11A). Despite there being a small number of eruptions not associated with ash fingers that could be studied, ash fingers are additionally found to form preferentially for $L^* \gg 1$ ($L^* > 15$) (equation 4.7; Figure 4.12A), whilst high particle concentration influences the development of ash fingers for $L^* < 15$. This is similar to the experiments of Fries et al. (2021), who reported the formation of fingers for $L^* > 5$ and described that the particle concentration controlled the tendency to generate fingers for $L^* < 5$. These observations suggest that ash fingers studied in this work predominantly form as a result of SDGIs. However, we find $W \approx 100 \times \delta_c$ instead of the theoretical scaling

$W = 2 \times \delta_c$ (Hoyal et al., 1999b; Carazzo and Jellinek, 2012; Manzella et al., 2015; Fries et al., 2021), where δ_c is calculated with equation (4.27). This discrepancy, along with the difference in the value of L^* separating conditions favourable and unfavourable to the formation of ash fingers, suggests that δ_c is underestimated by equation (4.27) that is validated only for simple experiments studying the sedimentation from a particle suspension into a denser, quiescent, aqueous ambient. Volcanic plumes are much more complex phenomena involving additional physical processes, notably including internal overturning motions in volcanic clouds (Freret-Lorgeril et al., 2020) and the presence of shear at the cloud base.

The studied ash fingers all formed beneath volcanic plumes bent-over by the wind, as illustrated in Figure 4.12B. This is first explained by the greater abundance of weak plumes that are much more frequently observed than strong, vertical, plumes. Moreover, visual observations of structures in tephra sedimentation is greatly facilitated for bent-over plumes. Finally, ash fingers can be favoured by wind-induced rolls forming in bent-over clouds (Freret-Lorgeril et al., 2020), as suggested by the scaling $h \approx d_0$ for plumes imaged at Etna volcano (Figure 4.11B). Furthermore, it is important to mention that shear at the cloud base, resulting from wind shear and/or gravitational spreading, can dampen the formation of ash fingers from SDGIs or diffusive convection (Konopliv et al., 2018). In fact, in the presence of environmental shear, dominant instability modes can be modified, depending on the particle settling velocity and shear intensity (Farenzena and Silvestrini, 2017). For volcanic ash clouds, this implies that ash fingers formed in the presence of shear are not purely resulting from SDGIs, but are modulated as a function of shear.

4.5.3 Limitations and future work

In this study, we only have used visual observations to characterise ash fingers. To do so, we have calibrated videos based on the procedure of Snee (2021), and have determined missing camera parameters from Google Earth images, with uncertainties on the assessment of the horizontal field of view θ_h. A better quantification of θ_h would allow us to refine our results.

In fact, although allowing for the characterisation of important fingers proper-

ties, analysing ash fingers from visual observations alone are associated with many unknowns, notably regarding the particle size and concentrations within ash fingers. Hence, similarly to Freret-Lorgeril et al. (2020) and Eliasson et al. (2014), employing a variety of measuring techniques in future works is needed to supplement visual observations (e.g., with radar, lidar, or drone/balloon based measurements). For example, direct measurements of X_p, independent of finger properties, would allow a better description of the relation between ash fingers characteristic length scales and X_p.

The role of L^* in predicting the development of ash fingers is also particularly limited, as only two eruptions not associated with the formation of ash fingers could be investigated (Figure 4.11A). In fact, conforming the absence of ash fingers is, in general, more complex than the inverse, and we were only able to estimate X_p for plumes associated with ash fingers in this work, further reducing the representativeness of our data.

Since most ash fingers are observed to form below bent-over plumes, appropriate experimental and numerical models analysing the sedimentation below particle-laden currents are required. Such models, similar to the experiments of Parsons et al. (2001), Davarpanah Jazi and Wells (2020, 2016) and Jarvis et al., or to the numerical simulations of Lemus et al. (in prep.), would allow study of the effect of wind and shear on the formation of ash fingers. The discrepancy between δ_c and natural observations of the size of ash fingers would notably be investigated in order to develop a more robust scaling law to predict the dimensions of ash fingers. Additionally, we have only been able to study ash fingers below weak volcanic plumes. Additional observations for other types of plumes and eruption dynamics are required in order to obtain a more complete view of ash fingers and of their formation mechanism. Moreover, we have investigated the formation of ash fingers close to the vent, imaging more distal parts of volcanic ash clouds is necessary to better understand the effect of diffusive convection and mammatus.

Finally, similarly to Manzella et al. (2015), this work reveals that tephra deposits were bimodal at the location where ash fingers reached the ground, at the same distance aggregates were observed to fall (Figure 4.9). However, the respective role

of ash fingers and aggregation on final deposits is still unclear. Field work on tephra deposits and sedimentation rates associated with eruptions for which ash fingers and aggregation are observed separately is required for improving our understanding of the effect of ash fingers on ash deposition. Moreover, laboratory and numerical models can address this issue, particularly because aggregation and ash fingers can be separated contrarily to the natural case.

4.6 Conclusions

A review of previous observations and new measurements of ash finger properties, based on visual observations at Etna, Sabancaya and Sakurajima volcanoes (associated with both lava-fountain fed and Vulcanian plumes), calibrated to account for the distortion of volcanic plumes into the wind direction (Snee, 2021), are presented in this work. We have recognised ash fingers below weak plumes bent by the wind. The main results of our analysis are:

1. The mean width W, spacing λ and downward velocities V_f of ash fingers studied here are $W = 123 \pm 83$ m, $\lambda = 304 \pm 123$ m and $V_f = 2.4 \pm 1.6$ m s^{-1}.

2. Ash fingers are found to potentially entrain volcanic ash particles with diameters up to 613 ± 130 µm. This favours the premature sedimentation of fine volcanic ash, potentially leading to the formation of tephra deposits characterised by bimodal grainsize distributions.

3. W scales as a function of the particle volume fraction X_p ($W \propto X_p^{-1/3}$). Previous scaling laws (Hoyal et al., 1999b; Carazzo and Jellinek, 2012; Fries et al., 2021), although reproducing the dependence of W on X_p, underestimate the characteristic length scales of ash fingers.

4. A weak agreement is found between the scaling law $\lambda = 3W/2$ and observations.

5. Fingers at Etna volcano form from a distance corresponding to the cloud thickness, as expected for fingers developing as a result of wind-induced stirring

(Freret-Lorgeril et al., 2020).

6. The formation of ash fingers seems to be favoured for thick ash clouds and high ash concentrations ($L^* \gg 1$), but more independent ash concentration measurements are required to better constrain X_p within volcanic plumes and fingers, as well as the conditions associated with their occurrence.

7. Observations of ash fingers are mostly associated with horizontal wind velocities greater than 10 m s^{-1}.

Our results suggest that the ash fingers studied in this work can result from settling-driven gravitational instabilities modulated by the wind. Moreover, besides considerably increasing quantitative observations of ash fingers, we have also extended the range of volcanic ash sizes potentially affected by ash fingers that was previously limited to particle diameters ≈ 200 µm. This further highlights that ash fingers can enhance volcanic ash sedimentation, with potential implications for the longevity and the dispersal of volcanic ash in the atmosphere.

Author contributions for Chapter 4

Allan Fries and Jonathan Lemus acquired videos at Sabancaya and Sakurajima volcanoes. Simona Scollo provided videos of eruptions at Mount Etna. Allan Fries conducted the analysis and drafted the manuscript under the supervision of Costanza Bonadonna and Paul A. Jarvis.

4.7 Appendix A4

Notations used in Chapter 4

Symbol	Name	Unit
b_1	distance between the vent and P_1	m
b_2	distance between the vent and P2	m
B	Ratio V_f over V_p	-
C	particle concentration	kg m-3

Symbol	Name	Unit
C_{mp}	plume maximum carrying capacity	-
d	particle diameter	m
d_0	horizontal distance between the vent and the closest ash finger	m
d_h	horizontal distance between P_1 and P_2	m
d_i	horizontal distance between the camera and the image plane containing the vent	m
$d_{\max}$	maximum particle diameter possibly entering fingers	m
f_{SW}	characteristic frequency of sedimentation waves	s^{-1}
F_D	diffusive convective flux	kg m^{-2} s^{-1}
F_I	flux by individual particle settling	kg m^{-2} s^{-1}
F^*	ratio F_D over F_I	-
g	gravitational acceleration	m s^{-2}
Gr	Grashof number	-
Gr_c	critical Grashof number	-
h	plume thickness	m
H_b	height of the neutral buoyancy level	m
H_t	top plume height	m
i_1	horizontal position of P_1 in the image	px
i_{vent}	horizontal position of the vent in the image	px
j_1	vertical position of P_1 in the image	px
j_{vent}	vertical position of the vent in the image	px
L^*	ratio h over δ_c	-
M_i	image width	px
N_i	image height	px
P_1	point of interest located on the image plane containing the vent	-
P_2	projection of P_1 on the wind-oriented plane	-

Symbol	Name	Unit
R_T	Stability ratio	-
Re_p	particle Reynolds number	-
St	Stokes number	-
t_p	timescale for individual particle settling	s
t_w	timescale of wind-induced rolls	s
T_p	plume temperature	K
V_f	finger downward velocity	m s^{-1}
V_p	individual particle settling velocity	m s^{-1}
V_{SW}	downward velocity of sedimentation waves	m s^{-1}
V_w	horizontal wind velocity	m s^{-1}
W	finger width	m
X_p	particle volume fraction	-
y_f	horizontal position of the finger front	m
y_{vent}	horizontal position of the vent	m
z_{cam}	altitude of the camera	m
z_f	altitude of the finger front	m
z_{vent}	altitude of the vent	m
α_h	horizontal angle subtended by i_1	-
α_T	volumetric expansion coefficient for heat	K^{-1}
α_v	vertical angle subtended by j_1	-
β_m	volumetric expansion coefficient for a particle suspension	-
δ_c	critical thickness of the PBL	m
δ_f	characteristic finger length scale	m
δ_{PBL}	PBL thickness	m
$\delta\theta_h$	horizontal angle subtended by an individual pixel	-
$\delta\theta_v$	vertical angle subtended by an individual pixel	-

Symbol	Name	Unit
ΔC_m	particle concentration difference between the volcanic cloud and the atmosphere (in mass fraction)	-
Δt	time step between successive analysed images	s
ΔT	temperature difference between the volcanic cloud and the atmosphere	K
Δx	horizontal offset between P_1 and P_2 (perpendicular to the camera line of sight)	m
Δy	horizontal offset between P_1 and P_2 (parallel to the camera line of sight)	m
Δz	vertical offset between P_1 and P_2	m
θ_h	horizontal field of view	-
θ_v	vertical field of view	-
κ_p	diffusion coefficient of particles	$m^2\ s^{-1}$
κ_T	diffusion coefficient of heat	$m^2\ s^{-1}$
λ	spacing between fingers	m
λ_{SW}	distance between successive sedimentation waves	m
μ	ambient dynamic viscosity	$kg\ m^{-1}\ s^{-1}$
ρ_a	ambient density	$kg\ m^{-3}$
ρ_p	particle density	$kg\ m^{-3}$
Σ	sedimentation number	-
ϕ_i	camera inclination	-

Table A4.1: List of symbols

Supplementary Figures

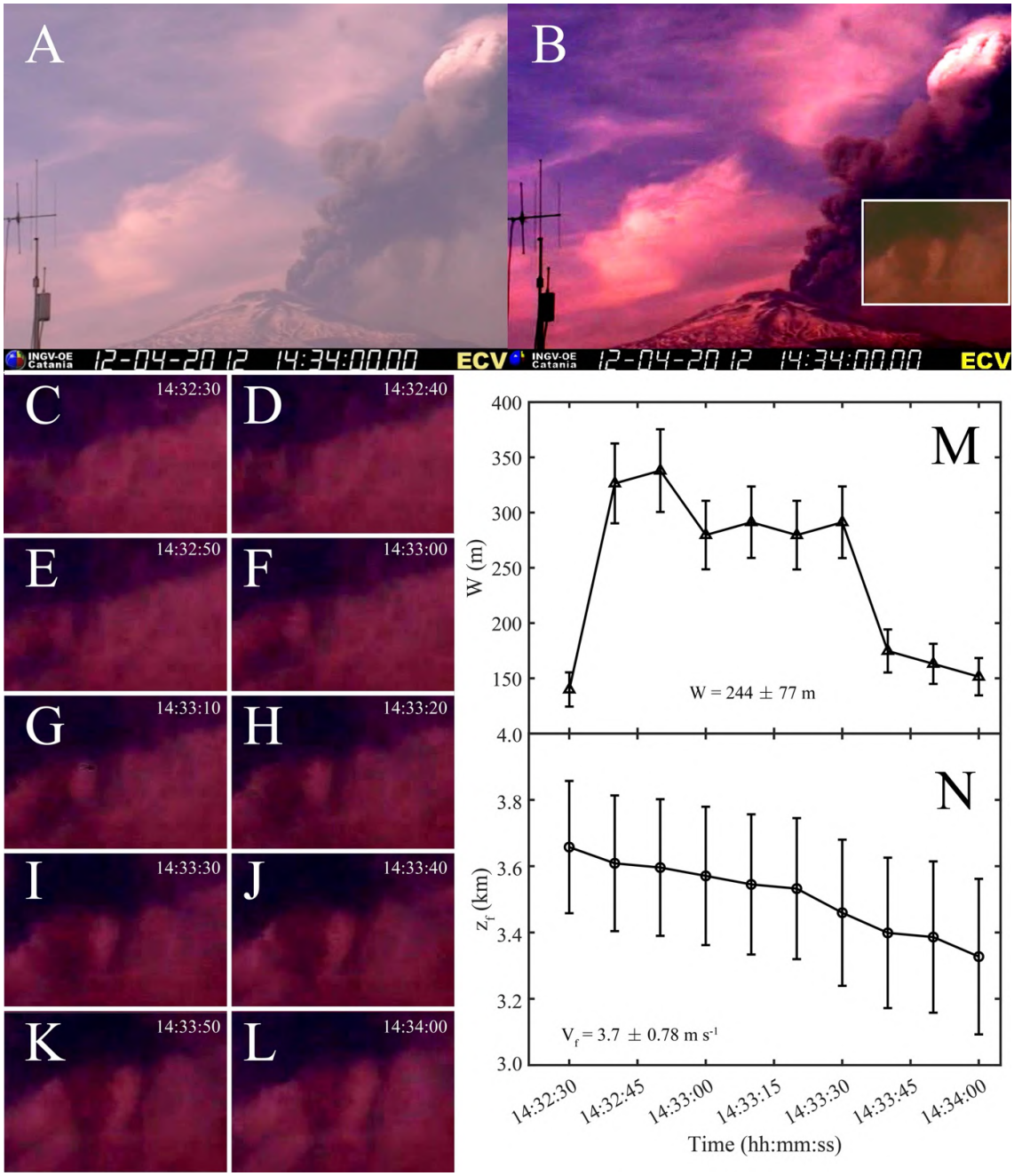

Figure A4.1: Analysis of ash fingers properties (Etna-1; Table 4.3). **A.** Original image. **B.** Processed image with increased contrast. **C-L.** Detailed view of an individual ash finger corresponding to the region highlighted by the yellow window in panel B. **M.** Evolution of the finger width W with time. **N.** Evolution of the finger front altitude z_f with time.

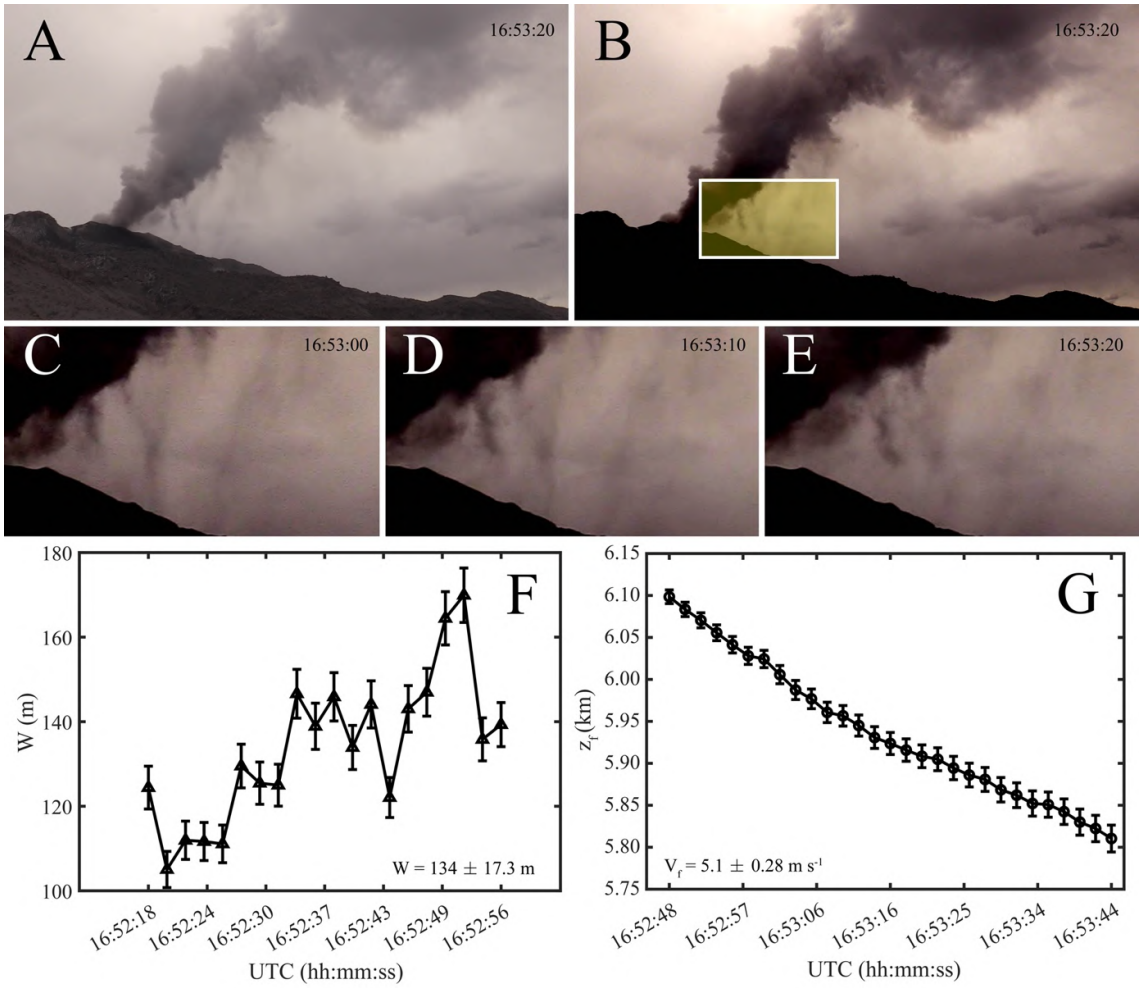

Figure A4.2: Analysis of ash fingers properties (Sab-6; Table 4.3). **A.** Original image. **B.** Processed image with increased contrast. **C-E.** Detailed view of an individual ash finger corresponding to the region highlighted by the yellow window in panel B. **F.** Evolution of the finger width W with time. **G.** Evolution of the finger front altitude z_f with time.

Chapter 5

The post-2016 long-lasting Vulcanian activity of Sabancaya volcano (Peru) and associated aeolian remobilisation of volcanic ash.[1]

5.1 Introduction

A variety of hazards are associated with volcanic eruptions that can act over potentially long periods of time (Siebert et al., 2010; Barclay et al., 2019). Furthermore, many volcanoes are known to experience stages during which frequent pulsatory explosions represent long-lasting hazards to the exposed communities over weeks to decades. Recent notable examples include Soufrière Hills, Montserrat (Bonadonna et al., 2002a,b; Druitt et al., 2002), Arenal, Costa Rica (Cole et al., 2005), Colima, Mexico (Varley et al., 2010), Tungurahua, Ecuador (Eychenne et al., 2013), Fuego, Guatemala (Naismith et al., 2019) and Sakurajima, Japan (Poulidis et al., 2019). A further example is Sabancaya in Peru, which has been characterised by multiple Vulcanian explosions per day between 1990-1998 (Gerbe and Thouret, 2004) and since November 2016 (Kern et al., 2017; Manrique et al., 2018). Despite being one of the most active volcanoes in Peru, and a persistent threat to the 30,000 inhabitants of

[1]To be submitted to *Journal of Volcanology and Geothermal Research* as: Fries, A., Dominguez, L., Jarvis, P. A., Pistolesi, M., Manrique Llenera, N., Aguilar Contreras, R., Valvidia Humerez, D., Rossi, E., Pollastri, S., Horwell, C. and Bonadonna, C. : The post-2016 long-lasting Vulcanian activity of Sabancaya volcano (Peru) and associated aeolian remobilisation of volcanic ash.

the Colca river valley, the explosive activity and the tephra deposits associated with Sabancaya remain only partially described.

Sequences of explosive events of similar intensity separated by time intervals varying from few seconds to several hours constitute pulsatory dynamics that are typical of Strombolian (Taddeucci et al., 2015) and Vulcanian (Clarke et al., 2015) eruptions. Hawaiian and Surtseyan eruptions can also be associated with pulsatory activity (Dominguez et al., 2016), quantified by the intensity and frequency of explosive events. Very frequent (i.e., very short repose times between explosions of the order of 0.1 to 10 s) explosions can produce sustained lava fountains resulting in the emission of steady plumes (Valentine and Gregg, 2008; Ripepe et al., 2013), whilst less frequent (i.e., longer repose times) explosions preferentially generate discrete plumes (Varley et al., 2006; Chojnicki et al., 2015). The variability of explosive events is, therefore, a key factor to determine the eruptive styles and dynamics, which can be studied based on the explosion frequency and magma viscosities (Dominguez et al., 2016).

Concomitantly with the Vulcanian eruption sequence, the wind remobilisation of loose volcanic ash from tephra deposits represents an additional, long-lasting, secondary hazard (Wilson et al., 2011; Forte et al., 2018). Remobilised ash can impact human health (Forbes et al., 2003; Horwell and Baxter, 2006; Baxter and Horwell, 2015), infrastructure, livestock and vegetation (Wilson et al., 2011; Forte et al., 2018) for extended periods of time (from syn-eruptive to millennia after an eruption) and over wider areas than those affected by primary fallouts (Dominguez et al., 2020b). Moreover, remobilisation of tephra by a wide variety of mechanisms has the potential to significantly alter the preservation of the deposits (Collins et al., 1983; Collins and Dunne, 1986; Manville et al., 2000; Blong et al., 2017; Cutler et al., 2018; Dugmore et al., 2018; Buckland et al., 2020; Bolós et al., 2021) which are key to assess the eruptive parameters of past eruptions (Pyle, 1989; Fierstein and Nathenson, 1992; Bonadonna et al., 2015b; Houghton and Carey, 2015).

Aeolian remobilisation processes include any sediment transport driven by the wind as a result of complex interactions between meteorological conditions, soil surface properties, particle characteristics, topography and local roughness elements

(Panebianco et al., 2017; Del Bello et al., 2018; Etyemezian et al., 2019; Dominguez et al., 2020a; Jarvis et al., 2020). The mobility of the particles mainly depends on their size and density, as well as on the wind friction velocity (Bagnold, 1941). Particles are lifted off the ground when aerodynamic forces become greater than resisting gravitational and cohesive forces. This force balance is typically quantified through the threshold friction velocity, and particles become mobile if the wind friction velocity becomes greater than the threshold friction velocity (Shao and Lu, 2000). We provide a more complete description of the calculation of the threshold friction velocity in Appendix A5.1. The easiest particles to aerodynamically entrain into the atmosphere by the action of the wind are those which minimise the threshold friction velocity, namely particles with diameters between 70 and 100 µm for terrestrial conditions. For coarser particles, increasing grainsize augments the gravitational forces, consequently increasing the value of the threshold friction velocity. For finer particles, decreasing grainsize increases cohesive forces, also increasing the threshold friction velocity (Dominguez et al., 2020a; Jarvis et al., 2020). However, these fine particles can also be lifted (splashed) due to the impact of coarser particles already in saltation with the ground (Shao et al., 1993; Kok et al., 2012). Once mobilised, the mode and duration of transport depend on the particle settling and wind friction velocities (Appendix A5.1; Scott et al., 1995; Kok et al., 2012; Mingari et al., 2020). For typical aeolian conditions on Earth, particles with diameters ranging from 70 to 500 µm will frequently undergo saltation, with coarser particles moving by creep and those finer becoming suspended on short ($\leq$ days) or long term (weeks-months) (Pye, 1987).

The understanding of aeolian remobilisation of volcanic ash is progressing through a combination of field, experimental and numerical work (Arnalds et al., 2013; Panebianco et al., 2017; Del Bello et al., 2018, 2021; Dominguez et al., 2020a,b; Jarvis et al., 2020; Mingari et al., 2020). Previous studies have mainly focussed on the characterisation of remobilisation affecting the deposits of short-lived (compared to the timescales of aeolian processes), or steady volcanic eruptions. In this supply-limited context, a large and finite volume of primary volcanic ash is almost instantaneously released during the eruption and aeolian processes are subsequently

influenced by the particle depletion with time (Dominguez et al., 2020b). However, in this chapter, we describe simultaneous aeolian remobilisation of tephra deposits produced by a long-lasting cycle of almost daily Vulcanian explosions that continuously releases wind-erodible primary volcanic ash since 2016.

Even though aeolian remobilisation of volcanic ash can largely impact the preservation potential of tephra deposits, the two processes (i.e., aeolian remobilisation and tephra sedimentation) are typically studied separately, hindering the determination of erupted volume. Here we propose a multidisciplinary study for the characterisation of both tephra sedimentation and syn-eruptive aeolian remobilisation. First, we have examined the primary tephra-fallout deposit based both on natural outcrops and on a network of dedicated collectors installed in February 2018. Second, we have characterised the pulsatory explosive activity of Sabancaya by analysing the variation in the repose intervals between explosions and the magma viscosity, as derived from geophysical data and geochemical models, respectively. Third, we have detailed observations of aeolian remobilisation events including their timing, intensity, and the important variables favouring their onset. Finally, we have analysed remobilised ash particles and compare their properties (i.e., size and morphology) with those from samples of airborne primary ash fallout deposits.

5.2 Sabancaya volcano

5.2.1 Geological setting

Sabancaya (5970 m above sea level; asl) in southern Peru is located in the Central Volcanic Zone (CVZ) of the Andes, 70 km northwest of Arequipa (Figure 5.1A). Volcanic activity in this zone results from the subduction of the Nazca oceanic plate below the south American continental lithosphere (Ramos, 1999; Wörner et al., 2018). At least seven volcanoes of the CVZ are known to have erupted in historical times, including Huaynaputina, that produced the largest historical eruption of the Andes in 1600 AD (Adams et al., 2001; Thouret et al., 2002; Verosub and Lippman, 2008; Prival et al., 2020). Sabancaya is the youngest and only historically active volcano of an alignment of three edifices oriented north-south that additionally includes

Ampato (6280 m asl) in the south and the eroded Hualca Hualca volcano (6025 m asl) in the north (Alcalá-Reygosa et al., 2011; Samaniego et al., 2016; MacQueen et al., 2020). The three volcanoes sit on the altiplano (altitude of approximately 4500 m asl), on the southern edge of the Colca river valley. The area around the volcano is sparsely populated, but Sabancaya nonetheless poses a threat to the communities inhabiting the Colca river valley (about 30000 inhabitants), 17 km north of the volcano, whilst volcanic ash has been reported to reach the city of Arequipa in the south, the second largest city of Peru (Manrique et al., 2018; Del Carpio Calienes et al., 2020).

The altiplano on which Sabancaya sits is an arid area, with scarce vegetation that is limited to shrubs and short grasses (<1 m) such as *Azorella compacta* (Wickens, 1995; Harpel et al., 2021) and *Jarava ichu* (Stouse, 1971; Galán de Mera and Linares Perea, 2012). Total annual precipitation is meagre, below 100 mm per year, with a dry and cold season from May to October and a wet and warm season from November to April (Supplementary Figure A5.1). Wind directions up to 5 km above the vent also exhibit a marked seasonality, with a prevailing direction towards the east during the dry season and towards the west during the rainy season (Thouret et al., 1994; Figure 5.1B). The meteorological conditions and the poor vegetation cover of the terrain around Sabancaya are favourable to the remobilisation of loose volcanic ash that stays exposed to the wind for long durations (Jarvis et al., 2020).

5.2.2 Explosive activity at Sabancaya

The current activity at Sabancaya started in 2012 with an increase in gas emissions and seismicity (Jay et al., 2015) before the onset of magmatic activity in November 2016 (Manrique et al., 2018; Del Carpio Calienes et al., 2020; MacQueen et al., 2020). Since then, Sabancaya has shown a pulsatory explosive activity up to the time of writing (March 2022) that is characterised by several Vulcanian explosions per day. In general, the heights of the plumes have progressively decreased since the start of the eruption (Coppola et al., 2022), with plumes up to 5500 m above the vent in July 2017 (Manrique et al., 2018) and to 4000 m above the vent in 2020 (Machacca Puma et al., 2021). Coppola et al. (2022) have identified 6 phases of

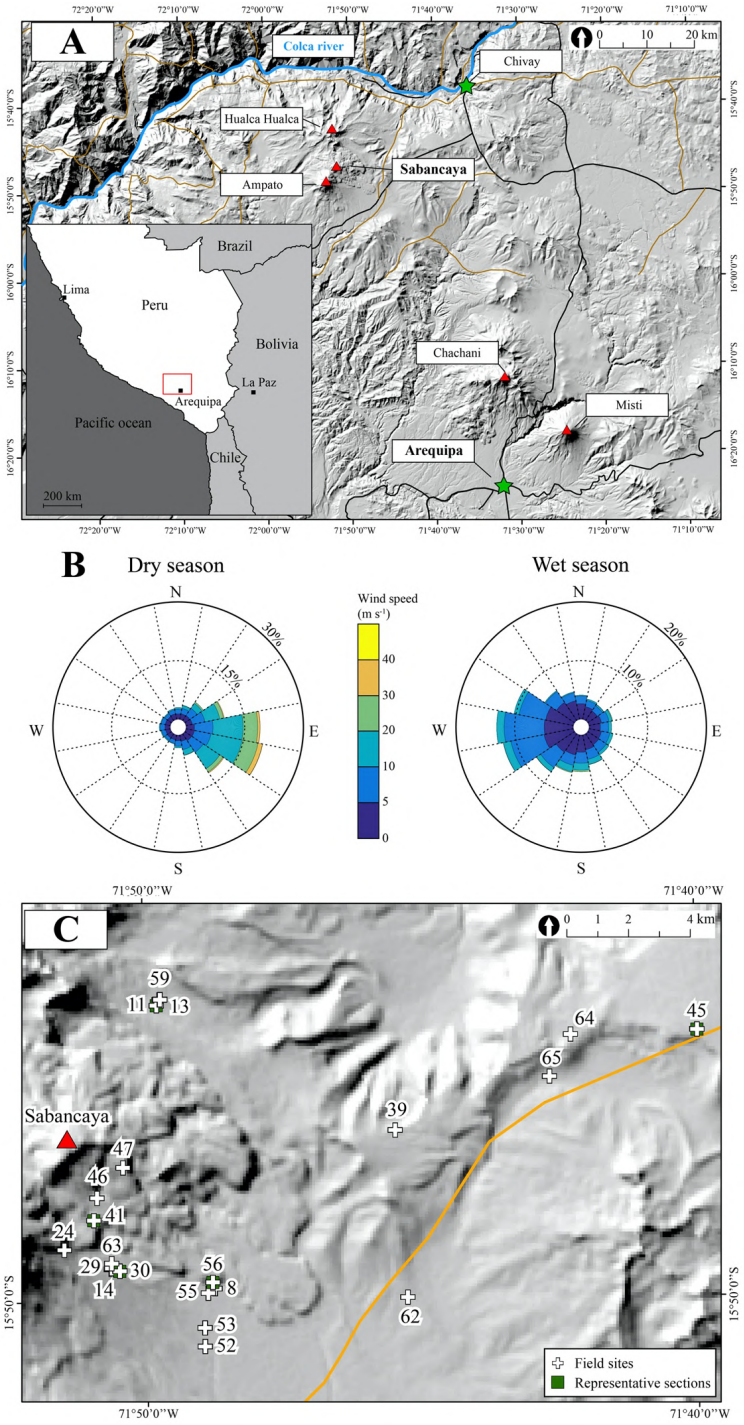

Figure 5.1: **A.** Location of Sabancaya volcano. The region presented here corresponds to the red area in the inset regional map. Green stars and red triangles indicate cities and volcanic edifices, respectively. The blue, black and brown lines, respectively, represent the Colca river and the main and secondary roads. **B.** Wind roses (i.e., the relative frequency of wind directions and speeds) at Sabancaya from November 2016 (start of the eruption) to November 2021. The wind roses are displayed separately for the dry (May to October) and the rainy (November to April) seasons. The wind directions are integrated from the height of the vent up to the maximum height of the volcanic plumes (between 5.9 and 11 km asl). Wind data are from the ECMWF (European Centre for Medium-range Weather Forecasts) ERA5 reanalysis dataset (Hersbach et al., 2020) using the Matlab package TephraProb, developed by Biass et al. (2016a). **C.** Close-up of Sabancaya volcano showing the location of stratigraphic sections. Numbers correspond to the field sites. The green rectangles indicate the location of the stratigraphic sections shown in Figure 5.4.

activity from November 2016 to December 2020. First, a short vent-clearing phase marks the beginning of the eruption with frequent explosions (Phase I: November – December 2016). This phase is followed by the growth of a first lava dome accompanied by an intense, but fluctuating, explosive activity (Phase II: December 2016 – January 2018). The number of explosions decreased and the growth of the lava dome stopped, during a phase of general stability (Phase III: January 2018 – March 2019). Following this period, both the growth of the dome and the explosive activity increased again (Phase IV: March – October 2019). The next phase is characterised by the lowest number of explosions associated with the collapse of the lava dome and the crater (Phase V: November 2019 – September 2020). Finally, Coppola et al. (2022) reported the formation of a second lava dome that started to grow in September 2020, accompanied with the renewal of the explosive activity (Phase VI: September – December 2020). Based on the height of the ash plumes that is related to the mass erupted by Vulcanian explosions (Bonadonna et al., 2002a; Druitt et al., 2002; Londono and Galvis, 2018), Coppola et al. (2022) estimated a tephra volume (recalculated as Dense Rock Equivalent, DRE, using magma and deposit densities of 2700 and 1000 kg m^{-3}, respectively) of 0.004-0.009 km^3 for the explosive period between November 2016 and December 2020, with a net decrease in the eruptive rate since 2018. Based on volume of lava domes, about 0.002 km^3 DRE has been calculated for the effusive phases in the same period. The whole-rock geochemistry of tephra samples (including ballistic clasts) collected in 2017 indicate homogeneous andesitic compositions, with a silica content representing 59.8-62.8 % of the mass (Manrique et al., 2018).

The seismicity and geodesy of the volcano are actively monitored by the Instituto Geofísico del Perú (IGP) through its Centro Vulcanológico Nacional (CENVUL) and the Observatorio Vulcanológico del INGEMMET (OVI) based on real-time data streaming and surveys that include visual observations (Machacca Puma et al., 2021; Coppola et al., 2022). Monitoring also comprises a dedicated tephra collector network distributed around the volcano in order to collect the primary tephra fallout material from which the accumulated mass load and the thickness can be determined over extended periods of time (several months).

Before the present activity of the volcano, a similar cycle of Vulcanian and phreatomagmatic explosions of andesitic to dacitic composition took place at Sabancaya between 1990 and 1998 (Thouret et al., 1994; Juvigné et al., 1998, 2008; Gerbe and Thouret, 2004; Samaniego et al., 2016) after a period of unrest that started in December 1986. During this eruptive cycle, the mean production rate of magma has been estimated to be low, at 0.001 – 0.01 km^3 per year, with a peak climatic phase from May to October 1990 that produced about 0.025 km^3 of tephra at the beginning of the eruption (Thouret et al., 1994; Gerbe and Thouret, 2004). The plume heights significantly decreased from plumes 3-7 km high in 1990-1992 to plumes <1 km after 1997. Simultaneously, the componentry of the ejecta substantially changed with time. In 1990, juvenile fragments constituted only 10-15 % of the ejecta. This proportion increased to 40-50 % of the material emitted in 1992-1997, with a slight decrease in 1995-1997. Juvenile fragments were eventually absent after 1997 (Gerbe and Thouret, 2004).

Few historical eruptions can be attributed to Sabancaya previously to the 1990-1998 eruptive cycle, with mentions in Spanish chronicles of only two events during the 18^{th} century (Thouret et al., 1994) confirmed by the presence of a 10-30 cm coarse ash layer dated at 265 ± 30 BP (Samaniego et al., 2016). Additionally, the study of peat sections near Sabancaya by Juvigné et al. (2008) reveals the presence of four phreatomagmatic tephra units dated at 1870-2120 BP, 2170-2440 BP, 4120-4520 BP and 9440 to 9770 BP and tentatively attributed to eruptions originating from the local volcanoes (Ampato and/or Sabancaya). They also discovered the presence of Plinian tephra fall layers that can be related to the large regional tephra fallout from the 1600 AD eruption of Huaynaputina, which Volcanic Explosivity Index (VEI) has been estimated at VEI 6 (Adams et al., 2001; Thouret et al., 2002; Prival et al., 2020); and to the 2030 BP eruption of Misti (Cobeñas et al., 2012). Their study suggests that the explosive activity at Sabancaya was sporadic before the 1990-1998 eruptive cycle, with long repose periods in between eruptions. This is confirmed by the study of Samaniego et al. (2016) who identified at least 6 eruptions in the last 4000-5000 years, including historical 1990-1998 and 18^{th} century events. Whilst the activity was mainly effusive 6000 to 3000 years ago during the formation

of Sabancaya edifice, it became mostly eruptive 3000 years ago. In general, the eruptive rate is estimated at 5-7 $\times$ 10^{-4} km^3 per year at Sabancaya in the last 3000 years (Samaniego et al., 2016).

5.3 Methods

5.3.1 Field Analysis of tephra deposits, collectors and real-time ash fallout sampling

We conducted a field campaign at Sabancaya from 27 July to 12 August 2018 during which we studied proximal to medial (<25 km from the source; Figure 5.1C) primary tephra deposits, tephra fallout and aeolian remobilisation processes. To do so, in addition to analysing the stratigraphy, we apply various sampling strategies for separately collecting primary tephra fallout and remobilised volcanic particles (Figures 5.2 and 5.3). The detailed list of field measurements and collected samples can be found in Supplementary Table A5.1.

During the field campaign we have studied 21 stratigraphic sections distributed in the north, south and east sectors of the volcanic edifice, and located at distances comprised between 1.9 to 21 km from the vent (Figure 5.1C; Table A5.1). Due to the difficult access in the western part and to the presence of blocky lava flows of about 300-400 m high on the eastern and north-eastern flank of Sabancaya (Bulmer et al., 1999; Samaniego et al., 2016), the detailed study of these areas around the volcano was not possible. We have, therefore, concentrated our efforts south of the edifice, in glacial valleys that are associated with gentle slopes (Alcalá-Reygosa et al., 2011). At least 3 tephra units were identified and measured throughout these stratigraphic sections. This study is focused on the top layer associated with the ongoing eruption of Sabancaya and the subsequent remobilisation of these deposits by the wind. The top layers have been thus sampled for grainsize and particle shape analysis. Samples have been also collected to estimate the Dense Rock Equivalent (DRE) density.

Since surface characteristics can influence the conservation of tephra deposits (Dugmore et al., 2018), stratigraphic sections have been studied in flat areas, where

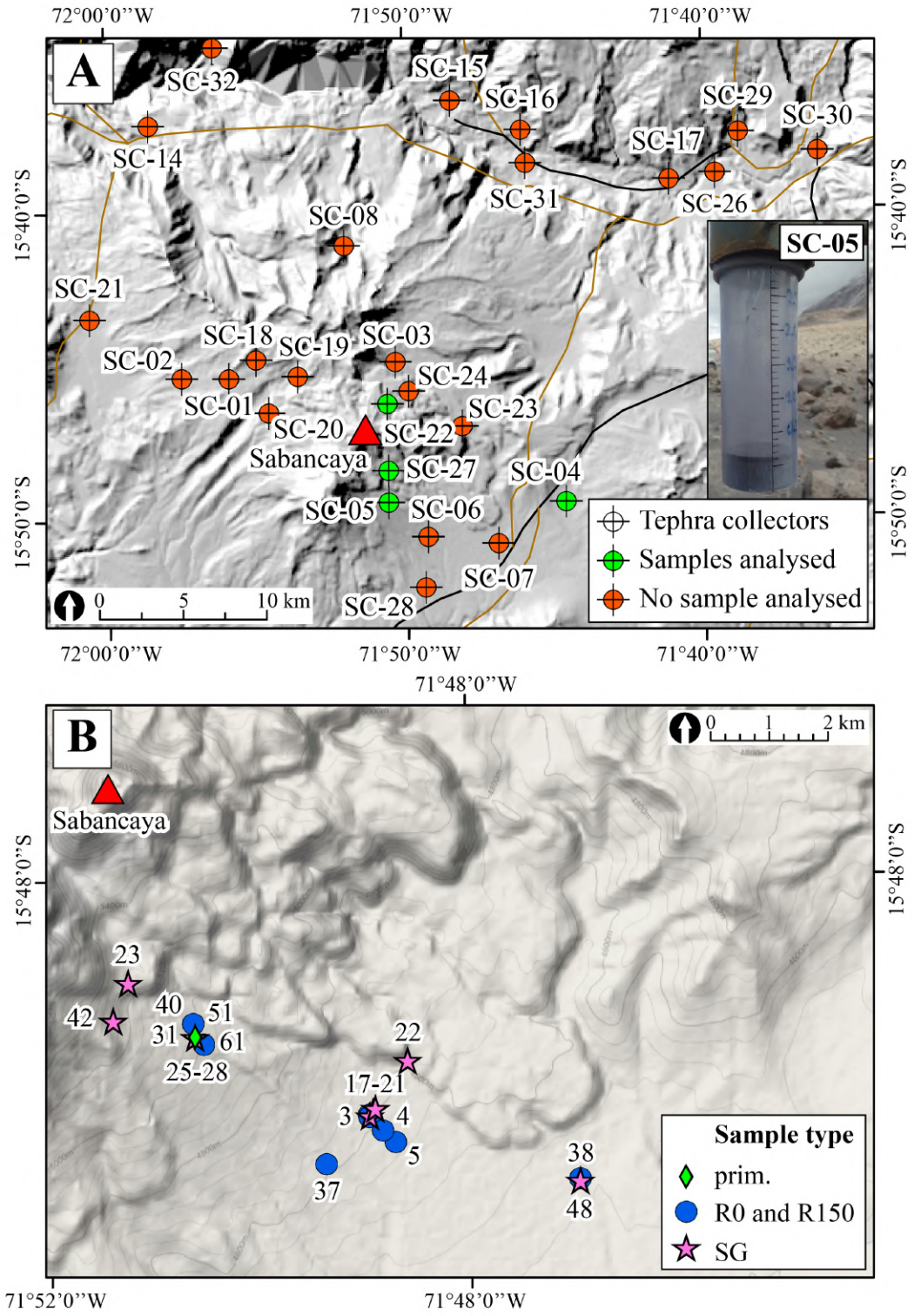

Figure 5.2: **A.** Location of the OVI ash collectors represented by the crossed circles. Inset in the bottom right shows the tephra collector SC-05 on the flanks of Ampato on 2 August 2018. Green circles highlight the location of tephra collectors for which samples have been analysed. **B.** Location of the samples of airborne material collected on adhesive paper, with primary ash fallouts (prim. samples), remobilised material (R0 and R150 samples) and samples of the most surficial ground layer (SG samples) represented by green diamonds, blue circles and pink stars, respectively. Numbers correspond to the field sites (Supplementary Table A5.1).

post-depositional slope processes were unlikely to have affected the primary deposits (Selby, 1982). We have noted the presence of local roughness elements that can affect the preservation of the deposits in their vicinity. For example, the preservation of tephra fallout deposits may be modified as a function of the vegetation type and abundance (Cutler et al., 2018; Dugmore et al., 2018). Accumulation of tephra inside and around plants, on both the windward and the leeward areas, commonly results in thicker layers of remobilised ash (Dominguez et al., 2020a). Similarly, rocks are also known to inhibit erosion by the wind and to protect the deposits on their leeward side (Kok et al., 2012; Dominguez et al., 2020a).

The OVI monitoring network includes 33 tephra collectors that have been installed within a 35 km radius around Sabancaya (Figure 5.2A) in order to measure the evolution of the cumulative mass of primary tephra fallout since February 2018 (Valdivia, 2019). Collectors are robust containers, funnel-shaped, upward facing, inspired from the design of Bernard (2013) (Valdivia, 2019). They can be used to study tephra accumulations up to 30 mm in thickness. Due to the challenging field conditions and the remoteness of their emplacement sites, collectors are unevenly distributed and tephra collection is performed by the INGEMMET staff during missions about two to three times a year. Additionally, there is a lack of collectors southwest of the vent and in the areas proximal to the vent (<5 km) (Figure 5.2A). We have analysed the morphology and grainsize of 17 tephra samples derived from tephra collectors (samples labelled sab; Table 5.1; Supplementary Table A5.1). The location of the collectors from which samples have been analysed is highlighted in Figure 5.2B.

In order to integrate the cumulative sampling of tephra collectors, we have performed real-time sampling of primary tephra fallouts on adhesive paper (samples labelled prim.; Supplementary Table A5.1), similarly to the setup of Bonadonna et al. (2011). Airborne particles stick on the adhesive paper, which is mounted onto a thin section for subsequent grainsize and shape analysis with a reflected light microscope. In total we collected 12 primary samples on the flanks of Ampato, 4 km south of the vent (Figure 5.2B), during two successive explosions on 2 August 2018.

Sample	Collector	Sampling dates	Sampling duration (days)	Latitude	Longitude	Distance from the vent (km)
sab-1726	SC-27	23 Jun. to 25 Jul. 2017	33	-15.647165	-71.660010	2.7
sab-1832	SC-27	07 Apr. to 25 May 2018	49	-15.647165	-71.660010	2.7
sab-1847	SC-22	22 May to 23 Jun. 2018	32	-15.764047	-71.831625	3.7
sab-1850	SC-27	27 May to 20 Jun. 2018	24	-15.647165	-71.660010	2.7
sab-1852	SC-04	25 May to 20 Jun. 2018	26	-15.824344	-71.744081	12.8
sab-1854	SC-05	25 May to 19 Jun. 2018	25	-15.824365	-71.843434	4.4
sab-1869	SC-05	19 Jun. to 28 Jul. 2018	39	-15.824365	-71.843434	4.4
sab-1890	SC-05	28 Jul. to 06 Dec. 2018	131	-15.824365	-71.843434	4.4
sab-1892	SC-27	20 Jun. to 06 Dec. 2018	169	-15.806825	-71.842863	2.7
sab-1895	SC-22	23 Jun. to 07 Dec. 2018	167	-15.764047	-71.831625	3.7
sab-1926	SC-27	15 Apr. to 20 Aug. 2019	127	-15.806825	-71.842863	2.7
sab-1927	SC-05	06 Apr. to 20 Aug. 2019	136	-15.824365	-71.843434	4.4
sab-1947	SC-04	21 Aug. to 22 Oct. 2019	62	-15.824344	-71.744081	12.8
sab-1948	SC-05	21 Aug. to 22 Oct. 2019	62	-15.824344	-71.744081	4.4
sab-1957	SC-22	15 May to 24 Oct. 2019	160	-15.764047	-71.831625	3.7
sab-1963	SC-27	20 Aug. to 28 Nov. 2019	100	-15.806825	-71.842863	2.7
sab-1967	SC-04	15 Oct. to 28 Nov. 2019	44	-15.641568	-71.765053	12.8

Table 5.1: Tephra collectors samples analysed with the BetterSizer S3 Plus to obtain the grainsize distribution and the morphology of primary ash fallouts.

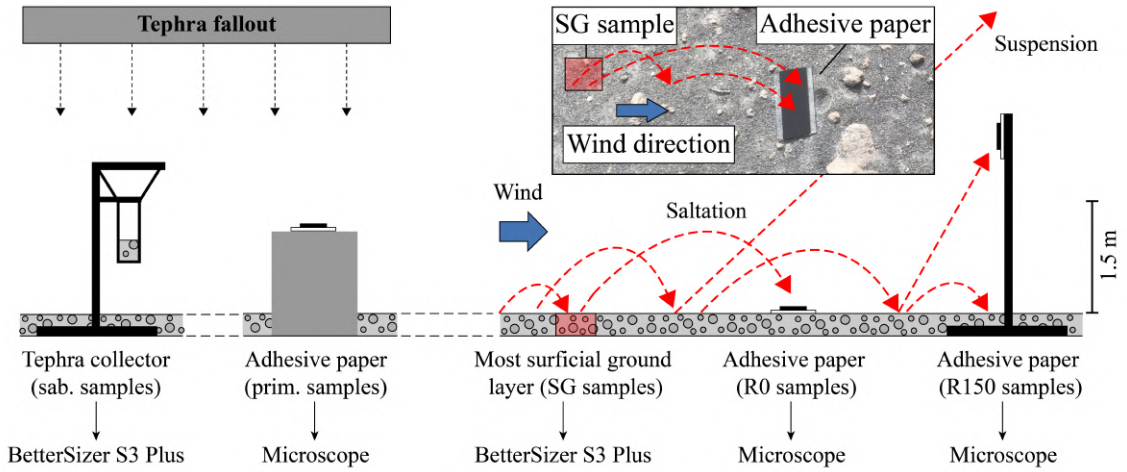

Figure 5.3: Sampling strategies applied for the collection of primary fallout and remobilised particles. Inset picture shows the collection of remobilised particles on adhesive paper at the level of the ground (R0 samples). Red arrows represent possible trajectories of remobilised particles.

5.3.2 Observation and real-time sampling of aeolian remobilisation

We also collected airborne particles associated with aeolian remobilisation events on adhesive paper at different sites (Figure 5.2B). We distinguished between particles sampled 1.5 m above the ground (samples labelled R150; Supplementary Table A5.1), with the thin section held vertically facing the upwind direction, and particles that have been sampled by placing the adhesive paper face up at ground level (samples labelled R0; Supplementary Table A5.1). During field experiments, we have complemented the sampling strategy by sampling the most surficial ground layer upwind of the thin section location (samples labelled SG; Supplementary Table A5.1). This sample is characteristic of the source material from which airborne remobilised particles originate. Figure 5.3 summarises the sampling strategies used to collect airborne remobilised particles.

In order to measure the concentration of fine ash in suspension (diameter $d \leq 10$ µm) and to complement the sampling of remobilised volcanic ash on adhesive paper, we have undertaken *in-situ* measurements of Particulate Matter with a diameter $\leq$10 µm (PM_{10}) near the location of the field experiments. PM_{10} measurements have been performed using a SidePak AM520 PM_{10} measurement device with a sampling frequency of 1 s. The evolution in the PM_{10} concentration has been recorded for

Site	Date	Time (hh:mm)	Duration (hh:mm)	Latitude	Longitude
5	29 Jul. 2018	12:06 – 14:30	02:24	-15.836799	-71.815849
12	30 Jul. 2018	09:46 – 11:46	02:00	-15.744903	-71.828286
15	31 Jul. 2018	11:35 – 15:46	04:11	-15.836247	-71.815980
31	03 Aug. 2018	09:27 – 15:22	04:55	-15.822000	-71.843777
36	04 Aug. 2018	10:36 – 11:47	01:11	-15.825111	-71.842083

Table 5.2: Date, duration (time is given in Peru standard time PET) and location of PM_{10} measurements.

durations of 1 to 5 hours (Table 5.2).

Finally, we have acquired High Definition (HD; 1920 × 1080 pixels) and High Speed (HS; 3200 frames s^{-1}) videos of remobilisation events, with a Canon Legria HFG40 and a Phantom Miro M110 HS Camera mounted with a 60 mm Nikon lens, respectively. HD videos have been used to image, describe and classify aeolian remobilisation events according to the categories of lithometeors proposed by Dominguez et al. (2020a), whilst HS videos have been used to investigate remobilisation mechanisms at the scale of the particles (38.5 µm px^{-1}). To do so, the HS camera was placed on the ground and triggered for a duration of 1 s when particles were seen in motion.

5.3.3 Particle characterisation

We have characterised the particles collected during the field campaign and have applied specific analytical strategies, depending on the type of sample. In particular, we have used distinct methods to analyse loose samples and the particles collected on adhesive paper (Figure 5.3).

Particle size and morphology

Tephra samples obtained from collectors, from stratigraphic sections (layers A, B and C) and from field experiments (i.e., samples of the most surficial ground layers), were dried for 24 h in an oven at 80°C before obtaining their grainsize distributions (GSD) by manual sieving up to 0 ϕ (i.e., 1 mm; $\phi = -\log_2 d$, with d the particle diameter in mm; Inman, 1952). The grainsize distribution of the fraction finer than 0 ϕ ($d < 1$ mm) has been measured by a combination of laser diffraction and dynamic

image analysis using a BetterSizer S3 Plus analyser. The final GSD of each sample has then been calculated from merging the grainsize distributions above and below 0 ϕ to obtain the weight percentage (m, wt%) of each size class i as follows

$$m_i^{wt\%} = \frac{(m_i^{BSwt\%} m_i^{>0\phi} + m_i^{<0\phi})}{m_t}, \tag{5.1}$$

where $m_i^{BSwt\%}$ is the weight percentage obtained with the BetterSizer S3 Plus, $m_i^{>0\phi}$ is the mass fraction larger than 0 ϕ ($d < 1$ mm), $m_i^{<0\phi}$ is the mass fraction smaller than 0 ϕ ($d > 1$ mm), and m_t is the total mass of the sample. Based on the final GSD, we calculated the median diameter Md_Φ and the sorting coefficient ofInman (1952) $\sigma_\Phi = (\sigma_{84\Phi} - \sigma_{16\Phi})/2$, with $\sigma_{16\Phi}$ and $\sigma_{84\Phi}$ being the 16$^{\text{th}}$ and 84$^{\text{th}}$ percentiles of the grainsize distribution in Φ units, respectively.

The morphology of particles finer than 0 ϕ ($d < 1$ mm) has been obtained from images acquired with two CCD cameras equipped on the BetterSizer S3 Plus. Individual particle images were first treated automatically and manually in order to remove touching and out-of-focus particles. The remaining images were then binarized and analysed in order to obtain the equivalent diameter d_{eq} ($d_{eq} = 4A_p/\pi$, with A_p the area of a particle) of the particles, as well as their form factor, solidity and convexity, that are important shape parameters for measuring the form and roughness of particles (Liu et al., 2015; Dominguez et al., 2020a). The form factor describes the general roundness of the particles, with values of 1 indicative of spherical particles. It is defined as a function of the area over the squared perimeter of a particle (form factor = $4\pi A_p/P_p^2$, with P_p the perimeter of a particle). Solidity corresponds to the ratio of the particle area to the area of its bounding convex hull (solidity = A_p/A_{ch}, with A_{ch} the area of the bounding convex hull) and provides a measure of the morphological roughness of the particles. The convexity, meanwhile, is defined as the ratio between the perimeters of the convex hull and the particle (convexity = P_{ch}/P_p, with P_{ch} the perimeter of the convex hull), and yields information on the textural morphology (i.e., the roughness of the particle surface). For both convexity and solidity, values close to 1 indicate that the particles are smooth and rounded.

Samples of airborne particles collected on adhesive paper have been analysed with

a reflected light microscope (Olympus BX61) equipped with an automated stage for Multi Image Alignment (MIA). MIA allows us to capture the entire surface of the adhesive paper in a single operation at a resolution of 2.2 µm px^{-1}. Images were then treated manually in order to contour the particles before binarization, that was facilitated by the high contrast between the light-coloured primary ash particles and the black tape (see Supplementary Figure A5.2). The binary images were analysed in ImageJ (Schneider et al., 2012) by using a macro based on the work of Liu et al. (2015) to calculate d_{eq} and shape descriptors for particles with pixel densities greater or equal to 250 px per particle. This, therefore, limits the analysis to particles with $d_{eq} \geq 10$ µm. Similarly to the analysis performed with the BetterSizer, we have obtained the form factor, solidity and convexity of the particles. Since the estimation of the particle morphology is different for loose material (i.e., dynamic image analysis) and for samples collected on adhesive paper (i.e., microscope analysis), here we compare only the shape descriptors of samples analysed with the same methods. Quantifying the discrepancies related to the difference in analytical methods is beyond the scope of this study.

The total volume of the particles in a size class i is given by the sum of the equivalent volumes V_i^{eq} of all the particles with a d_{eq} belonging to size class i. The GSD of the sample is then calculated in volume percentage (vol%) by dividing the volume of particles in each size class by the total volume of the particles in the sample V_t (Freret-Lorgeril et al., 2019)

$$V_i^{vol\%} = \sum_i \frac{V_i^{eq}}{V_t}, \tag{5.2}$$

where $V_i^{vol\%}$ is the vol% of particles in the size class i. GSDs in vol% are later converted in wt% by assuming that the particle density does not depend on the particle size for the diameter range analysed with the microscope.

Density and composition analyses

Density measurements have been performed for the size fractions finer than 0 ϕ (d < 1 mm). We have analysed three samples from tephra collectors (sab-1869, sab-

1890 and sab-1892; Table 5.2), one sample of each stratigraphic unit, including the most surficial ground layer. Using an Ultrapyc 1200e Helium pycnometer, we have measured the density of some crushed samples of primary ash fallouts to enable DRE estimates. Additionally, we have estimated the density of the deposits measuring the mass of 10 cm^3 samples from tephra collectors contained in a graduated cylinder with a Mettler Toledo PM100 high precision balance. The uncertainty on these density measurements has been constrained from the dispersion of the results obtained for 3 samples (sab-1869, sab-1890 and sab-1892).

The percentage of juvenile fragments from componentry analyses has been estimated for 2 primary ash samples (sab-1869 and sab-1895) and 3 different stratigraphic units (A – site 30, B – site 30 and C – site 13) identified during our fieldwork. For this purpose, we have manually separated the juvenile material with diameters lower than 0 Φ ($d > 1$ mm) from lithic clasts at the binocular microscope. Juvenile material consists of dark, poorly vesicular and highly porphyritic clasts (Manrique et al., 2018), similarly to the products of the 1990-1998 eruption (Gerbe and Thouret, 2004).

The groundmass glass composition has been obtained with a Jeol JXA-8200 electron microprobe at the University of Geneva. They were carried out on a dense ballistic fragments (sab-1813) ($d \sim 60$ cm) that followed a ballistic trajectory after ejection and that was sampled at a distance of about 500 m from the vent on 06 April 2018 (Supplementary Table A5.1). We have additionally analysed the groundmass glass composition of juvenile volcanic ash from 4 primary ash samples (sab-1726, sab-1832, sab-1869 and sab-1895) that are considered representative of the melt composition (Table 5.3) and collected from 3 different stratigraphic units (A – site 30, B – site 30 and C – site 13). Analytical conditions for this were a 15 kV accelerating voltage with an emission current of 6 nA and a beam diameter of 10 µm.

Sample	sab-2[(a)]	sab-9218[(a)]	sab-941a[(a)]	sab-943[(a)]	sab-9719[(a)]	sab-1726	sab-1813	sab-1832	sab-1869	sab-1895	A-30	B-30	C-13a	C-13b
Year	1990	1992	1994	1994	1997	2017	2018	2018	2018	2018	2016-2018	2016-2018	?	?
Juveniles (%)	10-15	40-50	40-50	40-50	< 40-50	-	-	-	91	94	87	77	< 25	< 25
Number of analysis	8	5	3	7	3	10	10	12	11	9	12	11	9	4
SiO_2	76.4 (1.3)	72.8 (0.8)	75.7 (0.6)	74.2 (1.8)	78.2 (0.4)	74.8 (1.2)	73.2 (0.8)	74.5 (2.6)	74.2 (2.5)	73.3 (3.6)	74.6 (1.6)	75.2 (1.2)	72.0 (2.0)	72.5 (1.4)
TiO_2	0.5 (0.1)	0.6 (0.1)	0.4 (0.3)	0.5 (0.1)	0.4 (0.05)	0.1 (0.01)	0.1 (0.01)	0.1 (0.02)	0.6 (0.2)	0.6 (0.1)	0.6 (0.1)	0.6 (0.1)	0.7 (0.3)	0.6 (0.1)
Al_2O_3	11.8 (0.8)	12.7 (0.5)	12.1 (0.5)	12.7 (0.9)	10.8 (0.2)	12.3 (0.6)	13.2 (0.2)	12.6 (1.4)	13.4 (1.4)	13.3 (2.9)	12.9 (1.0)	12.7 (1.1)	14.1 (1.2)	13.2 (1.8)
FeO	1.1 (0.2)	1.5 (0.1)	1.3 (0.2)	1.2 (0.1)	1.1 (0.1)	1.5 (0.1)	1.6 (0.1)	1.3 (0.6)	1.3 (0.3)	1.5 (0.2)	1.5 (0.2)	1.4 (0.1)	1.7 (0.8)	1.1 (0.2)
MgO	0.2 (0.1)	0.1 (0.05)	0.06 (0.02)	0.1 (0.1)	0.04 (0.01)	0.1 (0.05)	0.2 (0.01)	0.2 (0.3)	0.1 (0.1)	0.2 (0.1)	0.2 (0.1)	0.1 (0.04)	0.3 (0.2)	0.08 (0.03)
MnO	0.03 (0.03)	0.03 (0.05)	0 (0)	0.1 (0.2)	0.05 (0.01)	0.03 (0.03)	0.02 (0.02)	0.2 (0.3)	0.03 (0.02)	0.01 (0.01)	0.02 (0.02)	0.02 (0.02)	0.04 (0.01)	0.04 (0.02)
CaO	0.5 (0.2)	0.5 (0.1)	0.2 (0.1)	0.4 (0.1)	0.5 (0.1)	0.4 (0.1)	0.6 (0.03)	0.8 (0.6)	1.0 (0.8)	1.1 (1.7)	0.6 (0.2)	0.6 (0.5)	1.0 (0.5)	0.6 (0.5)
Na_2O	2.9 (0.5)	3.2 (0.3)	2.9 (0.1)	2.8 (0.7)	2.6 (0.4)	3.3 (0.3)	3.5 (0.4)	3.2 (0.6)	3.8 (0.6)	3.7 (0.6)	3.6 (0.6)	3.7 (0.3)	4.3 (0.5)	3.5 (0.6)
K_2O	5.8 (0.3)	6.1 (0.1)	6.0 (0.2)	6.2 (0.6)	5.7 (0.2)	5.6 (0.2)	5.4 (0.1)	5.3 (0.5)	5.3 (0.5)	5.3 (1.1)	5.4 (0.3)	5.5 (0.5)	5.3 (0.6)	6.1 (0.3)
Total	99.2	97.7	98.7	98.3	99.2	98.2	97.8	98.1	99.7	99.0	99.4	99.9	99.4	97.8

Table 5.3: Composition in major elements of groundmass glasses. The table presents average values, with standard deviation in brackets. [(a)]Analysis of tephra sampled during the previous eruption (1990-1998) are from Gerbe and Thouret (2004).

5.3.4 Erupted volume and mass

We have drawn isopach maps from the thicknesses of the different units measured during our field campaign (27 July to 12 August 2018). Isopach contours have been constrained only for the top tephra layers analysed at field sites corresponding to flat areas where deposits are undisturbed by surface elements (i.e., plants and rocks). Estimation of the volume of tephra fallout was inferred using methods based on the thinning of the deposits with distance from the vent, e.g. exponential (Pyle, 1989; Fierstein and Nathenson, 1992), power-law (Bonadonna and Houghton, 2005) and Weibull (Bonadonna and Costa, 2012, 2013) fits, using the Matlab function TephraFits (Biass et al., 2019).

Additionally, a cumulative isomass map was compiled based on mass load (kg m^{-2}) as derived from tephra collectors with observations spanning over three overlapping periods from April 2018 to November 2019. The three periods considered are: i) from April 2018 to October 2019, for tephra collectors west of the vent; ii) from May 2018 to October 2019, for tephra collectors mainly located east of the vent; and iii) from July 2018 to November 2019, for the most proximal and distal tephra collectors. These periods all include the period from July 2018 to October 2019 and respectively cover 19, 18 and 16 months. The period from July 2018 to November 2019 is associated with the shortest sampling duration and, therefore, provides minimum estimations for contouring tephra accumulation. The calculation of the cumulative mass of tephra was based on these three periods, as they were associated with the highest number of available measurements and the widest spatial distribution for constructing the isomass map. Similarly to volume calculations, we have estimated the erupted mass based on the exponential, power-law and Weibull methods. The erupted mass was converted to erupted volume based on the deposit density estimation.

5.3.5 Explosion frequency and classification

Pulsatory explosive behaviour of Sabancaya as seen from sporadic visual observations has been analysed based on the distribution of the repose times between explosions and the calculated viscosity of magma, following the methodology of

Dominguez et al. (2016). We have investigated the frequency of explosions and the repose intervals of consecutive single events by cross-checking geophysical data recorded by the OVI seismic stations and visual observations (Machacca Puma et al., 2021; Coppola et al., 2022) from the beginning of the explosive activity in November 2016 until May 2021. Although the geophysical data and the explosive activity at the surface are difficult to correlate, real-time and continuous monitoring of geophysical signals offers an uninterrupted proxy for the frequency of explosions, whilst visual observations can only be used during the day and under favourable weather conditions. However, visual data provided valuable insights in order to statistically constrain the threshold of seismic energy (>0.1 MJ) associated with visible explosions producing pyroclastic material, enabling filtering of the seismic signal. For the classification of the explosions based on their frequency, the distribution of the repose time between single events has been analysed by applying the log-logistic renewal process following the methodology of Dominguez et al. (2016). To this end, the magma viscosity was constrained based on the models of Giordano et al. (2008), for the melt viscosity, and Costa et al. (2009) for the bulk viscosity. The melt composition was constrained from the groundmass glass compositions of the tephra produced between June and July 2017 (sab-1726) and between April and May 2018 (sab-1832), whilst we have considered the same water content of 1.5 wt% and crystallinity of 22.5 vol% as reported by Gerbe and Thouret (2004), given the similarities in the magma composition between the current eruptive activity and the 1990-1998 cycle. A melt temperature of 900° C is assumed as an average value for similar magma compositions such as Santiaguito, Guatemala (Scott et al., 2012) and Ubinas, Peru (Rivera et al., 2014) eruptions.

5.4 Results

5.4.1 Tephra deposits

The tephra deposits located at distances <10 km from the vent can be divided into three main layers (A, B and C) that are described below. Figure 5.4 shows the correlation between the stratigraphic sections studied at increasing distances from

the vent, along with representative GSDs and particle shape analysis for sites 41 (2.6 km of SE the vent) and 30 (4.5 km SE of the vent) which are used as reference sections. Table 5.3 presents the composition in major elements of groundmass glasses and the percentage of juvenile fragments, for layers A, B and C, as well as for primary tephra samples and tephra emitted during the 1990-1998 eruption (Gerbe and Thouret, 2004). All samples are characterised by rhyolitic groundmass glass compositions highly enriched in K_2O (> 5 wt%).

Layer A represents the top of the stratigraphic sections. It is composed of uncompacted grey ash covered by a millimetric (<5 mm) layer of coarser ash. A is well sorted, with Md_Φ values between 1.5 and 2.6 Φ, and σ_Φ between 0.8 and 1.5 Φ. The top, slightly coarser ash (Md_Φ = 1.0 – 2.6 Φ) is less sorted, with σ_Φ varying from 0.8 to 3.3 Φ. The thickness of layer A varies locally, notably as a function of the surface elements (e.g., vegetation, boulders, topography; Supplementary Table A5.1). For example, at 6.5 km southeast from the vent, it varies between 5 cm inside plants and 2 cm outside. Moreover, the thickness of layer A does not decrease gradually with distance from the vent, but is rather uniform and generally between 2 and 3 cm in the entire studied area (Figure 5.4). The local variation in thickness, the presence of ripples at the surface of the deposits (Supplementary Figure A5.3) and of cross-bedding structures in A, along with the looseness of the material suggest that layer A has undergone wind erosion and is probably continuing to be remobilised.

Below A, layer B appears as a compacted layer of darker grey ash stratified in multiple sub-layers in most proximal locations (e.g., site 41; Figure 5.4). The grainsize distributions of A and B are very similar (Md_Φ = 1.4 – 3.3 Φ and σ_Φ = 0.8 – 2.7 Φ; Figure 5.4), and their groundmass glass composition is nearly identical, with similar percentages of juvenile fragments (87 % for A and 77 % for B at site 30; Table 5.3). The form factor values of particles in layers A and B are also comparable, with 90 % of the particles between 0.3 and 0.8, and median form factors of 0.7 (Figure 5.4). Similarly to A, the thickness of B varies at the local scale in association with the presence of surface elements (Supplementary Table A5.1). Conversely, the thickness of B clearly varies as a function of the distance from the vent along the prevailing wind direction and passes from 18 cm at 2 km E of the vent (site 47) to 1.5 cm at

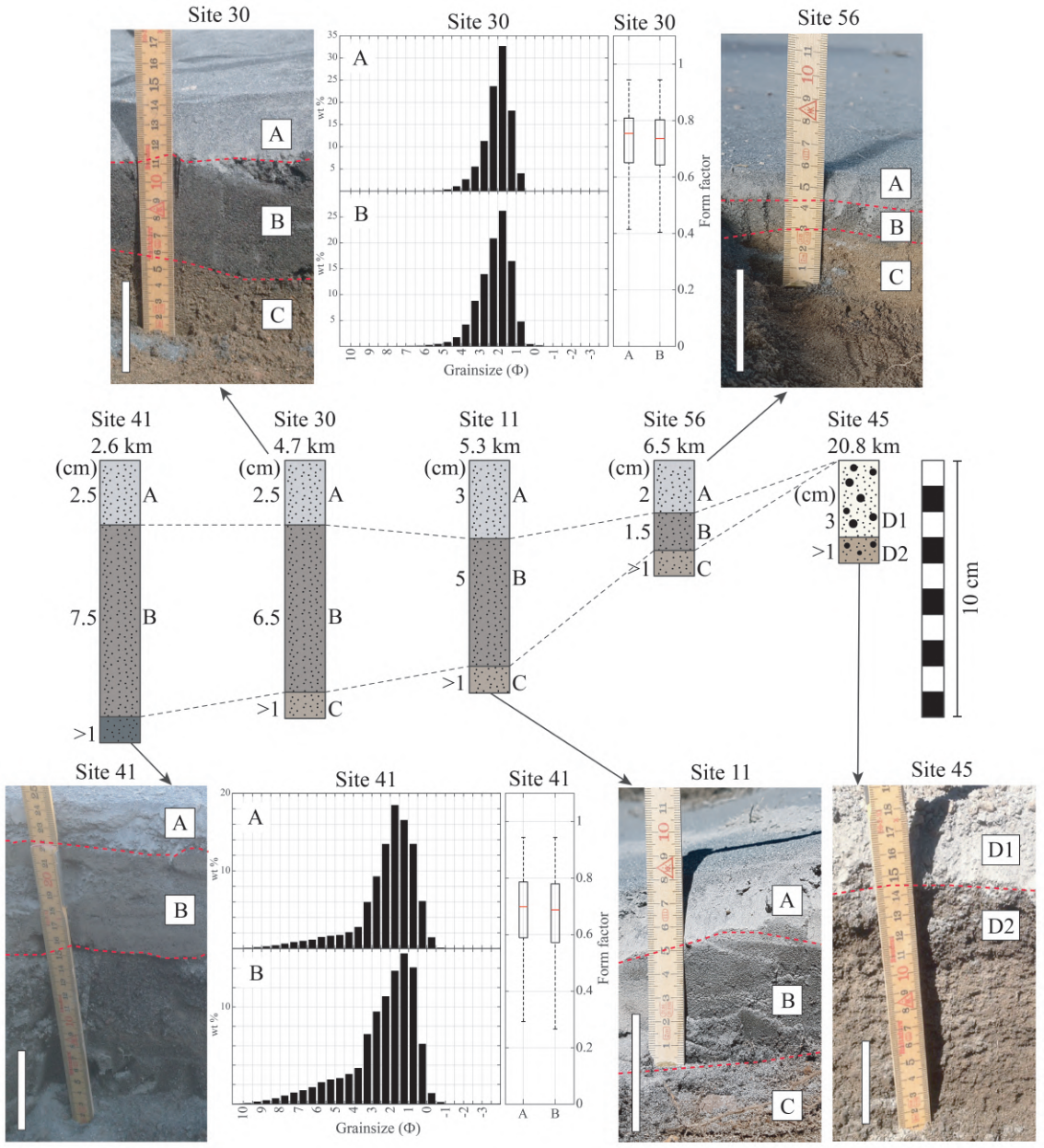

Figure 5.4: Stratigraphic sections of the most recent tephra deposits associated with Sabancaya. Tephra deposits are correlated between sections arranged from the closest to the furthest from the vent (from left to right) and correspond to the green rectangles in Figure 5.1C. Distances from the vent are given above sketches of the sections. Each section is illustrated by a photograph (the white bars 5 cm long in all images), with additional grainsize and morphology measurements for sites 41 and 30. The general roundness of the particles is expressed through the form factor shape parameter in whisker box plots, with the red lines representing the median of the distribution, the lower and upper limits of the boxes indicating the 25th and 75th percentiles and the dashed lines extending to the 1st and 99th percentiles.

6.5 km (site 56). Similarly to A, the local variation in the thickness of B, along with the presence of fine ash lenses (Dominguez et al., 2020a) suggests that B could have been affected by syn-eruptive remobilisation, as is the case for A, while the general trend suggests it represents a primary layer. Given the similarities between layers A and B in terms of composition, componentry and morphology and their distribution at the top of the stratigraphic sections, we consider that they correspond to tephra fallouts from the current cycle (post-2016) of explosions of Sabancaya. The only difference observed between A and B is the level of compactness, with the loose material of A emplaced above the compacted layer B.

Layer C is a brown, compacted tephra layer (Md_{Φ} = 2.6 – 2.8 Φ and σ_{Φ} = 0.9 – 1.5 Φ) that constitutes the base of the stratigraphic section (Figure 5.4). C is distinguished from A and B by its lower content of juvenile fragments (lower than 25 %; Table 5.3), and it appears less fresh and often representing a horizon in which small roots are often located. The groundmass glass composition of C is similar to that of A and B, and comparable to the that of tephra from the 1990-1998 eruption (Table 5.3; Gerbe and Thouret, 2004. Given the above, we attributed layer C to the previous (i.e. 1990-1998) cycle of activity at Sabancaya.

We observed that more distal tephra deposits (at distances >10 km from the vent; e.g., site 45 in Figure 5.4) are different from those observed in proximal areas. Tephra are considerably coarser (Md_{Φ} = -1.3 – 0.4 Φ) and poorly sorted (σ_{Φ} = 2.5 – 3.0 Φ). We nonetheless distinguish 2 layers, D1, an uncompacted layer at the top of the stratigraphic sections, and D2 directly underneath (Figure 5.4).

5.4.2 Tephra sampled in vertical collectors and adhesive paper

The GSDs of the primary tephra sampled in the ash collectors are unimodal and relatively fine, with a median particle diameter below 500 µm (Figure 5.5A). As expected for low-intensity explosions, such as those produced by Sabancaya, the mode of these GSDs rapidly decreases with distance from the source, passing from 355-500 µm at 2.7 km from the vent to 180-250 µm at 12.8 km from the vent. Md_{Φ} ranges from 1.5 to 2.1 Φ and σ_{Φ} ranges from 1.0 to 0.8 Φ. Values of the solidity

of primary tephra are principally between 0.8 and 1.0, with 90% of the particles in that range. The convexity is mostly between 0.9 and 1 for 90 % of the particles (Figure 5.5A). DRE density is 2802.2 ± 11.3 kg m^{-3}, while the bulk density of the material sampled in tephra collectors is 1560.1 ± 26.9 kg m^{-3}.

GSDs of primary tephra collected on adhesive paper are bimodal, with a fine (45-63 µm) and a coarser (180-250 µm) mode (Figure 5.5B). Traces of volcanic ash aggregates are often found on these adhesive paper, which most likely correspond to the particle clusters described by Brown et al. (2012) and Bagheri et al. (2016) that easily break upon impact. Solidity and convexity of these particles are between 0.57 and 0.90 and 0.63 and 0.97 for 90% or particles, respectively (Figure 5.5B). These values are indicative of less circular and smooth particles than those sampled in the tephra collectors.

5.4.3 Volume of tephra deposits

We constrained the cumulative volume of A and B that represents the volume of tephra emitted between the beginning of the eruption in November 2016 and our field campaign that took place from 27 July to 12 August 2018.

An isopach map has been compiled from the cumulative thickness of layers A and B (Figure 5.6A). However, the number of field sites available for constraining the isopach contours is spatially limited, notably because we have been unable to access the western part of the edifice. The elongation of isopach contours was, therefore, assumed to be both toward the east and the west, in agreement with the prevailing wind directions during the dry and wet season, respectively (Figure 5.1B; Thouret et al., 1994). The gradual decrease of the deposit thickness with distance was fitted with exponential, power-law and Weibull trends (Figure 5.6B). The details of the different fitting strategies are described in Appendix A5.2. For the power-law fitting, we find an exponent m less than 2 ($m = 1.2$), which is characteristic of poorly exposed deposits; and the estimation of the volume is, therefore, sensitive to the distal integration limit (Bonadonna et al., 2015a; Biass et al., 2019). In order to account for this sensitivity and provide uncertainties on volumes obtained from the power-law fitting strategy, we calculate the volume by averaging the estimates for

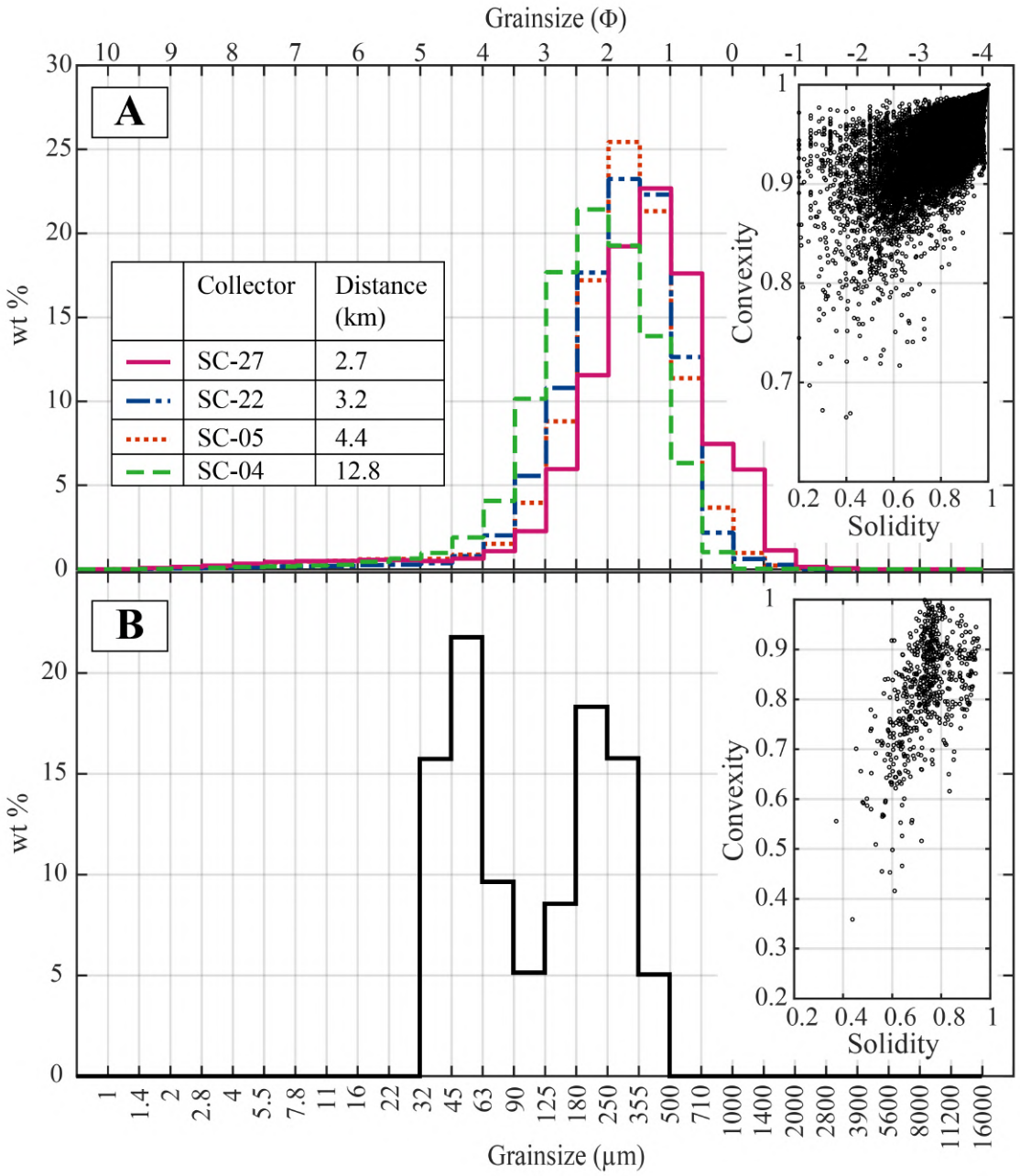

Figure 5.5: **A.** GSDs of the ash accumulated in primary ash collectors (sab. samples) for the different locations in wt%. The inset on the right shows the shape parameters, convexity and solidity, of primary particles sampled in ash collectors. **B.** GSD of primary ash fallout samples (prim. samples) collected on adhesive paper at sites 25-28 (4.4 km from the vent). The inset shows the convexity and solidity, of primary ash particles collected on adhesive paper.

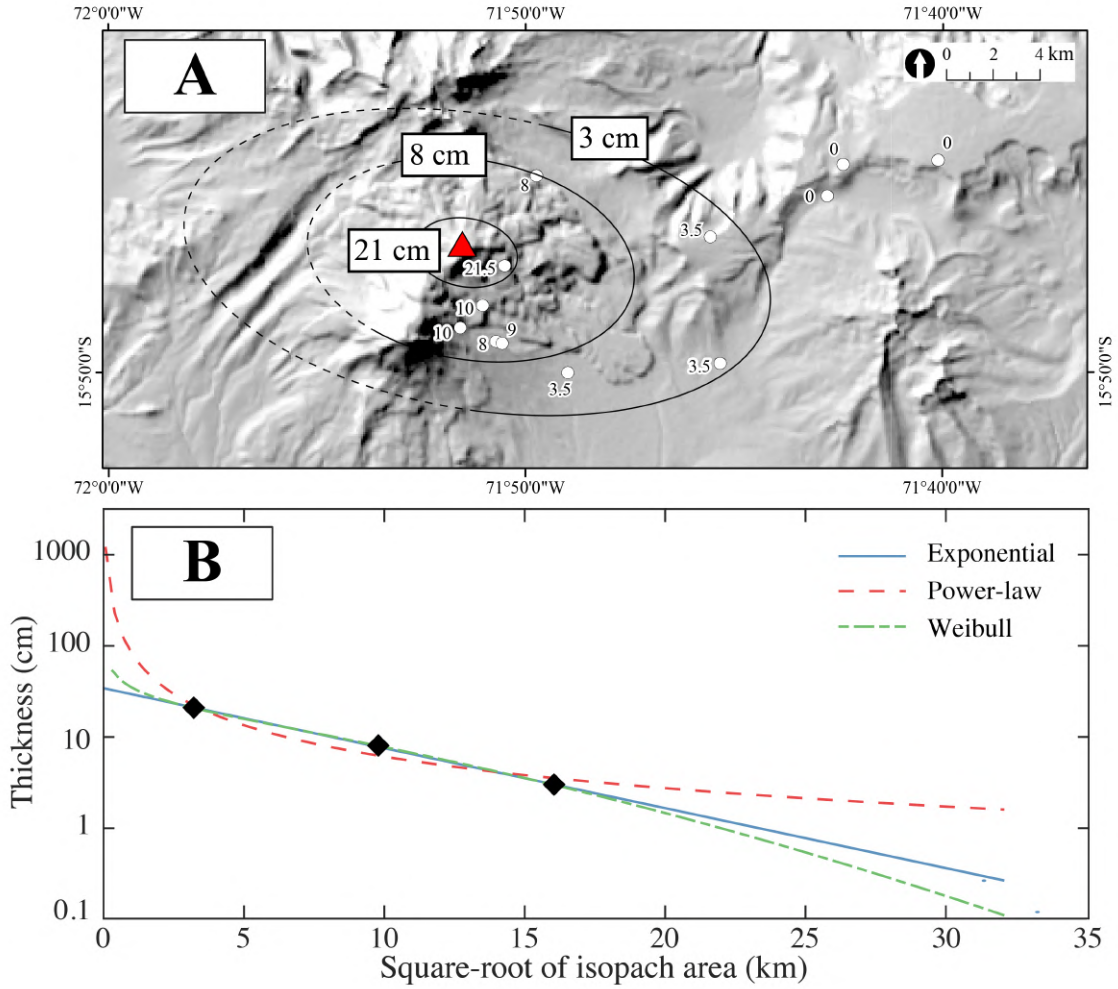

Figure 5.6: **A.** Isopach map (in cm) of layers A and B cumulated. The position of the vent is indicated by the red triangle. **B.** Semi-log plot of the deposits thickness against the square-root of isopach areas. Exponential, power-law and Weibull fits are represented by the solid blue, dashed red and dashed-dotted green lines, respectively.

two distal integration limits that correspond to the values of the square root areas at which the power-law trend equals to 0.01 and 0.001 cm (i.e., thickness becomes comparable to the diameter of individual fine particles).

The estimated volume of tephra deposits is 0.03, 0.06 and 0.03 km^3 with the exponential, power-law and Weibull fitting strategies, respectively. Based on the average and on the standard deviation of these estimates, we retain a volume of 0.04 $\pm$ 0.02 km^3 deposited between November 2016 and August 2018. This corresponds to a DRE volume of 0.02 $\pm$ 0.01 km^3 calculated from the values of the deposit and DRE densities presented above. Note that the uncertainties reported here only correspond to the dispersion of the results provided by the different fitting methods.

5.4.4 Mass of tephra collected in vertical collectors

A cumulative isomass map has been compiled from the data of the tephra collectors between April 2018 and November 2019 during which most measurements are available (Figure 5.7A). The number of data points available is yet limited, and we were only able to estimate three isomass contours. Additionally, the isomass map is not well constrained southwest of the vent, an area that lacks tephra collectors due to the difficulty of access on the steep edifice of Ampato volcano. Moreover, because of the morphology of the terrain and the small magnitude of the eruptions, only a few distal measurements are available west and north of the vent, in the valley of the Colca river, and we were unable to draw a distal isomass contour (i.e., for a load of 0.1 kg m^{-2}). The elongation of the isomass contours suggests fallout dispersion toward the east-southeast and the west-northwest, which reflects the prevailing wind direction at Sabancaya during the dry and the wet season (Figure 5.1B). Similarly to the deposit thickness, the gradual decrease of the tephra load with distance was fitted with exponential, power-law and Weibull trends (Figure 5.7B; Appendix A5.3). Again, we find m less than 2 ($m = 1.7$) for the power-law fitting, indicating that the estimation of the mass is sensitive to the distal integration limit. Hence, we calculate the mass by averaging the estimates for two distal integration limits that correspond to the values of the square root areas at which the power-law trend equals to 0.1 and 0.01 kg m^{-2}.

We obtain a cumulative mass of 1.1×10^9 kg using the exponential function, $2.3 \pm 0.7 \times 10^9$ kg with the power-law function and 1.4×10^9 kg with the Weibull function. From the average of the masses obtained with the different fitting strategies, we therefore retain a mass of $1.6 \pm 0.7 \times 10^9$ kg for the period from April 2018 to November 2019. Using the deposit and the DRE densities, this yields a cumulative bulk volume of $1.1 \pm 0.5 \times 10^{-3}$ km^3 for the total deposit and a DRE volume of $5.8 \pm 2.5 \times 10^{-4}$ km^3, for the period between April 2018 and November 2019 (20 months). This corresponds to a bulk volume of $5.5 \pm 2.5 \times 10^{-5}$ km^3 and a DRE volume of $2.9 \pm 1.3 \times 10^{-5}$ km^3 per month ($3.5 \pm 1.5 \times 10^{-4}$ km^3 DRE per year). Again, the uncertainties reported here on mass and volume estimates only correspond to the dispersion of the results provided by the different methods.

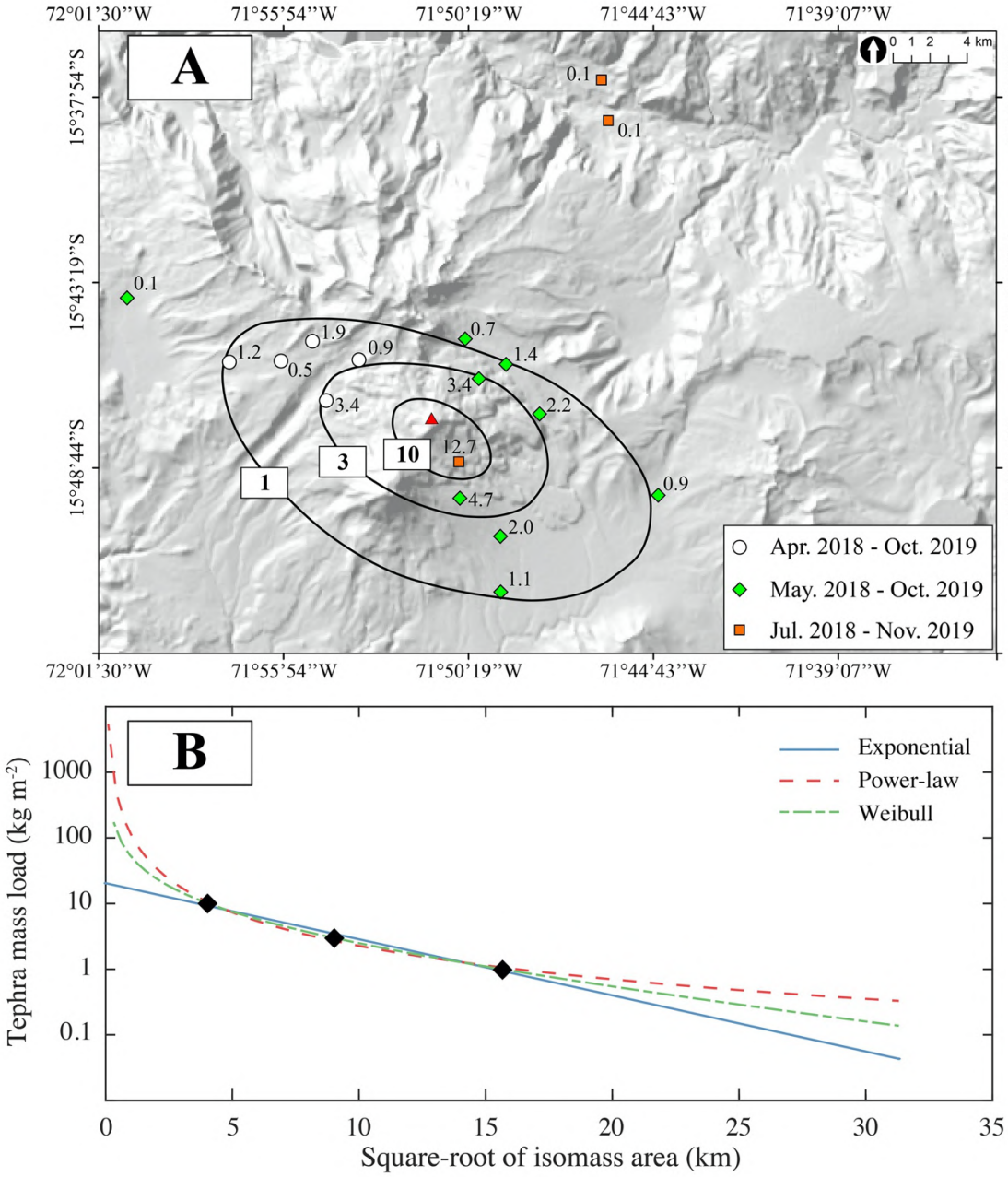

Figure 5.7: **A.** Isomass map in kg m^{-2} for the accumulation of tephra in ash collectors from April 2018 to November 2019. Sampling from three overlapping periods has been considered together in order to draw the isolines: from April 2018 to October 2019 in the white circles, from May 2018 to October 2019 in the green diamonds and from July 2018 to November 2019 in the orange squares. The position of the vent is indicated by the red triangle **B.** Mass decay profile computed from the isomass map in a semi-log plot of the tephra accumulation against the square root of isomass areas. Exponential, power-law and Weibull fits are represented by the solid blue, dashed red and dashed-dotted green lines, respectively.

5.4.5 Pulsatory explosive activity of Sabancaya

Eruptive activity at Sabancaya is characterised by a cyclic and pulsatory eruptive style since November 2016, when the first magmatic explosions took place. A detailed statistical analysis, and the application of the renewal log-logistic model to describe the temporal variation of the repose time between explosions, allows for the quantification of the unsteadiness of this activity. More information on the statistical analysis can be found in Appendix A5.4. Based on a comprehensive satellite and ground-based dataset including optical images, SO_2 fluxes and shallow seismicity, Coppola et al. (2022) defined 6 phases for the current eruption of Sabancaya from November 2016 to December 2020. In order to apply statistical renewal methods to correlate homogeneous eruptive styles, in this study we have analysed the stationarity of this activity based on a moving-average test over the same 6 phases (2016 – 2020) as well as with the period from January to May 2021. As shown in Figure 5.8A, phase II previously defined by Coppola et al. (2022) for being a phase of intense explosive activity accompanied of a dome growth has been sub-divided in 3 homogeneous sub-phases, IIa, IIb and IIc. Indeed, this phase was characterized by 3 deepening-refilling cycles marking the variations on frequency and energy of explosions (Coppola et al., 2022). Table 5.4 summarises the descriptive statistics of the 8 stationary phases including the median, mean and maximum repose interval as well as the frequency of explosions per phase.

The results of the detailed repose interval analysis show an intercalation of low (i.e., phases I, V, VII) to medium frequency (i.e., phases IIb, III, IVa, IVb, IVc, VI) with high frequency phases (i.e., IIa, IIc, IVd, VIII). In this line, phases I, V and VII, with 11, 10 and 6 explosions per day, represent the lowest frequency phases with significant variable median repose times of 70, 25 and 80 minutes; and highly contrasting maximum repose times of 38, 222 and 68 hours, respectively. The phases with higher frequency (IIa, IIc, IVd, VIII), with 38, 42, 55 and 42 explosions per day also have the shortest median repose times, between 18 and 23 min, and variable maximum repose times of 39, 29, 6 and 9 hours, respectively (Table 5.4). During our field campaign in July-August 2018, an average of 21 explosions per day, with a median repose interval of 41 minutes, were recorded (Figure 5.8A, Table 5.4).

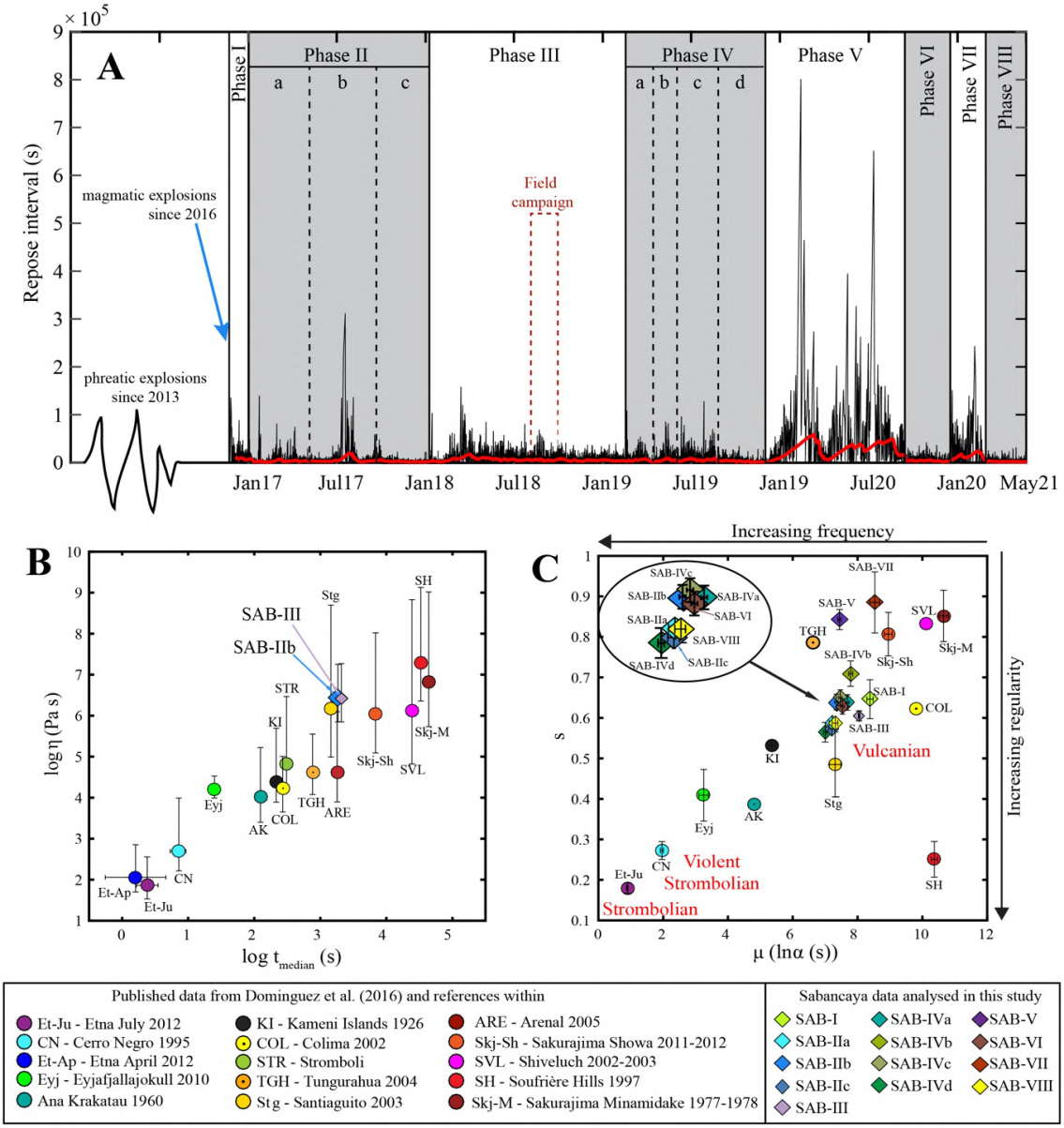

Figure 5.8: A. Time series of explosions at Sabancaya from the beginning of the eruption up to May 2021 shown by the repose interval between explosions. The red solid line corresponds to the moving-average of the repose interval. Based on the work of Coppola et al. (2022) and the variability of the time series, 8 phases have been identified. The dashed red box indicates the time of our field campaign. **B.** Variations of magma viscosity as a function of the median of the repose interval for several published data and for the phases IIb and III of Sabancaya where viscosity has been estimated. **C.** Classification of pulsatory activity based on the log-logistic parameters for the distribution of the repose time interval, μ and s, associated with the frequency and regularity of activity, respectively. Circles correspond to various eruptions of the dataset of Dominguez et al. (2016). Diamonds correspond to the eight phases of Sabancaya analysed in this study.

Phase	**Start date (DD/MM/YYYY)**	**End date**	**Median (min)**	**Mean (min)**	**Maximum (hours)**	**Frequency (explosions day^{-1})**
I	06/11/2016	23/12/2016	70	132	38	11
IIa	24/12/2016	24/03/2017	23	38	39	38
IIb	25/03/2017	25/08/2017	34	54	86	27
IIc	26/08/2017	23/01/2018	25	34	29	42
III	24/01/2018	13/03/2019	51	88	44	17
IVa	13/03/2019	11/05/2019	38	70	24	21
IVb	12/05/2019	31/07/2019	39	83	35	18
IVc	01/08/2019	25/09/2019	34	55	17	27
IVd	26/09/2019	23/10/2019	18	27	6	55
V	23/10/2019	30/08/2020	25	138	222	10
VI	01/09/2020	30/11/2020	35	56	13	26
VII	01/12/2020	02/02/2021	80	235	68	6
VIII	03/02/2021	05/05/2021	23	34	9	42
Field campaign	27/07/2018	12/08/2018	41	62	19	21

Table 5.4: Repose time interval for all the phases analysed at Sabancaya from 2016 to 2021. The period of the field campaign is also described.

Based on the median of the repose time and the magma viscosity correlation proposed by Dominguez et al. (2016), the 2 phases for which we were able to estimate the magma viscosity (i.e., phases IIb and III; Figure 5.8B) follow the trend of other pulsatory activities with similar compositions such as the 2003 cycle of Santiaguito (Guatemala). The log-logistic parameters of the repose interval distribution, μ (associated with α, the scale of the distribution) and s (associated with the shape of the distribution), which provide insights into the frequency and regularity of activity, respectively, are shown in Figure 5.8C for all the phases identified at Sabancaya and compared with a dataset of various pulsatory eruptions (Dominguez et al., 2016). Figure 5.8C shows that the most frequent phases (i.e., IIa, IIc, IVd, VIII) cluster with the lowest μ and s, indicating phases of frequent and regular activity; whilst the medium frequency phases (i.e., IIb, III, IVa, IVb, IVc, VI) cluster with a slightly higher μ and s. In contrast, the lowest frequency phases (i.e., I, V, VII) show a high variation in μ and s corresponding also to the high variation in the median of the repose interval and the irregularity of this activity, particularly for the phases V and VII with the highest values of s (Figure 5.8C).

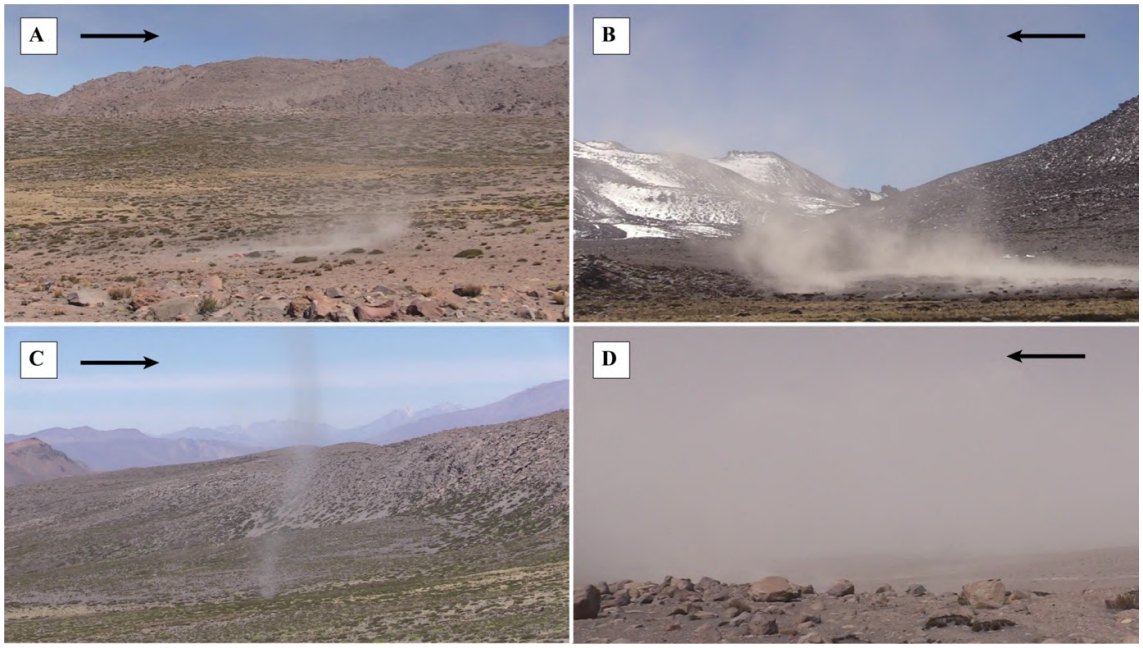

Figure 5.9: Aeolian remobilisation phenomena encountered at Sabancaya during the field campaign (from 27 July to 12 August 2018). **A.** drifting ash on 29 July 2018 **B.** blowing ash on 29 July 2018 **C.** ash whirl on 29 July 2018 **D.** ash storm on 03 August 2018. Black arrows point in the direction of the wind.

5.4.6 Remobilisation phenomena

We have encountered a variety of aeolian remobilisation phenomena during the field campaign that happened simultaneously with the explosive events. Notably based on the loss of visibility, these phenomena can be categorised according to the classification of Dominguez et al. (2020a) which has been adapted from the lithometeors of the World Meteorological Office (Figure 5.9). Here, we focus on the class of phenomena that describes the particles that are being raised in the atmosphere at the time of observation, as a result of an interaction between atmospheric and soil conditions. We do not describe phenomena that correspond to particles already suspended prior to the time of observation.

Drifting and blowing ash consist of ash raised by the wind to small ($<$1.80 m) and moderate ($\geq$1.80 m) heights, respectively, for durations on the order of minutes (Figure 5.9A-B; 5.7: Supplementary Video A5.1). They are the most common remobilisation phenomena that have been observed daily under all weather conditions. The main difference between drifting and blowing ash is that blowing ash can reach eye level (1.80 m above the ground) and reduce the visibility at that height, whilst

drifting ash remain too low to reduce the visibility at eye level.

Ash whirls (alternatively called "ash devils") share similarities with drifting and blowing ash, with the particularity that the ensembles of ash are raised in the form of a column that spins around an approximately vertical axis (Figure 5.9C; 5.7: Supplementary Video A5.2). The formation of ash whirls is powered by heating from insolation and their lifetime spans between tens of seconds and a few minutes (Sinclair, 1969; Balme and Greeley, 2006). They were recurrently identified on the field, with multiple ash devils observed every day.

Finally, ash storms are the most intense and rarest remobilisation phenomenon that were encountered in the field. Large quantities of ash are lifted to great heights by strong turbulent winds during ash storms and the visibility is greatly reduced (Figure 5.9D; 5.7: Supplementary Video A5.3). The occurrence of ash storms can raise particles for prolonged periods of time and trigger ash hazes (i.e., particles suspended in the atmosphere), even far from the source.

5.4.7 HS videos and PM_{10} measurements

We have imaged the remobilisation transport mechanisms at the scale of the particles. The remobilisation of the grains is intermittent, with short periods of gusts during which numerous particles were seen in motion separated by longer periods of rest. HS videos additionally offer an insight into the different remobilisation mechanisms, with coarse particles moving by creep on the ground surface, and finer particles transported by saltation (see 5.7; Supplementary Video A5.4). Unfortunately, the resolution of the images is not sufficient to image the very fine particles that have the potential to enter into suspension. However, it is particularly interesting to observe the splash effect during aeolian remobilisation events, when saltating particles hit the surface and trigger the motion of other particles upon impact, favouring their remobilisation and potential entrainment in suspension ((Shao et al., 1993); Supplementary Figure A5.4).

As seen in the HS videos, short-lived wind gusts can entrain numerous particles in suspension that were also evidenced in the PM_{10} concentration measurements. Temporal variations in the PM_{10} series show the intermittent nature of aeolian

remobilisation (Figure 5.10). Interestingly, PM_{10} concentrations tend to increase over the course of the day, in correlation with the diurnal evolution of soil surface and meteorological properties (Mingari et al., 2020). Specifically, we see that the increase in PM_{10} concentrations is associated with an increase in the wind speed and the surface temperature during the day (Figure 5.10). Thus, due to a reduction in soil moisture through surface heating, as well as increasing wind friction velocities, more particles are prone to be remobilised as cohesive forces of the most surficial layer might diminish over the day. For all the days studied here, the PM_{10} concentration regularly exceeds limits defined by the World Health Organisation for daily (0.15 mg m^{-3}) and yearly (0.05 mg m^{-3}) average exposures, especially during ash storms that have been analysed on the 03 and 04 August 2018 (Figure 5.10D-E).

5.4.8 Characterisation of remobilised ash

Figure 5.11 shows the GSDs of airborne remobilised particles collected on adhesive paper at the ground level (R0) and at heights >1.5 m (R150) (see Figure 5.3 that illustrates the differences between the sampling strategies). It is clear that the GSDs are distinct, possibly depending on the transport mechanism of the particles. R0 samples are associated with a fine modal diameter of 45-63 µm, whilst R150 samples exhibit a very fine mode below 20 µm at 11-16 µm (red and blue GSDs of Figure 5.11, respectively).

In order to better understand these differences in the sizes of remobilised particles, we compare the GSDs of airborne remobilised particles with the sample of the most surficial ground layer collected upwind that is representative of the source material (SG sample; Figure 5.12). Volcanic ash particles on the ground are coarser than airborne remobilised ash, with a modal diameter of 250-355 µm. This indicates that aeolian remobilisation is a size-selective process favouring the transport of fine particles, as already described in a number of studies (Shao and Lu, 2000; Kok et al., 2012; Jarvis et al., 2020).

The GSDs of remobilised and ground particles are additionally compared with the threshold friction velocity model, u_{*t}, of Shao and Lu (2000) and the model of Mingari et al. (2020) for transport mode (Figure 5.11). R0 samples are associated

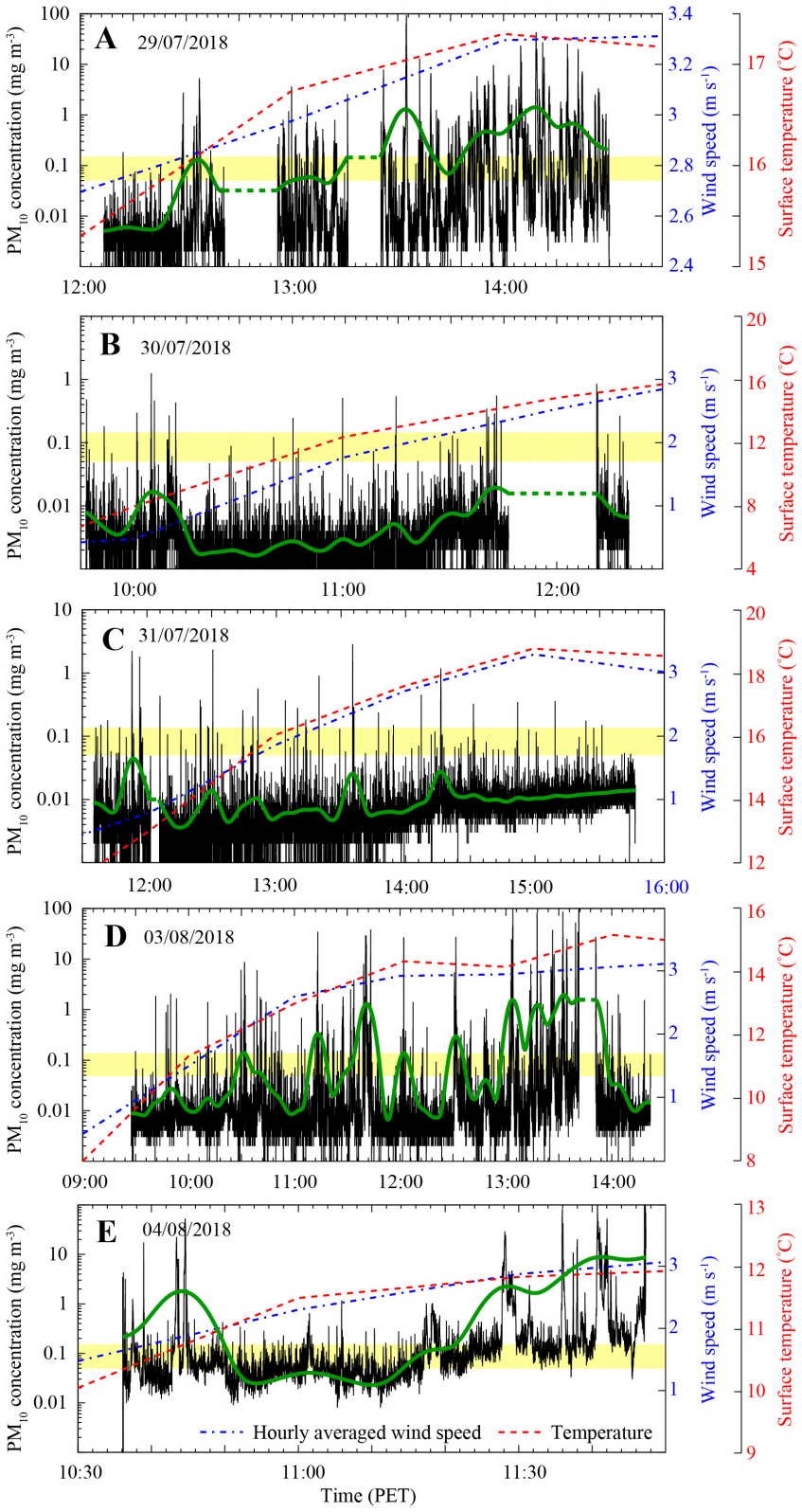

Figure 5.10: PM_{10} concentration measurements for the **A.** 29 July, **B.** 30 July, **C.** 31 July, **D.** 03 August and **E.** 04 August 2018 compared with hourly averaged wind speed at 10 m above the surface (dashed-dotted blue line) and temperature (dashed red line) obtained from the ECMWF ERA-Interim reanalysis. The solid green line is the moving average of the PM_{10} concentration performed over time spans of 2 minutes. Yellow regions indicate recommended PM_{10} limits of 0.05 and 0.15 mg m^{-3} for yearly and daily exposures (Elissondo et al., 2016; Mueller et al., 2020). Table 5.2 contains the location and the duration of the PM_{10} measurement presented here.

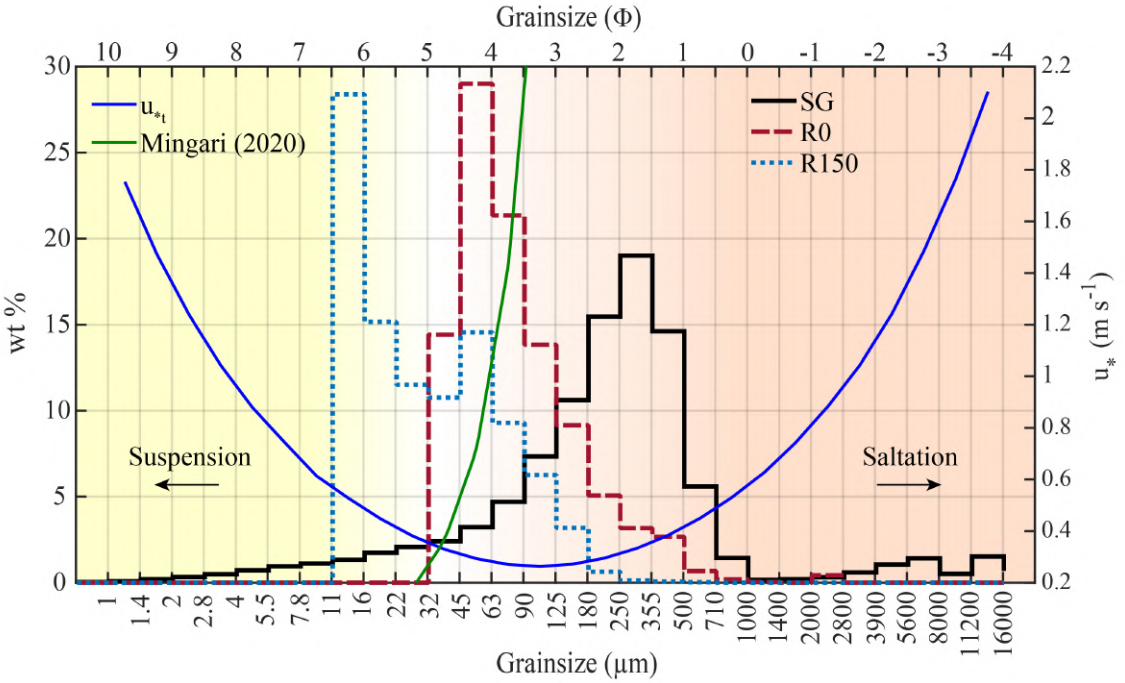

Figure 5.11: Representative GSDs of the most surficial ground layer (SG) upwind of airborne particles remobilised by the wind sampled at the ground level (R0) and at heights $>$ 1.5 m (R150). Samples have been collected at sites 31, 40, and 61, respectively at 4.1, 4.5 and 4.4 km from the vent (Supplementary Table A5.1). The GSDs are compared with the model of the threshold friction velocity (u_{*t}) of Shao and Lu (2000) (solid blue line) indicating the minimum wind friction velocity (u_*, on the right y-axis) for which grains become mobile and the model of Mingari et al. (2020) (solid green line) showing the critical grainsize at which a transition between suspended and saltating particles might occur. Both models are associated with the grainsize of the particles and the wind friction velocity. The yellow and orange shaded regions respectively cover the grainsizes that are transported in suspension and saltation for wind friction velocities of about 0.5 m s^{-1}.

with the grainsizes that minimise the threshold friction velocity, typically between 70 and 100 µm. Hence, they correspond to the particles that are most likely moving only under action of the wind, whilst both coarser and finer particles are respectively too heavy and too cohesive to easily lift off. Considering low and common wind friction velocities $\leq$0.5 m s^{-1} (Dominguez et al., 2020b; Mingari et al., 2020), the particles collected on R150 samples are unlikely to be remobilised only by the wind, but rather due to the impact of coarser saltating particles with the ground (Shao et al., 1993). Moreover, for the same range of wind friction velocities, particles with diameters below the range 32-45 µm are expected to stay in suspension once in the atmosphere, as their settling velocities are lower than the wind friction velocity (Mingari et al., 2020). This size threshold is found to correctly separate the modal grainsize of particles collected on R0 and R150 samples (Figure 5.11).

The morphologies of airborne primary (prim.) and remobilised (R0 and R150) particles collected on adhesive paper are presented in Figure 5.12. Similarly to Dominguez et al. (2020a), we have refined the shape analysis by separating the particles in three size classes: (i) below 63 µm (class 1), (ii) between 63 and 125 µm (class 2), and (iii) above 125 µm (class 3). In general, the shape descriptors of primary and remobilised ash are very similar, with differences in the median values $<$0.1. This indicates that volcanic ash particles at Sabancaya have comparable morphologies, regardless of their transport and deposition mechanisms. Remobilised particles are nonetheless systematically associated with slightly greater variability in the shape descriptors than primary ash, especially for the form factor in particles $<$125 µm (class 1 and 2, Figure 5.12C).

In more detail, R0 samples exhibit minor differences in classes 1 and 2. They have median values of convexity of 0.89 and 0.85 for classes 1 and 2, respectively, whilst primary ash has median values of 0.84 and 0.81. R150 samples have median convexity values close to those of primary ash (0.85 and 0.82 for classes 1 and 2, respectively) (Figure 5.12A). For classes 1 and 2, median solidity values of remobilised particles are almost identical to those of primary particles, with differences $\leq$ 0.02 (Figure 5.12B). The median form factor of the remobilised particles $\leq$125 µm collected on R0 samples is 0.52 for both class 1 and class 2. These values of

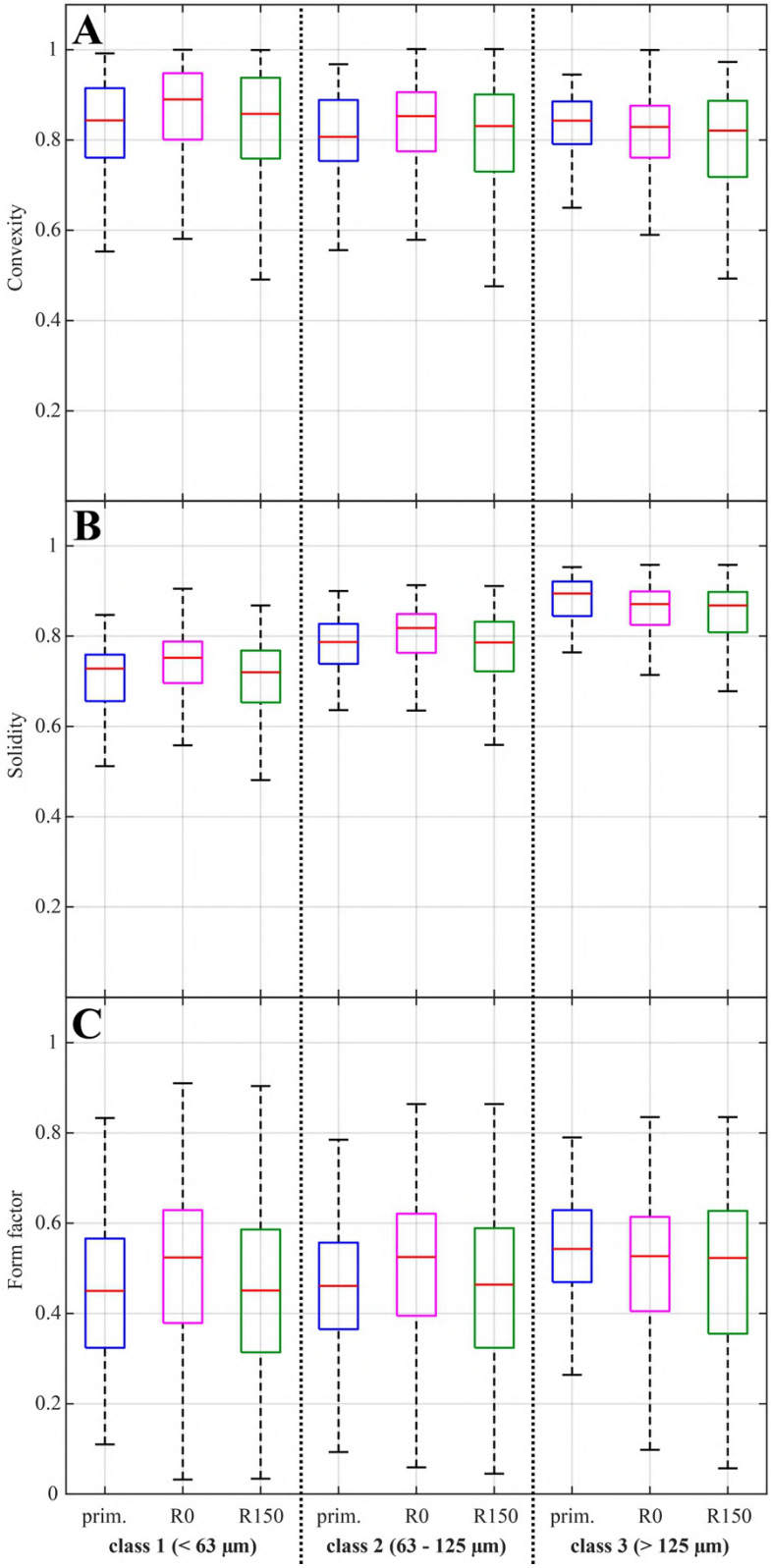

Figure 5.12: Box and whisker plots showing the comparison of **A.** the convexity, **B.** the solidity and **C.** the form factor between airborne primary (prim.) and remobilised (R0 and R150) ash particles collected on adhesive paper. Values close to 1 in these shape descriptors are indicative of smooth and rounded particles.

form factor are subtly greater than that of primary ash (0.45 and 0.46) and R150 samples (0.44 and 0.45) (Figure 5.12C). This suggests that particles collected on R0 samples are slightly more rounded and smoother than the particles collected on R150 samples. However, median shape descriptors values are very similar for all class 3 particles, with maximum differences of $\leq$0.03 for all shape parameters. All particle types have median convexity values ranging from 0.81 to 0.84, median solidity values are comprised between 0.86 and 0.89, and median form factor values span the range from 0.51 to 0.54.

5.5 Discussion

5.5.1 Preservation and interpretation of tephra deposits

We have distinguished 3 tephra layers at Sabancaya. Upper layers (A and B) can be related to the ongoing activity and rapidly thin out and vanish going from proximal to distal sections (Figures 5.4, 5.6A). This process is possibly accentuated by wind erosion. Since after the 1990-1998 Sabancaya eruption a repose interval of 200 years followed (Thouret et al., 1994; Gerbe and Thouret, 2004; Juvigné et al., 2008), this activity was associated with the layer C that notably shares similar percentages of juveniles and groundmass glass composition (Table 5.3). Similarities in the plume heights and andesitic magma compositions nonetheless exist between the previous eruptive episode (1990-1998) and the current activity (post-2016), further confirming the attribution. The succession of very similar eruptive episodes over a relatively short timescale at Sabancaya is, therefore, an additional challenge for the interpretation of the deposits and the study of separate eruptions.

Tephra deposits retain valuable information into the dynamics of past eruptions and are used to reconstruct the total GSD (Bonadonna and Houghton, 2005), magnitude (i.e., mass, volume), intensity (i.e., plume height, mass eruption rate) and duration of volcanic events (Carey and Sparks, 1986; Fierstein and Nathenson, 1992; Bonadonna and Costa, 2013; Houghton and Carey, 2015; Aubry et al., 2021). They therefore provide important information for understanding the eruptive history of a volcano and develop potential scenarios of future eruptions for hazard assessments

(Bonadonna, 2005b; Biass et al., 2016a; Bonadonna et al., 2021). Constraining eruptive parameters from tephra layers requires that they are representative of the original deposits. However, post-depositional processes, such as aeolian remobilisation, can affect the characteristics of the deposits (Engwell et al., 2013) and particularly in cyclic volcanic contexts during which small amounts of tephra are produced intermittently in very dynamic erosional conditions. At Sabancaya, both layers A and B show clear evidence of wind reworking. According to field observations, the loose layer A that constitute the very top of the stratigraphic sections is subject to continuous deposition of primary tephra and simultaneous subsequent remobilisation. The thickness of layer A does not decrease with distance from the vent and is rather homogeneous for the entire area studied during the field campaign (Figure 5.4, Supplementary Table A5.1), as it corresponds to the uncompacted tephra deposit that is continuously being remobilised and redistributed over the area surrounding the vent (Dugmore et al., 2020). We have seen that, in these arid areas of low vegetation cover, the deposit thickness is particularly sensitive to local variations in the windward and leeward sides of plants, which are notably a result of tephra entrapment and preservation in the vegetation during primary and secondary transport (Blong et al., 2017; Dugmore et al., 2018; Dominguez et al., 2020a). It is worth mentioning that additional water and glacial erosion take place at Sabancaya as well (Thouret et al., 1994). As a consequence, the interpretation of stratigraphic sections could, therefore, lead to inaccurate assessments of the eruptive parameters, and should be complemented by different sampling methods (e.g., ground and airborne material, vertical and horizontal mass fluxes), field observations (e.g., HS and high-resolution videos) as well as measurements in various environments (e.g., including sections in peat bogs; Juvigné et al., 2008; Fontijn et al., 2014) in order to comprehensively study tephra layers of pulsatory activity in dynamic weather terrains as is the case of Sabancaya.

5.5.2 Volume of tephra deposits

Based on measurements of the deposits thickness, we have estimated a bulk volume of 0.04 ± 0.02 km^3 and a DRE volume of 0.02 ± 0.01 km^3 emitted between

November 2016 and August 2018 (Figure 5.6). This corresponds to a Volcanic Explosivity Index (VEI) of 3 (Newhall and Self, 1982), and is comparable to the volume emitted from May to October 1990 (0.025 km^3) during the previous eruption of Sabancaya (Thouret et al., 1994; Gerbe and Thouret, 2004). However, the volume of the deposits estimated here is about one order of magnitude greater than the volume estimated from the height of the volcanic plumes, as calculated from recordings of the optical camera network (< 0.01 km^3; Coppola et al., 2022). The discrepancy between the two measurement strategies can be explained by the underestimation of the fraction of particles contributing to the thermal mass of the plumes (Bonadonna et al., 2002a; Druitt et al., 2002; Londono and Galvis, 2018), and by the caveats associated with the measurements of the height of volcanic plumes from optical cameras, i.e., impossibility to measure the plume heights during nights, and limitations of measurements that do not account for the distortion of plumes by the wind (Scollo et al., 2014). Additionally, the tephra deposits are poorly exposed, and we have not been able to measure their thickness in the western side of the volcanic edifice due to the challenging terrain. This leads to uncertainties in the estimation of the tephra volume which are difficult to assess (Klawonn et al., 2014a,b; Bonadonna et al., 2015a).

Besides, the measurement of the tephra volume from November 2016 to August 2018 are complemented by the tephra collector network, sampled from April 2018 to November 2019. During this latter period, we find that a mass of $1.6 \pm 0.7 \times 10^9$ kg has been emitted (Figure 5.7). This corresponds to a DRE volume of $5.8 \pm 2.5 \times 10^{-4}$ km^3 for the whole period and a DRE volume of $2.9 \pm 1.3 \times 10^{-5}$ km^3 per month. It is therefore evident that the volume of tephra emitted in this period is very low compared to the estimated volume based on the deposits of layers A and B. This is also illustrated by the measurements of Coppola et al. (2022), that show that significantly lower volumes of ash have been emitted since 2018. It is also interesting to compare the amount of tephra produced by similar eruptions. The volume of tephra estimated between April 2018 and November 2019 is very low in comparison with the large Vulcanian explosions of Soufrière Hills volcano (Montserrat), for which average tephra volumes are estimated at 1.1×10^{-4}

km^3 from August to October 1997 (Bonadonna et al., 2002b; Druitt et al., 2002). The size, magnitude and frequency of the explosions at Sabancaya are much more comparable to their counterparts at Sakurajima volcano. Between 2011 and 2015, Oishi et al. (2018) have estimated the monthly averaged volume of volcanic ash fallouts to range from 3×10^{-4} to 4×10^{-4} km^3 per month. These values are about one order of magnitude higher than those for the period between April 2018 to November 2019 at Sabancaya .

It is important to note that the uncertainties on the mass and volume of tephra deposit only account for the dispersion of the results obtained with various empirical methods. Other sources of uncertainties notably include the absence of field sites located west of the edifice and in proximal areas (<5 km from the vent) and the lack of proximal tephra collectors southwest of the vent . In addition, given the meteorological conditions at Sabancaya, it cannot be excluded that a small portion of the thin tephra layers deposited on the funnel of the collectors may have been lost and transported by the wind before depositing in the container, and/or that the accumulated material in the collectors contains a proportion of remobilised ash. Yet, both the decrease of the median grainsize (Figure 5.5A) and gradual thinning of the deposits (Figures 5.4, 5.6A, 5.7A) with distance are still observed, as expected for primary fallouts.

5.5.3 Vulcanian activity at Sabancaya volcano

The current eruptive cycle at Sabancaya is indistinctly characterised by a Vulcanian eruptive style as suggested by the repose time analysis of the whole cycle from 2016 to 2021 (Figure 5.8; Table 5.4). Explosive activity presents significant temporal variations regarding the frequency and the regularity of explosions, from which at least 8 phases have been identified. In general, there is an intercalation of low to high frequency phases suggesting significant changes on fragmentation processes that might be affected primarily by the extrusion and growing of domes, interplay among magma feeding and degassing inducing changes in rheology and ascent dynamics, overpressure in the conduit and shearing effects (Gonnermann, 2015; Pistolesi et al., 2015). The analysis of the magma viscosity and the median repose time between

explosions shows a robust correlation for the phases IIb and III of the Sabancaya dataset, following the trend of similar dacitic compositions such as the 2003 Santiaguito cycle (Figure 5.8B). Unfortunately, we were not able to constrain the effect of viscosity on the other phases which might play an important role on the construction and collapse of domes described at Sabancaya. Coppola et al. (2022) demonstrated that at least 3 phases have been associated with the growing of two domes (i.e., dome "Huk" during phases II and IV; and the dome "Iskay" during phase VI). The periodicity at which dome growth was observed for phases II, IV and VI is consistent with high frequency explosive phases with low median repose intervals between explosions (18 to 35 minutes; Table 5.4). Similarly, the collapse of dome "Huk" during phase V (Coppola et al., 2022) is associated with the lowest frequency period for the ongoing explosive cycle of Sabancaya, associated with median repose time of 25 minutes but with maximum intervals between explosions of up to 222 hours.

In addition, the log-logistic parameters of the repose time distributions show that explosions in different phases of Sabancaya's activity are as frequent as the 2003 Santiaguito and the 2011-2012 Sakurajima-Showa cycles, but with a less regular behaviour (Figure 5.8C). As observed by Dominguez et al. (2016) for other pulsatory volcanoes, the frequency of explosions decreases as μ increases and the regularity of the activity decreases with s. In the case of Sabancaya, we can see that the 8 phases follow a general linear trend within the range of Vulcanian activity (Figure 5.8C). In particular, the most frequent phases IIa, IIc, IVd and VIII, are as frequent as the 2003 Santiaguito activity but less regular; whilst the medium frequency phases IIb, III, IVa, IVb, IVc and VI are slightly less regular. Interestingly, phase V, associated with the collapse of dome "Huk" (Coppola et al., 2022) shows similar values of regularity as the 2011-2012 Sakurajima-Showa activity (Japan) but more frequent (Figure 5.8C). The cyclic eruptive processes of Sabancaya are correlated with a complex effusive and explosive dynamics controlled by the growing and collapse of domes, the magma-rise rate and fragmentation processes consistent with frequent but irregular Vulcanian eruptive styles.

5.5.4 Characteristics of remobilised material and identification of primary tephra

Aeolian remobilisation at Sabancaya is recurrent during the day and takes multiple forms from low intensity events, such as drifting ash, to strong turbulent ash storms (Figure 5.9). These observations are consistent with the aeolian reworking features found in tephra deposits. Field observations and prolonged PM_{10} concentration measurements highlight the effect of diurnal weather variations on aeolian phenomena. The concentration of suspended material (PM_{10}) typically increases as the day progresses and surface conditions evolve (e.g., increase in wind velocity and surface temperature) (Figure 5.10). It is important to note that, for all the days during which PM_{10} data have been acquired, the PM_{10} concentration had remained relatively high, greater than sanitary limits (0.05 and 0.15 mg m^{-3} for yearly and daily exposures, respectively; Elissondo et al. (2016); Mueller et al. (2020)). The PM_{10} concentration was particularly high in ash storms (Figure 5.10D-E) during which it exceeded potentially hazardous levels for prolonged periods of time. Together with the volcanic activity and tephra fallout, the frequent occurrence of high PM_{10} concentrations constitutes a recurrent respiratory hazard (Horwell and Baxter, 2006) to communities in the vicinity of Sabancaya volcano.

Differential sampling of airborne remobilised ash at the ground level (R0) and above 1.5 m (R150) (Figure 5.2A) shows that the GSDs depends greatly on the transport mechanism (Figure 5.11). Consistently, R0 samples are associated with a grainsize mode of 45-63 µm that minimises the threshold friction velocity as defined by Shao and Lu (2000). We can therefore estimate that R0 samples are associated with a predominant saltation (i.e., bouncing) mechanism. For probable low wind friction velocities $\leq$0.5 m s^{-1} (Dominguez et al., 2020b; Mingari et al., 2020), these particles are characterised by relatively high settling velocities compared to the wind friction velocity. On the other hand, particles collected on R150 samples are finer, with a mode $<$ 20 µm. These particles are characterised by grainsizes having settling velocities significantly lower than probable wind friction velocities in the order of 0.3 to 0.5 m s^{-1} (Mingari et al., 2020). It is therefore likely that these particles were already in the atmosphere at the moment of collection and that they possibly

underwent short- to long-term resuspension. Despite the fact that we were not able to measure friction and settling velocities, the simple sampling strategy developed here for collecting airborne remobilised material in real-time (Figure 5.3) represents a suitable technique to separately analyse saltating and suspending particles and the associated transport features.

Finally, it is not possible to reliably distinguish between primary and remobilised tephra based on particle morphologies at Sabancaya, and contrarily to other examples of remobilised deposits analysed some years after primary depositions (e.g., eruption of Cordón Caulle, Chile, in 2011-2012; Dominguez et al., 2020a). In fact, for the case of Cordón Caulle, tephra was deposited in Patagonia mostly in June-July 2011 (about 1 km^3; Pistolesi et al., 2015) and subsequently remobilised. Morphological analysis of primary tephra particles and remobilised ash then allowed the distinction of the two processes, with remobilised particles significantly rounder and smoother than the primary material because of abrasion due to secondary transport over several months and even years (Dominguez et al., 2020a). The situation of the remobilised ash collected at Sabancaya during sedimentation is different, since particles had no time to be rounded enough to be distinguished from the primary tephra. Consequently, we find that shape descriptors are very similar, regardless of the transport mechanism (Figure 5.12), suggesting that the effect of wind transport is not yet very pronounced on remobilised particles. We nonetheless find subtle variations indicating that remobilised ash $\leq$125 µm collected on R0 samples (i.e., probably transported by saltation) are slightly more circular and smoother than primary ash (Figure 5.12C). In fact, particles that undergo saltation experience regular collisions that result in abrasion and rounding of the particle surfaces. Although the difference in the shape descriptors is more ambiguous at Sabancaya, this is in agreement with the results of Dominguez et al. (2020a) who evidenced a more rapid abrasion of remobilised volcanic ash in Patagonia, less than five years after the eruption of Cordón Caulle. The particles collected on R150 samples with a mode $<$20 µm are more likely to be transported by suspension with less collisions and abrasion. Similarly, all particles $\geq$125 µm have very similar morphologies, as they are too heavy to easily get remobilised by the wind. A final observation is that the distribution

of all shape descriptors is more dispersed for remobilised particles than for primary ash. In the context of the persistent explosive activity at Sabancaya, this possibly reflects the fact that remobilised particles are a mixture of abraded, more circular remobilised particles with more angular primary ash that is continuously supplied by regular explosions. This can also be interpreted as the fact that remobilised particles are a mixture of particles that have been remobilised several times with others considerably less transported and closer to the morphology of primary ash.

5.6 Conclusions

The activity at Sabancaya is currently characterised by frequent Vulcanian explosions that produced a tephra deposit between November 2016 and August 2018 with a bulk volume of 0.04 ± 0.02 km^3 and a DRE volume of 0.02 ± 0.01 km^3 (VEI 3). Based on measurements in tephra collectors between April 2018 and November 2019, we additionally estimate a mass of $1.6 \pm 0.7 \times 10^9$ kg emitted during this period, which corresponds to a bulk volume of $5.5 \pm 2.5 \times 10^{-5}$ km^3 and a DRE volume of $2.9 \pm 1.3 \times 10^{-5}$ km^3 per month. The overall explosive activity between November 2016 and May 2021 is characterised by significant variations in the frequency and the regularity of explosions, such that at least 8 phases that can be identified and correlated with episodes of dome growth and collapse (Coppola et al., 2022). Simultaneously, intermittent aeolian remobilisation of tephra deposits is illustrated by high-definition videos, high-speed footages and PM_{10} concentration measurements. The aeolian remobilisation results in potentially intense wind erosion phenomena such as ash storms that can strongly affect the preservation of tephra deposits and, therefore, have an impact on the stratigraphic record. Hence, in such volcanic environments, the erupted volumes are better constrained based on multiple complementary sampling strategies, including tephra collection in dedicated vertical containers. Our analysis suggests that such nearly real-time sampling is crucial for the assessment of eruptive parameters at volcanoes that experience cycles of pulsatory weak explosions over long durations, since the preservation of tephra layers is likely affected by post-depositional processes. Furthermore, we have used an effec-

tive sampling method of remobilised particles that involved the separate collection of particles on adhesive paper at the ground level and above 1.5 m. Results indicate that particles sampled at the ground level are associated with sizes compatible with a transport by saltation that minimise the threshold friction velocity, whilst particles sampled above 1.5 m have sizes more consistent with a transport by suspension. This sampling strategy can, therefore, be deployed to characterise saltating and suspending particles separately. However, the morphology of the particles may not provide a reliable method to distinguish between primary and remobilised particles, as it could be the case for eruptions for which the morphology of fresh primary particles had the time to evolve after the cessation of the activity due to remobilisation effects. As illustrated by the comparison of the shape descriptors of primary and remobilised particles, although the particles undergoing transport by saltation are slightly more rounded, the differences are very subtle, resulting in possibly ambiguous recognition of the transport and deposition mechanisms (i.e., primary fallout and wind remobilisation). Overall, due to favourable meteorological and surface conditions, our work indicates that Sabancaya is an excellent natural laboratory for the study of aeolian remobilisation processes. In particular, it emphasises the complexity of simultaneous primary tephra deposition and wind erosion in a context where fresh volcanic ash is continuously supplied to the environment.

Author contributions for Chapter 5

All authors participated to the preparation of the field campaign. Costanza Bonadonna, Marco Pistolesi, Lucia Dominguez and Allan Fries studied tephra deposits. Nelida Manrique Llenera, Rigoberto Aguilar Contreras, David Valvidia Humerez sampled tephra in collectors and provided data for the analysis of the pulsatory activity of Sabancaya that was conducted by Lucia Dominguez. Eduardo Rossi and Stefano Pollastri acquired high-speed videos. Lucia Dominguez and Paul A. Jarvis performed PM_{10} measurements with the instrument provided by Claire Horwell. Particle characterisation was performed by Allan Fries and Lucia Dominguez. Allan Fries and Lucia Dominguez drafted the manuscript reviewed by all authors.

5.7 Appendix A5

Appendix A5.1 - Calculation of the threshold friction velocity u_{*t} and determination of the preferential transport mechanism during remobilisation

The threshold friction velocity u_{*t} is determined from the model of Shao and Lu (2000) as

$$u_{*t} = \sqrt{A_N \left(\frac{\rho_p g d}{\rho_a} + \frac{\gamma}{\rho_a d} \right)}, \tag{A5.1}$$

with $A_N = 0.0123$ the dimensionless threshold friction velocity for terrestrial surface conditions, $\gamma = 3 \times 10^{-4}$ kg s^{-2} an experimental parameter accounting for the effect of inter-particle cohesion, $g = 9.81$ m s^{-1} the acceleration due to gravity on Earth, ρ_p and ρ_a the particle and air density, respectively, and d the particle diameter. For this study, we measure the particle skeletal density (i.e., including non-connected pores) $\rho_p = 2697.4$ kg m^{-3} by Helium pycnometry and we consider that $\rho_a = 1$ kg m^{-3}.

In order to determine the preferential transport mechanism of remobilised particles, we define an ideal limit between saltating and suspended grains. This transition occurs for (Scott et al., 1995; Mingari et al., 2020)

$$V_p = \kappa u_*, \tag{A5.2}$$

where V_p is the particle settling velocity that depends on the particle size d, $\kappa = 0.4$ is the von Karman constant and u_* is the wind friction velocity. For $V_p > \kappa u_*$, grains are more likely to experience saltation when lifted of the surface. On the contrary, grains are expected to enter in suspension for $V_p < \kappa u_*$. Here, given that only particles with diameters < 100 µm (i.e., particle Reynolds number < 0.4 in the atmosphere) enter in suspension for realistic wind friction velocities < 2 m s^{-1}, we consider the particle settling velocity to scale as the Stokes velocity (Mingari et al., 2020)

$$V_p = \frac{g d^2 (\rho_p - \rho_a)}{18 \rho_a \nu}, \tag{A5.3}$$

with $\nu = 1.5$ m^2 s^{-1}, the air kinematic viscosity.

Appendix A5.2 - Calculation of tephra volumes

We calculate the volume of tephra deposits based on the decrease of their thickness with distance from the vent using three different fitting strategies. The first strategy involves fitting the deposits thickness T with an exponential trend (Pyle, 1989; Fierstein and Nathenson, 1992; Bonadonna and Houghton, 2005)

$$T = T_0 \exp(-k\sqrt{A}), \tag{A5.4}$$

with T_0 the extrapolated maximum tephra thickness, k the slope of the exponential segment in a semi-log plot and A the area of the isopach contour of thickness T. In this study, given the low quantity of data, we fit our observations with single exponential segments. The volume V of a single exponential segment can be estimated as

$$V = \frac{2T_0}{k^2}. \tag{A5.5}$$

We also apply power-law and a Weibull fitting strategies that have the advantage of better describing the decrease of the mass load for poorly exposed deposits. With a power-law fitting, the thickness of tephra deposits decreases with distance from the vent as (Bonadonna and Houghton, 2005)

$$T = T_{pl}\sqrt{A}^{-m}, \tag{A5.6}$$

where T_{pl} and m are the power-law coefficient and exponent, respectively. Equation (A5.3) cannot be integrated between zero and infinity. Hence, the proximal and distal integration limits (respectively B and C) need to be defined in order to estimate the volume

$$V = \frac{2T_{pl}}{2-m}\left(C^{2-m} - B^{2-m}\right). \tag{A5.7}$$

Here, we select B based on the extrapolation of the exponential fitting as

$$B = \left(\frac{T_0}{T_{pl}}\right)^{-\frac{1}{m}}. \tag{A5.8}$$

C is determined from the power-law trend, as the value of the square root area for which the tephra thickness equals to 0.01 and 0.001 cm (i.e., where the thickness becomes comparable to the diameter of individual fine particles). Finally, the Weibull function can fit the decrease of the thickness by (Bonadonna and Costa, 2012)

$$T = \theta \left(\frac{\sqrt{A}}{\lambda} \right)^{n-2} \exp \left[- \left(\frac{\sqrt{A}}{\lambda} \right)^{n-2} \right], \tag{A5.9}$$

with θ, λ and n the Weibull fit parameters. This expression is integrated to obtain the volume

$$V = \frac{2\theta\lambda^2}{n}. \tag{A5.10}$$

For our data, we find $T_0 = 34.633$ cm and $k = 0.152$ km^{-1} using exponential fitting strategy with a single segment. The adjustment coefficient R^2 is equal to 0.99. Using the exponential fitting method, we find a volume of 0.030 km^3. For the power-law, we find $T_{pl} = 86.798$ cm, $m = 1.151$, $B = 2.221$ km and chose $C = 54$ and 69 km, that respectively correspond to the square root area at which the power-law trend equals to 0.01 and 0.001 cm. The adjustment coefficient is $R^2 = 0.97$ and the power-law fitting method gives a volume estimate of 0.056 km^3 for $C = 54$ km, and 0.070 km^3, for $C = 69$ km. By averaging these two estimates, we retain a volume of 0.063 $\pm$ 0.010 km^3 for the power-law method. Finally, for the Weibull fitting method, we find $\theta = 13.989$ cm, $\lambda = 12.739$ km and $n = 1.629$ with $R^2 = 1$. This fitting strategy yields a volume of 0.028 km^3.

Appendix A5.3 - Calculation of tephra masses

For data obtained with tephra collectors, we calculate the cumulative mass of tephra based on the tephra mass load decrease with distance from the vent. The three strategies described in Appendix A5.2 are adapted to fit the tephra mass load Y with exponential, power-law and Weibull trends, respectively

$$Y = Y_0 \exp(-k\sqrt{A}), \tag{A5.11}$$

$$Y = Y_{pl} \sqrt{A}^{-m}, \tag{A5.12}$$

$$Y = \theta \left(\frac{\sqrt{A}}{\lambda} \right)^{n-2} \exp \left[- \left(\frac{\sqrt{A}}{\lambda} \right)^{n-2} \right], \tag{A5.13}$$

with Y_0 the extrapolated maximum mass load and Y_{pl} the power-law coefficient. The fitting parameters k, m, θ, λ and n are described in Appendix A5.2, and A corresponds to the area of the isomass contour of mass load Y. The mass M of a single exponential segment can be estimated as

$$M = \frac{2Y_0}{k^2}. \tag{A5.14}$$

The mass is estimated from the power-law fitting as

$$M = \frac{2Y_{pl}}{2-m} \left(C^{2-m} - B^{2-m} \right), \tag{A5.15}$$

where B is estimated by extrapolating the exponential fitting as

$$B = \left(\frac{Y_0}{Y_{pl}} \right)^{-\frac{1}{m}}. \tag{A5.16}$$

Here, we calculate C from the value of the square root area for which the power-law trend equals to 0.1 and 0.01 kg m^{-2}. Finally, the Weibull function is integrated to obtain the total mass

$$M = \frac{2\theta\lambda^2}{n}. \tag{A5.17}$$

We find $Y_0 = 20.437 \times 10^6$ kg km^{-2}, $k = 0.197$ km^{-1} and $M = 1.1 \times 10^9$ kg using the exponential fitting strategy with a single segment ($R^2 = 0.98$). For the power-law, we find $Y_{pl} = 111.505 \times 10^6$ kg km^{-2} and $m = 1.692$ ($R^2 = 0.99$). The integration limits are $B = 2.727$ km and $C = 63$ and 247 km, that respectively correspond to the square root area at which the power-law trend equals to 0.1 and 0.01 kg m^{-2}. The power-law fitting method gives a mass estimate of 1.6×10^9 kg, for $C = 63$ km, and 3×10^9 kg, for $C = 247$ km. By averaging these two estimates, we retain a mass of $2.3 \pm 0.7 \times 10^9$ kg for the power-law method. Finally, for the Weibull fitting method, we find $\theta = 4.667 \times 10^6$ kg km^{-2}, $\lambda = 12.156$ km and $n = 1.002$ with $R^2 = 1$. This fitting strategy yields a mass estimate of 1.377×10^9 kg.

Appendix A5.4 - Statistical analysis of pulsatory volcanic activity

For stationary time series of pulsatory volcanic activity, the probability of explosion as a function of the repose interval can be well-described by log-logistic models (Dominguez et al., 2016). Log-logistic probability distributions are fitted using the parameters α that is the median of the repose interval distribution (called *scale*) and β that defines the distribution shape. Two parameters are derived from α and β in order to better describe the frequency and variability of time series

$$\mu = \ln(\alpha), \tag{A5.18}$$

$$s = \frac{1}{\beta}. \tag{A5.19}$$

The parameters μ and s are obtained by fitting the probability density function $f(t)$ and the cumulative distribution function $F(t)$ by log-logistic distributions

$$f(t) = \frac{\exp(\frac{\ln(t)-\mu}{s})}{s[1+\exp(\frac{\ln(t)-\mu}{s})]^2}, \tag{A5.20}$$

$$F(t) = \frac{1}{1+\exp(\frac{\ln(t)-\mu}{s})}, \tag{A5.21}$$

with t the repose interval.

Supplementary Figures

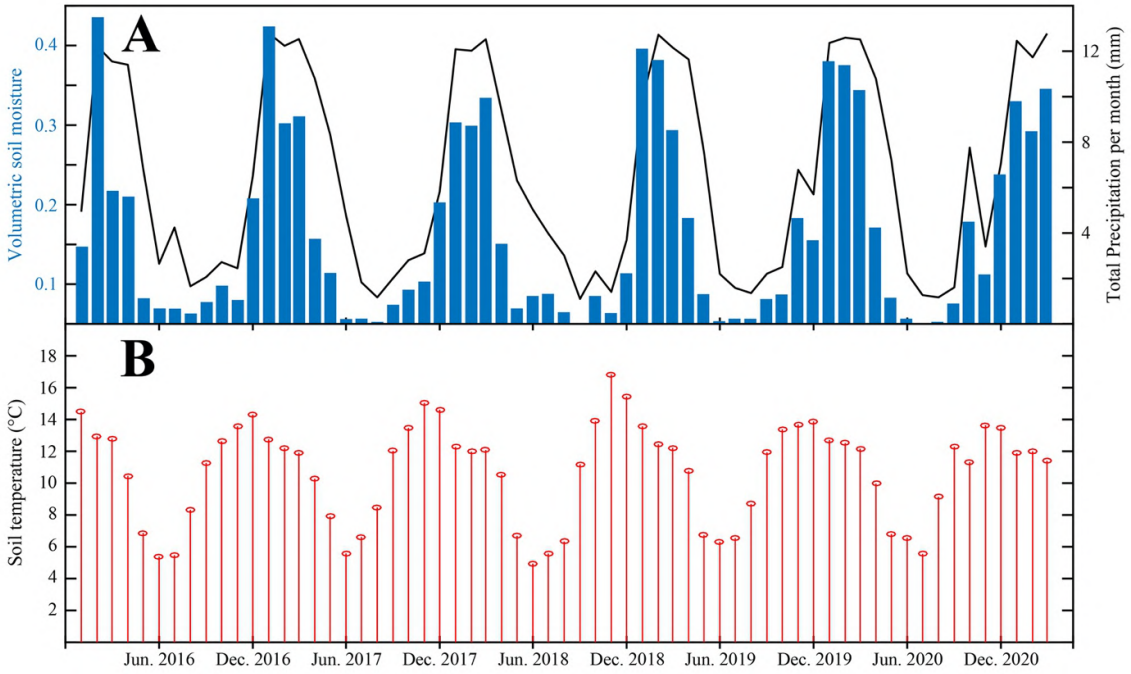

Figure A5.1: A. Blue bars show the evolution of the monthly total precipitation at Sabancaya from January 2016 to March 2021. The solid black line indicates the changes in volumetric soil moisture. **B.** Monthly averaged soil temperature. Surface (10 m) meteorological datasets displayed in B, C and D are from the ECMWF ERA-Interim reanalysis (Balsamo et al., 2015).

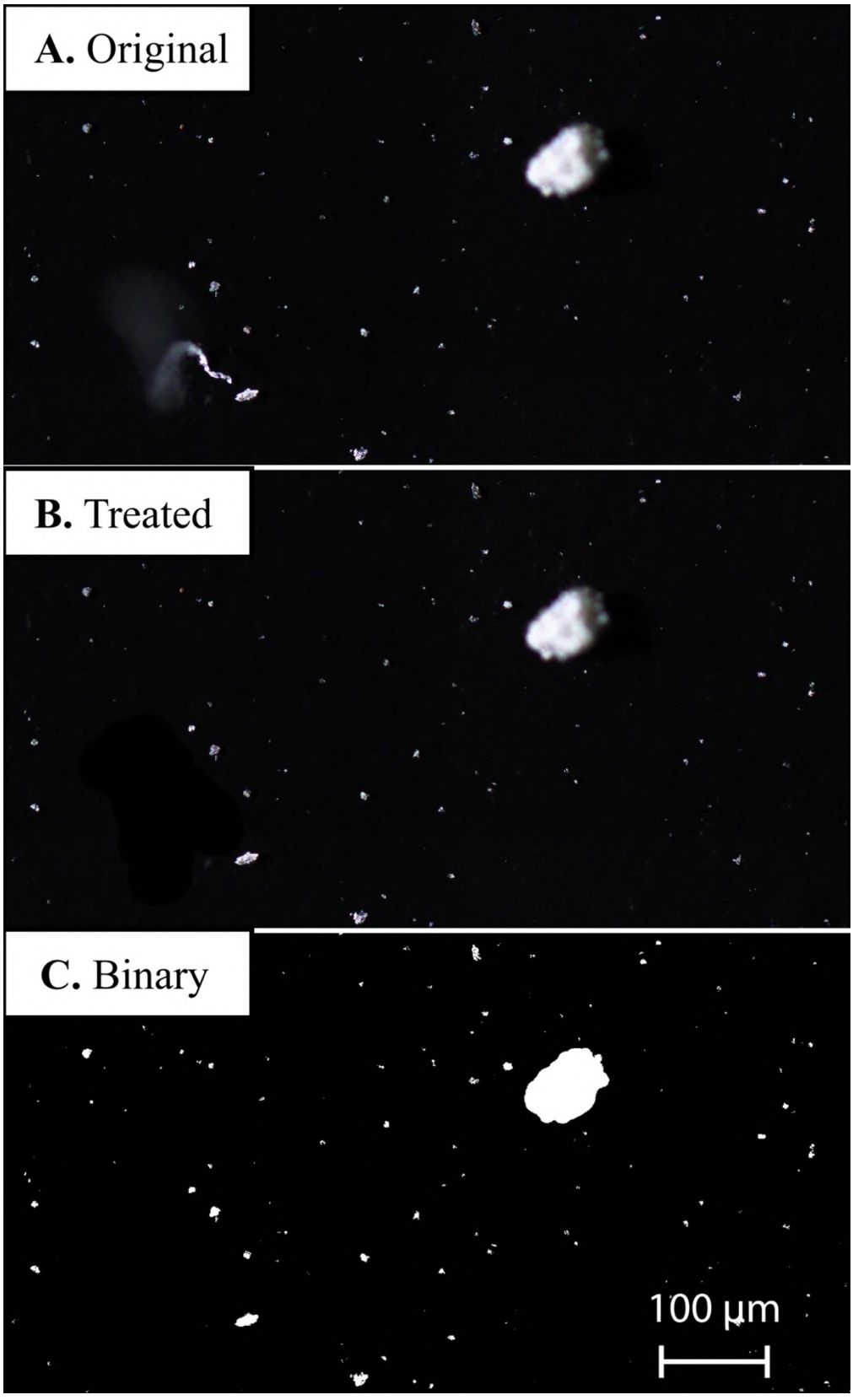

Figure A5.2: Treatment applied to microscope image prior to analysis. The original image (**A.**) is first manually treated (**B.**) before binarization (**C.**).

Figure A5.3: Wind-induced ripples at the surface of tephra deposits at site 42, 3.9 km from the vent.

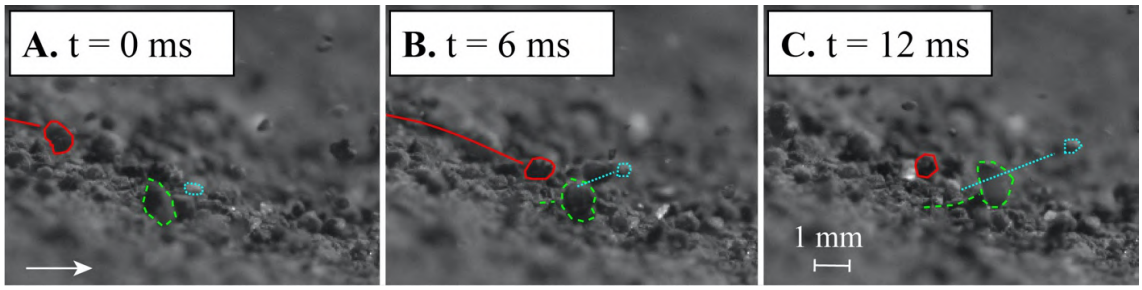

Figure A5.4: Snapshots of a High-Speed video of the aeolian remobilisation of particles on a granular surface at the field site 42. The splash effect of a saltating particle (contoured in red) hitting the surface is evidenced. In **A.**, the particle contoured in red is moving by saltation whilst the coarser, green-contoured, and the finer, blue-contoured, particles are at rest. Upon collision with the ground, the particle moving by saltation triggers the motion of both the coarser and the finer particles (**B.**). The coarse particle subsequently transported by rolling on the surface of the ground, whilst the finer particle lifts off (**C.**).

Supplementary Tables

Sample Name	Sampling date	Site	Latitude	Longitude	Distance from the vent (m)	Type of sample (collection method)	Layer	Thickness (cm)	Laboratory analysis	Md_Φ	σ_Φ
R150-3	29 Jul. 2018	3	-15.840604	-71.811938	7676	Airborne remobilised - height > 1.5 m (adhesive paper)	-	-	GSD and Morphology (microscope)	6.0	0.6
R150-4	29 Jul. 2018	4	-15.838678	-71.813741	7387	Airborne remobilised - height > 1.5 m (adhesive paper)	-	-	GSD and Morphology (microscope)	6.1	0.5
R150-5	29 Jul. 2018	5	-15.836799	-71.815849	7082	Airborne remobilised - height > 1.5 m (adhesive paper)	-	-	GSD and Morphology (microscope)	6.1	0.5
A-11	30 Jul. 2018	11	-15.746714	-71.829261	5323	Stratigraphic section	A	3	-	-	-
A-13	30 Jul. 2018	13	-15.7595026	-71.8267363	4402	Stratigraphic section (loose powder sample)	A	3	GSD and Morphology (Sieving and BetterSizer S3 Plus)	2.6	0.9
B-13-top	30 Jul. 2018	13	-15.745071	-71.828359	5529	Stratigraphic section (loose powder sample)	B	2	GSD and Morphology (Sieving and BetterSizer S3 Plus)	2.7	0.9
B-13-bottom	30 Jul. 2018	13	-15.745071	-71.828359	5529	Stratigraphic section (loose powder sample)	B	3	GSD and Morphology (Sieving and BetterSizer S3 Plus)	2.2	1.9
C-13	30 Jul. 2018	13	-15.745071	-71.828359	5529	Stratigraphic section (loose powder sample)	C	4	GSD, Morphology and glass composition (Sieving, BetterSizer S3 Plus and Jeol JXA-8200)	2.6	1.5
A-14	31 Jul. 2018	14	-15.823681	-71.843905	4325	Stratigraphic section (loose powder sample)	A	4	GSD and Morphology (Sieving and BetterSizer S3 Plus)	2.4	1.3
B-14	31 Jul. 2018	14	-15.823681	-71.843905	4325	Stratigraphic section (loose powder sample)	B	4	GSD and Morphology (Sieving and BetterSizer S3 Plus)	3.3	1.3
C-14	31 Jul. 2018	14	-15.823681	-71.843905	4325	Stratigraphic section (loose powder sample)	C	8	GSD and Morphology (Sieving and BetterSizer S3 Plus)	2.8	0.9
R0-17	31 Jul. 2018	17	-15.836146	-71.816003	7014	Field experiment (adhesive paper)	-	-	GSD and Morphology (microscope)	4.1	0.6
SG-17	31 Jul. 2018	17	-15.836146	-71.816003	7014	Field experiment - most superficial ground layer (loose powder sample)	A	-	GSD and Morphology (Sieving and BetterSizer S3 Plus)	1.9	0.9
R0-18i	31 Jul. 2018	18	-15.836124	-71.815977	7014	Field experiment (adhesive paper)	-	-	GSD and Morphology (microscope)	4.3	0.5
R0-18ii	31 Jul. 2018	18	-15.836124	-71.815977	7014	Field experiment (adhesive paper)	-	-	GSD and Morphology (microscope)	4.3	0.4

Sample Name	Sampling date	Site	Latitude	Longitude	Distance from the vent (m)	Type of sample (collection method)	Layer	Thickness (cm)	Laboratory analysis	Md_Φ	σ_Φ
SG-18	31 Jul. 2018	18	-15.836124	-71.815977	7014	Field experiment - most superficial ground layer (loose powder sample)	A	-	GSD and Morphology (Sieving and BetterSizer S3 Plus)	2.4	1.1
R0-19i	31 Jul. 2018	19	-15.836007	-71.815936	7007	Field experiment (adhesive paper)	-	-	GSD and Morphology (microscope)	4.3	0.4
R0-19ii	31 Jul. 2018	19	-15.836007	-71.815936	7007	Field experiment (adhesive paper)	-	-	GSD and Morphology (microscope)	4.3	0.5
SG-19	31 Jul. 2018	19	-15.836007	-71.815936	7007	Field experiment - most superficial ground layer (loose powder sample)	A	-	GSD and Morphology (Sieving and BetterSizer S3 Plus)	1.7	3.3
R0-20	31 Jul. 2018	20	-15.835327	-71.815304	6991	Field experiment (adhesive paper)	-	-	GSD and Morphology (microscope)	4.3	0.6
SG-20	31 Jul. 2018	20	-15.835327	-71.815304	6991	Field experiment - most superficial ground layer (loose powder sample)	A	-	GSD and Morphology (Sieving and BetterSizer S3 Plus)	2.6	3.4
R0-21	31 Jul. 2018	21	-15.835308	-71.81531	6989	Field experiment (adhesive paper)	-	-	GSD and Morphology (microscope)	4.2	0.7
SG-21	31 Jul. 2018	21	-15.835308	-71.81531	6989	Field experiment - most superficial ground layer (loose powder sample)	A	-	GSD and Morphology (Sieving and BetterSizer S3 Plus)	2.2	1.9
R0-22	31 Jul. 2018	22	-15.828204	-71.809538	6845	Field experiment (adhesive paper)	-	-	GSD and Morphology (microscope)	4.2	0.5
SG-22	31 Jul. 2018	22	-15.828204	-71.809538	6845	Field experiment - most superficial ground layer (loose powder sample)	A	-	GSD and Morphology (Sieving and BetterSizer S3 Plus)	3.4	2.2
R0-23	01 Aug. 2018	23	-15.815749	-71.853964	3239	Field experiment (adhesive paper)	-	-	GSD and Morphology (microscope)	4.3	0.5
SG-23	01 Aug. 2018	23	-15.815749	-71.853964	3239	Field experiment - most superficial ground layer (loose powder sample)	A	-	GSD and Morphology (Sieving and BetterSizer S3 Plus)	2.0	1.8
A-24-top	01 Aug. 2018	24	-15.817935	-71.858054	3477	Stratigraphic section (loose powder sample)	A	0.5	GSD and Morphology (Sieving and BetterSizer S3 Plus)	1.5	1.1
A-24-bottom	01 Aug. 2018	24	-15.817935	-71.858054	3477	Stratigraphic section (loose powder sample)	A	2	GSD and Morphology (Sieving and BetterSizer S3 Plus)	2.2	1.4
B-24-top	01 Aug. 2018	24	-15.817935	-71.858054	3477	Stratigraphic section (loose powder sample)	B	3	GSD and Morphology (Sieving and BetterSizer S3 Plus)	2.1	1.4
B-24-bottom	01 Aug. 2018	24	-15.817935	-71.858054	3477	Stratigraphic section (loose powder sample)	B	5	GSD and Morphology (Sieving and BetterSizer S3 Plus)	1.9	1.2

Sample Name	Sampling date	Site	Latitude	Longitude	Distance from the vent (m)	Type of sample (collection method)	Layer	Thickness (cm)	Laboratory analysis	Md_Φ	σ_Φ
prim-25ii	02 Aug. 2018	25	-15.824333	-71.843444	4409	Airborne primary (adhesive paper)	-	-	GSD and Morphology (microscope)	4.6	0.6
prim-25iii	02 Aug. 2018	25	-15.824333	-71.843444	4409	Airborne primary (adhesive paper)	-	-	GSD and Morphology (microscope)	4.2	0.7
prim-26ii	02 Aug. 2018	26	-15.824361	-71.843361	4415	Airborne primary (adhesive paper)	-	-	GSD and Morphology (microscope)	4.3	0.5
prim-26iii	02 Aug. 2018	26	-15.824361	-71.843361	4415	Airborne primary (adhesive paper)	-	-	GSD and Morphology (microscope)	4.3	0.4
prim-27ii	02 Aug. 2018	27	-15.824388	-71.843333	4419	Airborne primary (adhesive paper)	-	-	GSD and Morphology (microscope)	4.1	1.0
prim-27iii	02 Aug. 2018	27	-15.824388	-71.843333	4419	Airborne primary (adhesive paper)	-	-	GSD and Morphology (microscope)	4.2	1.3
prim-27iv	02 Aug. 2018	27	-15.824388	-71.843333	4419	Airborne primary (adhesive paper)	-	-	GSD and Morphology (microscope)	4.2	0.9
prim-27v	02 Aug. 2018	27	-15.824388	-71.843333	4419	Airborne primary (adhesive paper)	-	-	GSD and Morphology (microscope)	4.3	0.8
prim-27vi	02 Aug. 2018	27	-15.824388	-71.843333	4419	Airborne primary (adhesive paper)	-	-	GSD and Morphology (microscope)	4.2	0.9
prim-28i	02 Aug. 2018	28	-15.824361	-71.843305	4417	Airborne primary (adhesive paper)	-	-	GSD and Morphology (microscope)	4.4	0.4
prim-28ii	02 Aug. 2018	28	-15.824361	-71.843305	4417	Airborne primary (adhesive paper)	-	-	GSD and Morphology (microscope)	4.2	0.7
prim-28iii	02 Aug. 2018	28	-15.824361	-71.843305	4417	Airborne primary(adhesive paper)	-	-	GSD and Morphology (microscope)	4.2	0.6
A-29-top	03 Aug. 2018	29	-15.823416	-71.843777	4301	Stratigraphic section	A	0.5	-	-	-
A-29-bottom	03 Aug. 2018	29	-15.823416	-71.843777	4301	Stratigraphic section	A	2.5	-	-	-
B-29	03 Aug. 2018	29	-15.823416	-71.843777	4301	Stratigraphic section	B	6	-	-	-
C-29	03 Aug. 2018	29	-15.823416	-71.843777	4301	Stratigraphic section	C	-	-	-	-
A-30	03 Aug. 2018	30	-15.824219	-71.841305	4476	Stratigraphic section (loose powder sample)	A	2.5	GSD, Morphology and glass composition (Sieving, BetterSizer S3 Plus and Jeol JXA-8200)	2.1	0.8
B-30-top	03 Aug. 2018	30	-15.824219	-71.841305	4476	Stratigraphic section (loose powder sample)	B	3	GSD, Morphology and glass composition (Sieving, BetterSizer S3 Plus and Jeol JXA-8200)	2.7	0.8
B-30-bottom	03 Aug. 2018	30	-15.824219	-71.841305	4476	Stratigraphic section (loose powder sample)	B	3	GSD, Morphology and glass composition (Sieving, BetterSizer S3 Plus and Jeol JXA-8200)	2.3	1.0

Sample Name	Sampling date	Site	Latitude	Longitude	Distance from the vent (m)	Type of sample (collection method)	Layer	Thickness (cm)	Laboratory analysis	Md_Φ	σ_Φ
R150-31i	03 Aug. 2018	31	-15.822	-71.843777	4152	Airborne remobilised - height > 1.5 m (adhesive paper)	-	-	GSD and Morphology (microscope)	6.0	0.8
R150-31ii	03 Aug. 2018	31	-15.822	-71.843777	4152	Airborne remobilised - height > 1.5 m (adhesive paper)	-	-	GSD and Morphology (microscope)	6.0	0.8
R150-37	04 Aug. 2018	37	-15.843889	-71.822816	7317	Airborne remobilised - height > 1.5 m (adhesive paper)	-	-	GSD and Morphology (microscope)	6.1	0.5
R150-38i	04 Aug. 2018	38	-15.846555	-71.782556	10384	Airborne remobilised - height > 1.5 m (adhesive paper)	-	-	GSD and Morphology (microscope)	6.1	0.5
R150-38ii	04 Aug. 2018	38	-15.846555	-71.782556	10384	Airborne remobilised - height > 1.5 m (adhesive paper)	-	-	GSD and Morphology (microscope)	6.0	0.6
D1-39	04 Aug. 2018	39	-15.784	-71.757611	10672	Stratigraphic section	D1	1	-	-	-
D2-39	04 Aug. 2018	39	-15.784	-71.757611	10672	Stratigraphic section	D2	> 3	-	-	-
R150-40i	04 Aug. 2018	40	-15.82512	-71.8422	4536	Airborne remobilised - height > 1.5 m (adhesive paper)	-	-	GSD and Morphology (microscope)	6.1	0.5
R150-40ii	04 Aug. 2018	40	-15.82512	-71.8422	4536	Airborne remobilised - height > 1.5 m (adhesive paper)	-	-	GSD and Morphology (microscope)	6.1	0.5
A-41-top	06 Aug. 2018	41	-15.809444	-71.849027	2648	Stratigraphic section (loose powder sample)	A	0.5	GSD and Morphology (Sieving and BetterSizer S3 Plus)	1.7	1.5
A-41-bottom	06 Aug. 2018	41	-15.809444	-71.849027	2648	Stratigraphic section (loose powder sample)	A	2	GSD and Morphology (Sieving and BetterSizer S3 Plus)	2.0	1.4
B-41-top	06 Aug. 2018	41	-15.809444	-71.849027	2648	Stratigraphic section (loose powder sample)	B	2	GSD and Morphology (Sieving and BetterSizer S3 Plus)	1.9	1.1
B-41-middle	06 Aug. 2018	41	-15.809444	-71.849027	2648	Stratigraphic section (loose powder sample)	B	2.5	GSD and Morphology (Sieving and BetterSizer S3 Plus)	2.2	1.9
B-41-bottom	06 Aug. 2018	41	-15.809444	-71.849027	2648	Stratigraphic section (loose powder sample)	B	3	GSD and Morphology (Sieving and BetterSizer S3 Plus)	1.7	1.4
C-41	06 Aug. 2018	41	-15.809444	-71.849027	2648	Stratigraphic section (loose powder sample)	C	7	-	-	-
R0-42ii	06 Aug. 2018	42	-15.821583	-71.856472	3878	Field experiment (adhesive paper)	-	-	GSD and Morphology (microscope)	4.1	0.6
R0-42iii	06 Aug. 2018	42	-15.821583	-71.856472	3878	Field experiment (adhesive paper)	-	-	GSD and Morphology (microscope)	3.7	1.0

Sample Name	Sampling date	Site	Latitude	Longitude	Distance from the vent (m)	Type of sample (collection method)	Layer	Thickness (cm)	Laboratory analysis	Md_Φ	σ_Φ
R0-42iv	06 Aug. 2018	42	-15.821583	-71.856472	3878	Field experiment (adhesive paper)	-	-	GSD and Morphology (microscope)	4.2	0.5
SG-42	06 Aug. 2018	42	-15.821583	-71.856472	3878	Field experiment - most superficial ground layer (loose powder sample)	A	-	GSD and Morphology (Sieving and BetterSizer S3 Plus)	1.0	0.9
D1-45-top	08 Aug. 2018	45	-15.755583	-71.666128	20845	Stratigraphic section (loose powder sample)	D1	1	GSD and Morphology (Sieving and BetterSizer S3 Plus)	-1.3	3.0
D1-45-bottom	08 Aug. 2018	45	-15.755583	-71.666128	20845	Stratigraphic section (loose powder sample)	D1	3	GSD and Morphology (Sieving and BetterSizer S3 Plus)	0.4	2.5
D2-45	08 Aug. 2018	45	-15.755583	-71.666128	20845	Stratigraphic section (loose powder sample)	D2	-	GSD and Morphology (Sieving and BetterSizer S3 Plus)	-0.2	2.5
A-46-top	09 Aug. 2018	46	-15.802833	-71.847972	2007	Stratigraphic section (loose powder sample)	A	0.5	GSD and Morphology (Sieving and BetterSizer S3 Plus)	1.2	1.3
A-46-bottom	09 Aug. 2018	46	-15.802833	-71.847972	2007	Stratigraphic section (loose powder sample)	A	1	GSD and Morphology (Sieving and BetterSizer S3 Plus)	1.5	1.5
B-46-top	09 Aug. 2018	46	-15.802833	-71.847972	2007	Stratigraphic section (loose powder sample)	B	2	GSD and Morphology (Sieving and BetterSizer S3 Plus)	1.4	2.1
B-46-bottom	09 Aug. 2018	46	-15.802833	-71.847972	2007	Stratigraphic section (loose powder sample)	B	> 4	GSD and Morphology (Sieving and BetterSizer S3 Plus)	2.7	2.7
A-47	09 Aug. 2018	47	-15.794111	-71.839999	1947	Stratigraphic section	A	3.5	-	-	-
B-47	09 Aug. 2018	47	-15.794111	-71.839999	1947	Stratigraphic section	B	18	-	-	-
C-47	09 Aug. 2018	47	-15.794111	-71.839999	1947	Stratigraphic section	C	-	-	-	-
R0-48	10 Aug. 2018	48	-15.846916	-71.782694	10398	Field experiment (adhesive paper)	-	-	GSD and Morphology (microscope)	4.2	0.6
A-52-Plant	29 Jul. 2018	52	-15.846639	-71.815833	7972	Stratigraphic section inside plants	A	3	-	-	-
B-52-Plant	29 Jul. 2018	52	-15.846639	-71.815833	7972	Stratigraphic section inside plants	B	8	-	-	-
A-53	29 Jul. 2018	53	-15.841194	-71.815778	7477	Stratigraphic section	A	3	-	-	-
B-53	29 Jul. 2018	53	-15.841194	-71.815778	7477	Stratigraphic section	B	7	-	-	-
A-55-Plant	29 Jul. 2018	55	-15.831111	-71.814639	6683	Stratigraphic section inside plants	A	5	-	-	-
A-55	29 Jul. 2018	55	-15.831111	-71.814639	6683	Stratigraphic section outside plants	A	4	-	-	-
B-55-Plant	29 Jul. 2018	55	-15.831111	-71.814639	6683	Stratigraphic section inside plants	B	9	-	-	-
A-56	29 Jul. 2018	56	-15.827917	-71.81325	6531	Stratigraphic section	A	2	-	-	-
B-56	29 Jul. 2018	56	-15.827917	-71.81325	6531	Stratigraphic section	B	1.5	-	-	-

Sample Name	Sampling date	Site	Latitude	Longitude	Distance from the vent (m)	Type of sample (collection method)	Layer	Thickness (cm)	Laboratory analysis	Md_Φ	σ_Φ
A-59	30 Jul. 2018	59	-15.744917	-71.828096	5559	Stratigraphic section	A	3	-	-	-
R0-61i	03 Aug. 2018	61	-15.824222	-71.843416	4398	Airborne remobilised - on the ground (adhesive paper)	-	-	GSD and Morphology (microscope)	4.2	0.5
R0-61ii	03 Aug. 2018	61	-15.824222	-71.843416	4398	Airborne remobilised - on the ground (adhesive paper)	-	-	GSD and Morphology (microscope)	4.3	0.5
R0-61iii	03 Aug. 2018	61	-15.824222	-71.843416	4398	Airborne remobilised - on the ground (adhesive paper)	-	-	GSD and Morphology (microscope)	4.1	0.6
R0-61iv	03 Aug. 2018	61	-15.824222	-71.843416	4398	Airborne remobilised - on the ground (adhesive paper)	-	-	GSD and Morphology (microscope)	4.1	0.7
R0-61v	03 Aug. 2018	61	-15.824222	-71.843416	4398	Airborne remobilised - on the ground (adhesive paper)	-	-	GSD and Morphology (microscope)	4.2	0.6
R0-61vi	03 Aug. 2018	61	-15.824222	-71.843416	4398	Airborne remobilised - on the ground (adhesive paper)	-	-	GSD and Morphology (microscope)	4.1	0.7
R0-61vii	03 Aug. 2018	61	-15.824222	-71.843416	4398	Airborne remobilised - on the ground (adhesive paper)	-	-	GSD and Morphology (microscope)	4.1	0.7
R0-61viii	03 Aug. 2018	61	-15.824222	-71.843416	4398	Airborne remobilised - on the ground (adhesive paper)	-	-	GSD and Morphology (microscope)	4.0	0.7
A-62	02 Aug. 2018	62	-15.833027	-71.754388	12160	Stratigraphic section	A	3.5	-	-	-
A-63	03 Aug. 2018	63	-15.822	-71.843777	4152	Stratigraphic section	A	5	-	-	-
B-63	03 Aug. 2018	63	-15.822	-71.843777	4152	Stratigraphic section	B	5	-	-	-
C-63	03 Aug. 2018	63	-15.822	-71.843777	4152	Stratigraphic section	C	-	-	-	-
A-64	08 Aug. 2018	64	-15.756611	-71.704222	16776	Stratigraphic section	A	2.5	-	-	-
A-65	08 Aug. 2018	65	-15.768805	-71.710722	15861	Stratigraphic section	A	3.5	-	-	-
sab-1813	06 Apr. 2018	-	-15.781481	-71.852031	562	ballistic fragment	-	-	Glass composition (Jeol JXA-8200)	-	-
sab-1852	25 May to 20 Jun. 2018	SC-04	-15.824344	-71.744081	12831	Tephra collector	-	-	GSD and Morphology (Sieving and BetterSizer S3 Plus)	1.7	0.9
sab-1947	21 Aug. to 22 Oct. 2019	SC-04	-15.824344	-71.744081	12831	Tephra collector	-	-	GSD and Morphology (Sieving and BetterSizer S3 Plus)	2.4	0.8
sab-1967	15 Oct. to 28 Nov. 2019	SC-04	-15.641568	-71.765053	18916	Tephra collector	-	-	GSD and Morphology (Sieving and BetterSizer S3 Plus)	2.9	0.9

Sample Name	Sampling date	Site	Latitude	Longitude	Distance from the vent (m)	Type of sample (collection method)	Layer	Thickness (cm)	Laboratory analysis	Md_Φ	σ_Φ
sab-1854	25 May to 19 Jun. 2018	SC-05	-15.824365	-71.843434	4413	Tephra collector	-	-	GSD and Morphology (Sieving and BetterSizer S3 Plus)	1.8	0.8
sab-1869	19 Jun. to 28 Jul. 2018	SC-05	-15.824365	-71.843434	4413	Tephra collector	-	-	GSD, Morphology and glass composition (Sieving, BetterSizer S3 Plus and Jeol JXA-8200)	1.8	0.8
sab-1890	28 Jul. to 06 Dec. 2018	SC-05	-15.824365	-71.843434	4413	Tephra collector	-	-	GSD and Morphology (Sieving and BetterSizer S3 Plus)	2.2	1.0
sab-1927	06 Apr. to 20 Aug. 2019	SC-05	-15.824365	-71.843434	4413	Tephra collector	-	-	GSD and Morphology (Sieving and BetterSizer S3 Plus)	1.9	0.9
sab-1948	21 Aug. to 22 Oct. 2019	SC-05	-15.824344	-71.744081	12831	Tephra collector	-	-	GSD and Morphology (Sieving and BetterSizer S3 Plus)	2.1	1.2
sab-1847	22 May to 23 Jun. 2018	SC-22	-15.764047	-71.831625	3671	Tephra collector	-	-	GSD and Morphology (Sieving and BetterSizer S3 Plus)	1.7	0.8
sab-1895	23 Jun. to 07 Dec. 2018	SC-22	-15.764047	-71.831625	3671	Tephra collector	-	-	GSD, Morphology and glass composition (Sieving, BetterSizer S3 Plus and Jeol JXA-8200)	2.2	0.9
sab-1957	15 May to 24 Oct. 2019	SC-22	-15.764047	-71.831625	3671	Tephra collector	-	-	GSD and Morphology (Sieving and BetterSizer S3 Plus)	2.0	1.1
sab-1726	23 Jun. to 25 Jul. 2017	SC-27	-15.764047	-71.831625	3671	Tephra collector	-	-	GSD, Morphology and glass composition (Sieving, BetterSizer S3 Plus and Jeol JXA-8200)	1.3	1.2
sab-1832	07 Apr. to 25 May 2018	SC-27	-15.764047	-71.831625	3671	Tephra collector	-	-	GSD, Morphology and glass composition (Sieving, BetterSizer S3 Plus and Jeol JXA-8200)	1.9	1.2
sab-1850	27 May to 20 Jun. 2018	SC-27	-15.806825	-71.842863	2668	Tephra collector	-	-	GSD and Morphology (Sieving and BetterSizer S3 Plus)	1.2	1.0
sab-1892	20 Jun. to 06 Dec. 2018	SC-27	-15.806825	-71.842863	2668	Tephra collector	-	-	GSD and Morphology (Sieving and BetterSizer S3 Plus)	1.9	1.0
sab-1926	15 Apr. to 20 Aug. 2019	SC-27	-15.806825	-71.842863	2668	Tephra collector	-	-	GSD and Morphology (Sieving and BetterSizer S3 Plus)	1.6	1.2
sab-1963	20 Aug. to 28 Nov. 2019	SC-27	-15.806825	-71.842863	2668	Tephra collector	-	-	GSD and Morphology (Sieving and BetterSizer S3 Plus)	1.7	1.0

Table A5.1: List of samples.

Supplementary Videos

Links to supplementary videos:

- Supplementary Video A5.1: https://archive-ouverte.unige.ch/unige:163115/ATTACHMENT10
- Supplementary Video A5.2: https://archive-ouverte.unige.ch/unige:163115/ATTACHMENT11
- Supplementary Video A5.3: https://archive-ouverte.unige.ch/unige:163115/ATTACHMENT12
- Supplementary Video A5.4: https://archive-ouverte.unige.ch/unige:163115/ATTACHMENT13

Chapter 6

Conclusions and future perspectives

In this thesis, experimental and field analysis are combined in order to study the transport and sedimentation of volcanic ash in the atmosphere. In particular, the sedimentation of volcanic ash within ash fingers is investigated, as well as the aeolian remobilisation of tephra deposits in the specific setting of Sabancaya volcano (Peru). First, the formation of ash fingers by settling driven gravitational instabilities (SDGIs) is examined using simple scaled experiments (Chapters 2 and 3). Each of these studies individually contribute to identify key parameters controlling the formation and properties of ash fingers. In Chapter 2, the role of particle concentration on SDGIs and resulting fingers is quantified. Chapter 3 additionally presents the influence of particle size along with particle concentration. Second, occurrences of natural ash fingers reported in publications are reviewed, and new visual observations at Etna (Italy), Sabancaya and Sakurajima (Japan) volcanoes are analysed (Chapter 4). In this work, the properties of ash fingers are measured, then interpreted, notably using results from previous Chapters, with implications for the formation of ash fingers and volcanic ash sedimentation. Finally, the long-lasting eruption of Sabancaya and associated aeolian remobilisation of volcanic ash are described using a wide variety of field techniques (Chapter 5). Tephra deposits are studied to derive erupted volumes and mass by combining analysis of stratigraphic sections and continuous sampling of fallout in collectors. Frequent remobilisation of these deposits by the wind are characterised using various sampling strategies and particle descriptions.

6.1 Characterisation of ash fingers

Ash fingers are ash-laden currents driven by density differences that descend from volcanic ash clouds, entraining fine volcanic ash downward at speeds greater than their individual terminal fall velocity. As highlighted by the review presented in Chapter 4, ash fingers have been reported to form during various eruptions, but often called differently, confusing the observed phenomena (i.e., ash fingers) with their supposed formation mechanism. In fact, this review also highlights that ash fingers can result from different formation mechanisms, all implying that ash fingers are produced by density increases that trigger the detachment of heavy, unstable, parts at the base of volcanic ash clouds. Despite this similarity, the increase in density can originate from different processes, with implications for the conditions associated with the formation of ash fingers and for their physical properties.

The principal formation mechanism investigated in this thesis are SDGIs that arise when particles sediment across the interface separating an upper particle-laden fluid layer and a lower, initially denser, layer (Hoyal et al., 1999b). Chapters 2 and 3 reveal how particle settling creates a heavy region containing both particles and dense fluid below the interface (i.e., PBL). Measurements of the PBL thickness and of fingers characteristic length scales in Chapter 2 show that the PBL becomes unstable if sufficiently thick to reach a critical value of the Grashof number $Gr_c = 10^4$. When unstable, the PBL detaches and descends in the form of fingers, whose velocity and size are found to respectively increase and decrease with increasing particle concentration. SDGIs can arise at the lower interface between a volcanic ash cloud and the atmosphere (Carazzo and Jellinek, 2012; Manzella et al., 2015; Scollo et al., 2017), but the formation of ash fingers can also be modulated by factors other than pure particle settling (e.g., wind induced overturning motions in volcanic clouds; Freret-Lorgeril et al., 2020). In this thesis, as a first approximation, the fundamental dynamics of fingers resulting from SDGIs is considered as relevant for the study of ash fingers in general, even if produced by different mechanisms.

Conditions for the development of fingers resulting from SDGIs are studied experimentally. A new intuitive measure L^* comparing the thickness of cloud and PBL is derived and tested in Chapter 2. Taken together, these criteria can be used to

quantify the tendency for SDGI-driven fingers to form below particle suspensions. For natural ash fingers, L^* is particularly difficult to constrain, but a first attempt to apply this criterion to volcanic ash clouds is presented in Chapter 4. The second criterion studied in Chapter 3 depends on the ratio of the finger velocity over the velocity of individually settling particles (Hoyal et al., 1999b; Carazzo and Jellinek, 2012; Jacobs et al., 2015). It can be adapted to specifically estimate the particle sizes and concentrations associated with generation of fingers from SDGIs. As for any particle-laden current, only particles sufficiently coupled with the flow (Burgisser et al., 2005) can settle within fingers. This is used for interpreting field of observations in Chapter 4 and calculate maximum diameters expected to potentially sediment in ash fingers. As reported quantitative descriptions of ash fingers are very rare, the work presented in this thesis considerably increases the number of available observations.

6.1.1 Summary of main findings

The main findings regarding the characterisation of ash fingers can be summarised as follow:

- Natural ash fingers can result from SDGIs, but are modulated by processes other than pure particle settling, including wind-induced mechanisms.

- SDGIs can arise from very small density differences. This implies that fingers do not necessarily contain higher particle concentrations than the cloud from which they originate.

- Combining observations of plumes produced by lava fountains (Etna in 2012 - 2013) and Vulcanian explosions (Sabancaya in 2018 and Sakurajima in 2019), the mean width W, spacing λ and downward velocities V_f of natural ash fingers observed in this work are $W = 123 \pm 83$ m, $\lambda = 304 \pm 123$ m and $V_f = 2.4 \pm 1.6$ m s^{-1}.

- Ash fingers can only transport volcanic ash particles with terminal fall velocities slower or equal to the downward velocity of the flow. The formation of

ash fingers is therefore favoured for high particle concentrations and fine grain sizes. In general, this can be predicted by studying the degree of coupling between particles and the flow within fingers, as only coupled particles can settle within fingers. For the specific case of fingers produced by SDGIs, dimensionless numbers B_2 (ratio of the timescale for individual particle settling to the timescale for collective settling controlled by inertial drag) and B_3 (ratio of the finger characteristic velocity to the velocity of individual particles) are found to correctly characterise the conditions associated with the development of fingers in experiments.

- Based on the principle stated above, the largest particles transportable within ash fingers have terminal fall velocities equal to the downward velocity of ash fingers. Results suggests that ash fingers observed in this thesis potentially carried particles with diameters as large as $613 \pm 130\,\mu m$. This potentially extends the role of ash fingers on tephra deposition, as these sizes are found to be greater than previously estimated (Eliasson et al., 2014; Manzella et al., 2015; Freret-Lorgeril et al., 2020).

- The length scales characterising ash fingers (PBL thickness δ, W and λ) are all proportional to each other and decrease as a function of the particle volume fraction X_p, scaling with a Grashof number of 10^4 in experiments.

- Although the width of natural ash fingers is measured to be about two orders of magnitude greater than estimations based on the experimental Grashof number, similar scaling is found $W \propto X_p^{-1/3}$.

- In experiments, it is found that the potential to form SDGIs at the base of particle suspensions can be quantified as a function of the thickness of the particle suspension H_c and of δ through the ratio $L^* = H_c/\delta$. SDGIs and associated fingers form preferentially below thick upper layers and for high particle concentration, at $L^* \gg 1$. This criterion is tested for volcanic ash clouds, but lack of data does not allow to validate its relevance for predicting the development of ash fingers.

6.1.2 Main field and experimental limitations

Field measurements: Field results are only based on visual observations from which maximum transported particle diameters and concentrations are estimated. There is a crucial need for to validate these results against the characteristics of deposited particles and of the eruptions. This would allow to better define conditions for which ash fingers develop, as it is now limited by the number of observations, with very few eruptions for which the particle concentration has been estimated independently of fingers properties. Moreover, ash fingers are 3D objects that are only described by observations on 2D image planes, greatly reducing the observable complexity of ash fingers. Another key limitation in this thesis is that observed ash fingers all formed close to the vent below bent-over plumes. A more complete characterisation also requires observations at different distances (e.g., Hobbs et al., 1991), and for strong volcanic plumes.

Experimental studies: The experimental set-up used in this thesis is greatly simplified. Only monodisperse and relatively narrow grainsize distributions are used, contrarily to the wide size ranges that characterise natural volcanic eruptions. In general, although allowing for the basic description of fingers properties and of the processes by which they originate, important factors affecting the formation and dynamics of ash fingers are neglected. In particular, experiments are performed in a quiescent environment, and the effect of the wind on fingers is not studied. Moreover, as for many analogue models, the experiments cannot encompass the exact dynamical regime expected in nature. For example, volcanic ash clouds and ash fingers are fully turbulent, whereas the flows in experiments are only in a transitional regime. Similarly than for the field measurements, experimental fingers are illuminated by a planar laser and only imaged in 2D and do not address the dynamics of fingers in 3D.

6.2 Tephra deposits and aeolian remobilisation at Sabancaya volcano

The post-2016 activity of Sabancaya volcano and aeolian remobilisation of associated deposits are characterised in this thesis based on a combination of field strategies. Study of the evolution of the repose interval separating explosions reveals that the pulsatory eruptive dynamics of Sabancaya is unsteady, with changes consistent with alternating episodes of dome growth and collapse. Although repose intervals vary with time, Vulcanian explosions are frequent (21 explosions per day during the field campaign), and primary tephra fallout is sampled in collectors since 2018. Meteorological conditions at Sabancaya are favourable for the remobilisation of deposits by the wind, and the loose, most superficial, tephra layer is found to be frequently remobilised by the wind in a highly erodible environment. This is evidenced by a combination of visual observations, sampling of airborne remobilised particles on adhesive paper, and PM_{10} monitoring. Remobilised particles are compared with primary fallout particles, tephra deposits, and models describing aeolian remobilisation.

6.2.1 Summary of main findings

The main findings regarding the field study at Sabancaya can be summarised as follow:

- The pulsatory dynamics of Sabancaya volcano are Vulcanian in eruptive style. 8 distinct periods corresponding to episodes of dome growth and collapse (Coppola et al., 2022) and variations in the repose interval between explosions can be distinguished.

- The bulk volume of tephra deposits produced from November 2016 to August 2018 is 0.04 ± 0.02 km^3.

- Tephra collectors yield a bulk volume of about $1.1 \pm 0.5 \times 10^{-3}$ km^3 between April 2018 and November 2019, illustrating a significant decrease in the tephra production rate since 2018.

- Recurrent aeolian remobilisation of volcanic ash deposits is observed, in events as intense as ash storms. This notably motivates nearly real-time sampling of tephra fallout to estimate eruptive parameters, since tephra deposits may not be well-preserved in such erosive environment.

- PM_{10} concentrations in the surrounding of Sabancaya are found to potentially exceed health recommendations (0.15 mg m^{-3} for daily exposures).

- Sampling of remobilised particles is performed at different heights. Comparison of the size of remobilised particles with the grainsize distribution of tephra deposits from which they originate indicates that particles sizes at the level of the ground are compatible with a transport by saltation, whilst particles collected above 1.5 m are more consistent with a transport by saltation.

- Primary and remobilised particles cannot be efficiently distinguished at Sabancaya, as their shape descriptors are very similar. In fact, in such a syn-eruptive context, fresh volcanic ash is repeatedly deposited at the surface then remobilised. Rounding effects due to the abrasion of particles by secondary transport are not perceptible yet.

6.2.2 Limitations

The study of stratigraphic sections presented in this thesis is restricted to accessible areas, mainly in the south of the volcanic edifice. Hence, there is a lack of measurements that would be necessary to constrain erupted volumes more accurately. Tephra collectors are more widely dispersed, but data are only available since 2018, and the beginning of the eruption cannot be studied from collectors.

Besides, remobilisation phenomena reported in this thesis are only observed during a limited period of time. A more global view of aeolian remobilisation at Sabancaya would necessitate more prolonged observations, notably during different seasons. Similar limitations are associated with PM_{10} measurements that are performed for short durations, over which daily means cannot be accurately determined for evaluating potential hazards to health. Regarding the analysis of remobilisation mechanisms, the transport of remobilised particles is characterised only through

grainsize and particle morphology descriptions. These results are compared with a models predicting the onset of saltation and if particles can stay in suspension, but not directly observed. Moreover, important parameters, such as the wind friction velocity, could not be measured in the field and compared with our results.

6.3 Future research perspectives

Even though new observations of ash fingers are presented in this thesis, much more investigations are required to have an exhaustive description of ash fingers and of their effect on the sedimentation of volcanic ash. As discussed in Section 6.1.2, the work presented in this thesis is solely based on visual observations. Future work need to use a wide variety of techniques in order to reduce the number of unknown variables. First, tephra deposits need to be characterised at the distance ash fingers reach the vent in order to validate calculations of the maximum particle size settling within fingers, and identify signature characteristics left by ash fingers on deposits. Second, multiple techniques should be employed to characterise the particle concentration and size in clouds associated with ash fingers. This would allow to compare more accurately ash fingers with experiments, better understand the conditions favouring the development of natural ash fingers, as well as the key parameters controlling their dynamics. To do so, several techniques should be considered, including remote sensing methods (e.g., lidar measurements), direct sampling in volcanic ash clouds (e.g., soundings using optical particle counters), inversions of primary fallout and numerical simulations. The description of ash fingers in 3D could also be targetted, notably by using simultaneous observations from cameras at different locations, or through 3D simulations reproducing the sedimentation below volcanic ash clouds. Finally, the variability of ash fingers needs to be addressed, notably by studying volcanic ash clouds produced by other types of eruptions (e.g., stronger plumes) and under more atmospheric conditions. Facing this challenge would also require to characterise ash fingers as a function of distance from the vent.

More complete characterisation of ash fingers also requires new experimental investigations. First, additional processes affecting the formation and dynamics of

fingers need to be studied. In particular, it is evident from field observations that the occurrence of ash fingers is affected by the wind. Experiments on the sedimentation of particles below spreading particle-laden currents are necessary to improve our understanding of wind-induced effects on ash fingers. Second, experiments performed in this thesis involved homogeneous conditions (i.e., uniform concentrations in particle suspensions, monodisperse and narrow grainsizes, uniform ambient fluid, isothermal fluids). However, heterogeneities in natural volcanic ash clouds can have an effect on ash fingers. This can be investigated by using the simple experimental set-up presented in this thesis, but by varying initial conditions. For example, polydisperse particle suspensions with wider grainsize distributions can be studied to approach wide size ranges observed in natural volcanic ash clouds. Finally, alike field observations, experimental modelling needs to be complemented by numerical simulations in order to overcome limitations inherent to analogue models. This notably includes the study of ash fingers at the scale of volcanic ash clouds, for dynamical regimes similar to natural phenomena.

In this thesis, only the grainsize distribution and the morphology of particles were measured to analyse aeolian remobilisation. To advance the characterisation of aeolian remobilisation, future studies need to quantify more completely atmospheric conditions (e.g., wind friction velocities, surface temperature, air humidity) and deposit properties (e.g., surface moisture). For quantifying the surficial soil moisture, new techniques are needed, but atmospheric conditions can be measured using weather stations to calculate wind friction velocities. Another important aspect is to determine controls on the threshold friction velocity through laboratory and field measurements. For example, the threshold friction velocity can be measured directly in the field using portable wind tunnels to evaluate its variability as a function of atmospheric factors and deposit properties.

Bibliography

Adams, N., de Silva, S., Self, S., Salas, G., Schubring, S., Permenter, J., Arbesman, K., 2001. The physical volcanology of the 1600 eruption of Huaynaputina, southern Peru. Bulletin of Volcanology 62, 493–518. doi:10.1007/s004450000105.

Adrian, R.J., 2005. Twenty years of particle image velocimetry. Experiments in Fluids 39, 159–169. doi:10.1007/s00348-005-0991-7.

Aguilar, R., 2019. Exposure-based risk assessment of tephra- fall associated with long-lasting Vulcanian eruptions at Sabancaya volcano, Peru.

Alcalá-Reygosa, J., Palaciaos, D., Zamorano, J., Vázquez-Selem, L., 2011. Last Glacial Maximum and deglaciaton of Ampato volcanic complex, Southern Peru. Revista Cuaternario y Geomorfología 25, 121–136.

Alexander, D., 2013. Volcanic ash in the atmosphere and risks for civil aviation: A study in European crisis management. International Journal of Disaster Risk Science 4, 9–19. doi:10.1007/s13753-013-0003-0.

Andronico, D., Cannata, A., Di Grazia, G., Ferrari, F., 2021. The 1986–2021 paroxysmal episodes at the summit craters of Mt. Etna: Insights into volcano dynamics and hazard. Earth-Science Reviews 220, 103686. doi:10.1016/j.earscirev.2021.103686.

Andronico, D., Scollo, S., Cristaldi, A., 2015. Unexpected hazards from tephra fallouts at Mt Etna: The 23 November 2013 lava fountain. Journal of Volcanology and Geothermal Research 304, 118–125. doi:10.1016/j.jvolgeores.2015.08.007.

Ansmann, A., Tesche, M., Groß, S., Freudenthaler, V., Seifert, P., Hiebsch, A., Schmidt, J., Wandinger, U., Mattis, I., Müller, D., Wiegner, M., 2010. The 16 April 2010 major volcanic ash plume over central Europe: EARLINET lidar and AERONET photometer observations at Leipzig and Munich, Germany: EYJAFJOLL ASH PLUME OVER EUROPE. Geophysical Research Letters 37, n/a–n/a. doi:10.1029/2010GL043809.

Arnalds, O., 2013. The Influence of Volcanic Tephra (Ash) on Ecosystems, in: Advances in Agronomy. Elsevier. volume 121, pp. 331–380. doi:10.1016/B978-0-12-407685-3.00006-2.

Arnalds, O., Thorarinsdottir, E.F., Thorsson, J., Waldhauserova, P.D., Agustsdottir, A.M., 2013. An extreme wind erosion event of the fresh Eyjafjallajökull 2010 volcanic ash. Scientific Reports 3, 1257. doi:10.1038/srep01257.

Aubry, T.J., Engwell, S., Bonadonna, C., Carazzo, G., Scollo, S., Van Eaton, A.R., Taylor, I.A., Jessop, D., Eychenne, J., Gouhier, M., Mastin, L.G., Wallace, K.L., Biass, S., Bursik, M., Grainger, R.G., Jellinek, A.M., Schmidt, A., 2021. The Independent Volcanic Eruption Source Parameter Archive (IVESPA, version 1.0): A new observational database to support explosive eruptive column model validation and development. Journal of Volcanology and Geothermal Research 417, 107295. doi:10.1016/j.jvolgeores.2021.107295.

Auker, M.R., Sparks, R.S.J., Siebert, L., Crosweller, H.S., Ewert, J., 2013. A statistical analysis of the global historical volcanic fatalities record. Journal of Applied Volcanology 2, 2. doi:10.1186/2191-5040-2-2.

Bagheri, G., Bonadonna, C., 2016a. Aerodynamics of Volcanic Particles, in: Volcanic Ash. Elsevier, pp. 39–52. doi:10.1016/B978-0-08-100405-0.00005-7.

Bagheri, G., Bonadonna, C., 2016b. On the drag of freely falling non-spherical particles. Powder Technology 301, 526–544. doi:10.1016/j.powtec.2016.06.015.

Bagheri, G., Rossi, E., Biass, S., Bonadonna, C., 2016. Timing and nature of volcanic particle clusters based on field and numerical investigations. Journal of Volcanology and Geothermal Research 327, 520–530. doi:10.1016/j.jvolgeores.2016.09.009.

Bagnold, R., 1941. Bagnold, R. A.The physics of blown sand and desert dunes: New York. volume William Morrow & Company.

Balme, M., Greeley, R., 2006. Dust devils on Earth and Mars. Reviews of Geophysics 44, RG3003. doi:10.1029/2005RG000188.

Balsamo, G., Albergel, C., Beljaars, A., Boussetta, S., Brun, E., Cloke, H., Dee, D., Dutra, E., Muñoz-Sabater, J., Pappenberger, F., de Rosnay, P., Stockdale, T., Vitart, F., 2015. ERA-Interim/Land: a global land surface reanalysis data set. Hydrology and Earth System Sciences 19, 389–407. doi:10.5194/hess-19-389-2015.

Barclay, J., Few, R., Armijos, M.T., Phillips, J.C., Pyle, D.M., Hicks, A., Brown, S.K., Robertson, R.E.A., 2019. Livelihoods, Wellbeing and the Risk to Life During Volcanic Eruptions. Frontiers in Earth Science 7, 205. doi:10.3389/feart.2019.00205.

Barnard, J.M., 2021. On the dynamics of stratified particle-laden plumes. Journal of Fluid Mechanics 925, A33. doi:10.1017/jfm.2021.673.

Baxter, P.J., Horwell, C.J., 2015. Impacts of Eruptions on Human Health, in: The Encyclopedia of Volcanoes. Elsevier, pp. 1035–1047. doi:10.1016/B978-0-12-385938-9.00060-2.

Beckett, F., Rossi, E., Devenish, B., Witham, C., Bonadonna, C., 2022. Modelling the size distribution of aggregated volcanic ash and implications for operational

atmospheric dispersion modelling. Atmospheric Chemistry and Physics 22, 3409–3431. doi:10.5194/acp-22-3409-2022.

Bernard, B., 2013. Homemade ashmeter: a low-cost, high-efficiency solution to improve tephra field-data collection for contemporary explosive eruptions. Journal of Applied Volcanology 2, 1. doi:10.1186/2191-5040-2-1.

Biass, S., Bonadonna, C., Connor, L., Connor, C., 2016a. TephraProb: a Matlab package for probabilistic hazard assessments of tephra fallout. Journal of Applied Volcanology 5, 10. doi:10.1186/s13617-016-0050-5.

Biass, S., Bonadonna, C., Houghton, B.F., 2019. A step-by-step evaluation of empirical methods to quantify eruption source parameters from tephra-fall deposits. Journal of Applied Volcanology 8, 1. doi:10.1186/s13617-018-0081-1.

Biass, S., Falcone, J.L., Bonadonna, C., Di Traglia, F., Pistolesi, M., Rosi, M., Lestuzzi, P., 2016b. Great Balls of Fire: A probabilistic approach to quantify the hazard related to ballistics — A case study at La Fossa volcano, Vulcano Island, Italy. Journal of Volcanology and Geothermal Research 325, 1–14. doi:10.1016/j.jvolgeores.2016.06.006.

Blanchette, F., Bush, J.W.M., 2005. Particle concentration evolution and sedimentation-induced instabilities in a stably stratified environment. Physics of Fluids 17, 073302. doi:10.1063/1.1947987.

Blong, R., Enright, N., Grasso, P., 2017. Preservation of thin tephra. Journal of Applied Volcanology 6, 10. doi:10.1186/s13617-017-0059-4.

Blong, R.J., 1984. Volcanic Hazards. Elsevier. doi:10.1016/C2009-0-21853-8.

Bolós, X., Macias, J.L., Ocampo-Díaz, Y.Z.E., Tinoco, C., 2021. Implications of reworking processes on tephra distribution during volcanic eruptions: The case of Parícutin (1943–1952, western Mexico). Earth Surface Processes and Landforms , esp.5222doi:10.1002/esp.5222.

Bombrun, M., Jessop, D., Harris, A., Barra, V., 2018. An algorithm for the detection and characterisation of volcanic plumes using thermal camera imagery. Journal of Volcanology and Geothermal Research 352, 26–37. doi:10.1016/j.jvolgeores.2018.01.006.

Bonadonna, C., 2005a. Modeling tephra sedimentation from a Ruapehu weak plume eruption. Journal of Geophysical Research 110. doi:10.1029/2004JB003515.

Bonadonna, C., 2005b. Probabilistic modeling of tephra dispersal: Hazard assessment of a multiphase rhyolitic eruption at Tarawera, New Zealand. Journal of Geophysical Research 110, B03203. doi:10.1029/2003JB002896.

Bonadonna, C., Biass, S., Costa, A., 2015a. Physical characterization of explosive volcanic eruptions based on tephra deposits: Propagation of uncertainties and sensitivity analysis. Journal of Volcanology and Geothermal Research 296, 80–100. doi:10.1016/j.jvolgeores.2015.03.009.

Bonadonna, C., Biass, S., Menoni, S., Gregg, C.E., 2021. Assessment of risk associated with tephra-related hazards, in: Forecasting and Planning for Volcanic Hazards, Risks, and Disasters. Elsevier, pp. 329–378. doi:10.1016/B978-0-12-818082-2.00008-1.

Bonadonna, C., Costa, A., 2012. Estimating the volume of tephra deposits: A new simple strategy. Geology 40, 415–418. doi:10.1130/G32769.1.

Bonadonna, C., Costa, A., 2013. Plume height, volume, and classification of explosive volcanic eruptions based on the Weibull function. Bulletin of Volcanology 75. doi:10.1007/s00445-013-0742-1.

Bonadonna, C., Costa, A., Folch, A., Koyaguchi, T., 2015b. Tephra Dispersal and Sedimentation, in: The Encyclopedia of Volcanoes. Elsevier, pp. 587–597. doi:10.1016/B978-0-12-385938-9.00033-X.

Bonadonna, C., Ernst, G., Sparks, R., 1998. Thickness variations and volume estimates of tephra fall deposits: the importance of particle Reynolds number. Journal of Volcanology and Geothermal Research 81, 173–187. doi:10.1016/S0377-0273(98)00007-9.

Bonadonna, C., Folch, A., Loughlin, S., Puempel, H., 2012. Future developments in modelling and monitoring of volcanic ash clouds: outcomes from the first IAVCEI-WMO workshop on Ash Dispersal Forecast and Civil Aviation. Bulletin of Volcanology 74, 1–10. doi:10.1007/s00445-011-0508-6.

Bonadonna, C., Genco, R., Gouhier, M., Pistolesi, M., Cioni, R., Alfano, F., Hoskuldsson, A., Ripepe, M., 2011. Tephra sedimentation during the 2010 Eyjafjallajökull eruption (Iceland) from deposit, radar, and satellite observations. Journal of Geophysical Research 116. doi:10.1029/2011JB008462.

Bonadonna, C., Houghton, B.F., 2005. Total grain-size distribution and volume of tephra-fall deposits. Bulletin of Volcanology 67, 441–456. doi:10.1007/s00445-004-0386-2.

Bonadonna, C., Macedonio, G., Sparks, R.S.J., 2002a. Numerical modelling of tephra fallout associated with dome collapses and Vulcanian explosions: application to hazard assessment on Montserrat. Geological Society, London, Memoirs 21, 517–537. doi:10.1144/GSL.MEM.2002.021.01.23.

Bonadonna, C., Mayberry, G.C., Calder, E.S., Sparks, R.S.J., Choux, C., Jackson, P., Lejeune, A.M., Loughlin, S.C., Norton, G.E., Rose, W.I., Ryan, G., Young, S.R., 2002b. Tephra fallout in the eruption of Soufrière Hills Volcano, Montserrat. Geological Society, London, Memoirs 21, 483–516. doi:10.1144/GSL.MEM.2002.021.01.22.

Bonadonna, C., Phillips, J.C., 2003. Sedimentation from strong volcanic plumes. Journal of Geophysical Research: Solid Earth 108. doi:10.1029/2002JB002034.

Borg, A., Bolinder, J., Fuchs, L., 2001. Simultaneous velocity and concentration measurements in the near field of a turbulent low-pressure jet by digital particle image velocimetry–planar laser-induced fluorescence. Experiments in Fluids 31, 140–152. doi:10.1007/s003480000267.

Brown, R., Bonadonna, C., Durant, A., 2012. A review of volcanic ash aggregation. Physics and Chemistry of the Earth, Parts A/B/C 45-46, 65–78. doi:10.1016/j.pce.2011.11.001.

Brown, S.K., Jenkins, S.F., Sparks, R.S.J., Odbert, H., Auker, M.R., 2017. Volcanic fatalities database: analysis of volcanic threat with distance and victim classification. Journal of Applied Volcanology 6, 15. doi:10.1186/s13617-017-0067-4.

Buckland, H.M., Cashman, K.V., Engwell, S.L., Rust, A.C., 2020. Sources of uncertainty in the Mazama isopachs and the implications for interpreting distal tephra deposits from large magnitude eruptions. Bulletin of Volcanology 82, 23. doi:10.1007/s00445-020-1362-1.

Bulmer, M., Johnston, A., Engle, F., 1999. Analysis of Sabancaya Volcano, Southern Peru, using Radarsat and Lansat TM Data. Application Development and Research Opportunity (ADRO) .

Burgisser, A., Bergantz, G.W., 2002. Reconciling pyroclastic flow and surge: the multiphase physics of pyroclastic density currents. Earth and Planetary Science Letters 202, 405–418.

Burgisser, A., Bergantz, G.W., Breidenthal, R.E., 2005. Addressing complexity in laboratory experiments: the scaling of dilute multiphase flows in magmatic systems. Journal of Volcanology and Geothermal Research 141, 245–265. doi:10.1016/j.jvolgeores.2004.11.001.

Burns, P., Meiburg, E., 2012. Sediment-laden fresh water above salt water: linear stability analysis. Journal of Fluid Mechanics 691, 279–314. doi:10.1017/jfm.2011.474.

Burns, P., Meiburg, E., 2015. Sediment-laden fresh water above salt water: nonlinear simulations. Journal of Fluid Mechanics 762, 156–195. doi:10.1017/jfm.2014.645.

Bush, J.W.M., Thurber, B.A., Blanchette, F., 2003. Particle clouds in homogeneous and stratified environments. Journal of Fluid Mechanics 489, 29–54. doi:10.1017/S0022112003005160.

Carazzo, G., Jellinek, A., Turchyn, A., 2013. The remarkable longevity of submarine plumes: Implications for the hydrothermal input of iron to the deep-ocean. Earth and Planetary Science Letters 382, 66–76. doi:10.1016/j.epsl.2013.09.008.

Carazzo, G., Jellinek, A.M., 2012. A new view of the dynamics, stability and longevity of volcanic clouds. Earth and Planetary Science Letters 325-326, 39–51. doi:10.1016/j.epsl.2012.01.025.

Carazzo, G., Jellinek, A.M., 2013. Particle sedimentation and diffusive convection in volcanic ash-clouds. Journal of Geophysical Research: Solid Earth 118, 1420–1437. doi:10.1002/jgrb.50155.

Cardoso, S.S.S., Zarrebini, M., 2001. Convection driven by particle settling surrounding a turbulent plume. Chemical Engineering Science 56, 3365–3375. doi:10.1016/S0009-2509(01)00028-8.

Carey, S., 1997. Influence of convective sedimentation on the formation of widespread tephra fall layers in the deep sea. Geology 25, 839–842. doi:10.1130/0091-7613(1997)025<0839:IOCSOT>2.3.CO;2.

Carey, S., Sigurdsson, H., 1985. The May 18, 1980 eruption of Mount St. Helens: 2. Modeling of dynamics of the Plinian Phase. Journal of Geophysical Research 90, 2948. doi:10.1029/JB090iB04p02948.

Carey, S., Sparks, R.S.J., 1986. Quantitative models of the fallout and dispersal of tephra from volcanic eruption columns. Bulletin of Volcanology 48, 109–125. doi:10.1007/BF01046546.

Carey, S.N., Sigurdsson, H., 1982. Influence of particle aggregation on deposition of distal tephra from the MAy 18, 1980, eruption of Mount St. Helens volcano. Journal of Geophysical Research: Solid Earth 87, 7061–7072. doi:10.1029/JB087iB08p07061.

Cashman, K.V., Rust, A.C., 2020. Far-travelled ash in past and future eruptions: combining tephrochronology with volcanic studies. Journal of Quaternary Science 35, 11–22. doi:10.1002/jqs.3159.

Chen, C., 1997. Particle flux through sediment fingers. Deep Sea Research Part I: Oceanographic Research Papers 44, 1645–1654. doi:10.1016/S0967-0637(97)00042-3.

Chojnicki, K., Clarke, A., Phillips, J., Adrian, R., 2015. Rise dynamics of unsteady laboratory jets with implications for volcanic plumes. Earth and Planetary Science Letters 412, 186–196. doi:10.1016/j.epsl.2014.11.046.

Chou, Y.J., Shao, Y.C., 2016. Numerical study of particle-induced Rayleigh-Taylor instability: Effects of particle settling and entrainment. Physics of Fluids 28, 043302. doi:10.1063/1.4945652.

Clarke, A.B., Esposti Ongaro, T., Belousov, A., 2015. Vulcanian Eruptions, in: The Encyclopedia of Volcanoes. Elsevier, pp. 505–518. doi:10.1016/B978-0-12-385938-9.00028-6.

Cobeñas, G., Thouret, J.C., Bonadonna, C., Boivin, P., 2012. The c.2030yr BP Plinian eruption of El Misti volcano, Peru: Eruption dynamics and hazard implications. Journal of Volcanology and Geothermal Research 241-242, 105–120. doi:10.1016/j.jvolgeores.2012.06.006.

Cole, P.D., Fernandez, E., Duarte, E., Duncan, A.M., 2005. Explosive activity and generation mechanisms of pyroclastic flows at Arenal volcano, Costa Rica between 1987 and 2001. Bulletin of Volcanology 67, 695–716. doi:10.1007/s00445-004-0402-6.

Collins, B.D., Dunne, T., 1986. Erosion of tephra from the 1980 eruption of Mount St. Helens. GSA Bulletin 97, 896–905. doi:10.1130/0016-7606(1986)97<896:EOTFTE>2.0.CO;2.

Collins, B.D., Dunne, T., Lehre, A., 1983. Erosion of tephra-covered hillslopes north of Mount St. Helens, Washington: May 1980 - May 1981. Zeitschrift fur Geomorphologie Supplement , 103–121.

Coppola, D., Valade, S., Masias, P., Laiolo, M., Massimetti, F., Campus, A., Aguilar, R., Anccasi, R., Apaza, F., Ccallata, B., Cigolini, C., Cruz, L.F., Finizola, A., Gonzales, K., Macedo, O., Miranda, R., Ortega, M., Paxi, R., Taipe, E., Valdivia, D., 2022. Shallow magma convection evidenced by excess degassing and thermal radiation during the dome-forming Sabancaya eruption (2012–2020). Bulletin of Volcanology 84, 16. doi:10.1007/s00445-022-01523-1.

Corradini, S., Montopoli, M., Guerrieri, L., Ricci, M., Scollo, S., Merucci, L., Marzano, F., Pugnaghi, S., Prestifilippo, M., Ventress, L., Grainger, R., Carboni, E., Vulpiani, G., Coltelli, M., 2016. A Multi-Sensor Approach for Volcanic Ash Cloud Retrieval and Eruption Characterization: The 23 November 2013 Etna Lava Fountain. Remote Sensing 8, 58. doi:10.3390/rs8010058.

Costa, A., Caricchi, L., Bagdassarov, N., 2009. A model for the rheology of particle-bearing suspensions and partially molten rocks: RHEOLOGY OF PARTICLE-BEARING SUSPENSIONS. Geochemistry, Geophysics, Geosystems 10, n/a–n/a. doi:10.1029/2008GC002138.

Costa, A., Folch, A., Macedonio, G., 2010. A model for wet aggregation of ash particles in volcanic plumes and clouds: 1. Theoretical formulation. Journal of Geophysical Research 115, B09201. doi:10.1029/2009JB007175.

Crimaldi, J.P., 2008. Planar laser induced fluorescence in aqueous flows. Experiments in Fluids 44, 851–863. doi:10.1007/s00348-008-0496-2.

Crowe, C.T., Schwarzkopf, J.D., Sommerfeld, M., Tsuji, Y., 2011. Multiphase Flows with Droplets and Particles. 2nd edition ed., CRC Press. doi:https://doi.org/10.1201/b11103.

Cutler, N.A., Streeter, R.T., Marple, J., Shotter, L.R., Yeoh, J.S., Dugmore, A.J., 2018. Tephra transformations: variable preservation of tephra layers from two well-studied eruptions. Bulletin of Volcanology 80, 77. doi:10.1007/s00445-018-1251-z.

Dalziel, S.B., 1993. Rayleigh-Taylor instability: experiments with image analysis. Dynamics of Atmospheres and Oceans 20, 127–153. doi:10.1016/0377-0265(93)90051-8.

Davarpanah Jazi, S., Wells, M.G., 2016. Enhanced sedimentation beneath particle-laden flows in lakes and the ocean due to double-diffusive convection: Enhanced Sedimentation. Geophysical Research Letters 43, 10,883–10,890. doi:10.1002/2016GL069547.

Davarpanah Jazi, S., Wells, M.G., 2020. Dynamics of settling-driven convection beneath a sediment-laden buoyant overflow: Implications for the length-scale of deposition in lakes and the coastal ocean. Sedimentology 67, 699–720. doi:10.1111/sed.12660.

Davies Wykes, M., Dalziel, S., 2014. Efficient mixing in stratified flows: experimental study of a Rayleigh–Taylor unstable interface within an otherwise stable stratification. Journal of Fluid Mechanics 756, 1027–1057. doi:10.1017/jfm.2014.308.

Degruyter, W., Bonadonna, C., 2012. Improving on mass flow rate estimates of volcanic eruptions: MASS FLOW RATE VOLCANIC ERUPTIONS. Geophysical Research Letters 39, n/a–n/a. doi:10.1029/2012GL052566.

Del Bello, E., Taddeucci, J., Merrison, J., Rasmussen, K., Andronico, D., Ricci, T., Scarlato, P., Iversen, J., 2021. Field-based measurements of volcanic ash resuspension by wind. Earth and Planetary Science Letters 554, 116684. doi:10.1016/j.epsl.2020.116684.

Del Bello, E., Taddeucci, J., Merrison, J.P., Alois, S., Iversen, J.J., Scarlato, P., 2018. Experimental simulations of volcanic ash resuspension by wind under the effects of atmospheric humidity. Scientific Reports 8, 14509. doi:10.1038/s41598-018-32807-2.

Del Bello, E., Taddeucci, J., de' Michieli Vitturi, M., Scarlato, P., Andronico, D., Scollo, S., Kueppers, U., Ricci, T., 2017. Effect of particle volume fraction on the settling velocity of volcanic ash particles: insights from joint experimental and numerical simulations. Scientific Reports 7, 39620. doi:10.1038/srep39620.

Del Carpio Calienes, J.A., Rivera, M., Puma, N., Cruz, J., Torres, J.L., Vargas, K., Lazarte, I., Machaca, R., Concha, J., Scipión, D., Tavera, H., 2020. Evaluación geofísica del comportamiento dinámico actual del volcán Sabancaya, periodo 1 de diciembre de 2019-2 de febrero de 2020.

Dellino, P., Zimanowski, B., Büttner, R., La Volpe, L., Mele, D., Sulpizio, R., 2007. Large-scale experiments on the mechanics of pyroclastic flows: Design, engineering, and first results: EXPERIMENTS ON PYROCLASTIC FLOWS. Journal of Geophysical Research: Solid Earth 112. doi:10.1029/2006JB004313.

Dimonte, G., Youngs, D., Dimits, A., Weber, S., Marinak, M., Wunsch, S., Garasi, C., Robinson, A., Andrews, M., Ramaprabhu, P., et al., 2004. A comparative study of the turbulent rayleigh–taylor instability using high-resolution three-dimensional numerical simulations: the alpha-group collaboration. Physics of Fluids 16, 1668–1693.

Dominguez, L., Bonadonna, C., Forte, P., Jarvis, P.A., Cioni, R., Mingari, L., Bran, D., Panebianco, J.E., 2020a. Aeolian Remobilisation of the 2011-Cordón Caulle Tephra-Fallout Deposit: Example of an Important Process in the Life Cycle of Volcanic Ash. Frontiers in Earth Science 7, 343. doi:10.3389/feart.2019.00343.

Dominguez, L., Pioli, L., Bonadonna, C., Connor, C., Andronico, D., Harris, A., Ripepe, M., 2016. Quantifying unsteadiness and dynamics of pulsatory volcanic activity. Earth and Planetary Science Letters 444, 160–168. doi:10.1016/j.epsl.2016.03.048.

Dominguez, L., Rossi, E., Mingari, L., Bonadonna, C., Forte, P., Panebianco, J.E., Bran, D., 2020b. Mass flux decay timescales of volcanic particles due to aeolian processes in the Argentinian Patagonia steppe. Scientific Reports 10, 14456. doi:10.1038/s41598-020-71022-w.

Dossmann, Y., Bourget, B., Brouzet, C., Dauxois, T., Joubaud, S., Odier, P., 2016. Mixing by internal waves quantified using combined PIV/PLIF technique. Experiments in Fluids 57, 132. doi:10.1007/s00348-016-2212-y.

Druitt, T.H., Young, S.R., Baptie, B., Bonadonna, C., Calder, E.S., Clarke, A.B., Cole, P.D., Harford, C.L., Herd, R.A., Luckett, R., Ryan, G., Voight, B., 2002. Episodes of cyclic Vulcanian explosive activity yith fountain collapse at Soufrière Hills Volcano, Montserrat, in: The eruption of Soufrière Hills Volcano, Montserrat, from 1995 to 1999.. volume 21 of *Geological Society, London, Memoirs, eds Druitt T. H., Kokelaar B. P.*, pp. 281–306.

Dugmore, A., Streeter, R., Cutler, N., 2018. The role of vegetation cover and slope angle in tephra layer preservation and implications for Quaternary tephrostratigraphy. Palaeogeography, Palaeoclimatology, Palaeoecology 489, 105–116. doi:10.1016/j.palaeo.2017.10.002.

Dugmore, A.J., Thompson, P.I.J., Streeter, R.T., Cutler, N.A., Newton, A.J., Kirkbride, M.P., 2020. The interpretative value of transformed tephra sequences. Journal of Quaternary Science 35, 23–38. doi:10.1002/jqs.3174.

Durant, A., Brown, R., 2016. Ash Aggregation in Volcanic Clouds, in: Volcanic Ash. Elsevier, pp. 53–65. doi:10.1016/B978-0-08-100405-0.00006-9.

Durant, A.J., 2015. Toward a realistic formulation of fine-ash lifetime in volcanic clouds. Geology 43, 271–272. doi:10.1130/focus032015.1.

Durant, A.J., Rose, W.I., Sarna-Wojcicki, A.M., Carey, S., Volentik, A.C.M., 2009. Hydrometeor-enhanced tephra sedimentation: Constraints from the 18 May 1980 eruption of Mount St. Helens. Journal of Geophysical Research 114. doi:10.1029/2008JB005756.

Durant, A.J., Shaw, R.A., Rose, W.I., Mi, Y., Ernst, G.G.J., 2008. Ice nucleation and overseeding of ice in volcanic clouds. Journal of Geophysical Research 113. doi:10.1029/2007JD009064.

Edmonds, M., Grattan, J., Michnowicz, S., 2015. Volcanic Gases: Silent Killers, in: Fearnley, C.J., Bird, D.K., Haynes, K., McGuire, W.J., Jolly, G. (Eds.), Observing the Volcano World. Springer International Publishing, Cham, pp. 65–83. doi:10.1007/11157_2015_14. series Title: Advances in Volcanology.

Eliasson, J., 2020. New model for dispersion of volcanic ash and dust in the troposphere. International Journal of Geosciences 11, 544–561. doi:10.4236/ijg.2020.118029.

Eliasson, J., Watson, I., Weber, K., 2016. In Situ Observations of Airborne Ash From Manned Aircraft, in: Volcanic Ash. Elsevier, pp. 89–98. doi:10.1016/B978-0-08-100405-0.00009-4.

Eliasson, J., Yoshitani, J., Weber, K., Yasuda, N., Iguchi, M., Vogel, A., 2014. Airborne Measurement in the Ash Plume from Mount Sakurajima: Analysis of Gravitational Effects on Dispersion and Fallout. International Journal of Atmospheric Sciences 2014, 1–16. doi:10.1155/2014/372135.

Elissondo, M., Baumann, V., Bonadonna, C., Pistolesi, M., Cioni, R., Bertagnini, A., Biass, S., Herrero, J.C., Gonzalez, R., 2016. Chronology and impact of the 2011 Cordón Caulle eruption, Chile. Natural Hazards and Earth System Sciences 16, 675–704. doi:10.5194/nhess-16-675-2016.

Emanuel, K.A., 1981. A Similarity Theory for Unsaturated Downdrafts within Clouds. Journal of the Atmospheric Sciences 38, 1541–1557. doi:10.1175/1520-0469(1981)038<1541:ASTFUD>2.0.CO;2.

Engwell, S., Sparks, R., Aspinall, W., 2013. Quantifying uncertainties in the measurement of tephra fall thickness. Journal of Applied Volcanology 2, 5. doi:10.1186/2191-5040-2-5.

Escudier, M.P., Maxworthy, T., 1973. On the motion of turbulent thermals. Journal of Fluid Mechanics 61, 541–552. doi:10.1017/S0022112073000856.

Etyemezian, V., Gillies, J.A., Mastin, L.G., Crawford, A., Hasson, R., Van Eaton, A.R., Nikolich, G., 2019. Laboratory Experiments of Volcanic Ash Resuspension by Wind. Journal of Geophysical Research: Atmospheres 124, 9534–9560. doi:10.1029/2018JD030076.

Eychenne, J., Le Pennec, J.L., Ramón, P., Yepes, H., 2013. Dynamics of explosive paroxysms at open-vent andesitic systems: High-resolution mass distribution analyses of the 2006 Tungurahua fall deposit (Ecuador). Earth and Planetary Science Letters 361, 343–355. doi:10.1016/j.epsl.2012.11.002.

Eychenne, J., Rust, A.C., Cashman, K.V., Wobrock, W., 2017. Distal Enhanced Sedimentation From Volcanic Plumes: Insights From the Secondary Mass Maxima in the 1992 Mount Spurr Fallout Deposits: Mount Spurr's ASMMs. Journal of Geophysical Research: Solid Earth 122, 7679–7697. doi:10.1002/2017JB014412.

Farenzena, B.A., Silvestrini, J.H., 2017. Linear stability analysis of particle-laden hypopycnal plumes. Physics of Fluids 29, 124102. doi:10.1063/1.4999343.

Fierstein, J., Nathenson, M., 1992. Another look at the calculation of fallout tephra volumes. Bulletin of Volcanology 54, 156–167. doi:10.1007/BF00278005.

Fiske, R.S., Cashman, K.V., Shibata, A., Watanabe, K., 1998. Tephra dispersal from Myojinsho, Japan, during its shallow submarine eruption of 1952-1953. Bulletin of Volcanology 59, 262–275. doi:10.1007/s004450050190.

Folch, A., 2012. A review of tephra transport and dispersal models: Evolution, current status, and future perspectives. Journal of Volcanology and Geothermal Research 235-236, 96–115. doi:10.1016/j.jvolgeores.2012.05.020.

Folch, A., Costa, A., Macedonio, G., 2016. FPLUME-1.0: An integral volcanic plume model accounting for ash aggregation. Geoscientific Model Development 9, 431–450. doi:10.5194/gmd-9-431-2016.

Folch, A., Mingari, L., Gutierrez, N., Hanzich, M., Macedonio, G., Costa, A., 2020. FALL3D-8.0: a computational model for atmospheric transport and deposition of particles, aerosols and radionuclides – Part 1: Model physics and numerics. Geoscientific Model Development 13, 1431–1458. doi:10.5194/gmd-13-1431-2020.

Folch, A., Mingari, L., Osores, M.S., Collini, E., 2014. Modeling volcanic ash resuspension – application to the 14–18 October 2011 outbreak episode in central Patagonia, Argentina. Natural Hazards and Earth System Sciences 14, 119–133. doi:10.5194/nhess-14-119-2014.

Fontijn, K., Lachowycz, S.M., Rawson, H., Pyle, D.M., Mather, T.A., Naranjo, J.A., Moreno-Roa, H., 2014. Late Quaternary tephrostratigraphy of southern Chile and Argentina. Quaternary Science Reviews 89, 70–84. doi:10.1016/j.quascirev.2014.02.007.

Forbes, L., Jarvis, D., Potts, J., Baxter, P.J., 2003. Volcanic ash and respiratory symptoms in children on the island of Montserrat, British West Indies. Occupational and Environmental Medicine 60, 207–211. doi:10.1136/oem.60.3.207.

Forte, P., Domínguez, L., Bonadonna, C., Gregg, C.E., Bran, D., Bird, D., Castro, J.M., 2018. Ash resuspension related to the 2011–2012 Cordón Caulle eruption, Chile, in a rural community of Patagonia, Argentina. Journal of Volcanology and Geothermal Research 350, 18–32. doi:10.1016/j.jvolgeores.2017.11.021.

Freret-Lorgeril, V., Bonadonna, C., Rossi, E., Poulidis, A.P., Iguchi, M., 2022. New insights into real-time detection of tephra grainsize, settling velocity and sedimentation rate. Scientific Reports 12, 4650. doi:10.1038/s41598-022-08711-1.

Freret-Lorgeril, V., Donnadieu, F., Eychenne, J., Soriaux, C., Latchimy, T., 2019. In situ terminal settling velocity measurements at Stromboli volcano: Input from physical characterization of ash. Journal of Volcanology and Geothermal Research 374, 62–79. doi:10.1016/j.jvolgeores.2019.02.005.

Freret-Lorgeril, V., Gilchrist, J., Donnadieu, F., Jellinek, A., Delanoë, J., Latchimy, T., Vinson, J., Caudoux, C., Peyrin, F., Hervier, C., Valade, S., 2020. Ash sedimentation by fingering and sediment thermals from wind-affected volcanic plumes. Earth and Planetary Science Letters 534, 116072. doi:10.1016/j.epsl.2020.116072.

Fries, A., Lemus, J., Jarvis, P.A., Clarke, A.B., Phillips, J.C., Manzella, I., Bonadonna, C., 2021. The Influence of Particle Concentration on the Formation of Settling-Driven Gravitational Instabilities at the Base of Volcanic Clouds. Frontiers in Earth Science 9, 640090. doi:10.3389/feart.2021.640090.

Fu, G., Lin, H., Heemink, A., Segers, A., Lu, S., Palsson, T., 2015. Assimilating aircraft-based measurements to improve forecast accuracy of volcanic ash transport. Atmospheric Environment 115, 170–184. doi:10.1016/j.atmosenv.2015.05.061.

Ganser, G.H., 1993. A rational approach to drag prediction of spherical and nonspherical particles. Powder Technology 77, 143–152. doi:10.1016/0032-5910(93)80051-B.

Gerbe, M.C., Thouret, J.C., 2004. Role of magma mixing in the petrogenesis of tephra erupted during the 1990–98 explosive activity of Nevado Sabancaya, southern Peru. Bulletin of Volcanology 66, 541–561. doi:10.1007/s00445-004-0340-3.

Gilchrist, J.T., Jellinek, A.M., 2021. Sediment waves and the gravitational stability of volcanic jets. Bulletin of Volcanology 83, 64. doi:10.1007/s00445-021-01472-1.

Giordano, D., Russell, J.K., Dingwell, D.B., 2008. Viscosity of magmatic liquids: A model. Earth and Planetary Science Letters 271, 123–134. doi:10.1016/j.epsl.2008.03.038.

Gonnermann, H.M., 2015. Magma Fragmentation. Annual Review of Earth and Planetary Sciences 43, 431–458. doi:10.1146/annurev-earth-060614-105206.

Gouhier, M., Eychenne, J., Azzaoui, N., Guillin, A., Deslandes, M., Poret, M., Costa, A., Husson, P., 2019. Low efficiency of large volcanic eruptions in transporting very fine ash into the atmosphere. Scientific Reports 9, 1449. doi:10.1038/s41598-019-38595-7.

Grant, I., 1997. Particle image velocimetry: A review. Proceedings of the Institution of Mechanical Engineers, Part C: Journal of Mechanical Engineering Science 211, 55–76. doi:10.1243/0954406971521665.

Green, T., 1987. The importance of double diffusion to the settling of suspended material. Sedimentology 34, 319–331. doi:10.1111/j.1365-3091.1987.tb00780.x.

Gudmundsson, G., 2011. Respiratory health effects of volcanic ash with special reference to Iceland. A review. The Clinical Respiratory Journal 5, 2–9. doi:10.1111/j.1752-699X.2010.00231.x.

Guffanti, M., Mayberry, G.C., Casadevall, T.J., Wunderman, R., 2009. Volcanic hazards to airports. Natural Hazards 51, 287–302. doi:10.1007/s11069-008-9254-2.

Guffanti, M., Tupper, A., 2015. Volcanic Ash Hazards and Aviation Risk, in: Volcanic Hazards, Risks and Disasters. Elsevier, pp. 87–108. doi:10.1016/B978-0-12-396453-3.00004-6.

Harlow, F.H., Amsden, A.A., 1975. Numerical calculation of multiphase fluid flow. Journal of Computational Physics 17, 19–52. doi:https://doi.org/10.1016/0021-9991(75)90061-3.

Harpel, C.J., Kleier, C., Aguilar, R., 2021. Azorella compacta's long-term growth rate, longevity, and potential for dating geomorphological and archaeological features in the arid southern Peruvian Andes. Journal of Arid Environments 188, 104470. doi:10.1016/j.jaridenv.2021.104470.

Harris, A.J., 2015. Basaltic Lava Flow Hazard, in: Volcanic Hazards, Risks and Disasters. Elsevier, pp. 17–46. doi:10.1016/B978-0-12-396453-3.00002-2.

Harris, D.M., Rose, W.I., 1983. Estimating particle sizes, concentrations, and total mass of ash in volcanic clouds using weather radar. Journal of Geophysical Research 88, 10969. doi:10.1029/JC088iC15p10969.

Harris, D.M., Rose, W.I., Roe, R., Thompson, M.R., 1981. Radar observations of ash eruptions, in: The 1980 Eruptions of Mount St. Helens, Washington. Geological Survey Professional Paper.

Hassan, N.H., Zawawi, M.H., Mustafa Al Bakri, A.M., Rozainy, Z.M.R., Kamaruddin, M.A., M Nasir, W.N.Y.W., Mazlan, M.A.N., Irfan, A.R., 2020. A Review on Applications of Particle Image Velocimetry. IOP Conference Series: Materials Science and Engineering 864, 012149. doi:10.1088/1757-899X/864/1/012149.

He, X., Zhang, R., Chen, S., Doolen, G.D., 1999. On the three-dimensional Rayleigh–Taylor instability. Physics of Fluids 11, 1143–1152. doi:10.1063/1.869984.

Henniger, R., Kleiser, L., 2012. Temporal evolution, morphology, and settling of the sediment plume in a model estuary. Physics of Fluids 24, 086601. doi:10.1063/1.4739537.

Hersbach, H., Bell, B., Berrisford, P., Hirahara, S., Horányi, A., Muñoz-Sabater, J., Nicolas, J., Peubey, C., Radu, R., Schepers, D., Simmons, A., Soci, C., Abdalla, S., Abellan, X., Balsamo, G., Bechtold, P., Biavati, G., Bidlot, J., Bonavita, M., Chiara, G., Dahlgren, P., Dee, D., Diamantakis, M., Dragani, R., Flemming, J., Forbes, R., Fuentes, M., Geer, A., Haimberger, L., Healy, S., Hogan, R.J., Hólm, E., Janisková, M., Keeley, S., Laloyaux, P., Lopez, P., Lupu, C., Radnoti, G., Rosnay, P., Rozum, I., Vamborg, F., Villaume, S., Thépaut, J., 2020. The ERA5 global reanalysis. Quarterly Journal of the Royal Meteorological Society 146, 1999–2049. doi:10.1002/qj.3803.

Hobbs, P.V., Radke, L.F., Lyons, J.H., Ferek, R.J., Coffman, D.J., Casadevall, T.J., 1991. Airborne measurements of particle and gas emissions from the 1990 volcanic eruptions of Mount Redoubt. Journal of Geophysical Research 96, 18735. doi:10.1029/91JD01635.

Horwell, C.J., Baxter, P.J., 2006. The respiratory health hazards of volcanic ash: a review for volcanic risk mitigation. Bulletin of Volcanology 69, 1–24. doi:10.1007/s00445-006-0052-y.

Houghton, B., Carey, R.J., 2015. Pyroclastic Fall Deposits, in: The Encyclopedia of Volcanoes. Elsevier, pp. 599–616. doi:10.1016/B978-0-12-385938-9.00034-1.

Houze, R.A., Schmid, W., Fovell, R.G., Schiesser, H.H., 1993. Hailstorms in Switzerland: Left Movers, Right Movers, and False Hooks. Monthly Weather Review 121, 3345–3370. doi:10.1175/1520-0493(1993)121<3345:HISLMR>2.0.CO;2.

Hoyal, D.C., Bursik, M.I., Atkinson, J.F., 1999a. The influence of diffusive convection on sedimentation from buoyant plumes. Marine Geology 159, 205–220. doi:10.1016/S0025-3227(99)00005-5.

Hoyal, D.C.J.D., Bursik, M.I., Atkinson, J.F., 1999b. Settling-driven convection: A mechanism of sedimentation from stratified fluids. Journal of Geophysical Research: Oceans 104, 7953–7966. doi:10.1029/1998JC900065.

Hu, H., Saga, T., Kobayashi, T., Taniguchi, N., 2002. Simultaneous Velocity and Concentration Measurements of a Turbulent Jet Mixing Flow. Annals of the New York Academy of Sciences 972, 254–259. doi:10.1111/j.1749-6632.2002.tb04581.x.

Hurst, T., Davis, C., 2017. Forecasting volcanic ash deposition using HYSPLIT. Journal of Applied Volcanology 6, 5. doi:10.1186/s13617-017-0056-7.

Iguchi, M., Nakamichi, H., Tameguri, T., Sakurajima Volcano Research Center, Disaster Prevention Research Institute, Kyoto University 1722-19 Sakurajima-Yokoyama, Kagoshima, Kagoshima 891-1419, Japan, 2020. Integrated Study on Forecasting Volcanic Hazards of Sakurajima Volcano, Japan. Journal of Disaster Research 15, 174–186. doi:10.20965/jdr.2020.p0174.

Iguchi, M., Tameguri, T., Otha, Y., Ueki, S., Nakao, S., 2013. Characteristics of Volcanic Activity at Sakurajima Volcano's Showa Crater During the Period 2006 to 2011.

Inman, D.L., 1952. Measures for Describing the Size Distribution of Sediments. SEPM Journal of Sedimentary Research Vol. 22. doi:10.1306/D42694DB-2B26-11D7-8648000102C1865D.

Jacobs, C.T., Collins, G.S., Piggott, M.D., Kramer, S.C., Wilson, C.R.G., 2013. Multiphase flow modelling of volcanic ash particle settling in water using adaptive unstructured meshes. Geophysical Journal International 192, 647–665. doi:10.1093/gji/ggs059.

Jacobs, C.T., Goldin, T.J., Collins, G.S., Piggott, M.D., Kramer, S.C., Melosh, H.J., Wilson, C.R., Allison, P.A., 2015. An improved quantitative measure of the tendency for volcanic ash plumes to form in water: implications for the deposition of marine ash beds. Journal of Volcanology and Geothermal Research 290, 114–124. doi:10.1016/j.jvolgeores.2014.10.015.

Jarvis, P.A., Bonadonna, C., Dominguez, L., Forte, P., Frischknecht, C., Bran, D., Aguilar, R., Beckett, F., Elissondo, M., Gillies, J., Kueppers, U., Merrison, J., Varley, N., Wallace, K.L., 2020. Aeolian Remobilisation of Volcanic Ash: Outcomes of a Workshop in the Argentinian Patagonia. Frontiers in Earth Science 8. doi:10.3389/feart.2020.575184.

Jarvis, P.A., Fries, A., Lemus, J., Bonadonna, C., Clarke, A.B., Manzella, I., Phillips, J.C., . Kelvin-Helmholtz instabilities and mixing in surface-propagating gravity currents .

Jay, J.A., Delgado, F.J., Torres, J.L., Pritchard, M.E., Macedo, O., Aguilar, V., 2015. Deformation and seismicity near Sabancaya volcano, southern Peru, from 2002 to 2015: Deformation and seismicity at Sabancaya. Geophysical Research Letters 42, 2780–2788. doi:10.1002/2015GL063589.

Jenkins, S.F., Wilson, T.M., Magill, C., Miller, V., Stewart, C., Blong, R., Marzocchi, W., Boulton, M., Bonadonna, C., Costa, A., 2015. Volcanic ash fall hazard and risk, in: Loughlin, S.C., Sparks, S., Brown, S.K., Jenkins, S.F., Vye-Brown, C. (Eds.), Global volcanic hazards and risk. Cambridge Univ. Press, Cambridge, pp. 173–222.

Juvigné, E., Thouret, J., Loutsch, I., Lamadon, S., Frechen, M., Fontugne, M., Rivera, M., Dávila, J., Mariño, J., 2008. Retombées volcaniques dans des tourbières et lacs autour du massif des Nevados Ampato et Sabancaya (Pérou méridional, Andes Centrales). Quaternaire , 157–173doi:10.4000/quaternaire.3362.

Juvigné, E., Thouret, J.C., Gilot, E., Leclercq, L., Gourgaud, A., 1998. L'activité du volcan Nevado Sabancaya (Pérou) au cours de l'Holocène [Activity of Nevado Sabancaya volcano (Peru) throughout the Holocene]. Quaternaire 9, 45–51. doi:10.3406/quate.1998.2105.

Kanak, K.M., Straka, J.M., Schultz, D.M., 2008. Numerical Simulation of Mammatus. Journal of the Atmospheric Sciences 65, 1606–1621. doi:10.1175/2007JAS2469.1.

Kavanagh, J.L., Engwell, S.L., Martin, S.A., 2018. A review of laboratory and numerical modelling in volcanology. Solid Earth 9, 531–571. doi:10.5194/se-9-531-2018.

Keane, R.D., Adrian, R.J., 1992. Theory of cross-correlation analysis of PIV images. Applied Scientific Research 49, 191–215. doi:10.1007/BF00384623.

Kern, C., Masias, P., Apaza, F., Reath, K.A., Platt, U., 2017. Remote measurement of high preeruptive water vapor emissions at Sabancaya volcano by

passive differential optical absorption spectroscopy: Water Vapor DOAS at Sabancaya. Journal of Geophysical Research: Solid Earth 122, 3540–3564. doi:10.1002/2017JB014020.

Klawonn, M., Houghton, B.F., Swanson, D.A., Fagents, S.A., Wessel, P., Wolfe, C.J., 2014a. Constraining explosive volcanism: subjective choices during estimates of eruption magnitude. Bulletin of Volcanology 76, 793. doi:10.1007/s00445-013-0793-3.

Klawonn, M., Houghton, B.F., Swanson, D.A., Fagents, S.A., Wessel, P., Wolfe, C.J., 2014b. From field data to volumes: constraining uncertainties in pyroclastic eruption parameters. Bulletin of Volcanology 76, 839. doi:10.1007/s00445-014-0839-1.

Kok, J.F., Parteli, E.J.R., Michaels, T.I., Karam, D.B., 2012. The physics of wind-blown sand and dust. Reports on Progress in Physics 75, 106901. doi:10.1088/0034-4885/75/10/106901.

Konopliv, N., Lesshafft, L., Meiburg, E., 2018. The influence of shear on double-diffusive and settling-driven instabilities. Journal of Fluid Mechanics 849, 902–926. doi:10.1017/jfm.2018.432.

Koochesfahani, M.M., 1984. Experiments on turbulent mixing and chemical reactions in a liquid mixing layer. phd. California Institute of Technology. doi:10.7907/Y7BR-C556.

Koyaguchi, T., Suzuki, Y., 2013. 3D Numerical Simulations of Eruption Cloud Dynamics and Tephra Dispersal. Annual Report of the Earth Simulator Center April 2014.

Kull, H., 1991. Theory of the Rayleigh-Taylor instability. Physics Reports 206, 197–325. doi:10.1016/0370-1573(91)90153-D.

Lawrie, A.G.W., Dalziel, S.B., 2011. Rayleigh–Taylor mixing in an otherwise stable stratification. Journal of Fluid Mechanics 688, 507–527. doi:10.1017/jfm.2011.398.

Leadbetter, S.J., Hort, M.C., von Löwis, S., Weber, K., Witham, C.S., 2012. Modeling the resuspension of ash deposited during the eruption of Eyjafjallajökull in spring 2010: MODELING RESUSPENDED VOLCANIC ASH. Journal of Geophysical Research: Atmospheres 117. doi:10.1029/2011JD016802.

Lechner, P., Tupper, A., Guffanti, M., Loughlin, S., Casadevall, T., 2017. Volcanic Ash and Aviation—The Challenges of Real-Time, Global Communication of a Natural Hazard, in: Fearnley, C.J., Bird, D.K., Haynes, K., McGuire, W.J., Jolly, G. (Eds.), Observing the Volcano World. Springer International Publishing, Cham, pp. 51–64. doi:10.1007/11157_2016_49.

Lee, S., Jang, Y., Choi, C., Lee, T., 1992. Combined effect of sedimentation velocity fluctuation and self-sharpening on interface broadening. Physics of Fluids A: Fluid Dynamics 4, 2601–2606. doi:10.1063/1.858449.

Lemus, J., Fries, A., Jarvis, P., Bonadonna, C., Chopard, B., Latt, J., . Numerical investigation on the effect of shear on settling-driven gravitational instabilities at the base of volcanic ash clouds .

Lemus, J., Fries, A., Jarvis, P.A., Bonadonna, C., Chopard, B., Latt, J., 2021. Modelling Settling-Driven Gravitational Instabilities at the Base of Volcanic Clouds Using the Lattice Boltzmann Method. arXiv:2106.07694 [physics] ArXiv: 2106.07694.

Linden, P.F., Redondo, J.M., 1991. Molecular mixing in Rayleigh–Taylor instability. Part I: Global mixing. Physics of Fluids A: Fluid Dynamics 3, 1269–1277. doi:10.1063/1.858055.

Lindsay, J.M., Robertson, R.E.A., 2018. Integrating Volcanic Hazard Data in a Systematic Approach to Develop Volcanic Hazard Maps in the Lesser Antilles. Frontiers in Earth Science 6, 42. doi:10.3389/feart.2018.00042.

Liu, E., Cashman, K., Rust, A., 2015. Optimising shape analysis to quantify volcanic ash morphology. GeoResJ 8, 14–30. doi:10.1016/j.grj.2015.09.001.

Londono, J.M., Galvis, B., 2018. Seismic Data, Photographic Images and Physical Modeling of Volcanic Plumes as a Tool for Monitoring the Activity of Nevado del Ruiz Volcano, Colombia. Frontiers in Earth Science 6, 162. doi:10.3389/feart.2018.00162.

Lube, G., Breard, E.C.P., Cronin, S.J., Jones, J., 2015. Synthesizing large-scale pyroclastic flows: Experimental design, scaling, and first results from PELE: Large-scale PDC experiments. Journal of Geophysical Research: Solid Earth 120, 1487–1502. doi:10.1002/2014JB011666.

Machacca Puma, R., Del Carpio Calienes, J.A., Rivera Porras, M.A., Tavera Huarache, H.J., Macedo Franco, L.D., Concha Calle, J.A., Lazarte Zerpa, I.A., Centeno Quico, R.G., Puma Sacsi, N.C., Torres Aguilar, J.L., Vargas Alva, K.A., Cruz Igme, J.E., Velarde Quispe, L., Vilca Nina, J., Malpartida Garay, A.R., 2021. Monitoring of active volcanoes in Peru by the Instituto Geofísico del Perú. Volcanica 4, 49–71. doi:10.30909/vol.04.S1.4971.

MacQueen, P., Delgado, F., Reath, K., Pritchard, M.E., Bagnardi, M., Milillo, P., Lundgren, P., Macedo, O., Aguilar, V., Ortega, M., Anccasi, R., Lazarte Zerpa, I.A., Miranda, R., 2020. Volcano-Tectonic Interactions at Sabancaya Volcano, Peru: Eruptions, Magmatic Inflation, Moderate Earthquakes, and Fault Creep. Journal of Geophysical Research: Solid Earth 125. doi:10.1029/2019JB019281.

Manrique, N., Lazarte, I., Cueva, K., Rivera, M., Aguilar, R., 2018. Actividad del volcán Sabancaya (Perú) 2016-2017: Características de las emisiones de ceniza y análisis granulométrico.

Manville, V., Hodgson, K.A., Houghton, B.F., Keys, J.R.H., White, J.D.L., 2000. Tephra, snow and water: complex sedimentary responses at an active snow-capped stratovolcano, Ruapehu, New Zealand. Bulletin of Volcanology 62, 278–293. doi:10.1007/s004450000096.

Manville, V., Wilson, C., 2004. Vertical density currents: a review of their potential role in the deposition and interpretation of deep-sea ash layers. Journal of the Geological Society 161, 947–958. doi:10.1144/0016-764903-067.

Manzella, I., Bonadonna, C., Phillips, J.C., Monnard, H., 2015. The role of gravitational instabilities in deposition of volcanic ash. Geology 43, 211–214. doi:10.1130/G36252.1.

Marsh, B.D., 1988. Crystal capture, sorting, and retention in convecting magma. GSA Bulletin 100, 1720–1737. doi:10.1130/0016-7606(1988)100<1720:CCSARI>2.3.CO;2.

Martin, D., Nokes, R., 1989. A Fluid-Dynamical Study of Crystal Settling in Convecting Magmas. Journal of Petrology 30, 1471–1500. doi:10.1093/petrology/30.6.1471.

Martin, J., Rakotomalala, N., Salin, D., 1994. Hydrodynamic dispersion broadening of a sedimentation front. Physics of Fluids 6, 3215–3217. doi:10.1063/1.868051.

Marzano, F., Barbieri, S., Vulpiani, G., Rose, W., 2006. Volcanic Ash Cloud Retrieval by Ground-Based Microwave Weather Radar. IEEE Transactions on Geoscience and Remote Sensing 44, 3235–3246. doi:10.1109/TGRS.2006.879116.

Massaro, S., Rossi, E., Sandri, L., Bonadonna, C., Selva, J., Moretti, R., Komorowski, J.C., 2022. Assessing hazard and potential impact associated with volcanic ballistic projectiles: The example of La Soufrière de Guadeloupe volcano (Lesser Antilles). Journal of Volcanology and Geothermal Research 423, 107453. doi:10.1016/j.jvolgeores.2021.107453.

Maxworthy, T., 1999. The dynamics of sedimenting surface gravity currents. Journal of Fluid Mechanics 392, 27–44. doi:10.1017/S002211209900556X.

Mazzocchi, M., Hansstein, F., Ragona, M., 2010. The 2010 volcanic ash cloud and its financial impact on the European airline industry, in: CESifo Forum, München: ifo Institut für Wirtschaftsforschung an der Universität München. pp. 92–100. Issue: 2.

Mele, D., Dellino, P., Sulpizio, R., Braia, G., 2011. A systematic investigation on the aerodynamics of ash particles. Journal of Volcanology and Geothermal Research 203, 1–11. doi:10.1016/j.jvolgeores.2011.04.004.

Galán de Mera, A., Linares Perea, E., 2012. La vegetación de la región Arequipa, Perú. Impreso en el Taller Librería Junior, Arequipa, Perú. OCLC: 824610716.

Mereu, L., Scollo, S., Mori, S., Boselli, A., Leto, G., Marzano, F.S., 2018. Maximum-Likelihood Retrieval of Volcanic Ash Concentration and Particle Size From Ground-Based Scanning Lidar. IEEE Transactions on Geoscience and Remote Sensing 56, 5824–5842. doi:10.1109/TGRS.2018.2826839.

Mingari, L., Folch, A., Dominguez, L., Bonadonna, C., 2020. Volcanic Ash Resuspension in Patagonia: Numerical Simulations and Observations. Atmosphere 11, 977. doi:10.3390/atmos11090977.

Morton, B., Sir Geoffrey Taylor, F., Turner, J., 1956. Turbulent gravitational convection from maintained and instantaneous sources. Proceedings of the Royal Society of London vol. 234.

Mueller, W., Cowie, H., Horwell, C.J., Hurley, F., Baxter, P.J., 2020. Health Impact Assessment of Volcanic Ash Inhalation: A Comparison With Outdoor Air Pollution Methods. GeoHealth 4. doi:10.1029/2020GH000256.

Naismith, A.K., Matthew Watson, I., Escobar-Wolf, R., Chigna, G., Thomas, H., Coppola, D., Chun, C., 2019. Eruption frequency patterns through time for the current (1999–2018) activity cycle at Volcán de Fuego derived from remote sensing data: Evidence for an accelerating cycle of explosive paroxysms and potential implications of eruptive activity. Journal of Volcanology and Geothermal Research 371, 206–219. doi:10.1016/j.jvolgeores.2019.01.001.

Newhall, C.G., Self, S., 1982. The volcanic explosivity index (VEI) an estimate of explosive magnitude for historical volcanism. Journal of Geophysical Research 87, 1231. doi:10.1029/JC087iC02p01231.

Nicholas, A., Walling, D., 1996. The significance of particle aggregation in the overbank deposition of suspended sediment on river floodplains. Journal of Hydrology 186, 275–293. doi:10.1016/S0022-1694(96)03023-5.

Oishi, M., Nishiki, K., Geshi, N., Furukawa, R., Ishizuka, Y., Oikawa, T., Yamamoto, T., Nanayama, F., Tanaka, A., Hirota, A., Miwa, T., Miyabuchi, Y., 2018. Distribution and mass of tephra-fall deposits from volcanic eruptions of Sakurajima Volcano based on posteruption surveys. Bulletin of Volcanology 80, 42. doi:10.1007/s00445-018-1215-3.

Panebianco, J.E., Mendez, M.J., Buschiazzo, D.E., Bran, D., Gaitán, J.J., 2017. Dynamics of volcanic ash remobilisation by wind through the Patagonian steppe after the eruption of Cordón Caulle, 2011. Scientific Reports 7, 45529. doi:10.1038/srep45529.

Parsons, J.D., Bush, J.W.M., Syvitski, J.P.M., 2001. Hyperpycnal plume formation from riverine outflows with small sediment concentrations. Sedimentology 48, 465–478. doi:10.1046/j.1365-3091.2001.00384.x.

Peñas, P., Enríquez, O.R., Rodríguez-Rodríguez, J., 2021. Bubble-laden thermals in supersaturated water. Journal of Fluid Mechanics 924, A31. doi:10.1017/jfm.2021.655.

Pistolesi, M., Cioni, R., Bonadonna, C., Elissondo, M., Baumann, V., Bertagnini, A., Chiari, L., Gonzales, R., Rosi, M., Francalanci, L., 2015. Complex dynamics of small-moderate volcanic events: the example of the 2011 rhyolitic Cordón Caulle eruption, Chile. Bulletin of Volcanology 77. doi:10.1007/s00445-014-0898-3.

Pollastri, S., Rossi, E., Bonadonna, C., Merrison, J.P., 2021. Modelling the Effect of Electrification on Volcanic Ash Aggregation. Frontiers in Earth Science 8, 574106. doi:10.3389/feart.2020.574106.

Poret, M., Corradini, S., Merucci, L., Costa, A., Andronico, D., Montopoli, M., Vulpiani, G., Freret-Lorgeril, V., 2018. Reconstructing volcanic plume evolution integrating satellite and ground-based data: application to the 23 November 2013 Etna eruption. Atmospheric Chemistry and Physics 18, 4695–4714. doi:10.5194/acp-18-4695-2018.

Poulidis, A.P., Biass, S., Bagheri, G., Takemi, T., Iguchi, M., 2021. Atmospheric vertical velocity - a crucial component in understanding proximal deposition of volcanic ash. Earth and Planetary Science Letters 566, 116980. doi:10.1016/j.epsl.2021.116980.

Poulidis, A.P., Phillips, J.C., Renfrew, I.A., Barclay, J., Hogg, A., Jenkins, S.F., Robertson, R., Pyle, D.M., 2018. Meteorological Controls on Local and Regional Volcanic Ash Dispersal. Scientific Reports 8, 6873. doi:10.1038/s41598-018-24651-1.

Poulidis, A.P., Takemi, T., Iguchi, M., Disaster Prevention Research Institute (DPRI), Kyoto University Gokasho, Uji, Kyoto 611-0011, Japan, Sakurajima Volcano Research Center, Disaster Prevention Research Institute (DPRI), Kyoto University, Kagoshima, Japan, 2019. Experimental High-Resolution Forecasting of Volcanic Ash Hazard at Sakurajima, Japan. Journal of Disaster Research 14, 786–797. doi:10.20965/jdr.2019.p0786.

Poulidis, A.P., Takemi, T., Iguchi, M., Renfrew, I.A., 2017. Orographic effects on the transport and deposition of volcanic ash: A case study of Mount Sakurajima, Japan. Journal of Geophysical Research: Atmospheres 122, 9332–9350. doi:10.1002/2017JD026595.

Prata, A.J., 2009. Satellite detection of hazardous volcanic clouds and the risk to global air traffic. Natural Hazards 51, 303–324. doi:10.1007/s11069-008-9273-z.

Prata, A.J., Tupper, A., 2009. Aviation hazards from volcanoes: the state of the science. Natural Hazards 51, 239–244. doi:10.1007/s11069-009-9415-y.

Prata, F., Rose, B., 2015. Volcanic Ash Hazards to Aviation, in: The Encyclopedia of Volcanoes. Elsevier, pp. 911–934. doi:10.1016/B978-0-12-385938-9.00052-3.

Prata, F., Woodhouse, M., Huppert, H.E., Prata, A., Thordarson, T., Carn, S., 2017. Atmospheric processes affecting the separation of volcanic ash and SO2 in volcanic eruptions: inferences from the May 2011 Grímsvötn eruption. Atmospheric Chemistry and Physics 17, 10709–10732. doi:10.5194/acp-17-10709-2017.

Prival, J.M., Thouret, J.C., Japura, S., Gurioli, L., Bonadonna, C., Mariño, J., Cueva, K., 2020. New insights into eruption source parameters of the 1600 CE Huaynaputina Plinian eruption, Peru. Bulletin of Volcanology 82, 7. doi:10.1007/s00445-019-1340-7.

Pye, K., 1987. Aeolian dust and dust deposits. Academic Press, London ; Orlando.

Pyle, D.M., 1989. The thickness, volume and grainsize of tephra fall deposits. Bulletin of Volcanology 51, 1–15. doi:10.1007/BF01086757.

Rahimipour, H., Wilkinson, D., 1992. Dynamic behaviour of particle clouds. 11th Australasian Fluid Mechanics Conference University of Tasmania, Hobart, Australia .

Ramaprabhu, P., Andrews, M.J., 2004. Experimental investigation of RayleighTaylor mixing at small Atwood numbers. Journal of Fluid Mechanics 502, 233–271. doi:10.1017/S0022112003007419.

Ramos, V.A., 1999. Plate tectonic setting of the Andean Cordillera. Episodes 22, 183–190. doi:10.18814/epiiugs/1999/v22i3/005.

Ravichandran, S., Meiburg, E., Govindarajan, R., 2020. Mammatus cloud formation by settling and evaporation. Journal of Fluid Mechanics 899, A27. doi:10.1017/jfm.2020.439.

Reckziegel, F., Bustos, E., Mingari, L., Báez, W., Villarosa, G., Folch, A., Collini, E., Viramonte, J., Romero, J., Osores, S., 2016. Forecasting volcanic ash dispersal and coeval resuspension during the April–May 2015 Calbuco eruption. Journal of Volcanology and Geothermal Research 321, 44–57. doi:10.1016/j.jvolgeores.2016.04.033.

Reynolds, O., 1883. An experimental investigation of the circumstances which determine whether the motion of water shall be direct or sinuous, and of the law of resistance in parallel channels. Philosophical Transactions of the Royal Society of London 174, 935–982. doi:10.1098/rstl.1883.0029.

Ripepe, M., Bonadonna, C., Folch, A., Delle Donne, D., Lacanna, G., Marchetti, E., Höskuldsson, A., 2013. Ash-plume dynamics and eruption source parameters by infrasound and thermal imagery: The 2010 Eyjafjallajökull eruption. Earth and Planetary Science Letters 366, 112–121. doi:10.1016/j.epsl.2013.02.005.

Ristorcelli, J.R., Clark, T.T., 2004. Rayleigh–Taylor turbulence: self-similar analysis and direct numerical simulations. Journal of Fluid Mechanics 507, 213–253. doi:10.1017/S0022112004008286.

Rivera, M., Thouret, J.C., Samaniego, P., Le Pennec, J.L., 2014. The 2006–2009 activity of the Ubinas volcano (Peru): Petrology of the 2006 eruptive products and insights into genesis of andesite magmas, magma recharge and plumbing system. Journal of Volcanology and Geothermal Research 270, 122–141. doi:10.1016/j.jvolgeores.2013.11.010.

Roche, O., Carazzo, G., 2019. The contribution of experimental volcanology to the study of the physics of eruptive processes, and related scaling issues: A review. Journal of Volcanology and Geothermal Research 384, 103–150. doi:10.1016/j.jvolgeores.2019.07.011.

Rose, W.I., Durant, A.J., 2011. Fate of volcanic ash: Aggregation and fallout. Geology 39, 895–896. ISBN: 1943-2682 Publisher: Geological Society of America.

Ross, P.S., White, J., Valentine, G., Taddeucci, J., Sonder, I., Andrews, R., 2013. Experimental birth of a maar–diatreme volcano. Journal of Volcanology and Geothermal Research 260, 1–12. doi:10.1016/j.jvolgeores.2013.05.005.

Rossi, E., Bagheri, G., Beckett, F., Bonadonna, C., 2021. The fate of volcanic ash: premature or delayed sedimentation? Nature Communications 12, 1303. doi:10.1038/s41467-021-21568-8.

Ruggaber, G.J., 2000. Dynamics of particle clouds related to open-water sediment disposal. Ph.D. thesis. Massachusetts Institute of Technology.

Samaniego, P., Rivera, M., Mariño, J., Guillou, H., Liorzou, C., Zerathe, S., Delgado, R., Valderrama, P., Scao, V., 2016. The eruptive chronology of the Ampato–Sabancaya volcanic complex (Southern Peru). Journal of Volcanology and Geothermal Research 323, 110–128. doi:10.1016/j.jvolgeores.2016.04.038.

Saxby, J., Beckett, F., Cashman, K., Rust, A., Tennant, E., 2018. The impact of particle shape on fall velocity: Implications for volcanic ash dispersion modelling. Journal of Volcanology and Geothermal Research 362, 32–48. doi:10.1016/j.jvolgeores.2018.08.006.

Scasso, R.A., Corbella, H., Tiberi, P., 1994. Sedimentological analysis of the tephra from the 12–15 August 1991 eruption of Hudson volcano. Bulletin of Volcanology 56, 121–132. doi:10.1007/BF00304107.

Schneider, C.A., Rasband, W.S., Eliceiri, K.W., 2012. NIH Image to ImageJ: 25 years of image analysis. Nature Methods 9, 671–675. doi:10.1038/nmeth.2089.

Schultz, D.M., Kanak, K.M., Straka, J.M., Trapp, R.J., Gordon, B.A., Zrnić, D.S., Bryan, G.H., Durant, A.J., Garrett, T.J., Klein, P.M., Lilly, D.K., 2006. The Mysteries of Mammatus Clouds: Observations and Formation Mechanisms. Journal of the Atmospheric Sciences 63, 2409–2435. doi:10.1175/JAS3758.1.

Schumacher, R., Schmincke, H.U., 1995. Models for the origin of accretionary lapilli. Bulletin of Volcanology 56, 626–639. doi:10.1007/BF00301467.

Scollo, S., Bonadonna, C., Manzella, I., 2017. Settling-driven gravitational instabilities associated with volcanic clouds: new insights from experimental investigations. Bulletin of Volcanology 79. doi:10.1007/s00445-017-1124-x.

Scollo, S., Boselli, A., Coltelli, M., Leto, G., Pisani, G., Spinelli, N., Wang, X., 2012. Monitoring Etna volcanic plumes using a scanning LiDAR. Bulletin of Volcanology 74, 2383–2395. doi:10.1007/s00445-012-0669-y.

Scollo, S., Coltelli, M., Bonadonna, C., Del Carlo, P., 2013. Tephra hazard assessment at Mt. Etna (Italy). Natural Hazards and Earth System Sciences 13, 3221–3233. doi:10.5194/nhess-13-3221-2013.

Scollo, S., Prestifilippo, M., Bonadonna, C., Cioni, R., Corradini, S., Degruyter, W., Rossi, E., Silvestri, M., Biale, E., Carparelli, G., Cassisi, C., Merucci, L., Musacchio, M., Pecora, E., 2019. Near-Real-Time Tephra Fallout Assessment at Mt. Etna, Italy. Remote Sensing 11, 2987. doi:10.3390/rs11242987.

Scollo, S., Prestifilippo, M., Pecora, E., Corradini, S., Merucci, L., Spata, G., Coltelli, M., 2014. Eruption column height estimation of the 2011-2013 Etna lava fountains. Annals of Geophysics doi:10.4401/ag-6396.

Scollo, S., Tarantola, S., Bonadonna, C., Coltelli, M., Saltelli, A., 2008. Sensitivity analysis and uncertainty estimation for tephra dispersal models. Journal of Geophysical Research: Solid Earth 113.

Scott, J.A., Mather, T.A., Pyle, D.M., Rose, W.I., Chigna, G., 2012. The magmatic plumbing system beneath Santiaguito Volcano, Guatemala. Journal of Volcanology and Geothermal Research 237-238, 54–68. doi:10.1016/j.jvolgeores.2012.05.014.

Scott, W.D., Hopwood, J.M., Summers, K.J., 1995. A mathematical model of suspension with saltation. Acta Mechanica 108, 1–22. doi:10.1007/BF01177324.

Searcy, C., Dean, K., Stringer, W., 1998. PUFF: A high-resolution volcanic ash tracking model. Journal of Volcanology and Geothermal Research 80, 1–16. doi:10.1016/S0377-0273(97)00037-1.

Selby, M.J., 1982. Hillslope materials and processes. Oxford University Press, Oxford [Oxfordshire] ; New York.

Shao, Y., Lu, H., 2000. A simple expression for wind erosion threshold friction velocity. Journal of Geophysical Research: Atmospheres 105, 22437–22443. doi:10.1029/2000JD900304.

Shao, Y., Raupach, M.R., Findlater, P.A., 1993. Effect of saltation bombardment on the entrainment of dust by wind. Journal of Geophysical Research 98, 12719. doi:10.1029/93JD00396.

Sharp, D., 1984. An overview of Rayleigh-Taylor instability. Physica D: Nonlinear Phenomena 12, 3–18. doi:10.1016/0167-2789(84)90510-4.

Siebert, L., Simkin, T., Kimberly, P., 2010. Volcanoes of the world. 3rd ed ed., Smithsonian Institution, Washington, D.C. : Berkeley ; University of California Press. OCLC: ocn647772311.

Simionato, R., Jarvis, P.A., Rossi, E., Bonadonna, C., 2022. Plumetrap: A new matlab-based algorithm to detect and parametrize volcanic plumes from visible-wavelength images. Remote Sensing 14, 1766.

Sinclair, P.C., 1969. General Characteristics of Dust Devils. Journal of Applied Meteorology and Climatology 8, 32–45. doi:10.1175/1520-0450(1969)008<0032:GCODD>2.0.CO;2. place: Boston MA, USA Publisher: American Meteorological Society.

Snee, E., 2021. Volcanic plumes from explosive basaltic eruptions: the case of Mount Etna (Italy). PhD Thesis, Cardiff University.

Sparks, R.S.J., 1986. The dimensions and dynamics of volcanic eruption columns. Bulletin of Volcanology 48, 3–15. doi:10.1007/BF01073509.

Spence, R.J.S., Kelman, I., Baxter, P.J., Zuccaro, G., Petrazzuoli, S., 2005. Residential building and occupant vulnerability to tephra fall. Natural Hazards and Earth System Sciences 5, 477–494.

Stouse, P.A.D., 1971. Regional Specialization in Developing Areas: The Altiplano of Bolivia. Revista Geográfica , 51–70.

Sulpizio, R., Dellino, P., Doronzo, D., Sarocchi, D., 2014. Pyroclastic density currents: state of the art and perspectives. Journal of Volcanology and Geothermal Research 283, 36–65. doi:10.1016/j.jvolgeores.2014.06.014.

Sutherland, B.R., Gingras, M.K., Knudson, C., Steverango, L., Surma, C., 2018. Particle-bearing currents in uniform density and two-layer fluids. Physical Review Fluids 3, 023801. doi:10.1103/PhysRevFluids.3.023801.

Suzuki, Y.J., Koyaguchi, T., 2009. A three-dimensional numerical simulation of spreading umbrella clouds. Journal of Geophysical Research 114, B03209. doi:10.1029/2007JB005369.

Taddeucci, J., Alatorre-Ibargüengoitia, M.A., Cruz-Vázquez, O., Del Bello, E., Scarlato, P., Ricci, T., 2017. In-flight dynamics of volcanic ballistic projectiles: Volcanic Ballistic Projectiles. Reviews of Geophysics 55, 675–718. doi:10.1002/2017RG000564.

Taddeucci, J., Edmonds, M., Houghton, B., James, M.R., Vergniolle, S., 2015. Hawaiian and Strombolian Eruptions, in: The Encyclopedia of Volcanoes. Elsevier, pp. 485–503. doi:10.1016/B978-0-12-385938-9.00027-4.

Takemi, T., Poulidis, A.P., Iguchi, M., 2021. High–Resolution Modeling of Airflows and Particle Deposition over Complex Terrain at Sakurajima Volcano. Atmosphere 12, 325. doi:10.3390/atmos12030325.

Tesche, M., Glantz, P., Johansson, C., Norman, M., Hiebsch, A., Ansmann, A., Althausen, D., Engelmann, R., Seifert, P., 2012. Volcanic ash over Scandinavia originating from the Grímsvötn eruptions in May 2011: GRÍMSVÖTN VOLCANIC ASH OVER SCANDINAVIA. Journal of Geophysical Research: Atmospheres 117, n/a–n/a. doi:10.1029/2011JD017090.

Textor, C., Graf, H., Herzog, M., Oberhuber, J., Rose, W.I., Ernst, G., 2006. Volcanic particle aggregation in explosive eruption columns. Part I: Parameterization of the microphysics of hydrometeors and ash. Journal of Volcanology and Geothermal Research 150, 359–377. doi:10.1016/j.jvolgeores.2005.09.007.

Thorarinsson, S., 1944. Tefrokronologiska studier på Island: Þjórsárdalur och dess förödelse. Geografiska annaler 26, 1–217. ISBN: 2001-4422 Publisher: Taylor & Francis.

Thouret, J.C., Antoine, S., Magill, C., Ollier, C., 2020. Lahars and debris flows: Characteristics and impacts. Earth-Science Reviews 201, 103003. doi:10.1016/j.earscirev.2019.103003.

Thouret, J.C., Guillande, R., Huaman, D., Gourgaud, A., Salas, G., Chorowicz, J., 1994. L'Activite actuelle du Nevado Sabancaya (sud Perou); reconnaissance geologique et satellitaire, evaluation et cartographie des menaces volcaniques. Bulletin de la Société Géologique de France 165, 49–63.

Thouret, J.C., Juvigné, E., Gourgaud, A., Boivin, P., Dávila, J., 2002. Reconstruction of the AD 1600 Huaynaputina eruption based on the correlation of geologic evidence with early Spanish chronicles 1 1Data Repository at http://www.elsevier.com/locate/jvolgeores see 'Electronic Supplements'. Journal of Volcanology and Geothermal Research 115, 529–570. doi:10.1016/S0377-0273(01)00323-7.

Troy, C.D., Koseff, J.R., 2005. The generation and quantitative visualization of breaking internal waves. Experiments in Fluids 38, 549–562. doi:10.1007/s00348-004-0909-9.

Tsuji, T., Nishizaka, N., Ohnishi, K., 2020. Influence of particle aggregation on the tephra dispersal and sedimentation from the October 8, 2016, eruption of Aso volcano. Earth, Planets and Space 72, 104. doi:10.1186/s40623-020-01233-y.

Turner, J., 1967. Salt fingers across a density interface. Deep Sea Research and Oceanographic Abstracts 14, 599–611. doi:10.1016/0011-7471(67)90066-6.

Turner, J.S., 1962. The 'starting plume' in neutral surroundings. Journal of Fluid Mechanics 13, 356–368. doi:10.1017/S0022112062000762.

Turner, J.S., 1969. Buoyant Plumes and Thermals. Annual Review of Fluid Mechanics 1, 29–44. doi:10.1146/annurev.fl.01.010169.000333.

Turner, J.S., 1973. Buoyancy Effects in Fluids. 1 ed., Cambridge University Press. doi:10.1017/CBO9780511608827.

Valade, S., Harris, A., Cerminara, M., 2014. Plume Ascent Tracker: Interactive Matlab software for analysis of ascending plumes in image data. Computers & Geosciences 66, 132–144. doi:10.1016/j.cageo.2013.12.015.

Valdivia, D., 2019. Muestreo de cenizas en los alrededores del volcán Sabancaya.

Valentine, G., Gregg, T., 2008. Continental basaltic volcanoes — Processes and problems. Journal of Volcanology and Geothermal Research 177, 857–873. doi:10.1016/j.jvolgeores.2008.01.050.

Valentine, G.A., Wohletz, K.H., 1989. Numerical models of Plinian eruption columns and pyroclastic flows. Journal of Geophysical Research 94, 1867. doi:10.1029/JB094iB02p01867.

Varley, N., Arámbula-Mendoza, R., Reyes-Dávila, G., Sanderson, R., Stevenson, J., 2010. Generation of Vulcanian activity and long-period seismicity at Volcán de Colima, Mexico. Journal of Volcanology and Geothermal Research 198, 45–56. doi:10.1016/j.jvolgeores.2010.08.009.

Varley, N., Johnson, J., Ruiz, M., Reyes, G., Martin, K., 2006. Applying statistical analysis to understanding the dynamics of volcanic explosions. Statistics in volcanology 1, 57. ISBN: 1862392080 Publisher: Geological Society of London.

Vecino, M.C.D., Rossi, E., Freret-Lorgeril, V., Fries, A., Gabellini, P., Lemus, J., Pollastri, S., Poulidis, A.P., Iguchi, M., Bonadonna, C., 2022. Aerodynamic characteristics and genesis of aggregates at Sakurajima Volcano, Japan. Scientific Reports 12, 2044. doi:10.1038/s41598-022-05854-z.

Verosub, K.L., Lippman, J., 2008. Global Impacts of the 1600 Eruption of Peru's Huaynaputina Volcano. Eos, Transactions American Geophysical Union 89, 141. doi:10.1029/2008EO150001.

Völtz, C., Pesch, W., Rehberg, I., 2001. Rayleigh-Taylor instability in a sedimenting suspension. Physical Review E 65, 011404. doi:10.1103/PhysRevE.65.011404.

Waddell, J.T., Niederhaus, C.E., Jacobs, J.W., 2001. Experimental study of Rayleigh–Taylor instability: Low Atwood number liquid systems with single-mode initial perturbations. Physics of Fluids 13, 1263–1273. doi:10.1063/1.1359762.

Watt, S.F.L., Gilbert, J.S., Folch, A., Phillips, J.C., Cai, X.M., 2015. An example of enhanced tephra deposition driven by topographically induced atmospheric turbulence. Bulletin of Volcanology 77, 35. doi:10.1007/s00445-015-0927-x.

Weber, K., Eliasson, J., Vogel, A., Fischer, C., Pohl, T., van Haren, G., Meier, M., Grobéty, B., Dahmann, D., 2012. Airborne in-situ investigations of the Eyjafjallajökull volcanic ash plume on Iceland and over north-western Germany with light aircrafts and optical particle counters. Atmospheric Environment 48, 9–21. doi:10.1016/j.atmosenv.2011.10.030.

Whitehead, J.A., Luther, D.S., 1975. Dynamics of laboratory diapir and plume models. Journal of Geophysical Research (1896-1977) 80, 705–717. doi:10.1029/JB080i005p00705.

Wickens, G.E., 1995. Llareta (Azorella Compacta, Umbelliferae): A review. Economic Botany 49, 207–212. doi:10.1007/BF02862926.

Wilson, L., Sparks, R.S.J., Huang, T.C., Watkins, N.D., 1978. The control of volcanic column heights by eruption energetics and dynamics. Journal of Geophysical Research: Solid Earth 83, 1829–1836. doi:10.1029/JB083iB04p01829.

Wilson, P.N., Andrews, M.J., 2002. Spectral measurements of Rayleigh–Taylor mixing at small Atwood number. Physics of Fluids 14, 938–945. doi:10.1063/1.1445418.

Wilson, T.M., Cole, J.W., Stewart, C., Cronin, S.J., Johnston, D.M., 2011. Ash storms: impacts of wind-remobilised volcanic ash on rural communities and agriculture following the 1991 Hudson eruption, southern Patagonia, Chile. Bulletin of Volcanology 73, 223–239. doi:10.1007/s00445-010-0396-1.

Wilson, T.M., Jenkins, S., Stewart, C., 2015. Impacts from Volcanic Ash Fall, in: Volcanic Hazards, Risks and Disasters. Elsevier, pp. 47–86. doi:10.1016/B978-0-12-396453-3.00003-4.

Wilson, T.M., Stewart, C., Sword-Daniels, V., Leonard, G.S., Johnston, D.M., Cole, J.W., Wardman, J., Wilson, G., Barnard, S.T., 2012. Volcanic ash impacts on critical infrastructure. Physics and Chemistry of the Earth, Parts A/B/C 45, 5–23. doi:10.1016/j.pce.2011.06.006.

Wörner, G., Mamani, M., Blum-Oeste, M., 2018. Magmatism in the Central Andes. Elements 14, 237–244. doi:10.2138/gselements.14.4.237.

Yu, X., Hsu, T.J., Balachandar, S., 2013. Convective instability in sedimentation: Linear stability analysis. Journal of Geophysical Research: Oceans 118, 256–272. doi:10.1029/2012JC008255.

Yu, X., Hsu, T.J., Balachandar, S., 2014. Convective instability in sedimentation: 3-D numerical study. Journal of Geophysical Research: Oceans 119, 8141–8161. doi:10.1002/2014JC010123.

Zehentbauer, F.M., Moretto, C., Stephen, R., Thevar, T., Gilchrist, J.R., Pokrajac, D., Richard, K.L., Kiefer, J., 2014. Fluorescence spectroscopy of Rhodamine 6G: Concentration and solvent effects. Spectrochimica Acta Part A: Molecular and Biomolecular Spectroscopy 121, 147–151. doi:10.1016/j.saa.2013.10.062.

van Zelst, I., Crameri, F., Pusok, A.E., Glerum, A., Dannberg, J., Thieulot, C., 2022. 101 geodynamic modelling: how to design, interpret, and communicate numerical studies of the solid Earth. Solid Earth 13, 583–637. doi:10.5194/se-13-583-2022.

Zhang, P., Sherman, D.J., Li, B., 2021. Aeolian creep transport: A review. Aeolian Research 51, 100711. doi:10.1016/j.aeolia.2021.100711.

Zhang, Z., 1999. Flexible camera calibration by viewing a plane from unknown orientations, in: Proceedings of the Seventh IEEE International Conference on Computer Vision, IEEE, Kerkyra, Greece. pp. 666–673 vol.1. doi:10.1109/ICCV.1999.791289.

Zhao, B., Law, A., Adams, E., Er, J., 2014. Formation of particle clouds. Journal of Fluid Mechanics 746, 193–213. doi:10.1017/jfm.2014.121.

Zimmermann-Timm, H., 2002. Characteristics, Dynamics and Importance of Aggregates in Rivers – An Invited Review. International Review of Hydrobiology 87, 197–240. doi:10.1002/1522-2632(200205)87:2/3<197::AID-IROH197>3.0.CO;2-7.